



ΕΘΝΙΚΟ ΜΕΤΣΟΒΙΟ ΠΟΛΥΤΕΧΝΕΙΟ
ΤΜΗΜΑ ΜΗΧΑΝΟΛΟΓΩΝ ΜΗΧΑΝΙΚΩΝ
ΤΟΜΕΑΣ ΡΕΥΣΤΩΝ

ΔΙΠΛΩΜΑΤΙΚΗ ΕΡΓΑΣΙΑ
ΠΡΟΓΡΑΜΜΑ ERASMUS
ΕΜΠ
CITY UNIVERSITY LONDON

ΜΕΛΕΤΗ ΤΗΣ ΠΑΡΑΓΩΓΗΣ ΕΝΕΡΓΕΙΑΣ ΑΠΟ ΤΗΝ ΟΣΜΩΤΙΚΗ
ΠΙΕΣΗ ΜΕ ΧΡΗΣΗ ΥΠΟΛΟΓΙΣΤΙΚΗΣ ΡΕΥΣΤΟΜΗΧΑΝΙΚΗΣ (CFD)

ΣΤΕΦΑΝΙΤΣΗΣ ΔΙΟΝΥΣΙΟΣ

ΑΘΗΝΑ 2012

**NATIONAL TECHNICAL UNIVERSITY OF ATHENS
SCHOOL OF MECHANICAL ENGINEERING
FLUIDS SECTION**

DIPLOMA THESIS

ERASMUS Program

**NATIONAL TECHNICAL UNIVERSITY OF ATHENS
CITY UNIVERSITY LONDON
March-September 2011**

**Power Production through the Utilization of the Pressure
Retarded Osmosis (PRO) Concept-
Computational Fluid Dynamics Simulations in PRO Systems**

DIONYSIOS STEFANITSIS

Athens 2012

TABLE OF CONTENTS

ACKNOWLEDGMENTS	7
OBJECTIVES	7
CHAPTER 1. INTRODUCTION.....	8
1.1 Energy Supply and Demand Status.....	8
CHAPTER 2. RENEWABLE ENERGY TECHNOLOGIES.....	9
2.1 Ocean Energy Technologies.....	10
2.2 Ocean Thermal Energy Conversion.....	10
2.3 Tidal Energy.....	11
2.4 Wave Energy.....	11
2.5 Solar Energy Technologies.....	12
2.5.1 Photovoltaics.....	12
2.5.2 Concentrating Solar Power.....	12
2.5.3 Solar Energy Resources.....	13
2.6 Thermoelectric power.....	14
2.7 Osmotic power.....	14
2.8 Renewables in Electricity Production.....	15
CHAPTER 3. PRESSURE RETARDED OSMOSIS (PRO).....	16
3.1 Introduction.....	16
3.2 Basic principles of pressure retarded osmosis.....	17
3.2.1 Mixing of freshwater and seawater.....	17
3.2.2 Definition of osmosis and osmotic pressure.....	17
3.2.3 Osmotic processes.....	18
3.2.4 Osmotic pressure and power generation in PRO.....	19
3.3 Membrane theory.....	20
3.3.1 Definition of a membrane.....	20
3.3.2 Structure of osmotic membranes.....	21
3.3.3 Water flux in PRO under real conditions – The effect of salt permeability and concentration polarization (PRO model).....	21
3.3.4 Power density in PRO under real conditions.....	24
3.3.5 Membrane fouling.....	25
3.3.6 Membrane module.....	25
3.3.7 Membrane types in PRO applications.....	30
3.3.8 Recent experiments by using a small laboratory-scale apparatus.....	32
CHAPTER 4. PRESSURE RETARDED OSMOSIS (PRO) POWER PLANT.....	40
4.1 Description.....	40
4.2 Location.....	41
4.3 Power generated and cost.....	43

4.4 Size.....	44
4.5 The first PRO power plant.....	44
CHAPTER 5. GEOMETRY, MODELING, EXPERIMENTAL.....	48
5.1 Description of the geometry	48
5.2 Modeling.....	51
5.2.1 Modeling the flow of water on both sides.....	51
5.2.2 Modeling the flow through the membrane.....	52
5.2.3 Modeling the diffusion of freshwater in saltwater.....	52
5.3 Experimental Setup.....	52
CHAPTER 6. CFD SIMULATIONS.....	56
6.1 Solid Works 2010.....	56
6.2 Gambit 2.4.6.....	57
6.3 ANSYS FLUENT 12.....	58
6.3.1 FLUENT 12 Solver Theory.....	58
6.3.2 Applied settings and configurations in FLUENT 12.....	88
for the current project	
6.4 Techplot 360.....	90
CHAPTER 7. RESULTS & DISCUSSION.....	91
7.1 Cases 1-3.....	93
7.1.1 Simulation Conditions.....	93
7.1.2 Grid Sensitivity Study	93
7.1.2.1 Results of the grid sensitivity study.....	94
7.1.3 Results and discussion cases 1-3.....	98
7.1.3.1 Flow Field.....	98
7.2 Case 4	99
7.2.1 Simulation Conditions.....	99
7.2.2 Results and discussion.....	101
7.2.2.1 Flow field	101
7.3 Cases 5-10.....	105
7.3.1 Simulation Conditions.....	105
7.3.1.1 Boundary Condition on the membrane surface.....	106
7.4 Case 5.....	107
7.4.1 Boundary Conditions on the inlet and outlet.....	107
7.4.2 Results and discussion	107
7.4.2.1 Volumetric flow rate through the membrane	107
and generated power	
7.4.2.2 Flow field	107
7.5 Case 6.....	111
7.5.1 Boundary conditions on the inlet and outlet.....	111
7.5.2 Results and discussion.....	111
7.5.2.1 Volumetric flow rate through the membrane	
and generated power.....	111
7.5.2.2 Flow field.....	111
7.6 Case 7.....	111

7.6.1 Boundary conditions on the inlet and outlet.....	111
7.6.2 Results and discussion.....	111
7.6.2.1 Volumetric flow rate through the membrane and generated power.....	111
7.6.2.2 Flow field.....	111
7.7 Case 8.....	112
7.7.1 Boundary conditions on the inlet and outlet.....	112
7.7.2 Results and discussion.....	112
7.7.2.1 Volumetric flow rate through the membrane and generated power.....	112
7.7.2.2 Flow field.....	112
7.8 Case 9.....	113
7.8.1 Boundary conditions on the inlet and outlet.....	113
7.8.2 Results and discussion.....	113
7.8.2.1 Volumetric flow rate through the membrane and generated power	113
7.8.2.2 Flow field.....	113
7.9 Cases 5-9 Parametric Diagrams.....	116
7.9.1 Diagrams i and ii.....	116
7.9.1.1 Discussion of the results	118
7.9.2 Diagram iii.....	118
7.9.2.1 Discussion of the results.....	119
7.9.3 Diagram iv.....	119
7.9.3.1 Discussion of the results	120
7.10 Case 10.....	120
7.10.1 Boundary conditions.....	120
7.10.2 Results and discussion.....	121
7.10.2.1 Volumetric flow rate through the membrane and generated power.....	121
7.10.2.2 Flow field.....	121
7.11 Cases 11-12.....	121
7.11.1 Boundary conditions.....	121
7.11.2 Case 11 design No. 2.....	121
7.11.2.1 Flow field.....	122
7.11.3 Case 12 design No.3	125
7.11.3.1 Flow field.....	125
7.11.4 Comparison of the three designs – cases 9, 11, 12.....	127
7.11.4.1 Discussion of the results.....	128
7.12 Volumetric flow rate through the membrane calculated for each different grid density	128
7.12.1 Discussion of the results.....	128
7.13 Volumetric flow rate through the membrane calculated	129
for each different spatial discretization method of the momentum equation in FLUENT 12	
7.13.1 Discussion of the results.....	129
CHAPTER 8. CONCLUSIONS & FUTURE WORK.....	129
8.1 Summary of the final results.....	129
8.2 Conclusions & Future Work.....	131
8.2.1 Accuracy of the CFD model using FLUENT 12	131

and future improvements	
8.2.2 Relation between the flow from the inlet135	135
and the flow through the membrane -	
the need for optimization	
8.2.3 Modification of the design136	136
and further investigation for its improvement	
8.2.4 Effect of the performance of the membrane.....137	137
and the salt concentration difference in the PRO process	
8.2.5 Overview137	137
REFERENCES.....138	138
ABSTRACT.....141	141
APPENDIX.....142	142
ΕΚΤΕΤΑΜΕΝΗ ΠΕΡΙΛΗΨΗ ΣΤΑ ΕΛΛΗΝΙΚΑ.....144	144

ACKNOWLEDGMENTS

This Diploma Thesis was performed in the School of Engineering & Mathematical Sciences of City University of London in the framework of the ERASMUS program between NTUA and CUL.

This work consists of 8 chapters in particular Chapters 2,3,4 are a literature review of the subject while paragraphs marked with the relevant literature have been transferred unchanged from the publication. Chapters 5-8 are the experimental part and the results of this study.

First of all, I would like to thank my supervisor Prof. George Bergeles (NTUA) for the assignment of the subject of my Diploma Thesis, giving me the opportunity to work with his group, helped me with his academic insights and ongoing scientific guidance. Also, I am especially thankful to co-supervisor Prof. Manolis Gavaises, Director of the Energy & Transport Research Center of CUL who welcomes me in his Laboratory at CUL and guided me through the process of thesis.

In particular, I would like to thank Dr. Dimitris Papoulias, CUL for imparting me some of his knowledge of Computational Fluid Dynamics and supported me to complete this thesis.

Finally, I want to thank my family and friends for their moral support.

OBJECTIVES

The subject of this Diploma Thesis is the study of renewable energy production through the utilization of the Pressure Retarded Osmosis (PRO) concept. The utilization of renewable energy is a key subject of research conducted worldwide and pressure retarded osmosis is a technology known for years which came into the surface recently because of the energy crisis.

Osmosis is the flow of water from a low salt concentration solution (e.g. freshwater) to a high salt concentration solution (e.g. seawater) across a selectively permeable membrane (permeable for water, non-permeable for salt), driven by a difference in pressure, called osmotic pressure. Osmotic pressure is attributed to the salt concentration difference across the membrane and is triggered by Nature's force to establish equilibrium between different concentrations in liquids. Power is produced by depressurizing a portion of the diluted seawater in a turbine. Provided that PRO technology is applied to the river estuaries it can produce renewable, carbon-free, stable power 24 hours a day, for the whole year and also it can produce power in places where other renewable energy sources are not efficient enough.

The idea of PRO dates in the mid-1950s, but only a few researches have been done since then, mainly due to the unsuitable membranes. Researches have been focused on testing different membranes and modules, and also on the design of models to describe the PRO concept and evaluate what is needed to increase its efficiency. The design of the membrane and module, and also that flow conditions of the freshwater and seawater play a very important role.

This work aims, for the first time, to simulate the performance of Pressure Retarded Osmosis (PRO) process in a specially designed PRO test cell by using Computational Fluid Dynamic (CFD). Also, the effects of key parameters, namely the pressure, volumetric flow and concentration of salt in the seawater, and also the membrane characteristics, on the performance of the process will be investigated. In addition, the effect of the design of the PRO

test cell will be studied, by testing different designs. The accuracy and precision of the results will also be examined.

CHAPTER 1.

INTRODUCTION

1.1 Energy Supply and Demand Status

Human society, like any system composed of dynamic processes, depends on an external energy source. Historically, that source has always been the sun, which provides heat, light, and photosynthesis for food to support work energy by man and animal, and affects wind and water motion. Since the early 19th century, though, the discovery of and access to a vast supply of fossil fuels has enabled the industrial revolution, near exponential growth of population, technologies, and wealth. That period could well be named the energy revolution [1]. But over the past few years, awareness has grown that the availability of oil and gas may remain limited as a result of a variety of political and economic impediments, while world demand for oil and gas will continue to grow. The 1973 oil crisis confronted several European countries with their reliance on oil. It made them realize that a steady supply of fossil energy sources could easily be jeopardized by geo-political disturbances. Governments re-evaluated their energy policies, and security of supply became an important issue. Policy attention and financial support was mostly directed towards nuclear power. Several geopolitical and economic developments in the first decade of the twenty-first century have heightened Europe's sense of vulnerability in respect to its energy supplies. On the demand side, China's and India's growing energy consumption and their efforts to secure supplies have intensified global competition over scarce fossil based resources. These changes in the landscape of the global energy market, in combination with diminishing supply due to shrinking spare capacity and a low level of investment, have driven oil and natural gas prices up [2].

The energy debate also takes shape in a different context. In 1972 the Club of Rome commissioned the study *The Limits of Growth*, which concluded that if growth trends in world population, industrialization, pollution, food production and resource depletion were to continue, the limits to growth on earth would be reached within a hundred years [3]. So, in response to increasing environmental concerns and to the perceived need to improve self-reliance in energy supply, also the potential of domestic renewable energy sources was explored. Globally, in the 1980s there arose growing concerns about anthropogenic climate change. In 1987, the Brundtland commission of the United Nations Commission on Environment and Development (UNCED) published *Our Common Future*. Hereby they drew attention to the need for economic development without limiting the ability of future generations to meet their needs [4]. Sustainable development was presented as a positive-sum picture. Economic growth, environmental protection, distributive justice and long-term sustainability could be mutually reinforcing [5]. To reach sustainable development, technological, social and institutional changes would be needed. The concerns about climate change also generated attention for renewable energy sources. In 1992, the UNCED Conference in Rio de Janeiro presented *Agenda 21*, a follow-up on the Brundtland report. It stressed the need to involve people at the level of the communities in order to deal with global environmental challenges. The Rio Conference resulted in the United Nations Framework Convention on Climate Change, a treaty that aims at reducing greenhouse gas emissions. This treaty was the predecessor of the Kyoto protocol. Several meetings in Kyoto (1997), Bonn (1999), and The Hague (2000) showed how difficult it was to make internationally binding agreements on emission reduction.

Due to growing international environmental concerns, the EU concentrated on climate change issues. The EU dedicated itself to reducing greenhouse gas emissions by 8 % below the 1990

level in the period from 2008 to 2012. Increase of the use of renewable energy sources was regarded as an important part of the set of measures needed to meet the Kyoto Protocol. In 1997, the European Commission published a White Paper on Renewable Energy, in which the Commission stated that the dependence on energy imports is already 50 percent and expected to be 70 percent in 2020. The directive aims to increase the EU's share of electricity produced from renewable energy sources from 15 % in 2001 to 21 %, and to reach a 12 % energy consumption from renewable energy sources by 2010 [6]. Moreover, the "Green Paper" on energy efficiency of July 22, 2005 describes if the energy consumption reduced by about 20% in the European Union by 2020 will save a total of around 60 billion € annually [7]. So no one understands how important this issue is not only the environment but also for the economy.

Renewable energy resources could provide an enormous potential for energy generation. They also offer the possibility to address environmental problems associated with the generation, transportation, supply and use of fossil energy resources. The burning of fossil fuels is the main anthropogenic source of carbon dioxide (CO₂) and the electricity sector is responsible for a third of these CO₂ emissions. Although technological innovations have decreased these emissions per unit the use of fossil fuels accounts for more than 80 percent of overall energy supply in most industrialized countries [8]. Transition towards a more sustainable energy system would involve cleaner use of fossil fuels, energy efficiency and saving and the development of renewable energy sources.

CHAPTER 2

RENEWABLE ENERGY TECHNOLOGIES

Renewable energy technologies produce sustainable, clean energy from sources such as the sun, the wind, plants, and water. Renewable energy technologies have the potential to strengthen energy security, improve environmental quality, and contribute to a strong energy economy [1]. The main technologies are:

- Biomass
- Geothermal
- Hydrogen
- Hydropower
- Ocean
- Solar Energy
- Wind
- Thermoelectric
- Pressure Retarded Osmosis

2.1 Ocean Energy Technologies



Oceans cover more than 70% of the Earth's surface. As the world's largest solar collectors, oceans contain thermal energy from the sun and can produce mechanical energy from tides and waves. Even though the sun affects all ocean activity, the gravitational pull of the moon primarily drives tides, and wind powers ocean waves. Ocean energy technologies include:

- Ocean Thermal Energy Conversion
- Tidal Energy
- Wave Energy
- Ocean Resources

2.2 Ocean Thermal Energy Conversion

A process called *ocean thermal energy conversion* (OTEC) uses the heat energy stored in the Earth's oceans to generate electricity.

OTEC works best when the temperature difference between the warmer, top layer of the ocean and the colder, deep ocean water is about 20°C. These conditions exist in tropical coastal areas, roughly between the Tropic of Capricorn and the Tropic of Cancer. To bring the cold water to the surface, ocean thermal energy conversion plants require an expensive, large-diameter intake pipe, which is submerged a mile or more into the ocean's depths.

Some energy experts believe that if ocean thermal energy conversion can become cost-competitive with conventional power technologies, it could be used to produce billions of watts of electrical power.

2.3 Tidal Energy



Some of the oldest ocean energy technologies use tidal power. All coastal areas experience two high tides and two low tides over a period of slightly more than 24 hours. For those tidal differences to be harnessed into electricity, the difference between high and low tides must be more than 16 feet (or at least 5 meters). However, there are only about 40 sites on Earth with tidal ranges of this magnitude.

2.4 Wave Energy



Wave energy technologies extract energy directly from surface waves or from pressure fluctuations below the surface. Renewable energy analysts believe there is enough energy in ocean waves to provide up to 2 terawatts of electricity.

However, wave energy cannot be harnessed everywhere. Wave power-rich areas of the world include the western coasts of Scotland, northern Canada, southern Africa, and Australia as well as the northeastern and northwestern coasts of the United States. In the Pacific Northwest alone, it is feasible that wave energy could produce 40–70 kilowatts (kW) per meter of western coastline.

2.5 Solar Energy Technologies

Solar energy technologies produce electricity from the energy of the sun. Small solar energy systems can provide electricity for homes, businesses, and remote power needs. Larger solar energy systems provide more electricity for contribution to the electric power system:

- Photovoltaics
- Concentrating Solar Power
- Solar Energy Resources

2.5.1 Photovoltaics

Photovoltaic (PV) materials and devices convert sunlight into electrical energy, and PV cells are commonly known as solar cells. Photovoltaics can literally be translated as light-electricity.

First used in about 1890, "photovoltaic" has two parts: *photo*, derived from the Greek word for light, and *volt*, relating to electricity pioneer Alessandro Volta. And this is what photovoltaic materials and devices do—they convert light energy into electrical energy, as French physicist Edmond Becquerel discovered as early as 1839.

Becquerel discovered the process of using sunlight to produce an electric current in a solid material. But it took more than another century to truly understand this process. Scientists eventually learned that the photoelectric or photovoltaic effect caused certain materials to convert light energy into electrical energy at the atomic level.

PV systems are already an important part of our daily lives. Simple PV systems provide power for small consumer items such as calculators and wristwatches. More complicated systems provide power for communications satellites, water pumps, and the lights, appliances, and machines in some homes and workplaces. Many road and traffic signs also are now powered by PV. In many cases, PV power is the least expensive form of electricity for these tasks.

2.5.2 Concentrating Solar Power

Concentrating solar power (CSP) technologies use mirrors to reflect and concentrate sunlight onto receivers that collect solar energy and convert it to heat. This thermal energy can then be used to produce electricity via a steam turbine or heat engine that drives a generator.

Concentrating solar power offers a utility-scale, firm, dispatchable renewable energy option. CSP plants produce power by first using mirrors to focus sunlight to heat a working fluid. Ultimately, this high-temperature fluid is used to spin a turbine or power an engine that drives a generator. The final product is electricity.



Fig. 2.1 this solar concentrator has a fixed-focus faceted dish with a concentration of about 250 suns. This system can be used for large fields connected to the utility grid, hydrogen generation, or water pumping. [2]

Smaller CSP systems can be located directly where power is needed. For example, single dish/engine systems can produce 3 to 25 kilowatts of power and are well suited for distributed applications.

There are several varieties of CSP systems:

- Linear Concentrator Systems
- Dish/Engine Systems
- Power Tower Systems
- Thermal Storage Systems.

2.5.3 Solar Energy Resources

Solar radiation, often called the solar resource, is a general term for the electromagnetic radiation emitted by the sun. Solar radiation can be captured and turned into useful forms of energy, such as heat and electricity, using a variety of technologies. However, the technical feasibility and economical operation of these technologies at a specific location depends on the available solar resource.

2.6 Thermoelectric power

Thermoelectric modules can be used to convert heat energy to electricity. Using a principle known as "the Seebeck Effect" a temperature differential between the two sides of a thermoelectric module, electricity can be generated. Because this type of system depends upon a consistent temperature differential to provide electricity, the modules are often combined with a known heat source such as natural gas or propane for remote power generation or waste heat recovery. They are often used in remote locations where power is required but solar energy is unreliable or insufficient, such as offshore engineering, oil pipelines, remote telemetry and data collection.

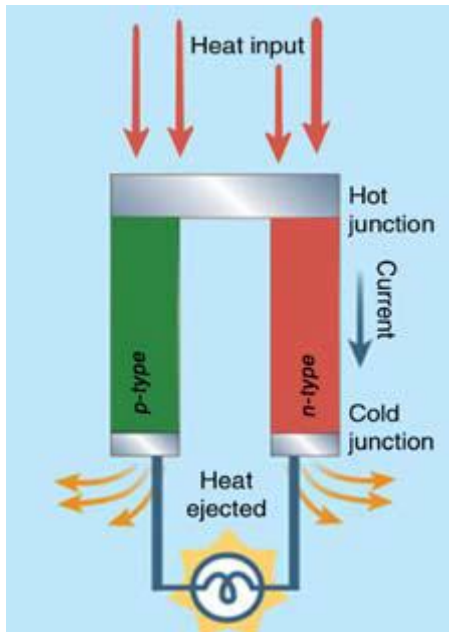


Fig. 2.2 TEG based on the Seebeck effect.

A device of this type is commonly referred to as a thermoelectric generator (TEG). The temperature difference (ΔT) between the hot and cold sources leads to a difference in the Fermi energy (ΔE_F) across the thermoelectric material yielding a potential difference, which drives a current.

2.7 Osmotic power

Osmotic power or **salinity gradient power** is the energy available from the difference in the salt concentration between seawater and river water. Two practical methods for this are reverse electrodialysis (RED) and pressure-retarded osmosis (PRO).

Both processes rely on osmosis with ion specific membranes. The key waste product is brackish water. This byproduct is the result of natural forces that are being harnessed: the flow of fresh water into seas that are made up of salt water.

The technologies have been confirmed in laboratory conditions. They are being developed into commercial use in the Netherlands (RED) and Norway (PRO). The cost of the membrane has been an obstacle. A new, cheap membrane, based on an electrically modified polyethylene plastic, made it fit for potential commercial use.

Other methods have been proposed and are currently under development. Among them, a method based on electric double-layer capacitor technology and a method based on vapor pressure difference.

2.8 Renewables in Electricity Production

Fig. 2.3 presents the data on 2008 worldwide renewable-energy sources.

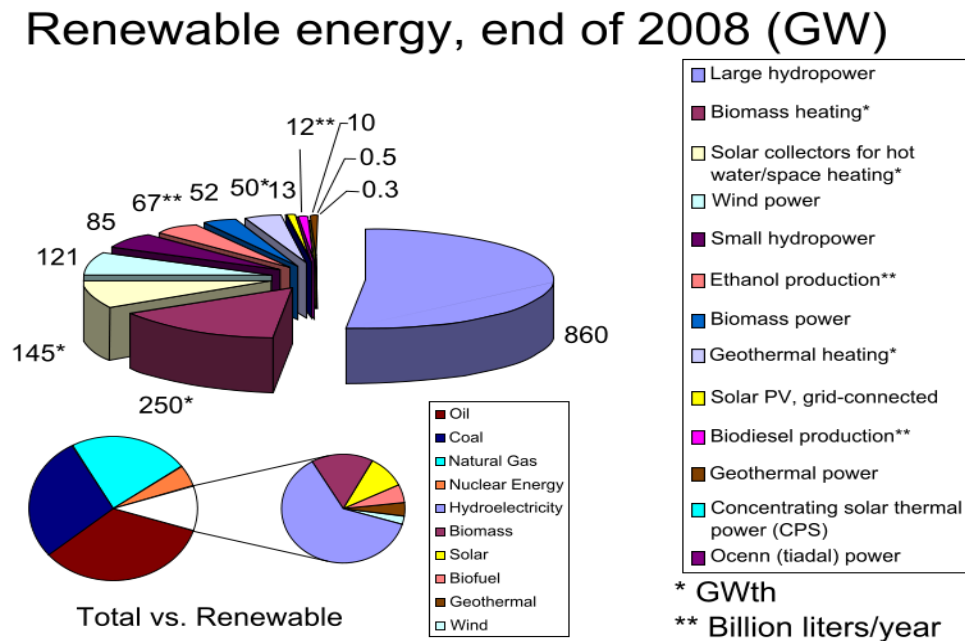


Fig. 2.3 2008 worldwide renewable-energy sources. [3]

In 2010, renewable energy supplied an estimated 16% of global final energy consumption and delivered close to 20% of global electricity. Renewable capacity now comprises about a quarter of total global power-generating capacity [4].

Global solar PV production and markets more than doubled in comparison with 2009, thanks to government incentive programs and the continued fall in PV module prices.

Globally, wind power added the most new capacity (followed by hydropower and solar PV), but for the first time ever, Europe added more PV than wind capacity.

Renewable energy policies continue to be the main driver behind renewable energy growth. By early 2011, at least 119 countries had some type of policy target or renewable support policy at the national level, more than doubling from 55 countries in early 2005. More than half of these countries are in the developing world [5].

CHAPTER 3

PRESSURE RETARDED OSMOSIS (PRO)

Osmosis, Basic principles of PRO, Membrane theory

3.1 Introduction

It has been known for centuries that the mixing of freshwater and seawater releases energy. For example will a river flowing into the salty ocean releases large amounts of energy. The challenge is to utilise this energy, since the energy released from the occurring mixing only gives a very small increase in the local temperature of the water. During the last few decades at least two concepts for converting this energy into electricity instead of heat has been identified. These are Reversed Electro dialysis and Pressure Retarded Osmosis (PRO) [1].

Osmosis is a physical phenomenon that has been exploited by human beings since the early days of mankind. Early cultures realized that salt could be used to desiccate foods for long-term preservation. In saline environments, most bacteria, fungi, and other potentially pathogenic organisms become dehydrated and die or become temporarily inactivated because of osmosis. Conventionally, osmosis is defined as the net movement of water across a selectively permeable membrane driven by a difference in osmotic pressure across the membrane. Present-day applications of the osmosis phenomenon extend from water treatment and food processing to power generation and novel methods for controlled drug release [2].

For Pressure Retarded Osmosis (PRO), also known as osmotic power, the released chemical energy is transferred into pressure instead of heat. The concept of harvesting energy generated during mixing of fresh and salt water was developed in the mid-1950s. Following the 1973 oil crisis, the interest in PRO for power generation spiked and led to several investigations of the technical and economic feasibility of PRO. Prof. Sidney Loeb in the early 70's designed the world's first semi-permeable membrane for desalination purposes using reverse osmosis. However, the lack of suitable membranes and modules hindered the efforts to establish PRO technology [3]. After this research limited effort has been made to bring this technology to a commercial level. There have been some minor studies and testing, but it was not until 2009 when the first prototype instalation of PRO was established in Norway that the development picked up momentum. Since this work started around 1996, research has been focused on designing a suitable membrane for PRO, and at the same time researchers have worked with system design and several studies of the feasibility of the concept as a commercial source of energy. The development of an efficient membrane for osmotic power has been the major focus of these efforts. The current power density of the membrane is approximately 3 W/m^2 , which is up from less than 0.1 W/m^2 a few years back, while the target is 5 W/m^2 , which combined with other technological improvements it is estimated that would make osmotic power costs comparable to those of other new renewable sources.

In osmotic power one can utilise the natural occurring osmosis. Sea water and fresh water have a strong force towards mixing, and this will occur as long as the pressure difference between the liquids is less than the osmotic pressure difference. For sea water and fresh water this would be in the range of 24 to 26 bars based on the salt concentration of sea water [1]. By using PRO technology it will be possible to utilise the enormous potential of a new, renewable energy source. With a constant supply of electricity, 24 hours per day, independent of weather conditions, on global basis this potential represents the production of more than 1600-1700 TWh of electricity per year (180 TWh in Europe), while the estimated global energy production from all renewable sources is approaching 10,000 TWh per year [4], [5].

3.2 Basic principles of pressure retarded osmosis

3.2.1 Mixing of freshwater and seawater

Freshwater that flows into the sea is mixed irreversibly with seawater. The enthalpy of mixing for these fluids is close to 0. The temperature in the mixing zone will depend on the temperature of the freshwater, the seawater temperature and the effective mixing volumes. If the **mixing** process is performed in a reversible manner in a device constructed specifically for the purpose, work can be extracted. The change in Gibbs free energy for mixing 1 mol of freshwater with an infinite amount of seawater can be expressed by

$$\Delta G_{\text{mix}} = R \cdot T \cdot \ln x_{\text{H}_2\text{O}} \quad (3.1)$$

assuming ideal fluids and where $x_{\text{H}_2\text{O}}$ is the mole fraction of water in the seawater. Seawater has the same osmoticity (An indirect measure of the osmotic characteristics of a solution, in terms of a comparable sodium chloride solution) as a solution of 32 gNaCl/l. In this solution the concentrations of NaCl and water are 0.549 (1.1 equiv. of ions) and 54.92 mol/l, respectively. At 20 °C the values given above inserted into eq. (3.1) gives $\Delta G_{\text{mix}} = -48.1 \text{ J/mol}$ or -2.7 kJ/kg freshwater. This amount of energy can be extracted as work in a device that mixes freshwater and saltwater reversibly. With a molar volume of water of $18 \cdot 10^{-6} \text{ m}^3/\text{mol}$ this corresponds to an osmotic pressure (see section 3.2.2) of 26.7 bar (ideal solution).

The mixing process of freshwater and seawater will be close to adiabatic, i.e. there is no heat exchange with the surroundings ($dq = 0$). Since the enthalpy of mixing is close to 0 and work (dw) is extracted from the process, the law of energy conservation gives:

$$dE = c_p \cdot dT = dq + dw = dw \quad (3.2)$$

where dE is the change in internal energy and c_p is the heat capacity of the system. Extraction of work from the mixing process will result in a cooling of the mixture according to eq. (2). Assume that, e.g. 1 mol of freshwater is mixed with 3 mol of seawater, less than 48.1 J can be extracted from the process: with a heat capacity of 4.18 J/g the close to 72 g diluted seawater (4mol) will be cooled by less than 0.17 °C. In a process optimised for energy production less than half of the reversible work will be taken out and the corresponding mixture thus will be cooled less than 0.08 °C [6].

3.2.2 Definition of osmosis and osmotic pressure

Osmosis is the movement of water molecules through a selectively-permeable membrane down a water potential gradient. More specifically, it is the movement of water across a selectively permeable membrane from an area of high water potential (low solute concentration) to an area of low water potential (high solute concentration). It is a physical process in which a solvent moves, without input of energy, across a semipermeable membrane (permeable to the

solvent, but not the solute) separating two solutions of different concentrations. Osmosis is a passive process, like diffusion.

Net movement of solvent is from the less-concentrated to the more-concentrated solution, triggered by Nature's drive to establish equilibrium between different concentrations in liquids. The **osmotic pressure** is defined to be the pressure which if applied as a hydraulic pressure to the more concentrated solution, would prevent net transport of solvent across the membrane. Osmotic pressure is a colligative property, meaning that the osmotic pressure depends on the molar concentration of the solute but not on its identity [7].

3.2.3 Osmotic processes

There are three **types** of osmotic processes: forward osmosis (FO), reverse osmosis (RO) and pressure retarded osmosis (PRO).

Forward osmosis uses the osmotic pressure differential ($\Delta\pi$) across the membrane as the driving force for transport of water through the membrane. The FO process results in concentration of a low concentrated stream (referred to as feed stream) and dilution of a highly concentrated stream (referred to as the draw solution). Flux in FO is from the feed solution to the draw solution. In the literature appear applications on the use of FO for water treatment/Engineering but not as much as those of RO [3].

Reverse osmosis uses hydraulic pressure (ΔP) to oppose, and exceed, the osmotic pressure of an aqueous feed solution (in RO, the feed solution is the high concentrated) to produce purified water. In RO, the applied pressure is the driving force for mass transport through the membrane. Flux in RO is in the opposite direction of FO. Numerous publications on the use of RO for water treatment and wastewater reclamation appear in the literature [2].

Pressure retarded osmosis can be viewed as an intermediate process between FO and RO, hydraulic pressure is applied to the draw solution (similar to RO) but the net water flux is still in the direction of the concentrated draw solution (similar to FO).

The **general equation** describing water transport in FO, RO, and PRO is

$$J_w = A \cdot (\Delta\pi - \Delta P) \quad (3.3)$$

where J_w is the water flux, A is the water permeability coefficient of the membrane, $\Delta\pi$ the osmotic pressure differential and ΔP the hydraulic pressure differential across the membrane. For FO, ΔP is zero; for RO, $\Delta P > \Delta\pi$; and for PRO, $\Delta P < \Delta\pi$. The flux reversal point occurs where $\Delta P = \Delta\pi$. The flux directions of the permeating water in FO, PRO, and RO are illustrated in fig.3.1 [3].

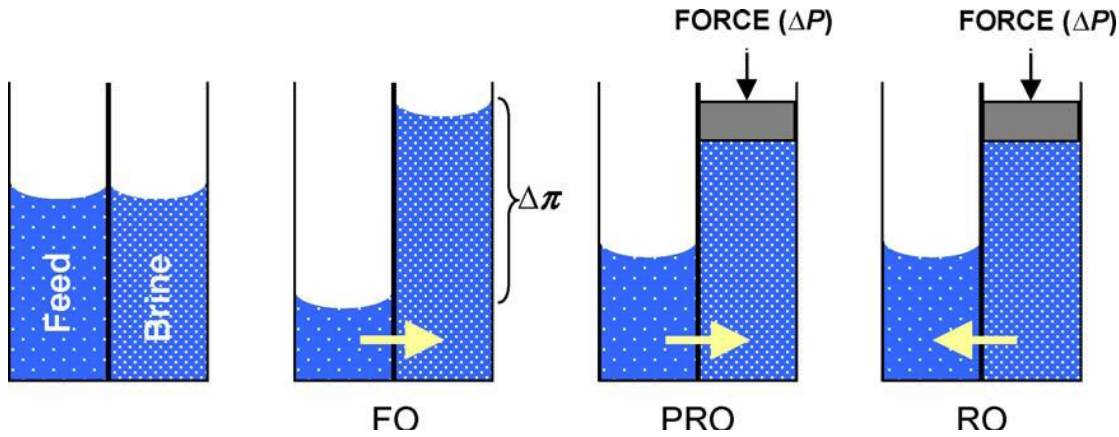


Fig. 3.1 Solvent flows in FO, PRO, and RO [2].

Flux directions and driving forces for the three processes were characterized in the early 1980s by Lee. The FO point, PRO zone, and RO zone, along with the flux reversal point, are illustrated in fig. 3.1.

3.2.4 Osmotic pressure and power generation in PRO

In PRO, the driving force is capable of elevating the salt water level above the fresh water level, whereas the potential energy is obtained from the static water height. The process stops when the hydraulic pressure is equal to the potential osmotic pressure of the salt water.

Osmotic pressure (Π_{osmotic}) can be calculated by the van't Hoff equation (for dilute solutions):

$$\Pi_{\text{osmotic}} = 2 \cdot c_{\text{NaCl}} \cdot R \cdot T \quad (3.4)$$

where R is the gas constant, T , the absolute temperature and c the concentration of NaCl. For a 35 g/l NaCl solution, which is approximately the concentration of salt in sea water, eq. (3.4) gives a theoretical osmotic pressure of 29 bars (2.9×10^6 Pa) at 20°C. This corresponds to a water column of 296m [8].

The **power** that can be generated per unit membrane area (i.e., the power density) is equal to the product of the water flux and the hydraulic pressure differential across the membrane:

$$W = J_w \cdot \Delta P = A \cdot (\Delta \pi - \Delta P) \cdot \Delta P \quad (3.5)$$

By differentiating eq. (3.5) with respect to ΔP , it can be shown that W reaches a maximum when $\Delta P = \Delta \pi / 2$. (fig. 3.2) Substituting this value for ΔP in eq. (3.5) yields:

$$W_{\text{max}} = A \cdot \frac{\Delta \pi^2}{4} \quad (3.6)$$

Fig. 3.2 illustrates ideal W and W_{max} in the PRO zone [3].

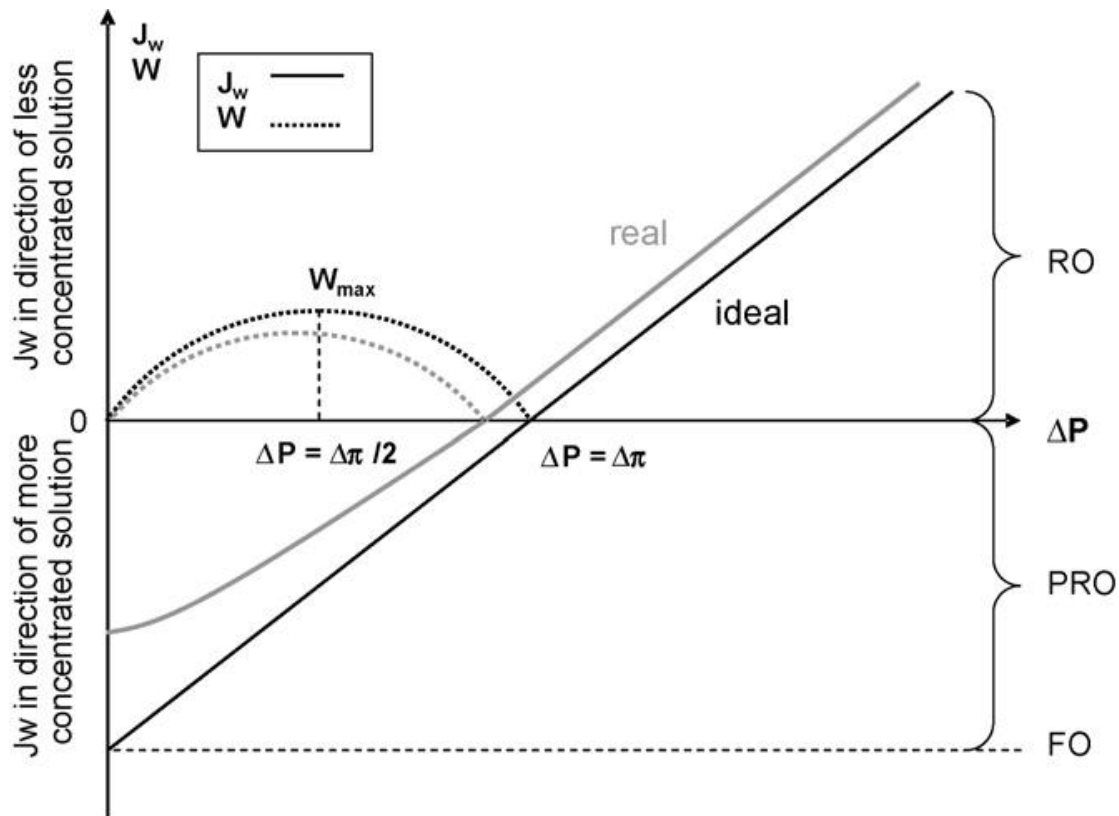


Fig. 3.2 Direction and magnitude of water flux as a function of applied pressure (ΔP) in FO, PRO, RO and magnitude of W for PRO [3].

3.3 Membrane theory

3.3.1 Definition of a membrane

A precise and complete definition of a membrane which covers all its aspects is rather difficult, even when the discussion is limited to synthetic structure as in this outline. In the most general sense, a synthetic membrane is a barrier which separates two phases and restricts the transport of the various chemical species in a rather specific manner. A membrane can be homogeneous or heterogeneous, symmetric or asymmetric in structure; it may be solid or liquid; it may be neutral, may carry positive or negative charges, or may be bipolar. Its thickness may vary between less than 100 nm to more than a centimeter. The electrical resistance may vary from several megaohms to a fraction of an ohm. Mass transport through a membrane may be caused by convection or by diffusion of individual molecules, included by an electrical field, or a concentration, pressure or temperature gradient.

The term “membrane”, therefore, includes a great variety of materials and structures, and a membrane can often be better described in terms of what it does rather than what it is. Some materials, though not meant to be membranes, show typical membrane properties, and in fact are membranes, e.g., protective coatings, or packaging materials. All materials functioning as membranes have one characteristic property in common: they restrict the passage of various chemical species in a very specific manner [19].

3.3.2 Structure of osmotic membranes

In osmotic applications membranes restrict the passage of salt and permit that of the fresh water. They are typically asymmetric, **comprised** of a thin non-porous dense layer, called skin, on top of a porous support layer, as shown in fig. 3.3. The osmotic process in PRO occurs in the semi-permeable skin layer of the membrane. The mass transport through the rest of the membrane is dominated by hydraulic flow. The porous structures in the membrane mainly serve to support the skin mechanically, but they reduce the efficiency of the membrane. In PRO applications, the dense layer of the membrane faces the draw solution and the porous support layer faces the feed solution (fig. 3.3), as in FO applications, while in RO applications membranes have the opposite orientation. This configuration is necessary to ensure that the membrane can sustain the hydraulic pressure induced on the draw solution side [3], [6].

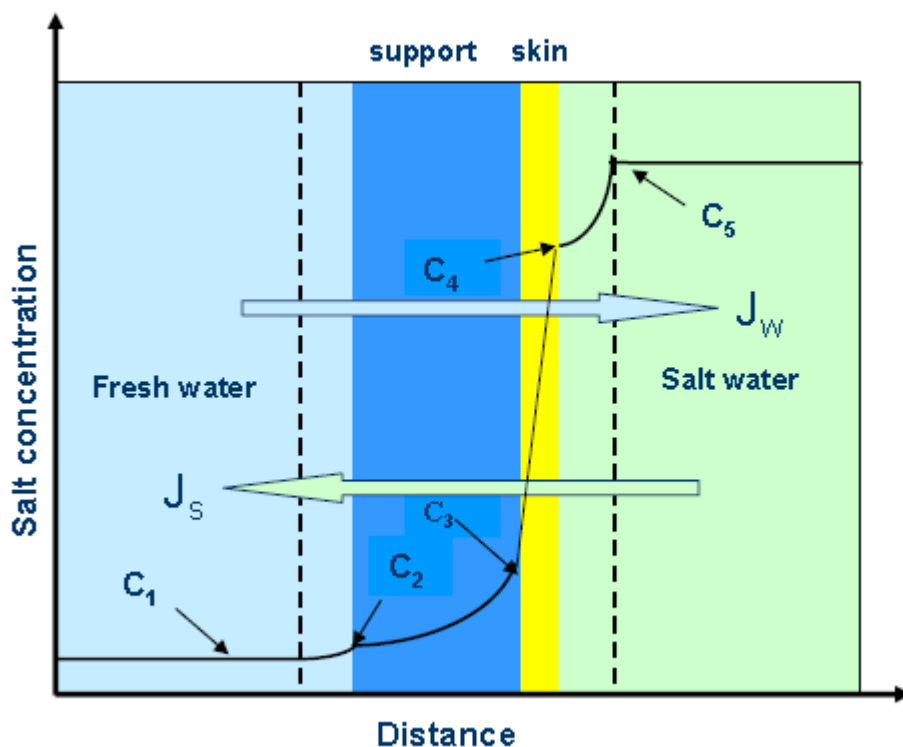


Fig. 3.3 Layers of a PRO membrane, flow conditions and concentration gradient across the system [5].

3.3.3 Water flux in PRO under real conditions – The effect of salt permeability and concentration polarization (PRO model)

A **PRO model** was developed firstly by Lee et al. [20] and expanded by Achilli et al. [3] to predict water flux and power density under specific experimental conditions.

No skin is perfectly semi-permeable and some salt will diffuse through the skin. With saltwater on the skin side of the membrane this salt will diffuse into the porous substructure toward the freshwater, and the salt concentration will thus increase on the freshwater side downstream in the module [6]. The **salt flux** across the skin, J_s , can be written as:

$$-J_s = B \cdot \Delta C_{\text{skin}} = B \cdot (C_4 - C_3) \quad (3.8)$$

where B is the salt permeability coefficient. The salt flux is negative because the direction of salt flow is opposite to that of the water flow. B is given by the equation:

$$B = \frac{A \cdot (1 - R) \cdot (\Delta P - \Delta \pi)}{R} \quad (3.9)$$

where A is the water permeability coefficient (eq.3.3) and R is salt rejection defined as [20]:

$$R = 1 - \frac{\text{salt concentration in the permeate solution}}{\text{salt concentration in the feed solution}} = \frac{C_1}{C_5} \quad (3.10)$$

Reverse salt diffusion reduces the effective osmotic pressure difference across the membrane, $\Delta \pi$, as osmotic pressure is proportionate to salt concentration (eq. 3.4), and consequently the driving force.

In addition, with salt flux across the membrane another more severe phenomenon takes place, which also reduces the effective osmotic pressure difference across the membrane, called concentration polarization. **Concentration polarization** is the accumulation or depletion of solutes near an interface. This is caused by the flow of salt and water through the membrane in opposite directions. Because the membranes used for osmotic processes are typically asymmetric, concentration polarization occurs externally on the dense layer side and the support layer, and internally in the support layer side [3]. The effect of concentration polarization is that the effective pressure difference across the membrane, $\Delta \pi$, is $\pi_4 - \pi_3$, corresponding to the salt concentrations C_4 and C_3 , instead of $\pi_5 - \pi_1$, corresponding to C_5 and C_1 , which is higher. (fig. 14)

Concentrative **internal concentration polarization (ICP)** is concentration polarization that results in the solute being concentrated inside the support layer of the membrane. For the calculation of the effect of the internal concentration polarization, it is assumed that external concentration polarization has been reduced to negligible levels, i.e. $C_1 = C_2$ and $C_4 = C_5$. In the porous layer, the salt flow consists of two components acting in opposite directions: a diffusive part due to diffusion down the salt concentration gradient, and a convective part due to the bulk flow of water through the membrane. With a mass balance through the membrane, the salt flux across the layer can thus be written:

$$-J_s = D_s \cdot \varepsilon \cdot \frac{dC(x)}{dx} - J_w C(x) \quad (3.11)$$

where ε is the porosity of the porous layer and is assumed equal to the volume fraction occupied by capillary water in the membrane, and D_s is the diffusion coefficient of salt in the porous layer, which is a function of the fresh water stream. The distance x is measured from the membrane-solution interface on the porous layer side. Equations (3.8) and (3.11) can be combined to yield:

$$B \cdot (C_4 - C_3) = D_s \cdot \varepsilon \cdot \frac{dC(x)}{dx} - J_w C(x) \quad (12)$$

The appropriate boundary conditions are:

$$C(x) = C_2 \text{ at } x = 0$$

$$C(x) = C_3 \text{ at } x = \tau \cdot t$$

where t is the thickness and τ is the tortuosity of the porous layer. With these boundary conditions, eq. (3.12) can be integrated to give

$$\frac{C_3}{C_4} = \frac{B \cdot [\exp(J_w \cdot K) - 1] + J_w \cdot \frac{C_2}{C_4} \cdot \exp(J_w \cdot K)}{B \cdot [\exp(J_w \cdot K) - 1] + J_w} \quad (3.13)$$

where $K = \tau t / D_s \varepsilon$, and is a measure of the resistance to salt transport in the porous layer. The term $\tau t / \varepsilon$ represents the structural characteristic of the membrane support layer, is called structure parameter and is symbolized with the letter $S(m)$. Assuming that the ratio of salt concentrations is approximately equal to the ratio of osmotic pressures to arrive at:

$$\frac{\Delta \pi_{eff}}{\Delta \pi} = \frac{\pi_4 - \pi_3}{\pi_4 - \pi_2} \cong \frac{C_4 - C_3}{C_4 - C_2} = \left(\frac{1}{1 - \frac{C_2}{C_4}} \right) \cdot \frac{1 - \frac{C_2}{C_4} \cdot \exp(J_w \cdot K)}{\frac{B}{J_w} \cdot [\exp(J_w \cdot K) - 1] + 1} \quad (3.14)$$

where $\Delta \pi_{eff}$ is the effective osmotic pressure difference across the skin, as osmotic process occurs in the skin layer.

The equation $J_w = A \cdot (\Delta \pi_{eff} - \Delta P) = A \cdot (\pi_4 - \pi_3 - \Delta P)$ (eq. 3.3) combined with eq. (3.14) gives [20]:

$$J_w = A \cdot \left[\pi_4 \cdot \frac{1 - \frac{C_2}{C_4} \cdot \exp(J_w \cdot K)}{1 + \frac{B}{J_w} \cdot [\exp(J_w \cdot K) - 1]} - \Delta P \right] \quad (3.15)$$

Dilutive **external concentration polarization (ECP)** is concentration polarization that results in the solute being diluted on the draw solution side of the membrane (the external concentration polarization in the support layer is considered negligible ($C_2 = C_1$)). Dilutive external concentration polarization can be calculated from film theory. The external concentration polarization modulus (π_4 / π_5) is calculated using:

$$\frac{\pi_4}{\pi_5} = \exp\left(-\frac{J_w}{k}\right) \quad (3.16)$$

J_w is negative in this equation because the water flux is in the direction of the more concentrated solution and the concentration polarization effect is dilutive ($\pi_4 < \pi_5$). k is the mass transfer coefficient in the draw solution and is calculated using:

$$k = \frac{Sh \cdot D}{d_h} \quad (3.17)$$

where D is the diffusion coefficient of salt in the draw solution and d_h is the hydraulic diameter of the flow channel. It has been shown that in spacer-filled flow channels the flow becomes

turbulent at relatively low Reynolds numbers (Re) (e.g., Re < 50). Under these conditions, the Sherwood number (Sh) is determined using the correlation:

$$Sh = 0.2 \cdot Re^{0.57} \cdot Sc^{0.40} \quad (3.18)$$

where Sc is the Schmidt number.

In order to consider the effects of both internal and external concentration polarization on water flux in PRO, eq. (3.15) can be modified by assuming that $C_2/C_4 = \pi_2/\pi_4$, and substituting $\pi_4 = \pi_5 \exp(-J_w/k)$ (from eq. (3.16)). The resulting equation for **water flux** in the presence of both internal and external concentration polarization is:

$$J_w = A \left[\pi_5 \exp\left(-\frac{J_w}{k}\right) \frac{1 - \frac{\pi_2}{\pi_5} \exp(J_w K) \exp\left(\frac{J_w}{k}\right)}{1 + \frac{B}{J_w} [\exp(J_w K) - 1]} - \Delta P \right] \quad (3.19)$$

where J_w is a function of the membrane characteristics (A and B), mass transfer coefficient in the draw solution (k), solute resistivity for diffusion within the porous layer (K), bulk osmotic pressures ($\pi_1 = \pi_2$ and π_5), and applied hydraulic pressure (ΔP).

The parameters necessary to calculate water flux in PRO (eq. (3.19)) are obtained from RO and FO experiments and from calculation. k is calculated using Eqs. (3.16) – (3.18). A and B are determined under RO conditions; A is calculated using eq. (3.3) and measuring J_w and ΔP when $\Delta\pi = 0$ and B is calculated using eqs. (3.9) and (3.10). K is obtained from FO experiments ($\Delta P = 0$) with deionized (DI) water (0 g/L NaCl) as the feed and using eq. (3.15). In this case eq. (3.15) is rearranged to [3]:

$$K = \frac{1}{J_w} \ln\left(\frac{A\pi_5 \exp\left(-\frac{J_w}{k}\right) - J_w}{B} + 1\right) \quad (3.20)$$

External polarization can be reduced effectively with the use of stirring but this does not affect internal polarization, which is a very serious problem as it reduces a lot the water flux in PRO [20].

3.3.4 Power density in PRO under real conditions

The power density of the membrane in PRO, which is an index of the membrane efficiency, is equal to the product of the water flux through the membrane and the hydraulic pressure differential across the membrane (eq. 3.3). In the case of current generation membranes (experiencing reverse salt diffusion and concentration polarization), with the combination of eq. 3.5 and eq. 3.19, the equation governing the process is:

$$W = J_w \Delta P = A \left[\pi_5 \exp\left(-\frac{J_w}{k}\right) \frac{1 - \frac{\pi_2}{\pi_5} \exp(J_w K) \exp\left(\frac{J_w}{k}\right)}{1 + \frac{B}{J_w} [\exp(J_w K) - 1]} - \Delta P \right] \Delta P \quad (3.21)$$

After eq. (3.19) is solved numerically to determine J_w , eq. (3.21) can be solved algebraically to determine W as a function of ΔP .

Fig. 3.2 shows J_w and W as function of ΔP under real conditions. Reverse salt diffusion (represented by B) and concentration polarization (represented by k and K) cause the effective osmotic pressure differential ($\Delta\pi$) across the membrane to be lower than the bulk osmotic pressure differential. This phenomenon, as mentioned before, reduces the attainable J_w and thus the W compared to the ideal membrane case [3].

It appears that the **osmotic efficiency** of the membrane itself can be described entirely by the values of A and B of the skin and one single parameter for the porous support layer S . The lower the structure parameter, the better the performance of the membrane under PRO conditions. The desired value for the structure parameter is lower than 0.0015 m [6].

3.3.5 Membrane fouling

In osmotic processes it is important that the freshwater and seawater be as clean as possible. Substances in the water may get captured within the membrane's support structure or on the membrane surfaces, reducing the flow through the membrane and therefore the power output. This phenomenon, which is called fouling, is linked to the design of the system, to the characteristics of the membrane, and to the membrane element [9].

There are two **types** of membrane fouling: external-surface (temporary) and internal-pore (permanent) fouling.

External fouling appears as an evenly deposited layer on the membrane surface and involves three distinct mechanisms: (1) scale formation, i.e., heterogeneous crystallization of mineral salts on the membrane; (2) cake formation, i.e., accumulation of rejected solids on the membrane; and (3) biofilm formation, i.e., colonization of the membrane module by viable microorganisms. Multiple surface fouling mechanisms can operate simultaneously, producing synergistic or antagonistic effects. All three forms of external fouling are influenced by operating conditions, solution chemistry, temperature, membrane properties, and module geometry, while biofilm formation is additionally governed by the biogrowth potential of a feed water. External fouling is minimized through pretreatment and is mitigated by cleaning.

Internal fouling is a change in membrane structure due to physical compaction or chemical degradation—each of which alters solute and solvent transport. Chemical degradation occurs when a specific chemical attacks the polymer structure. Physical compaction occurs when polymeric membranes are subjected to high hydraulic pressures. Macro-voids and micro-voids within the membrane structure can collapse when exposed to pressures exceeding their elastic modulus. Internal fouling is largely irreversible, therefore it determines the lifetime of the membrane [21].

3.3.6 Membrane module

In order to facilitate a working PRO process the membrane must be configured in **modules** like in RO, in a plate-and-frame, spiral, fiber, tubular or in other forms (mainly on laboratory-scale applications). Flat-sheet membranes are packed in either plate-and-frame or spiral wound modules. Tubular membranes are packed in hollow fiber or tubular modules. An essential feature of the PRO module is the flow of the two water phases along both opposite surfaces of the membrane, called cross-flow in membrane filtration terminology. This is different from RO where there is cross-flow all through the module on the saltwater side of the membrane only [6]. Membrane modules in RO application are described separately below. It would be useful to

remind here that in RO feed stream is the sea water and permeate is the fresh water. Their use in PRO applications is similar with some modification.

i) Plate-and-frame

Plate-and-frame modules use flat-sheet membranes that are layered between spacers and supports. The feed water flows across the flat sheets (feed-side spacer), where a portion permeates the membranes and flows vertically in the supports, which form a channel for the permeate water (permeate-side spacer). The feed water continues from one layer to the next [22].

Fig. 3.4 shows the layers of a plate-and-frame module and fig. 3.5 the whole module.

Plate-and-frame modules offer easy maintenance but they lack adequate membrane support and their packing density is low.

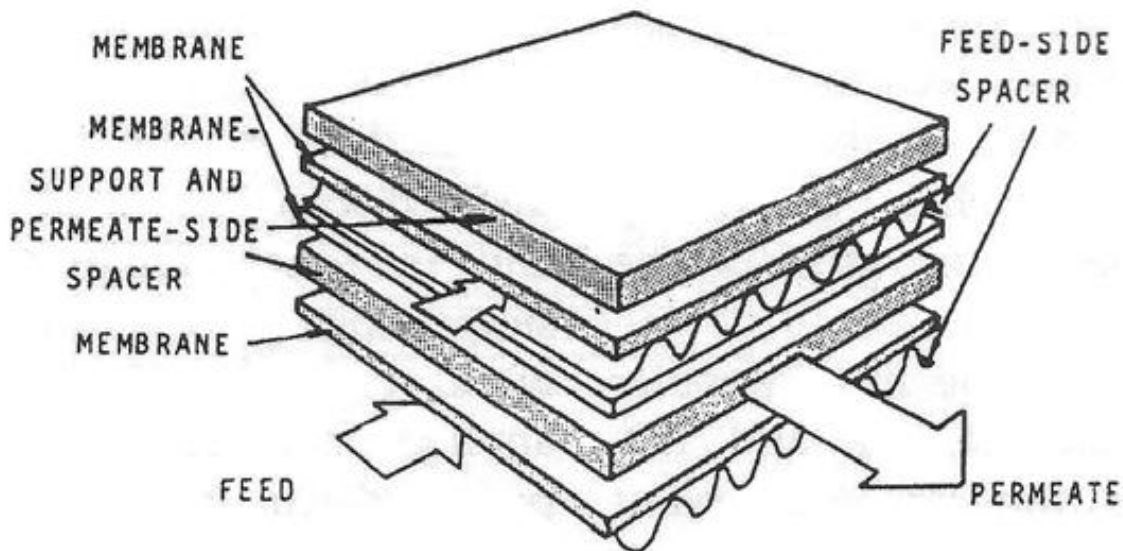


Fig. 3.4 Layers in a plate-and-frame module

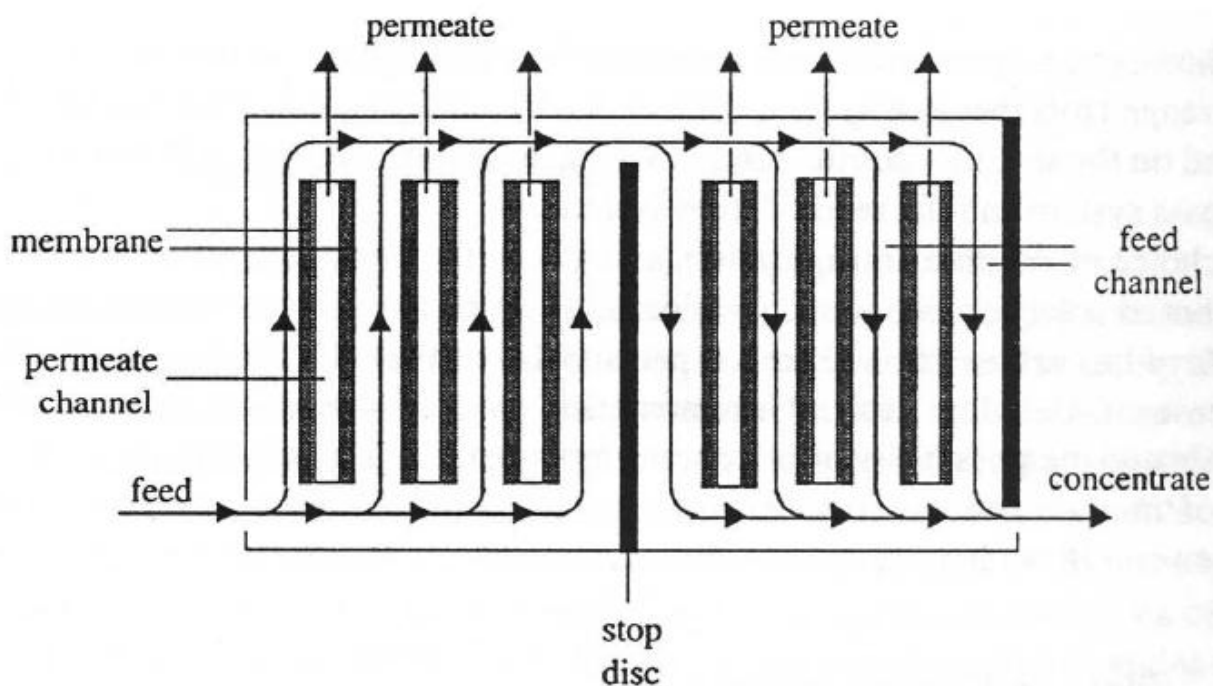


Fig. 3.5 Plate-and-frame module

ii) Spiral wound

Spiral-wound modules use a “sandwich” of flat sheet membranes and supports, wrapped spirally around a collection tube. The feed flows in against one end of the rolled spiral and along one side of the membrane “sandwich”. A portion of the feed solution permeates into the membrane envelope, where it spirals (flows tangentially) toward the center and exits through the collection tube.

In fig. 3.6 is shown a spiral wound module and in fig. 3.7 the tangential flow in such a module. Spiral wound modules offer greater packing densities, but maintenance is difficult [22].

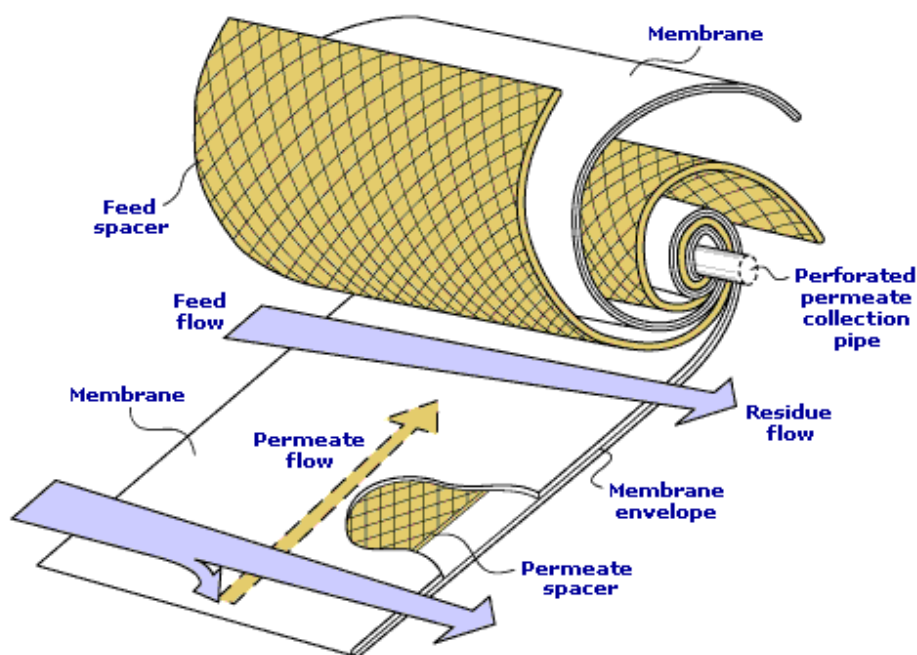


Fig. 3.6 Spiral wound module (www.mtrinc.com)

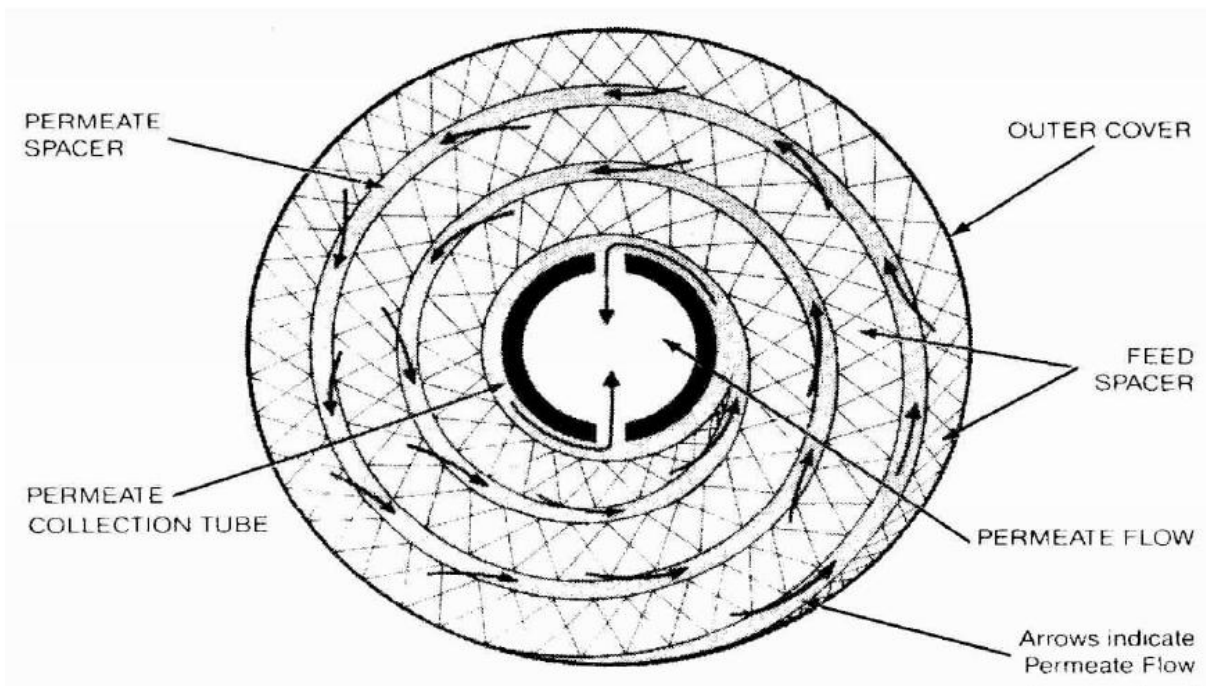


Fig. 3.7 Tangential flow in a spiral wound module

iii) Tubular

Tubular membranes are usually made by casting a membrane onto the inside of a pre-formed tube, which is referred to as the substrate tube. There are mainly two types of housing system for tubular membrane module, which known to be the supported and unsupported tubes housing system. Basically, in supported housing system, membrane tube is supported by perforated or porous stainless steel tubes. A bundle of these membrane tubes is mounted into a vessel that collect permeation and caps are fitted to the end to give different flow pattern. Exhibiting high mechanical strength, this type of module can be used at high pressure (up to 60 bar) separation process. In the unsupported housing design, the membrane is supported only by substrate tube and a cartridge is constructed by potting the ends of a bundle of tubes in an epoxy resin [23].

Fig. 3.8 shows a tubular membrane module

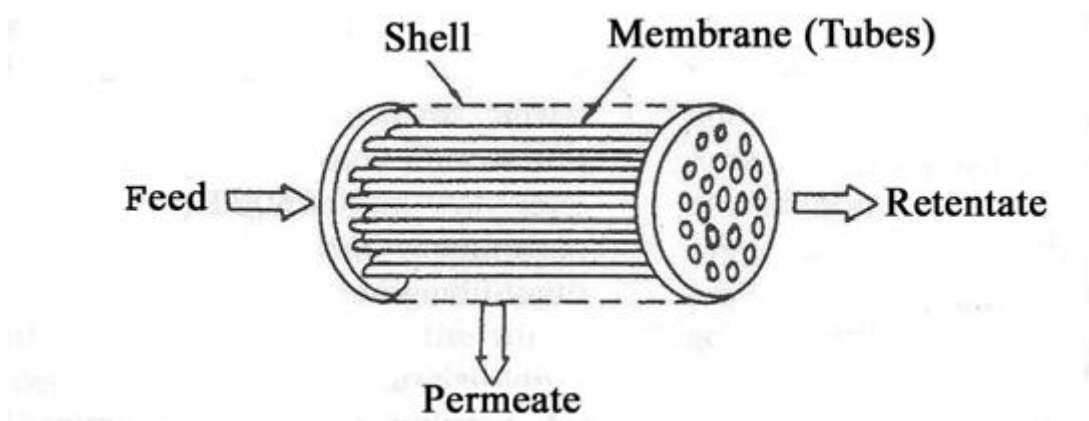


Fig. 3.8 Tubular membrane module [23].

iv) Hollow fiber

There are two basic configurations for hollow-fiber membrane module. The first is the closed-end design. In this module, a loop of fiber or a closed bundle is contained in a pressure vessel. The system is pressurized from the shell side and permeate passes through the fiber wall and exits via the other fiber ends, which are open. The second basic design, the opened-end, is more common. In this case, the fibers are laid out parallel to each other in bundles and the open ends are then cast into two resin blocks which are bonded into shrouds to form a cartridge. In order to minimize the pressure drops in the inside of the fibers, the fibers often have larger diameters than fine fibers used in closed loop system [23].

Hollow-fiber modules offer the greatest packing densities of the configurations described.

In fig. 3.9 is presented a hollow fiber module with open-end design and in fig. 3.10 one with closed-end design.

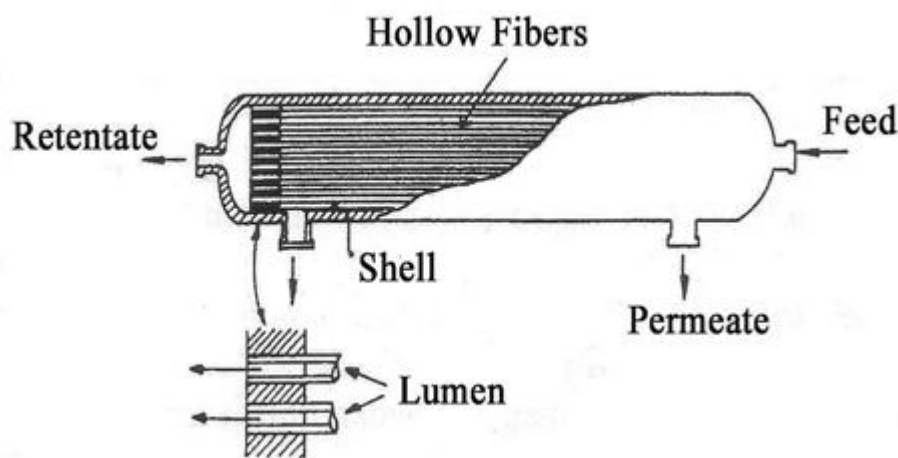


Fig. 3.9 Hollow fiber module with open-end design [23].

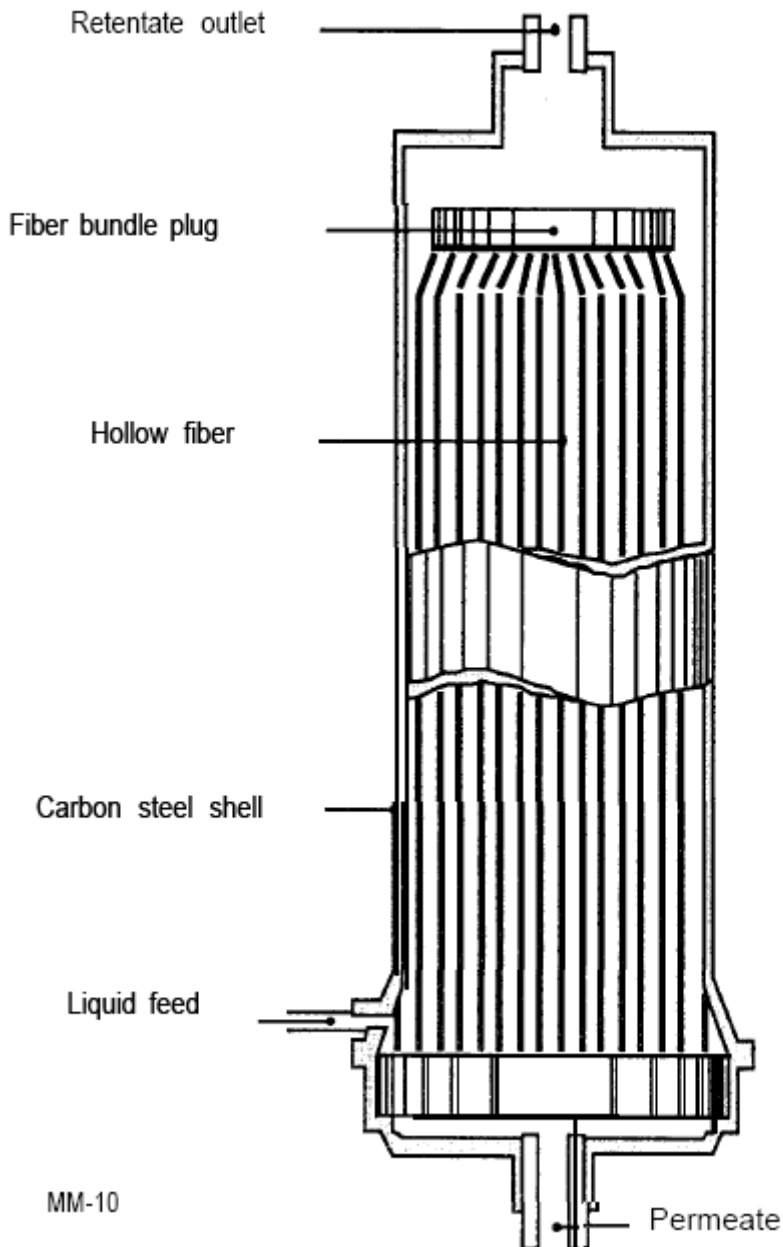


Fig. 3.10 Hollow fiber module with close-end design [23].

3.3.7 Membrane types in PRO applications

In PRO applications are mainly used two **types** of membranes: cellulose acetate (CA) and thin-film composite (TFC), which are commercially available for RO and FO application and can be used in PRO with some modification for improved performance. The main differences from RO applications is that in the PRO process pressures are much lower, and thus the thick compaction resistant support layer that induces high internal concentration polarization is unnecessary, as a thinner one would be able to resist PRO pressures without inducing high internal polarization. Also, salt and water are flowing in opposite directions. Commercial cellulose acetate membranes for FO applications can be used in PRO applications with acceptable performance.

i) Thin-film composite membranes

The term “thin-film composite” describes the manner in which these membranes are fabricated. Thin-film composite membranes usually consist of layers of dissimilar materials joined together to form a single membrane. This layered construction permits use of material combinations that optimize the performance and durability of the membrane.

Although a variety of materials are used in the fabrication of thin-film composite membranes, membranes utilizing an aromatic polyamide barrier layer over a polysulfone base have been shown to provide the best overall combination of productivity, performance, and durability [24].

In fig. 3.11 is shown the cross section of a TFC membrane.

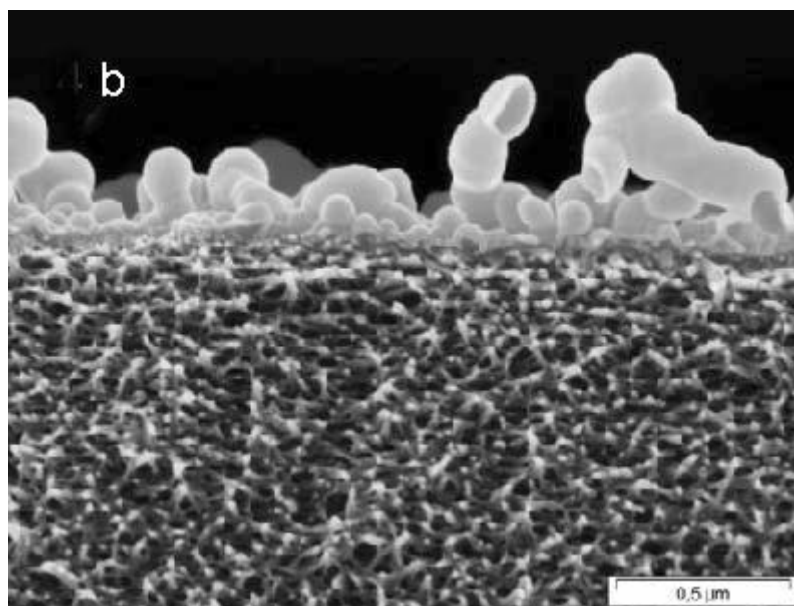


Fig. 3.11 Cross section of a thin-film composite membrane [8].

ii) Cellulose acetate membranes

Cellulose acetate membranes get their name not from their structure, but from the material used in their fabrication. They are available in diacetate and triacetate (CTA) grades, and in blends of these grades (CA/CTA) [24]. They are cheaper than TFC membranes but their semi-permeable properties are inferior.

Fig. 3.12 shows the cross section of a CA membrane.

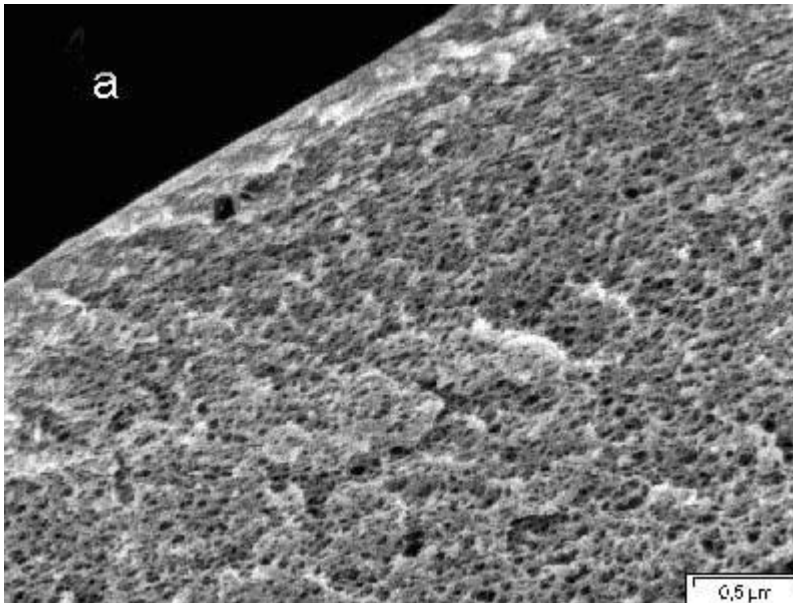


Fig. 3.12 Cross section of a CA membrane [8].

3.3.8 Recent experiments by using a small laboratory-scale apparatus

In the study of Gerstandt et al.[8], cellulose acetate (CA) and thin film composite (TFC) membranes were tested in the PRO process. Over 50 different support materials for the TFC membrane and a range of asymmetric membrane types made from polymers other than CA were produced to find the optimal PRO membrane.

A typical casting solution for CA membranes, according to a GKSS patent, consists out of cellulose diacetate, cellulose triacetate, dioxane, acetone, acetic acid and methanol. This composition was kept in this study, but the casting parameters were changed in order to improve the performance of these membranes.

Measurements of CA membranes have proven that many of these membranes behave as, or close to, ideal osmotic behaviour. Some of the prototype membranes exhibit very high water permeabilities, but the corresponding salt retention is still too low, which restricts the power production in PRO. Investigations of commercial CA membranes showed a verified power of below 1 W/m^2 ; in some cases a power production of 1.6 W/m^2 was reported. In this study an improvement from 0.6 W/m^2 up to 1.3 W/m^2 was achieved for both the potential and also for the measured power.

When a high-performance TFC RO membrane is used in the PRO process, its performance is usually poor due to salt concentration build-up in the support layer (internal polarization). Therefore, in this study the microporous support layer was made as thin and open as possible, resulting in a reduction of the structure parameter, S , and in an improvement of the PRO membrane.

Starting with TFC membranes designed for RO, with an energy density of less than 0.1 W/m^2 , only very recently an energy density of 3.5 W/m^2 has been verified. However, the potential of this type of membrane was calculated using a membrane performance simulator to be close to 5 W/m^2 .

The difference of the calculated and the measured performance was not or only slightly present for the CA membranes. For the TFC membranes this is an undesired but present effect.

In fig. 3.13 the power densities for CA and TFC membranes are presented.

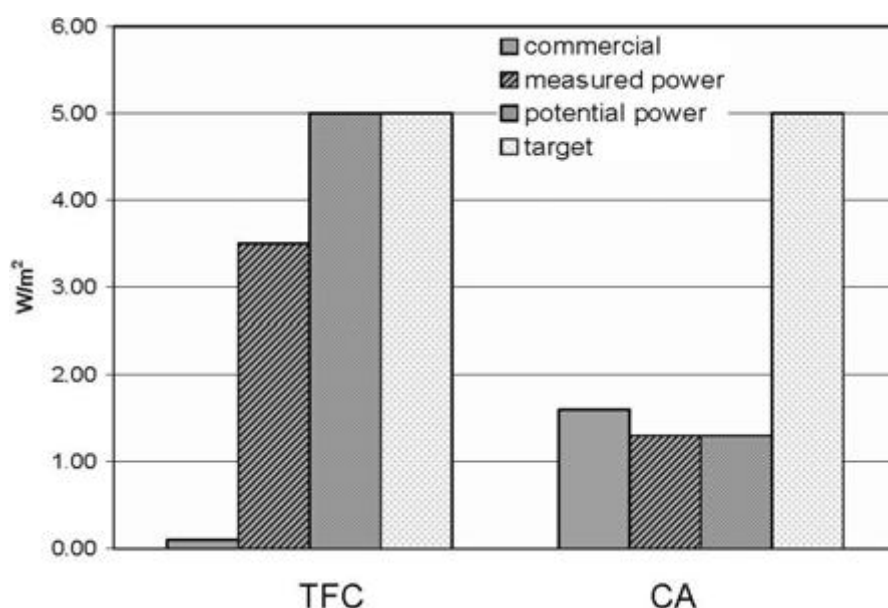


Fig. 3.13 Power densities for CA and TFC membranes [8].

In the study of A. Achilli et al. [3], water flux in a PRO bench-scale system was measured as a function of the applied hydraulic pressure for three feed solution concentrations (0 g/L NaCl, i.e. Deionized (DI) water, 2.5 g/L NaCl and 5 g/L NaCl) and two draw solution concentrations (35 g/L NaCl and 60 g/L NaCl). Given the measured value of the water flux, power density was calculated as a function of hydraulic pressure. Also, the water flux performance was calculated using the ICP-ECP model. The mass transport coefficient k was calculated for 20, 35 and 60 g/L NaCl draw solution concentrations and DI water (0 g/L NaCl) as feed solution concentration. The membrane coefficients A and B were calculated in a RO bench-scale system. The solute resistivity for diffusion within the porous layer K for the three draw solution concentrations was calculated using the PRO system with $\Delta P=0$ (i.e. FO mode).

A flat-sheet cellulose triacetate (CTA) FO membrane (Hydration Technology Innovations, HTI, Albany, OR) was used in the experiments. The physical characteristics of this membrane are unique compared to other commercially available semi-permeable membranes and it has been determined to be the best available membrane for most FO applications. These characteristics would be high density of the active layer for high solute rejection; a thin membrane with minimum porosity of the support layer for low internal concentration polarization, and therefore, higher water flux; hydrophilicity for enhanced flux and reduced membrane fouling; and high mechanical strength to sustain hydraulic pressure [2].

A schematic drawing of the flat-sheet bench-scale PRO system is shown in fig. 3.14. The custom-made membrane module had symmetric channels on both sides of the membrane. This allowed for both the feed and draw solutions to flow tangential to the membrane. The channels were 75mm long, 25mm wide, and 2.5mm deep. The effective membrane area was 18.75cm² (channels and membrane area are the same for RO experiments). A variable-speed gear pump (Cole-Palmer, Vernon Hills, IL) was used to recirculate the feed solution at 0.5 L/min. A high-pressure positive displacement pump (Wanner Engineering Inc., Minneapolis, MN) was used to

recirculate the draw solution at 0.5 L/min. The feed solution was contained in a 5.4-L constant-level reservoir; the volume was kept constant by a float valve and DI water continuously replenished the water that crossed the membrane. The DI water reservoir was placed on an analytical balance linked to a computer that collected data continuously. Flux through the membrane was calculated based on the change of weight of water in the DI water reservoir. Hydraulic pressures on the feed and draw solutions were monitored and recorded. The hydraulic pressure of the draw solution loop was controlled with a needle valve. The draw solution concentration was held constant by continuous reconcentration with a pilot-scale RO subsystem. The RO subsystem (different from the bench-scale RO system used for conducting membrane characteristics tests) is described in a previous publication [25].

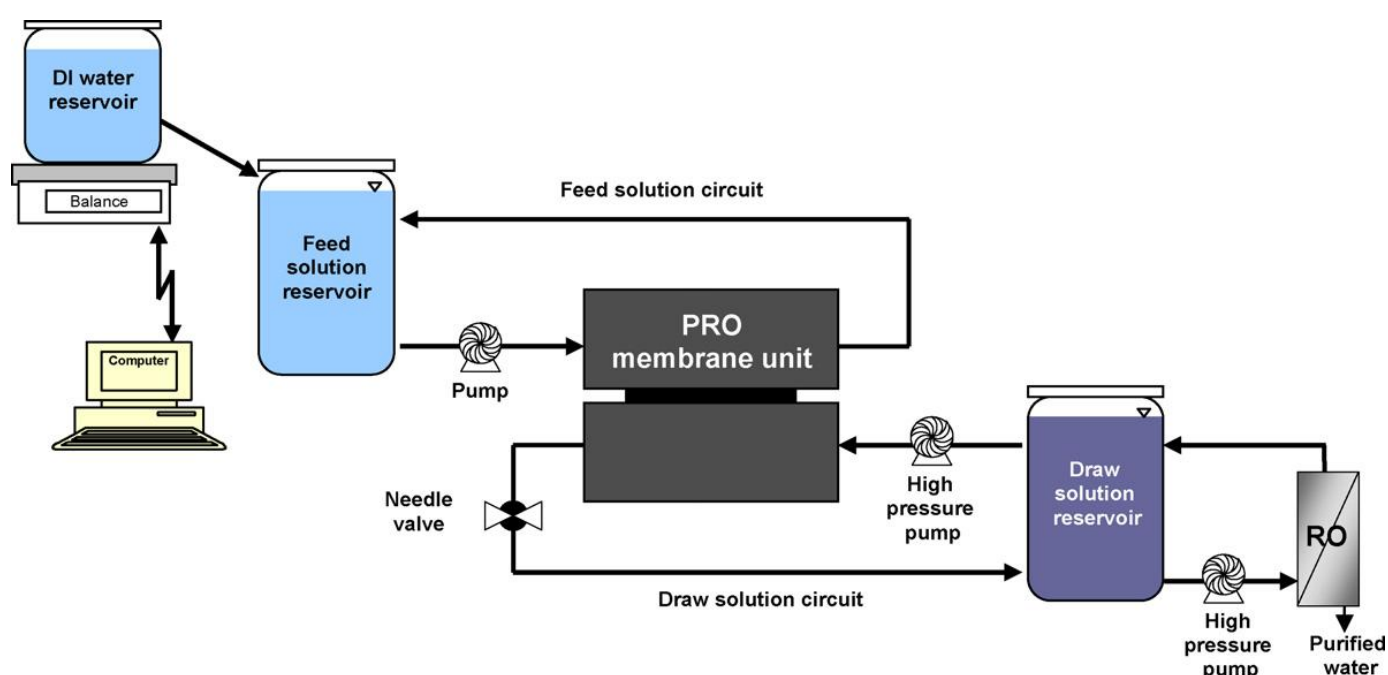


Fig. 3.14 Schematic of the bench-scale PRO system [3].

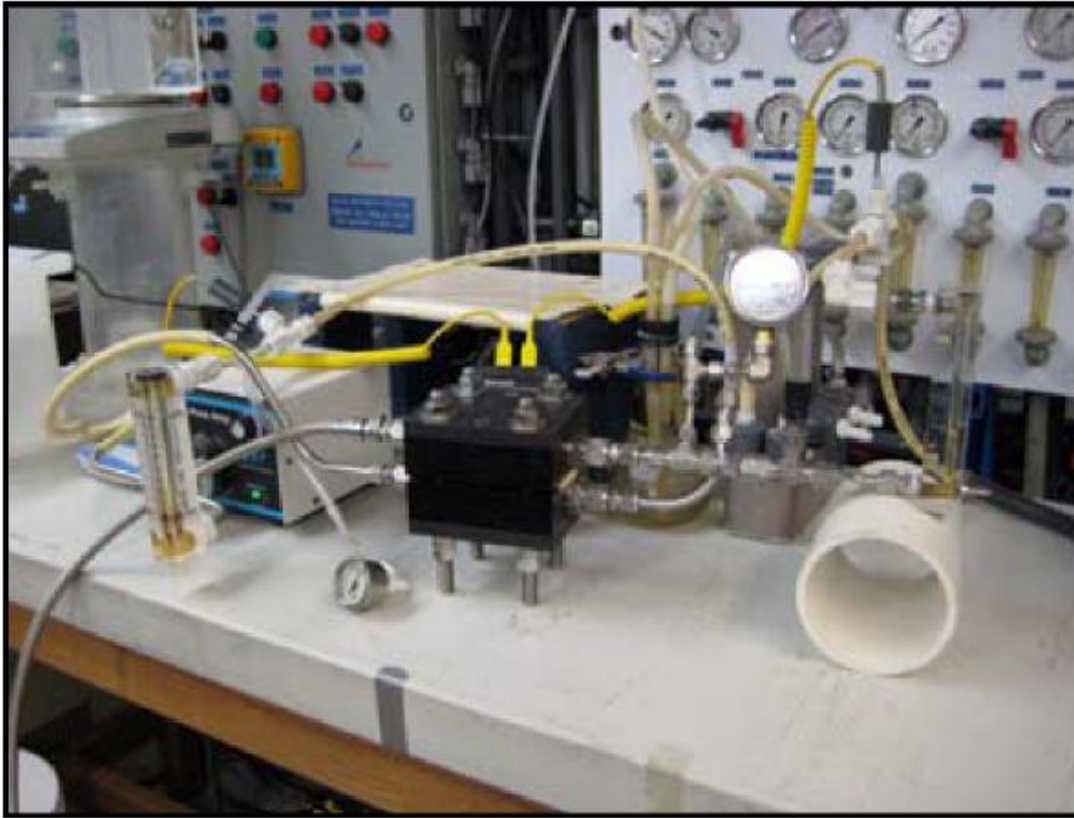


Fig. 3.15 Photo of the bench-scale PRO MBR (membrane bioreactor) system [26].

Data collected from the PRO experiments closely matched model predictions. At 970 kPa hydraulic pressure on the draw solution side, the power densities achieved were up to 2.8 W/m^2 for the 35 g/L NaCl draw solution and up to 5.1 W/m^2 for the 60 g/L NaCl draw solution, while the water flux was $2.88 \cdot 10^{-6} \text{ m/s}$ and $5.25 \cdot 10^{-6} \text{ m/s}$, respectively. For the CTA membrane employed, the power density was substantially reduced due to severe internal concentration polarization and, to a lesser degree, to reverse salt diffusion. External concentration polarization was found to exhibit a relatively small effect on reducing the osmotic driving force.

In the study of T. Thorsen & T. Holt [6], three membranes were tested about their performance in a PRO system in several different conditions. A commercial CA (SS10 from Osmonics) RO sheet membrane, an experimental flat sheet CA membrane made without fabric reinforcement (naked) for this study and an experimental TFC membrane made in the study (by GKSS Forschungszentrum, Geesthacht, Germany). Also, the water flux was calculated using a classical ICP model expanded in this study to calculate the effect of ECP (different from the model developed by Achilli et al.[3]). By fitting the measured water and salt fluxes to the models, the values of A , B and S can be calculated as the values that give the best fit of the model to the experimental results, provided that PRO experiments are done with several different conditions during the experiment, like various saltwater pressures.

An apparatus was built that uses 65 cm^2 of sheet membranes in a small cell to do PRO experiments with actual cross-flow along the membrane surfaces. The cell uses the same type of spacers that are used in spiral RO modules. The apparatus is equipped with common precision instruments to measure and control the saltwater and freshwater pressure and pressure drop along the spacers. The mass transfer is calculated based on change in mass of a water reservoir connected to the freshwater (low pressure) side only. Piping is stainless steel

and reinforced tubing. The cell was constructed as part of this study. It was made of a stainless steel flat sheet design of similar construction as used in most institutes working with RO experiments. The main difference is that cross flow is possible on both sides of the membrane. A simplified schematic drawing of the equipment is shown in fig. 3.16. A reservoir in the saltwater loop is not shown. The saltwater pressure is maintained constant by a backpressure valve and the fluxes are measured by balances. Further, a pressure system, not shown in the figure, makes it possible to run continuous hysteresis of PRO-RO by adjusting the pressures on both sides of the membrane.

Several smaller apparatus using stirred cells instead of the cross-flow cell were also used. These smaller cells are in principle similar to the equipment used by Lee [20]. Glass cells made for osmotic flow measurements at ambient pressure have open membrane areas of 1.2 cm^2 in the plate that separates the two half cells. A cell made of Hastelloy C for PRO measurements can use membranes with effective areas of either 7 or approximately 0.5 cm^2 (due to the low membrane area the mass transfer is relatively low and there is some scattering in the calculated flux). The largest area requires a mechanical support of the membrane that significantly increases the effective diffusion length of the transport system. Without a mechanical support an aperture in the metal plate that separates the two half cells is only 7mm. Due to bulging of the unsupported membrane the area is increased to approximately 0.5 cm^2 .

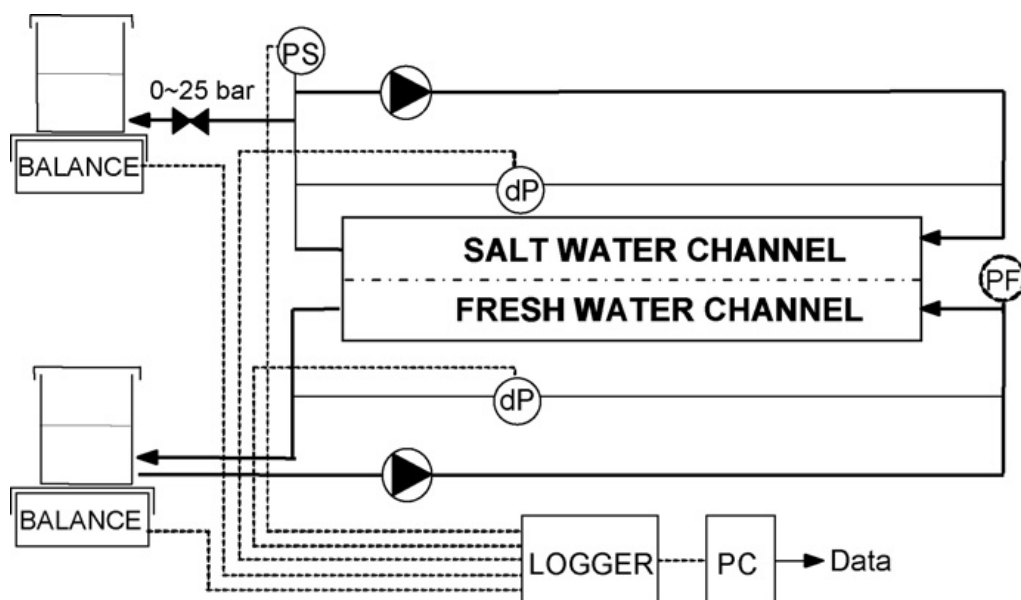


Fig. 3.16 Schematic of the apparatus for PRO experiments [6].

For the CA naked membrane, with 23.5 g/L salt concentration difference between bulk flows, the achieved maximum power density was 1.6 W/m^2 at an applied pressure of 0.68 bar, while the water flux was $2.35 \cdot 10^{-6} \text{ m/s}$. However, the expected average salt concentration in a power plant is approximately 28 g/l NaCl which gives specific power for this membrane approximately 2.1 W/m^2 . From the TFC membrane made in this study, with 30.6 g/l NaCl salt concentration difference, it was possible to extract approximately 2.7 W/m^2 with $2.5 \cdot 10^{-6} \text{ m/s}$ water flux, compared with typically less than 0.1 W/m^2 for most commercial RO types tested. CA membranes behave well but their semi-permeable properties are inferior to TFC membranes, as is well known for application in RO. It has been observed from experiments with commercial TFC types for RO that these membranes have inherent properties that make them less efficient in PRO. This was already noted in experiments with PRO by Lee et al. [20]. Therefore, in order to realise their full PRO performance they need to be redesigned. So far the development of

TFC membranes has improved the measured performance significantly compared to commercial RO types.

In the study of Yuan Xu et al. [27], a spiral wound module was tested in the PRO process by applying different hydraulic pressures and measuring the water flux. Also, the flux performance of the spiral wound module was modeled via classical ICP models and a dillution model, which was developed in this study (dillution effects on the draw solution need to be explicitly accounted for in a spiral wound module). The Hydrowell® membrane and membrane module were purchased from HTI. The membrane was especially developed for FO applications with an ultrathin polyester screen mesh support and an active rejection layer based on cellulose triacetate.

To allow the application of hydraulic pressure as required for PRO tests, the Hydrowell® element was housed in a pressure vessel self-manufactured with a maximum pressure rating of 30 bar. The pressure vessel was connected to a feed water tank (unpressurized) and a circulation pump was used for controlling the cross-flow rate at the feed solution side. A separate pump was used to circulate the draw solution from a 40-L stainless steel pressure tank. The pressure inside the draw solution tank was controlled by adjusting a needle valve located at the top of the tank, and it was measured by a mechanical pressure gauge. The volumetric flow rate through the Hydrowell® module was determined by measuring the time needed to fill up a volumetric cylinder (20 ml or 50 ml). The average flux was calculated by normalizing the volumetric flow rate by the effective membrane area according to the equation:

$$\bar{J}_w = \frac{Q_p}{A_m} \quad (3.22)$$

where Q_p is the total permeate flow rate through the entire membrane module and A_m is the effective membrane area.

A schematic drawing of the PRO unit is shown in fig. 3.17. Also, in fig. 3.18 is shown the spiral wound membrane module open.

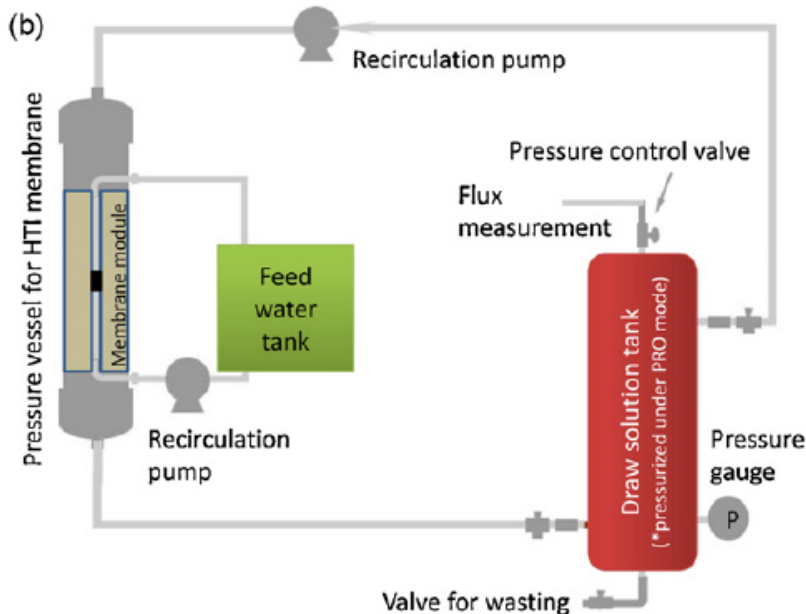


Fig. 3.17 Schematic drawing of PRO unit [27].

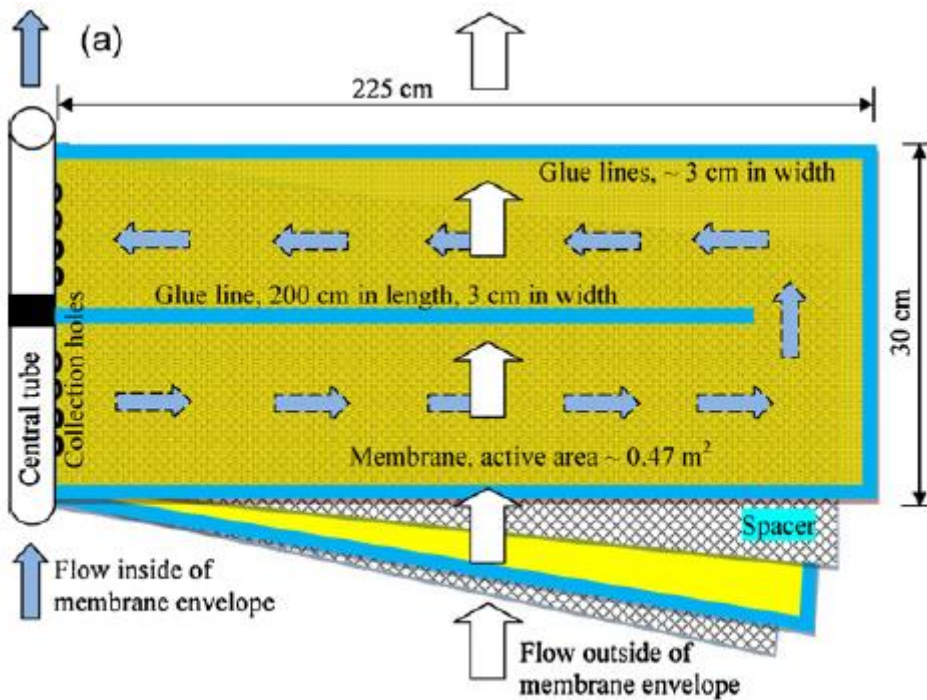


Fig. 3.18 Spiral wound membrane module open [27].

The PRO membrane was tested with the draw solution either inside the membrane envelope in direct contact with the porous membrane support (x-PRO-in configuration) or outside of the envelope (x-PRO-out configuration) in direct contact with the active membrane layer (fig. 3.19). Major leakage of draw solution in x-PRO-in configuration was identified at a pressure of ~ 3 bar which forced the experiment to be stopped. Therefore, it was concluded that the Hydrowell[®] module is not suitable for the x-PRO-in configuration, except where applied pressure is relatively low. In the x-PRO-out configuration with 0.5 M NaCl draw solution, the maximum power density was 1.5 W/m^2 occurring at an applied pressure of 10–11 bar, while the water flux was $1.43 \cdot 10^{-6} \text{ m/s}$. Improved module/spacer design and proper management of draw solution and feed water cross-flows are therefore required for optimized power performance from a PRO spiral wound module. The model prediction agreed well with the experimental results when mass transfer resistance on the feed water side was insignificant. However, the model overestimates membrane flux when ECP on the feed solution side is significant.

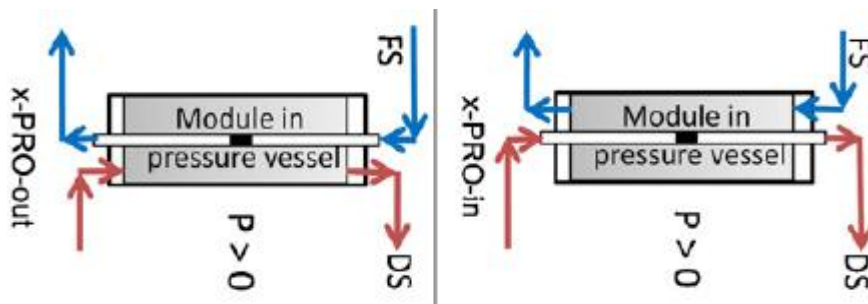


Fig. 3.19 Feed and draw solution stream in the two configurations [27].

The performance of CA hollow fiber membranes, which were made as part of the study of Jincai Su et al [28], was tested using a lab-scale FO set-up. Each membrane module had a filtration area of about 50 cm^2 . The tests were conducted in the PRO mode, i.e., the draw

solution (MgCl_2) and the feed solution (DI water) counter-currently flowing at the shell and lumen sides of the membrane module, respectively (fig. 3.20). The volumetric flow rates of the draw and feed solutions were 300 and 20 mLmin^{-1} , respectively. The pressure at the lumen side was $<2 \text{ psi}$ to maintain a flow rate of 20 mLmin^{-1} . The amount of water permeating from the feed to the draw solution over a selected period of time was measured using a digital balance. The water permeation flux, J_w (LMH), was then determined based on the weight change of the feed and the effective membrane area as follows:

$$J_w = \frac{\Delta m}{\Delta t} \frac{1}{A_m} \quad (3.23)$$

where A_m (m^2) is the effective membrane area and Δm (kg) is the weight of water permeated from the feed to the draw solution over a predetermined time Δt (h) during PRO tests. The value of J_s was determined from the increase in the feed conductivity:

$$J_s = \frac{(C_t V_t) - (C_0 V_0)}{\Delta t} \frac{1}{A_m} \quad (3.24)$$

where C_0 (mol L^{-1}) and V_0 (L) are the initial salt concentration and the initial volume of the feed, respectively, while C_t (mol L^{-1}) and V_t (L) are the salt concentration and the volume of the feed over a predetermined time Δt (h), respectively, during the tests.

Fig. 3.20 shows the flow of the draw and feed solution in a membrane tube inside the module. Also, a schematic drawing of the PRO system is presented in fig. 3.21.

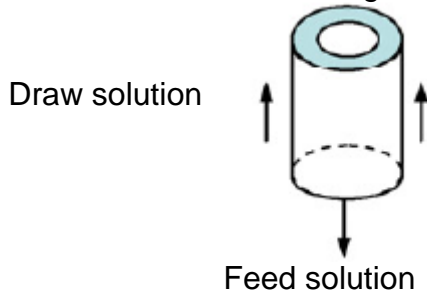


Fig. 3.20 Draw and feed solution flow in a membrane tube [29]

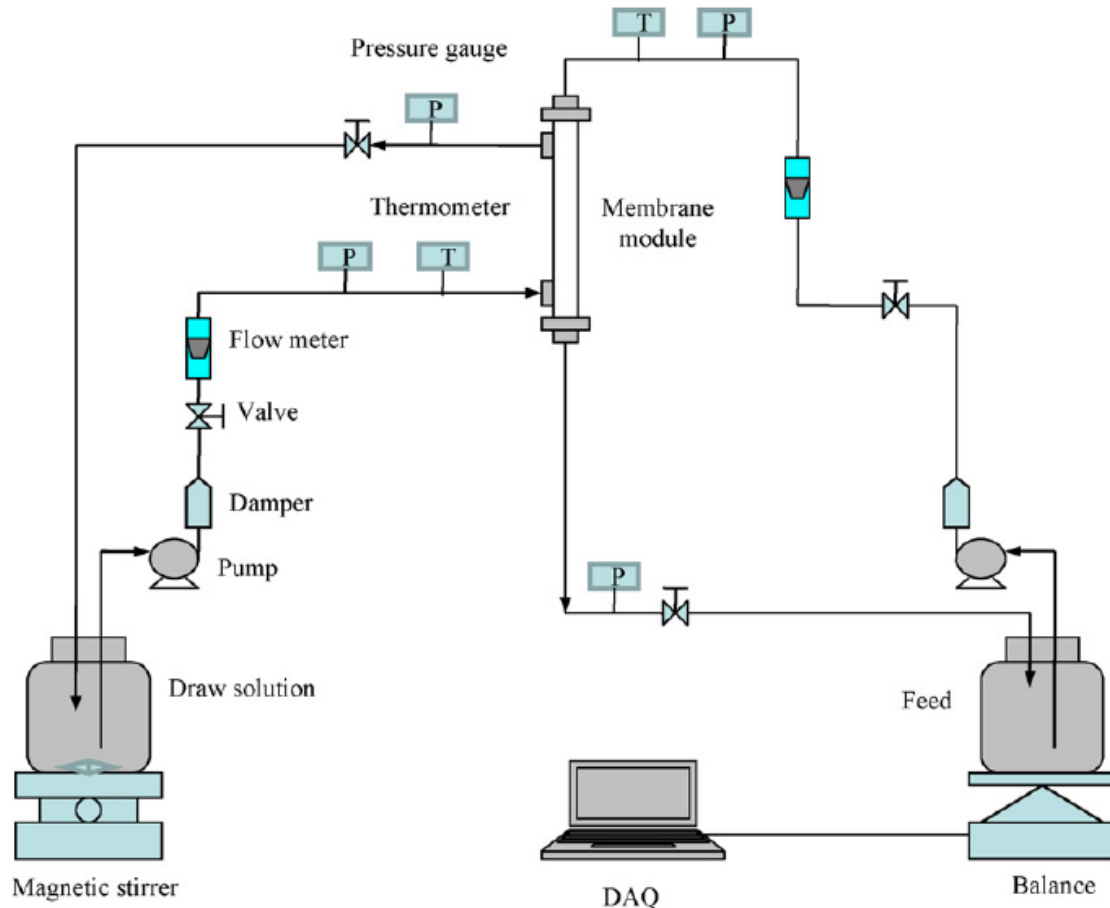


Fig. 3.21 Schematic drawing of the PRO system [29]

CHAPTER 4.

PRESSURE RETARDED OSMOSIS POWER PLANT

4.1 Description

The PRO plant can be described as a desalination plant running backwards. A desalination plant uses a RO process operating against the osmotic force. However, a PRO plant utilizes the same osmotic force to produce energy from the mixing of fresh water and salt water.

In a simplified process freshwater is fed into the plant from a river and filtered before entering the membrane modules. Seawater is supplied by a pump. In the membrane module (flat-sheet for a simplified plant) (see chapter c.6), 80–90% of fresh water is transferred by osmosis across the membrane into the pressurized filtered seawater. The osmotic process increases the volumetric flow of high pressure seawater and is the key energy transfer in the plant. The brackish water from the membrane module is split into two flows. About 1/3 of the water goes to the turbine to generate power and 2/3 returns to the pressure exchanger to pressurize the seawater feed. Since the volumetric flow handled by the turbine is higher than the flow rate handled by the pump, the system delivers net work output. The net work output is the difference in the work delivered by the turbine and the work required by the pump. Typical operating pressure is in the range of 11–15 bars. This is equivalent to a water head of 100–145 m in a hydropower plant. The fresh water operates in ambient pressure [8].

A simplified PRO power plant is shown in fig. 4.1.

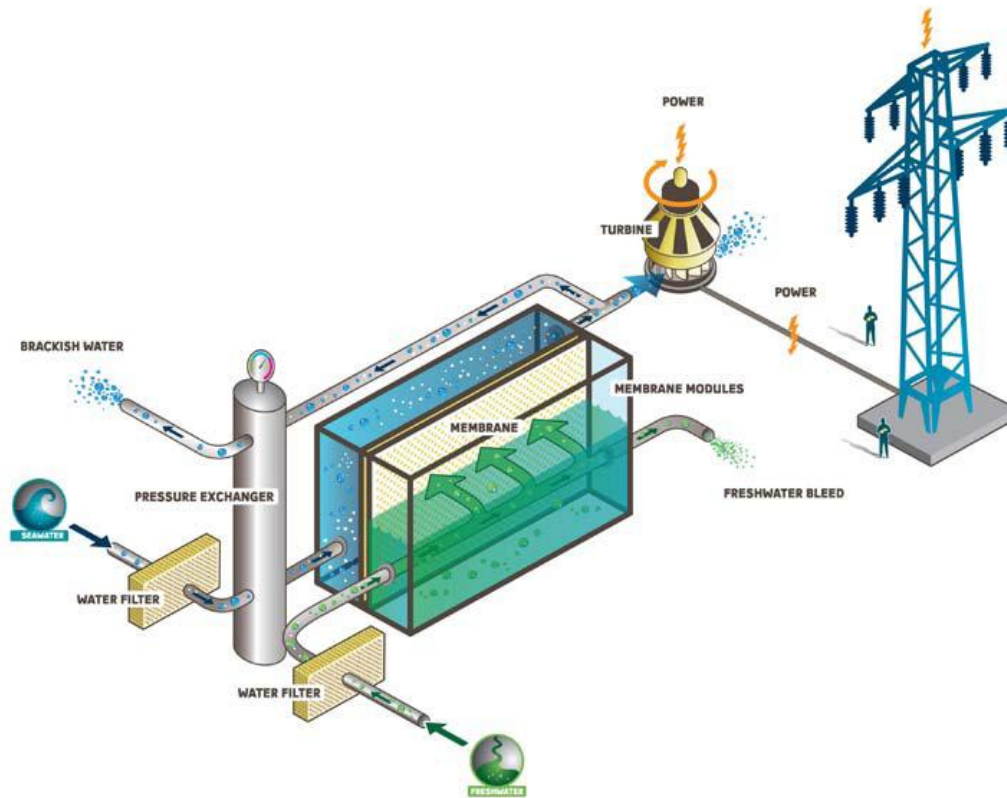


Fig. 4.1 Simplified PRO power plant [9].

4.2 Location

As a PRO power plant requires a constant flow of fresh water and salt water, it is necessary to be placed near rivers or lakes, which will support the plant with fresh water, and the sea level, which provides the salt water. An ideal location is the estuary of a river as it's close to both locations.

Several plant designs have been developed for PRO power generation. Fig. 4.2 shows a typical plant placed at **sea level**. Fresh water is taken from a river close to its outlet. Seawater is fed into the plant by underground pipes. The brackish water is let to the natural brackish water zone of the estuary thus maintaining the flow of water in the river. In many respects this PRO process can be designed as a run-of-river hydropower plant [8].



Fig. 4.2 Sea level PRO power plant [10].

Another major concept utilizes the gravity instead of the pressure exchanger to pressurize the incoming seawater. By placing the whole plant 100 to 130 meters **below sea level** the efficiency of the process can be increased significantly. The concept comprises a normal hydropower plant running on water from a river or a lake utilizing the extra water head. A membrane plant pumps the water out of the sub-sea cavern (fig. 4.3) [8].

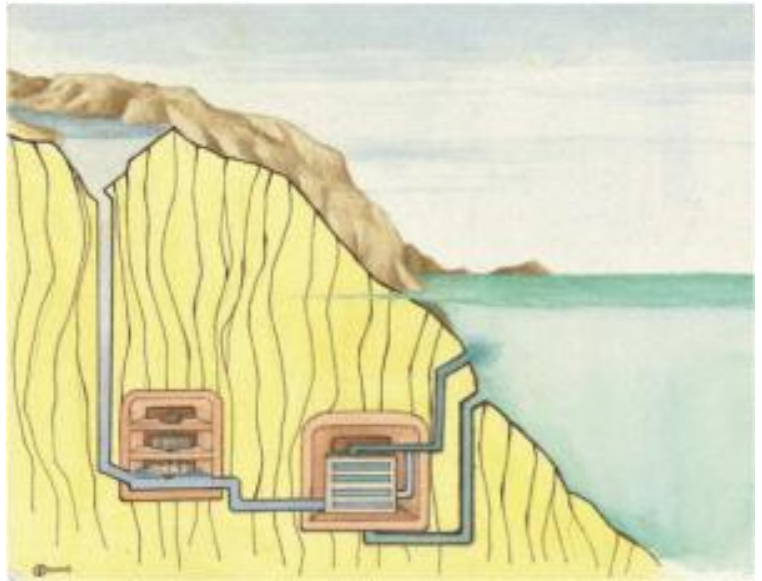


Fig. 4.4 Sub-sea PRO power plant [11].

Osmotic power can also be used for pumping of water across dikes, for example from IJsselmeer in the Netherlands to the North Sea. The flexible design of the PRO plant allows the combined power and pumping station (yellow circle in fig. 4.5) to be fitted **between existing infrastructures** as the fig. 4.5 suggests. The membrane section can be located below ground. Filtration units for saltwater and freshwater as well as turbine halls can be placed on appropriate locations in the area. This concept produces power at the same time as it drains the dike. An additional advantage is that the water going into the ocean will be cleaner than the unprocessed freshwater [12].



Fig. 4.6 Power and pumping station (yellow circle)

4.3 Power generated and cost

The higher the gradient between salinity in the fresh- and saltwater, the more pressure will build up in the system. Similarly, the more water that enters the system, the more power can be produced. Given the sufficient control of the pressure on the salt water side, approximately half the theoretical energy (from the 24-26 bars of the theoretical osmotic pressure) can be transformed to electrical power, meaning that the operating pressure are in the range of 11-15 bars, which is equivalent to a water head of 100–145 m in a hydropower plant, enabling the **generation** of 1 MW per m³/sec of freshwater [9].

The estimated energy **cost** of osmotic power is comparable and competitive with the other new renewable energy sources, such as wave, tidal, biomass and offshore wind being in the range of 50-100 €/MWh. The capital cost of installed capacity is high compared to other renewable energy sources. However, each MW installed is very productive, with an average operation time above 8,000 hours a year. This should generate approximately twice the energy supplied (GWh) per installed MW per year compared for example to a wind mill.

These estimations have been made with the target power density of the membrane, 5 W/m², and other future technological improvements [5].

To evaluate the current economic feasibility of PRO, estimates of PRO facility revenue per membrane area per year can be determined using:

$$\frac{\text{Revenue}}{\text{Membrane area} \cdot \text{year}} = \text{Power density} \cdot \text{Energy price} \quad (4.1)$$

Considering an achievable power density of 5 W/m² and a current energy price of 0.10 \$/kWh, a facility revenue of 4.4 dollars per square meter of membrane per year (\$/m²y) would result. In order to better understand this, fig. 7 illustrates the facility revenue generated by each square meter of membrane (\$/m²) as a function of energy price, considering different membrane lifetimes (see section 3.4.5), and based on 5 W/ m² of power density. As would be expected, revenues increase with increasing energy price and membrane life. At current energy prices and achievable power densities, for an expected membrane life of 5 years, the membrane revenue is 22 \$/m². This value is at the lowest of the range of the current estimated bulk cost of membranes per square meter, 20–40 \$/m² (estimation based on RO-type membranes). Thus, currently PRO does not appear to be able to produce energy at a competitive cost. In order for PRO to be more competitive, a substantial increase in power density, decrease in membrane cost, or increase in membrane life (or some combination thereof) must be achieved [13].

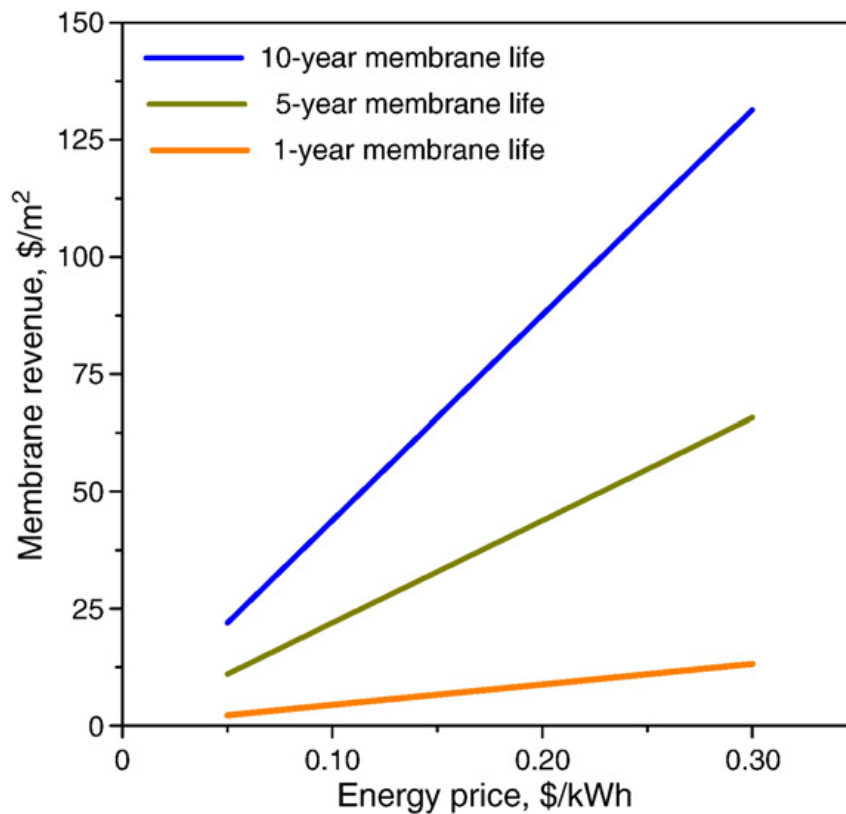


Fig. 4.7 Sensitivity analysis for membrane revenue as a function of energy price and membrane life. Membrane revenue is calculated as the product between the power density and the energy price. A power density of 5 W/m² is assumed [13].

4.4 Size

The size of PRO power plant depends mainly on the produced power and less on the level of the existing technology (especially the power density of the membrane). The prototype plant (capacity 10kW – see section 4.5) consists of about 2,000 m² of membrane, 66 pressure pipes, a cleaning unit, pressure exchangers, and a turbine. It is estimated that a full-size 25-MW osmotic power plant, which could supply around 30000 European households with electricity, would require 5 million m² of membrane. That would require a plant the **size** of a football stadium. The operational scale of such a plant is stunning: To achieve an output of 1 MW, as mentioned above, 1 cubic meter (m³) of freshwater per second must be mixed with 2 m³ of seawater at 12 bar. This means that a typical 25-MW plant would need 25 m³ of freshwater and 50 m³ of seawater per second [14].

4.5 The first PRO power plant

After more than a decade of collaborative research and development, and a little more than a year of construction, the world's first prototype plant put into operation in spring 2009 in the southeast of **Norway**, at **Tofte** on the Oslo fjord. The location is within the facility of a pulp factory in operation, which simplifies the approval process and at the same time gives good access to existing infrastructure. In addition, the location has good access to sea water from the ocean, and fresh water from a nearby lake.

The prototype plant is designed as a typical plant placed at sea level. Freshwater is taken from the lake via pipes. Seawater is fed into the plant by underground pipes, and the brackish water is lead to the natural brackish water zone [5]. The plant, as mentioned above, comprises about

2,000 m² of membrane, 66 pressure pipes, a cleaning unit, pressure exchangers, and a turbine [14]. The membrane unit consists of a bank of modified spiral wound modules [13].

In fig. 4.8 is shown a model of the prototype.

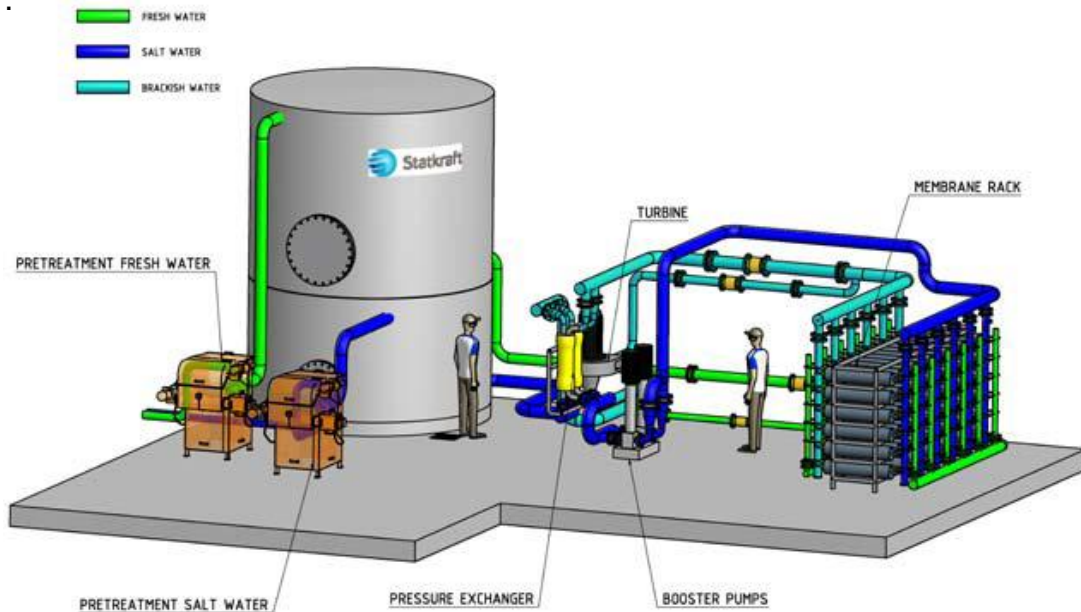


Fig. 4.8 Model of the prototype [5].

Since this is the first plant built for PRO operation, severe precautions have been taken to make sure that possible pollution in the water does not destroy the membranes. For the sea water regular pressure screens are used, and for the fresh water from the lake the pre-treatment is similar to that being used for drinking water. The ambitions are that the fresh water can be treated similar to the sea water. This will however be based on the operational experiences.

The main objectives of the prototype are twofold. Firstly, confirming that the designed system can produce power on a reliable 24-hour/day production. Secondly, the plant will be used for further testing of technology achieved from parallel research activities to substantially increase the efficiency. These activities will mainly be focused on membrane modules, pressure exchanger equipment and power generation (turbine and generator). In addition, there will be a focus on further development of control systems, water pre-treatment equipment, as well as infrastructure with regards to water inlets and outlets. Furthermore, the interface and integration for all the components in the system can be studied together in operation, not only as individual parts of a system. Finally, the prototype will be a meeting place for all stakeholders in the development of osmotic power, such as research, industry and governmental representatives.

Although the design capacity is in the range of 10 kW, the capacity in the first phase is less, about 2 to 4 kW. The membranes have room for improvement, as they have power density less than 1w/m², and there are high expectations for optimizations for the whole system as such. After operation and further testing, the experience gained will be based on both operational changes as well as changes to the system and replacement of parts. This is in order to increase the efficiency and optimize the power generation [5]. In a longer perspective this would be used as a basis to develop a power plant with installed capacity between 1-2 MW. If viable, project results will be used to develop a commercial osmotic power facility (25 MW) by 2015 [15].

Fig. 4.9 shows a photo of the prototype PRO power plant along with the pulp factory. In fig. 4.10 is presented the plant alone and in fig. 4.11-4.13 some parts of the infrastructure.



Fig. 4.9 Prototype PRO power plant along with the pulp factory [16].



Fig. 4.10 Prototype PRO power plant [17].

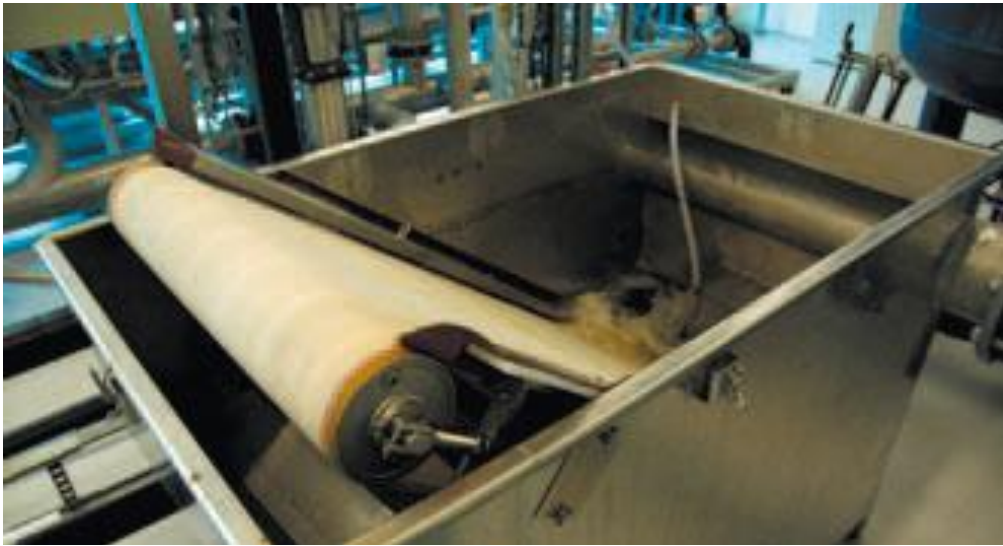


Fig. 4.11 Water filtering [18].



Fig. 4.12 Membranes coiled up inside pressure vessels [18].

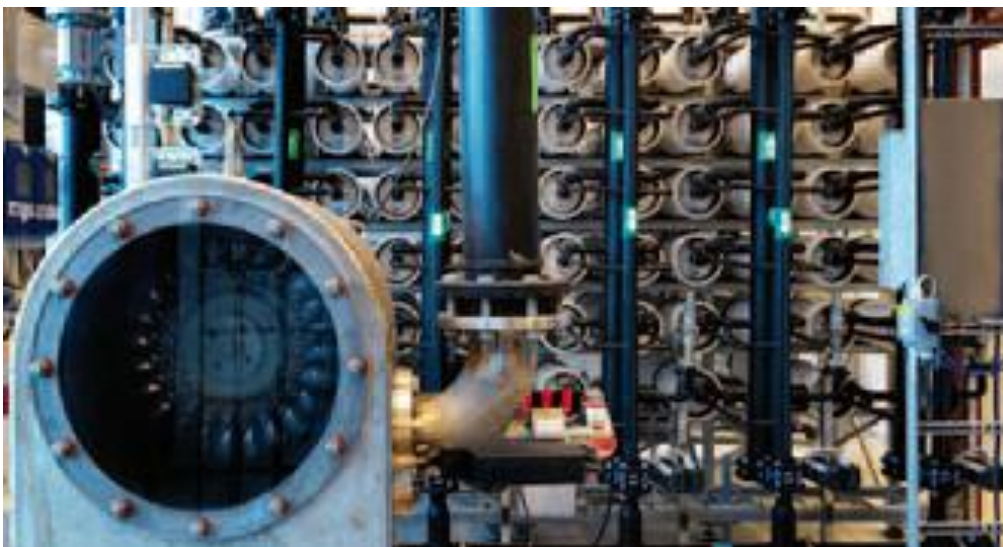


Fig. 4.13 Hydraulic turbine and behind the membrane unit [18].

CHAPTER 5.

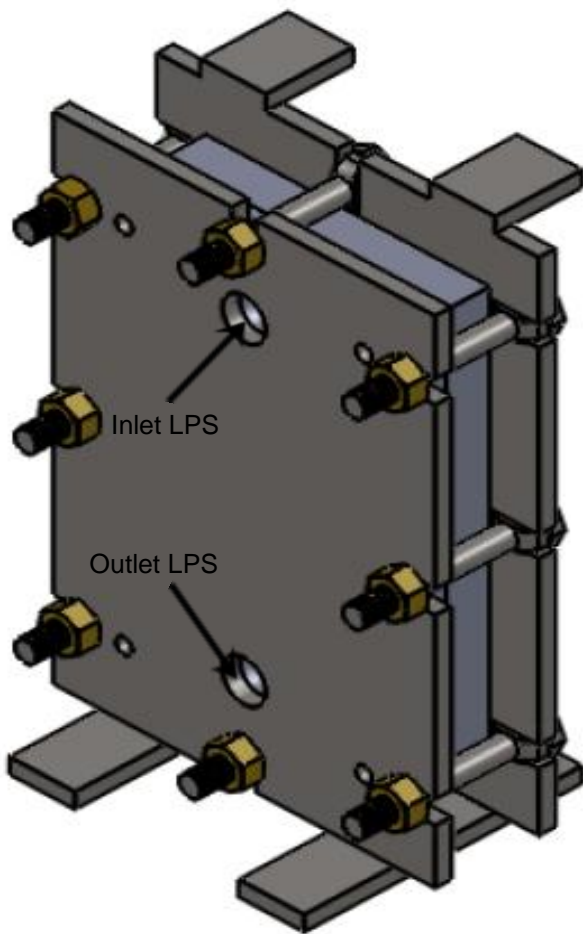
GEOMETRY, MODELING, EXPERIMENTAL

Description of the geometry, Modeling, Experimental setup

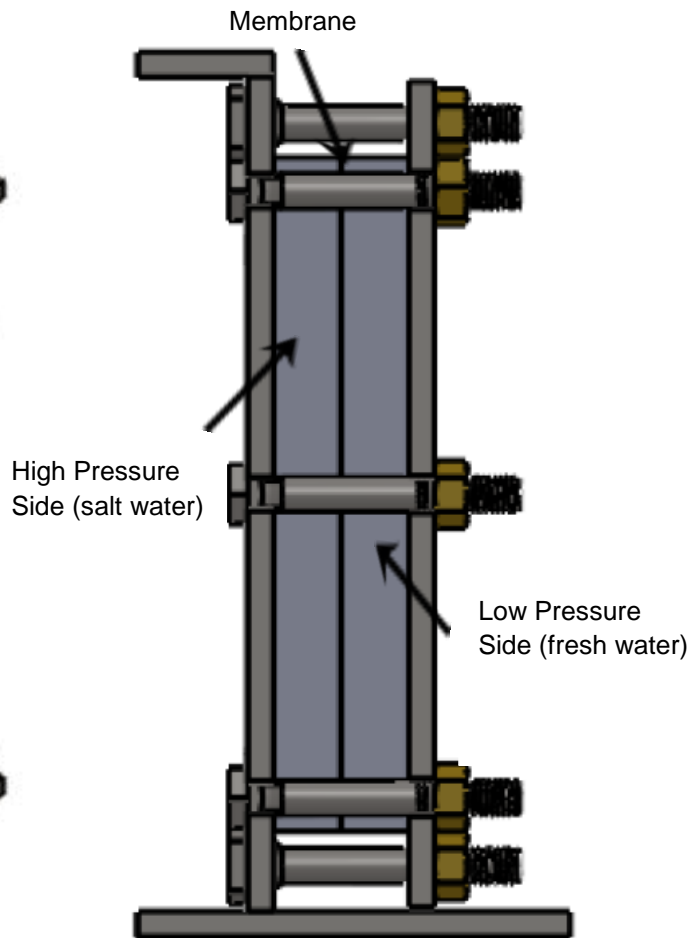
5.1 Description of the geometry

Initially in this work, the pressure retarded osmosis process was investigated in a test cell (module) of the company Hydration Technology Innovations (HTI), which is used for PRO and FO experiments. The flow in this cell has been simulated using computational fluid dynamics in order to: i) compare the results of CFD with experimental results and test if PRO concept can be simulated using computational methods, and ii) investigate the effect of key parameters in the process such as pressure, inlet flow rate, membrane characteristics and salt concentration. Finally, two new designs have been tested for their performance in PRO and compared with the HTI test cell.

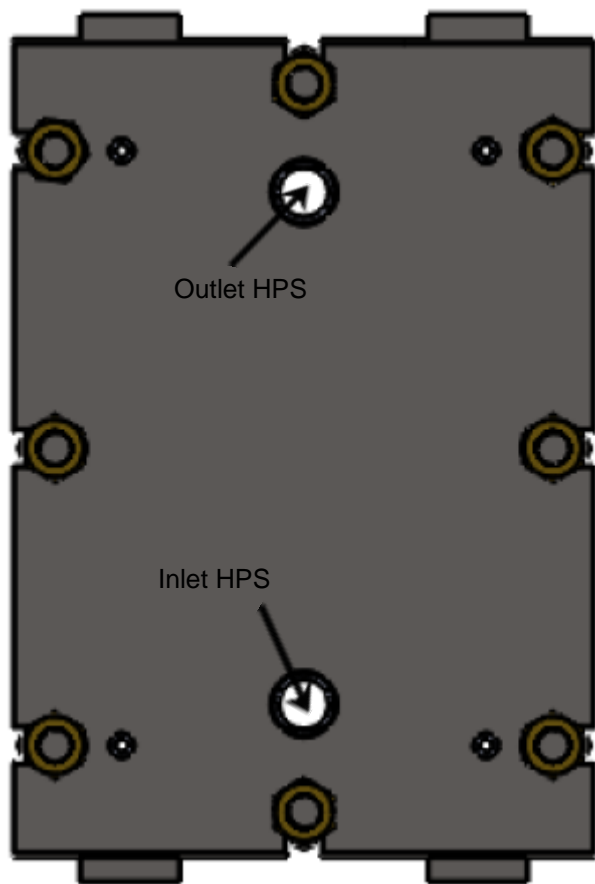
The following figure depicts the HTI test cell in 3 views:



i) View from a random spot



ii) Side view



iii) Back view

Fig. 5.1 HTI test cell

The HTI test cell, as shown in the figure above, consists of two sides, high pressure side (HPS) and low pressure side (LPS), where the salt and fresh water flow respectively, a membrane jammed between the two sides and two plates fixed to both sides to prevent the construction from breaking because of the high pressure.

The drawings of the two sides are shown in the figures below (dimensions in inches):

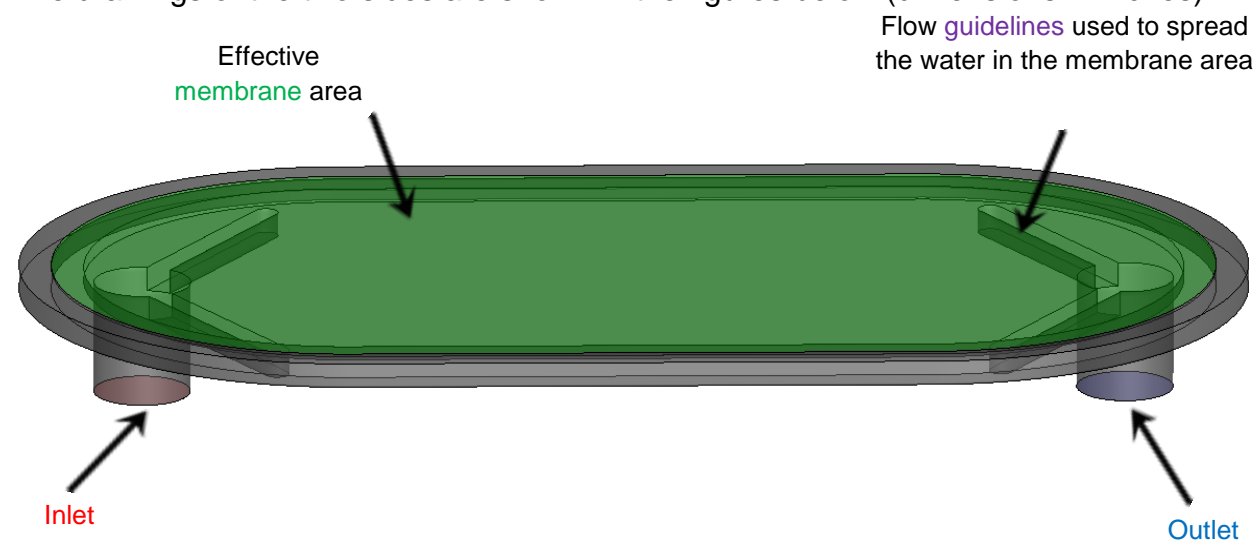


Fig. 5.2 3D view of high pressure side flow volume

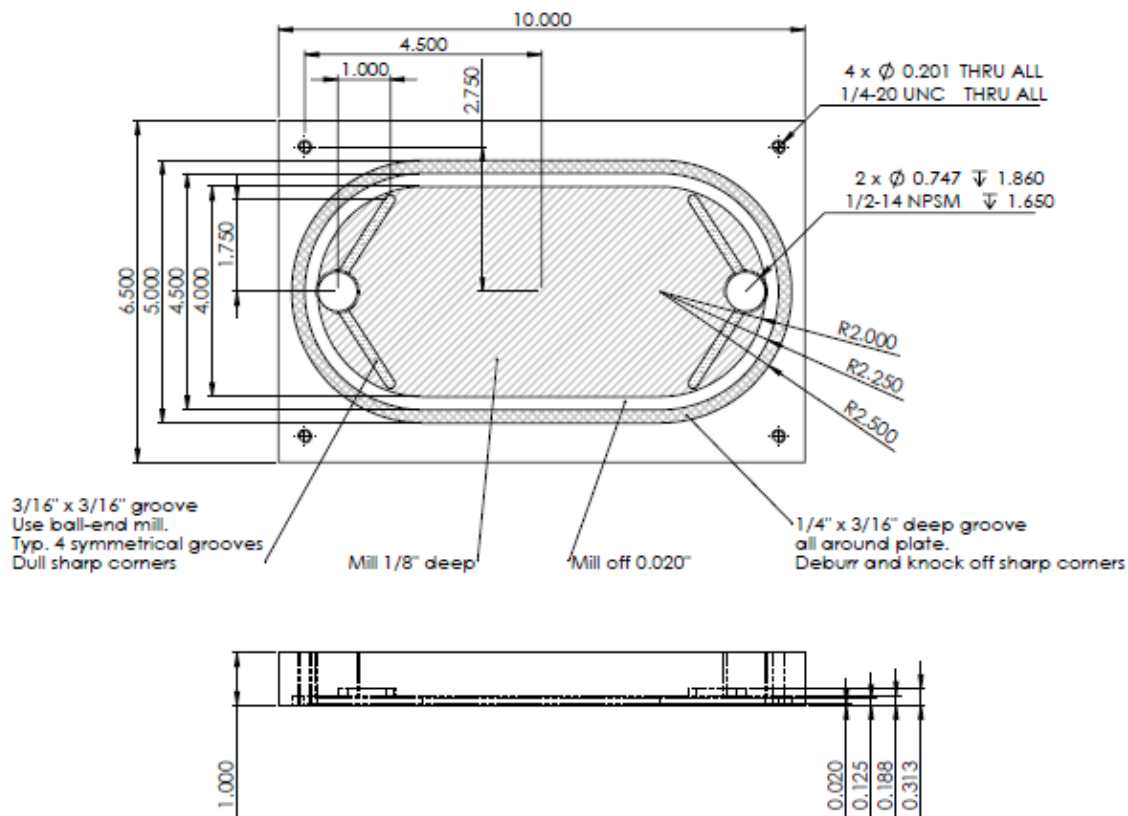


Fig. 5.3 Top, side and front view of high pressure side

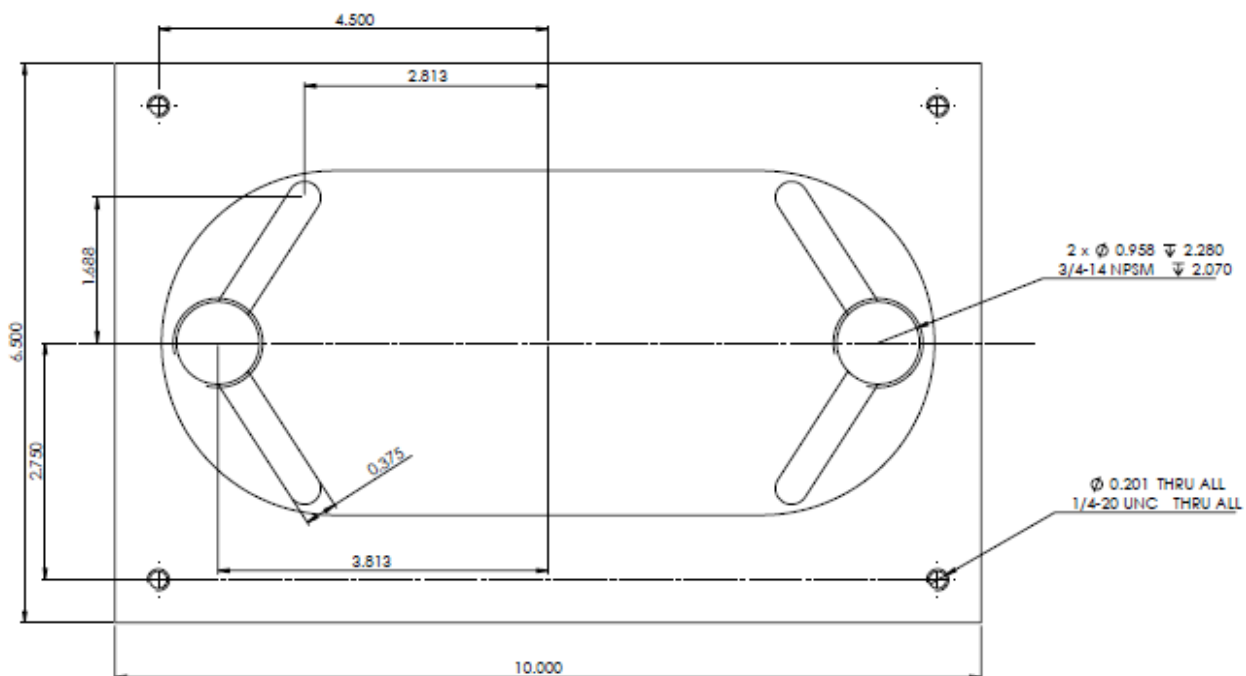


Fig. 5.4 Top view of low pressure side

The water (fresh and salt respectively) flows on both sides from the inlet towards the outlet following opposite directions: downward in the low pressure side and upward in the high pressure side, as shown in fig. 1. This formation in fig.1 is indicative as the inlet and outlet on both sides can be reversed and also the whole cell can be horizontal. The pressure retarded osmosis concept takes place in the membrane area where fresh water from the low pressure side moves through the membrane into the salt water on the high pressure side, driven by the osmotic pressure difference between the two sides. The fresh water is carried away by the salt water and is driven into the outlet.

5.2 Modeling

The osmotic process in the PRO test cell has been modeled using 4 basic equations: two for the flow of water on both sides, one for the flow of freshwater through the membrane and one for the diffusion of freshwater in saltwater. The flow of salt through the membrane and on the fresh water side is considered negligible.

5.2.1 Modeling the flow of water on both sides

For the flow of freshwater and saltwater on both sides are used the conservation equations for mass and momentum, which, if the flow is considered laminar and steady, and the effect of gravity is considered negligible, are written:

$$\nabla \cdot (\rho \vec{u}) = 0 \quad (5.1), \text{ the mass conservation equation and}$$

$$\nabla \cdot (\rho \vec{u} \vec{u}) = -\nabla p + \nabla \cdot \bar{\tau} \quad (5.2), \text{ the momentum conservation equation,}$$

where u is the absolute velocity, ρ the density and p the pressure of the fluid, and τ the stress tensor which is given by the equation:

$$\bar{\tau} = \mu \left[(\nabla \vec{u} + \nabla \vec{u}^T) - \frac{2}{3} \nabla \cdot \vec{u} I \right] \quad (5.3)$$

where μ is the molecular viscosity and I is the unit tensor.

5.2.2 Modeling the flow through the membrane

The flow (velocity) of freshwater through the membrane has been modeled using the general equation of osmosis:

$$U = A \cdot (\Delta\pi - \Delta P) \quad (5.4),$$

where U is the velocity of freshwater through the membrane which is considered vertical, A is the water permeability coefficient of the membrane, ΔP the hydraulic pressure difference between the fresh and salt water side, and $\Delta\pi$ is osmotic pressure difference between the two sides and is given by the van't Hoff equation:

$$\Delta\pi = 2 \cdot \Delta C_{\text{NaCl}} \cdot R \cdot T \quad (5.5),$$

where ΔC_{NaCl} is the salt concentration difference between the two sides, R is the gas constant calculated for salt and T is the absolute temperature of the fresh and salt water.

5.2.3 Modeling the diffusion of freshwater in saltwater

The diffusion flux of species i ($i=2$ for salt and fresh water) (\vec{J}_i), which arises due to gradients of concentration (the gradients of temperature are negligible), have been modeled using the dilute approximation (Fick's law):

$$\vec{J}_i = -\rho D_{i,m} \nabla Y_i \quad (5.6),$$

where $D_{i,m}$ is the mass diffusion coefficient and Y_i the local mass fraction for species i in the mixture.

5.3 Experimental Setup

An experimental apparatus as shown in figure 5.5 can be used for PRO experiments:

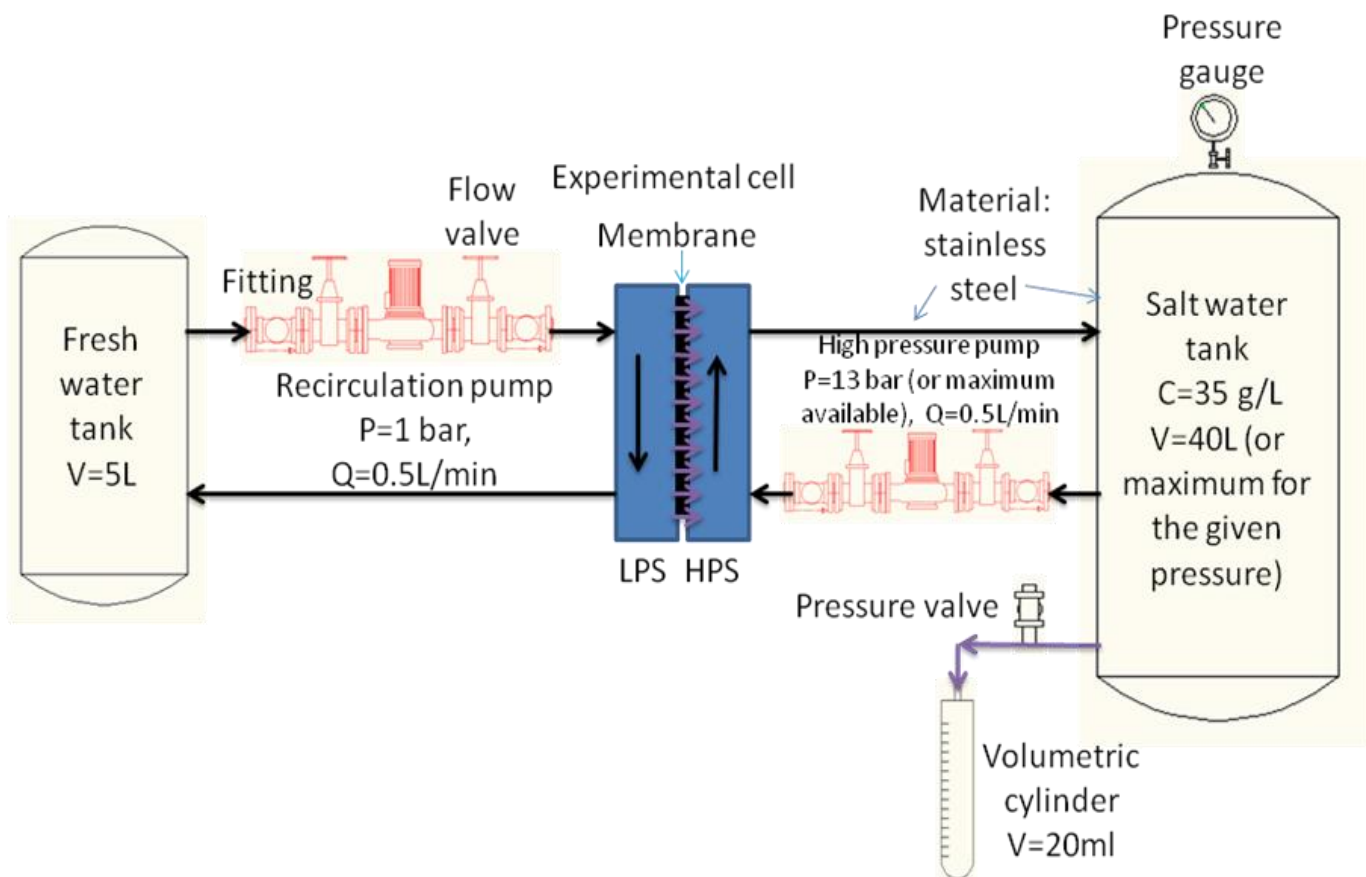


Fig. 5.5 Experimental Apparatus for PRO

The apparatus consist of:

1. The HTI test cell as described in the previous section. The material that can be used for the construction of the test cell is either stainless steel for the plates and polypropylene for the inside or a transparent material for both (such as plexiglass) which can bare the high pressure (15.8 bar) and allows the use of a laser technique (such as Laser-induced breakdown fluorescence) [1] for the measurement of salt concentration in different spots on the test cell.
2. The membrane which has been supplied by the HTI. It is a membrane for forward osmosis (FO) made from cellulose triacetate (CA) with water permeability coefficient $A = 1.87 \times 10^{-12} \text{ [m/(s*Pa)]}$ and dimensions 10X6.5 inches to fit in the test cell. (figures 5.6, 5.7 and 5.8)
3. Two tanks one with 5L capacity for the fresh water and one with 40 L for the salt water (40 L are sufficient to ensure that the fresh water which enters the salt water circuit through the membrane is negligible). Both tanks are made of stainless steel.
4. One recirculation pump for the fresh water which provides a volumetric flow 0.5 L/min and one high pressure pump for the salt water for pressure up to 15.8 bar and volumetric flow 0.5L/min, which can work with salt water.

5. A pressure gauge for measuring the pressure in the high pressure circuit and a pressure valve for keeping it constant at 15.8 bar.
6. A volumetric cylinder 20 ml which receives the excessive water from the high pressure circuit and is used for measuring the flow through the membrane (the excessive water is actually the water which comes from the fresh water side through the membrane and divided by the time which is needed to fill the cylinder can give the velocity through the membrane and therefore the volumetric flow).
7. Seven tubes made of stainless steel.
8. Four fittings and four flow valves for the integration of the pumps.
9. Apart from the laser technique for the measurement of salt concentration on the test cell, it can be used salinity meters [2], each one integrated in the test cell on a different spot.

The figures 5.6, 5.7 and 5.8 show images of the membrane taken using Scanning Electron Microscopy (SEM). The figures 5.6 and 5.7 show the thin dense non-porous layer of the membrane called skin, which is used for the rejection of salt and the figure 5.8 show the support porous layer which is used to the skin mechanically . The main ingredient of the membrane is sensitive to electrons and therefore an in-depth investigation of the membrane cannot be performed using this technique. The SEM images of HTI membrane have been taken at the Electron Microscopy and Nanomaterials Laboratory of N.C.S.R Demokritos, Athens .

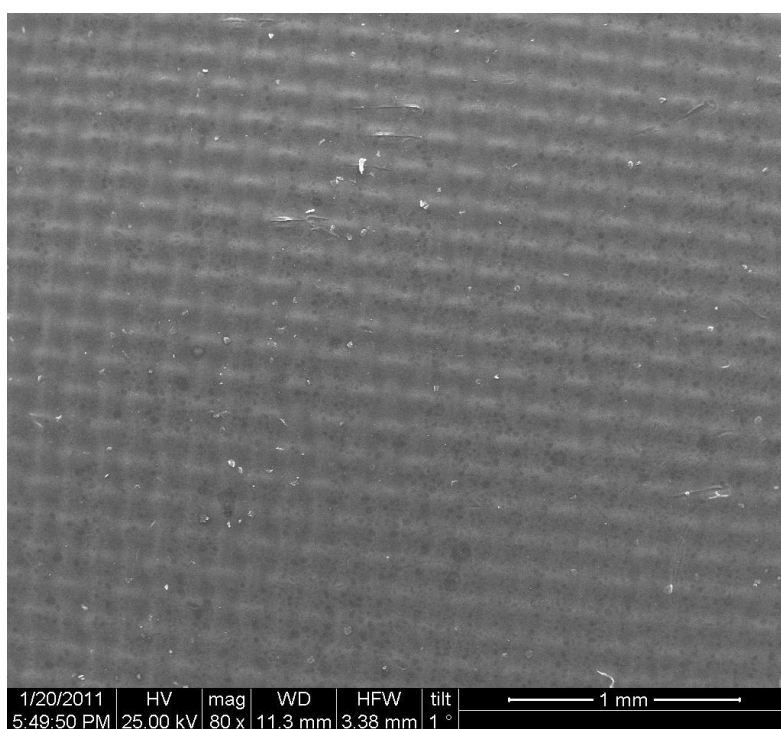


Fig.5.6 Skin layer of membrane using electron microscopy (zoom x80)

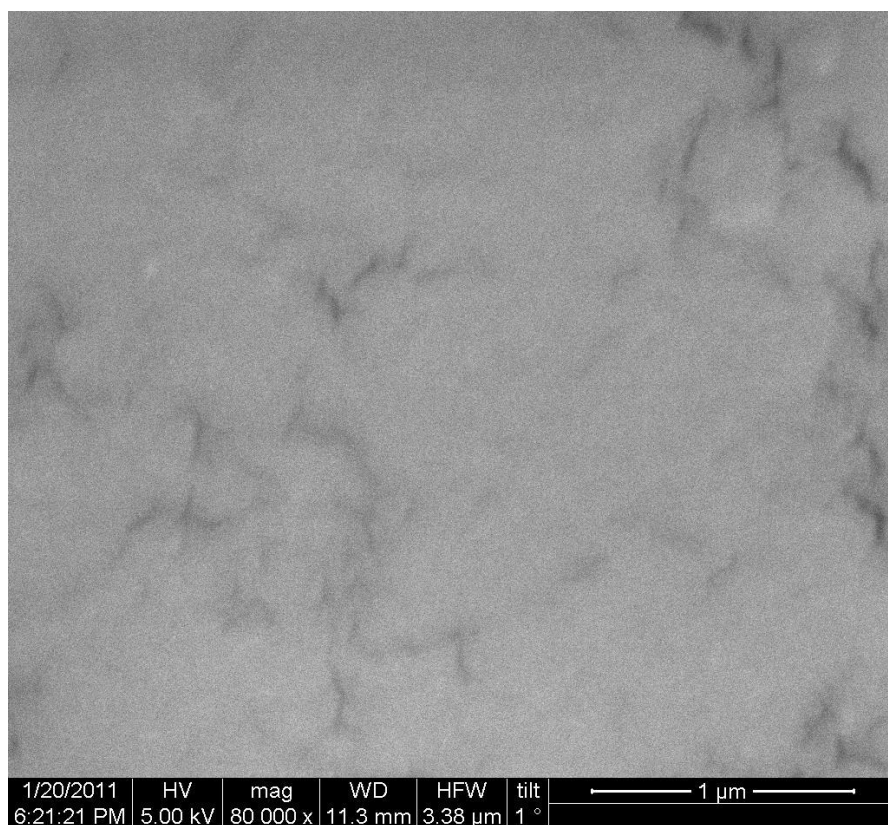


Fig. 5.7 Skin layer of membrane using electron microscopy (zoom x80000)

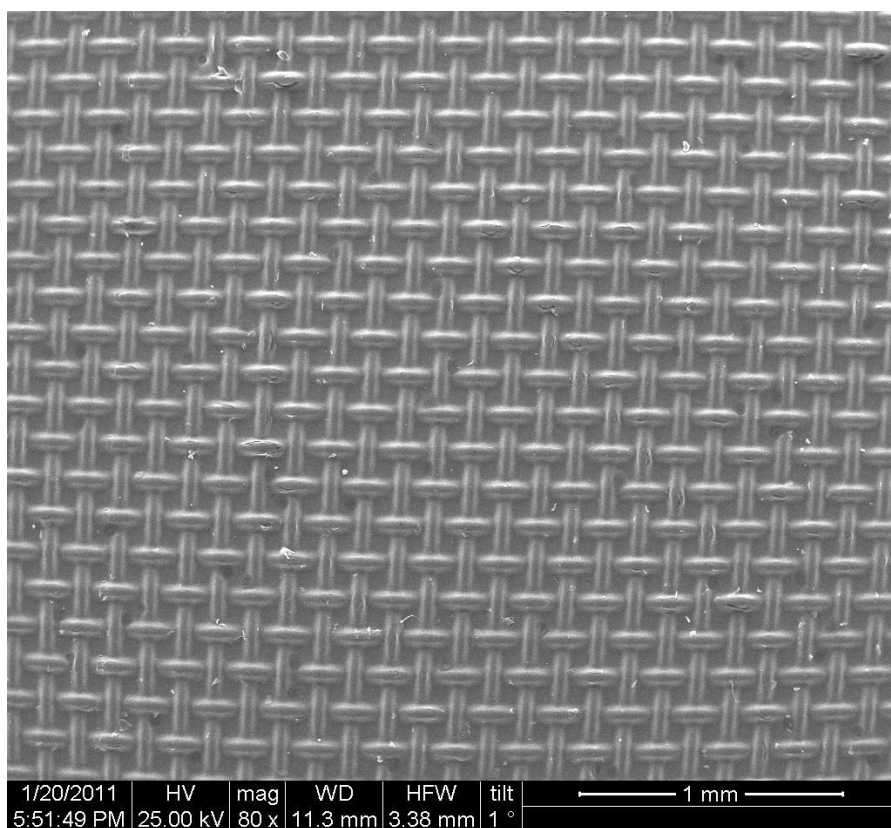


Fig. 5.8 Support layer of the membrane using electron microscopy (zoom x80)

CHAPTER 6.

COMPUTATIONAL FLUID DYNAMICS (CFD) SIMULATIONS

Computational Fluid Dynamics Simulation using ANSYS FLUENT 12

For the simulation of the osmotic power process in the PRO test cell four programs have been used with the following order: Solid Works 2010, Gambit 2.4.6, ANSYS FLUENT 12 and Techplot 360 2009. Only the high pressure side (saltwater) of the test cell has been simulated as the low pressure side (freshwater) is considered to contain only freshwater, and no salt, and have ambient conditions, and also the membrane is considered to have negligible thickness.

6.1 Solid Works 2010

In the first phase solid works 2010 has been used to draw a 3D drawing of the high pressure side, as shown in fig.6.1.

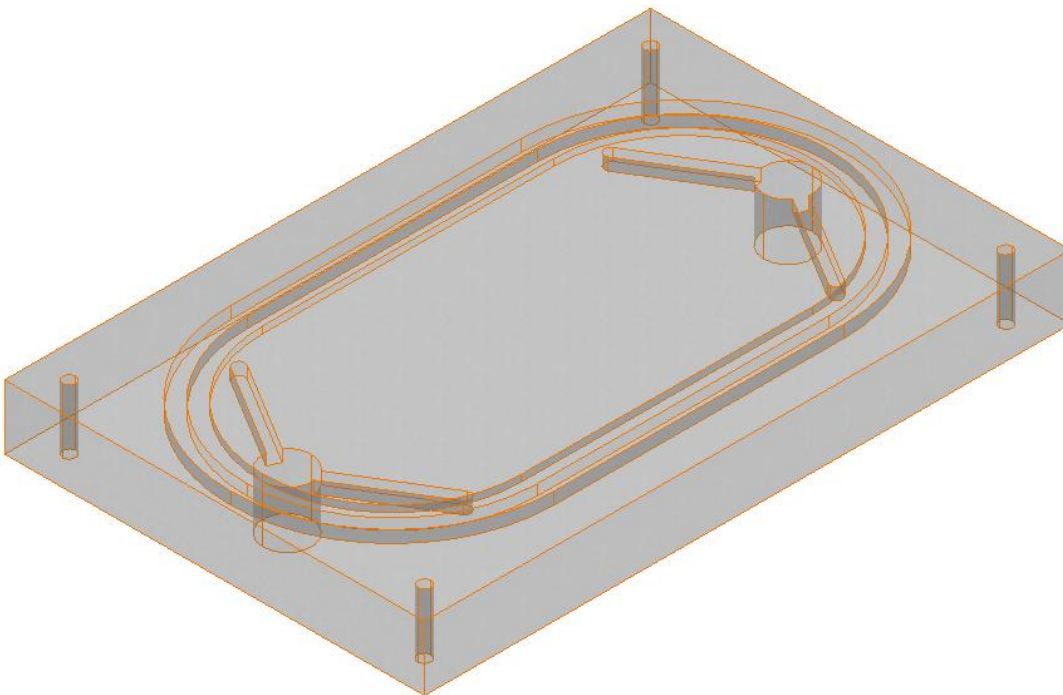


Fig. 6.1 3D drawing of the high pressure side in solid works (overall view)

6.2 Gambit 2.4.6

Given the drawing Gambit 2.4.6 has been used to generate a sufficient grid. For this purpose three grid densities have been generated: 700 thousands, 1.5 million and 3 million cells. The grid sensitivity study is presented in chapter 7. Here are presented only 2 photos of the high pressure side in Gambit: one of the drawing (fig. 6.2) and one of the mesh (fig. 6.3).

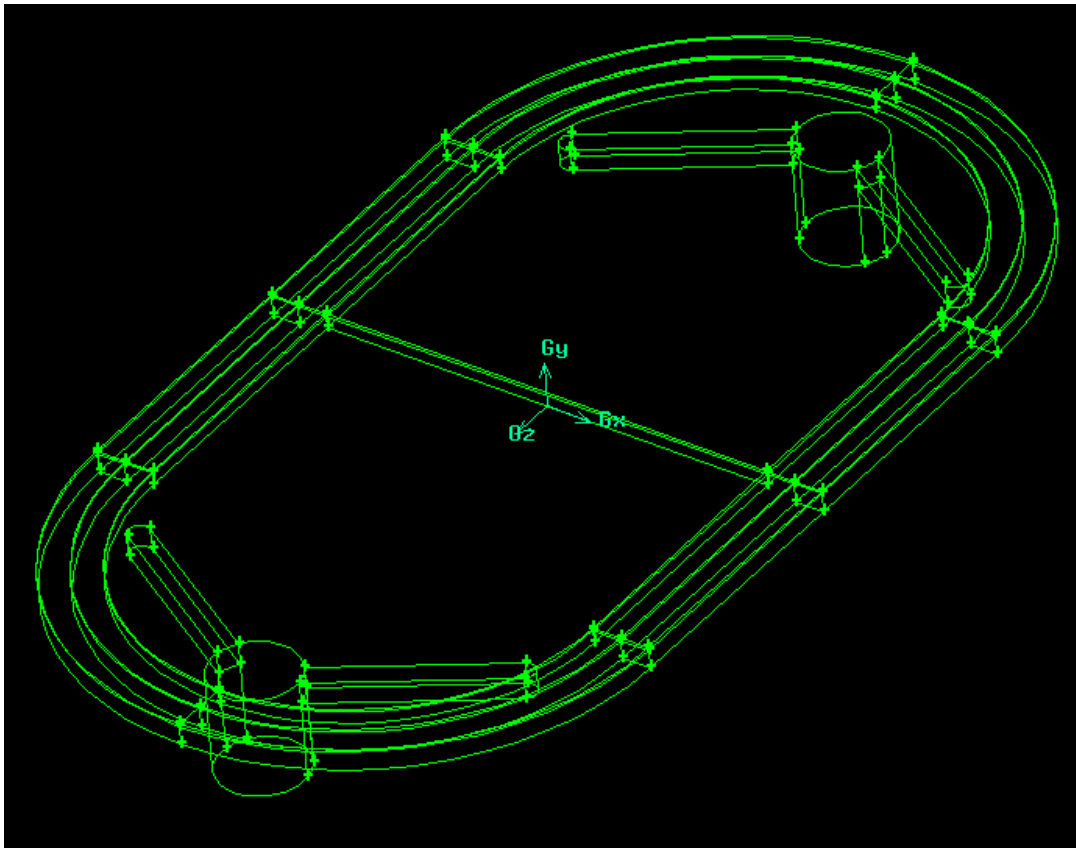


Fig. 6.2 drawing of the HPS in Gambit (overall view)

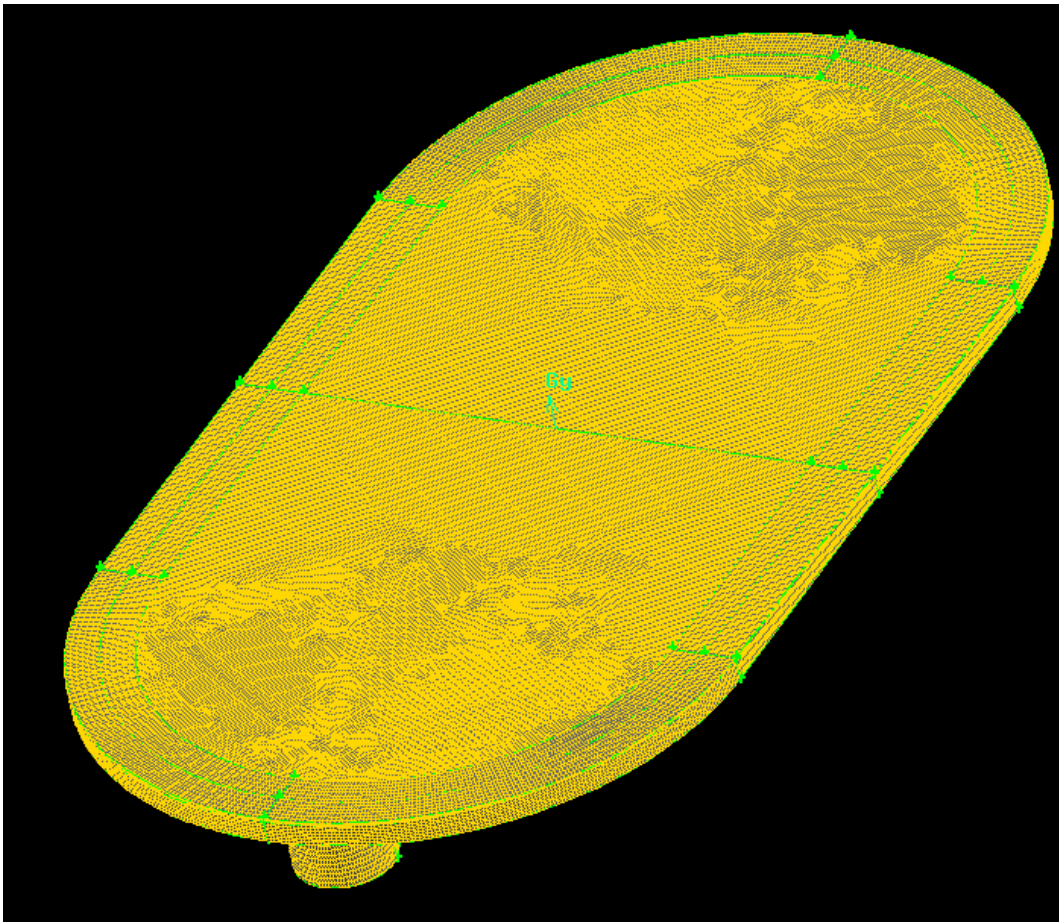


Fig.6.3 mesh of the HPS in Gambit (overall view)

6.3 ANSYS FLUENT 12

Fluent 12 has been used to solve numerically the equations which are described on the previous chapter and to provide a flow-field.

6.3.1 FLUENT 12 Solver Theory [30]

Overview of Flow Solvers

FLUENT allows you to choose either of two numerical methods:

- pressure-based solver
- density-based solver

Historically speaking, the pressure-based approach was developed for low-speed incompressible flows, while the density-based approach was mainly used for high-speed

compressible flows. However, recently both methods have been extended and reformulated to solve and operate for a wide range of flow conditions beyond their traditional or original intent.

In both methods the velocity field is obtained from the momentum equations. In the density-based approach, the continuity equation is used to obtain the density field while the pressure field is determined from the equation of state.

On the other hand, in the pressure-based approach, the pressure field is extracted by solving a pressure or pressure correction equation which is obtained by manipulating continuity and momentum equations.

FLUENT will solve the governing integral equations for the conservation of mass and momentum, and (when appropriate) for energy and other scalars such as turbulence and chemical species. In both cases a control-volume-based technique is used that consists of:

- Division of the domain into discrete control volumes using a computational grid.
- Integration of the governing equations on the individual control volumes to construct algebraic equations for the discrete dependent variables ("unknowns") such as velocities, pressure, temperature, and conserved scalars.
- Linearization of the discretized equations and solution of the resultant linear equation system to yield updated values of the dependent variables.

The two numerical methods employ a similar discretization process (finite-volume), but the approach used to linearize and solve the discretized equations is different.

Pressure-based Solver

The pressure-based solver employs an algorithm which belongs to a general class of methods called the projection method [31]. In the projection method, wherein the constraint of mass conservation (continuity) of the velocity field is achieved by solving a pressure (or pressure correction) equation. The pressure equation is derived from the continuity and the momentum equations in such a way that the velocity field, corrected by the pressure, satisfies the continuity. Since the governing equations are nonlinear and coupled to one another, the solution process involves iterations wherein the entire set of governing equations is solved repeatedly until the solution converges.

Two pressure-based solver algorithms are available in ANSYS FLUENT. A segregated algorithm and a coupled algorithm. These two approaches are discussed in the sections below.

The Pressure-Based Segregated Algorithm

The pressure-based solver uses a solution algorithm where the governing equations are solved sequentially (i.e., segregated from one another). Because the governing equations are nonlinear and coupled, the solution loop must be carried out iteratively in order to obtain a converged numerical solution.

In the segregated algorithm, the individual governing equations for the solution variables (e.g. u , w , P , T , k , ϵ , etc.) are solved one after another. Each governing equation, while being solved, is "decoupled" or "segregated" from other equations, hence its name. The segregated algorithm is memory-efficient, since the discretized equations need only be stored in the memory one at a time. However, the solution convergence is relatively slow, inasmuch as the equations are solved in a decoupled manner.

With the segregated algorithm, each iteration consists of the steps illustrated in Figure 4 and outlined below:

1. Update fluid properties (e.g, density, viscosity, specific heat) including turbulent viscosity (diffusivity) based on the current solution.
2. Solve the momentum equations, one after another, using the recently updated values of pressure and face mass fluxes.
3. Solve the pressure correction equation using the recently obtained velocity field and the mass-flux.
4. Correct face mass fluxes, pressure, and the velocity field using the pressure correction obtained from Step 3.
5. Solve the equations for additional scalars, if any, such as turbulent quantities, energy, species, and radiation intensity using the current values of the solution variables.
6. Update the source terms arising from the interactions among different phases (e.g., source term for the carrier phase due to discrete particles).
7. Check for the convergence of the equations.

These steps are continued until the convergence criteria are met.

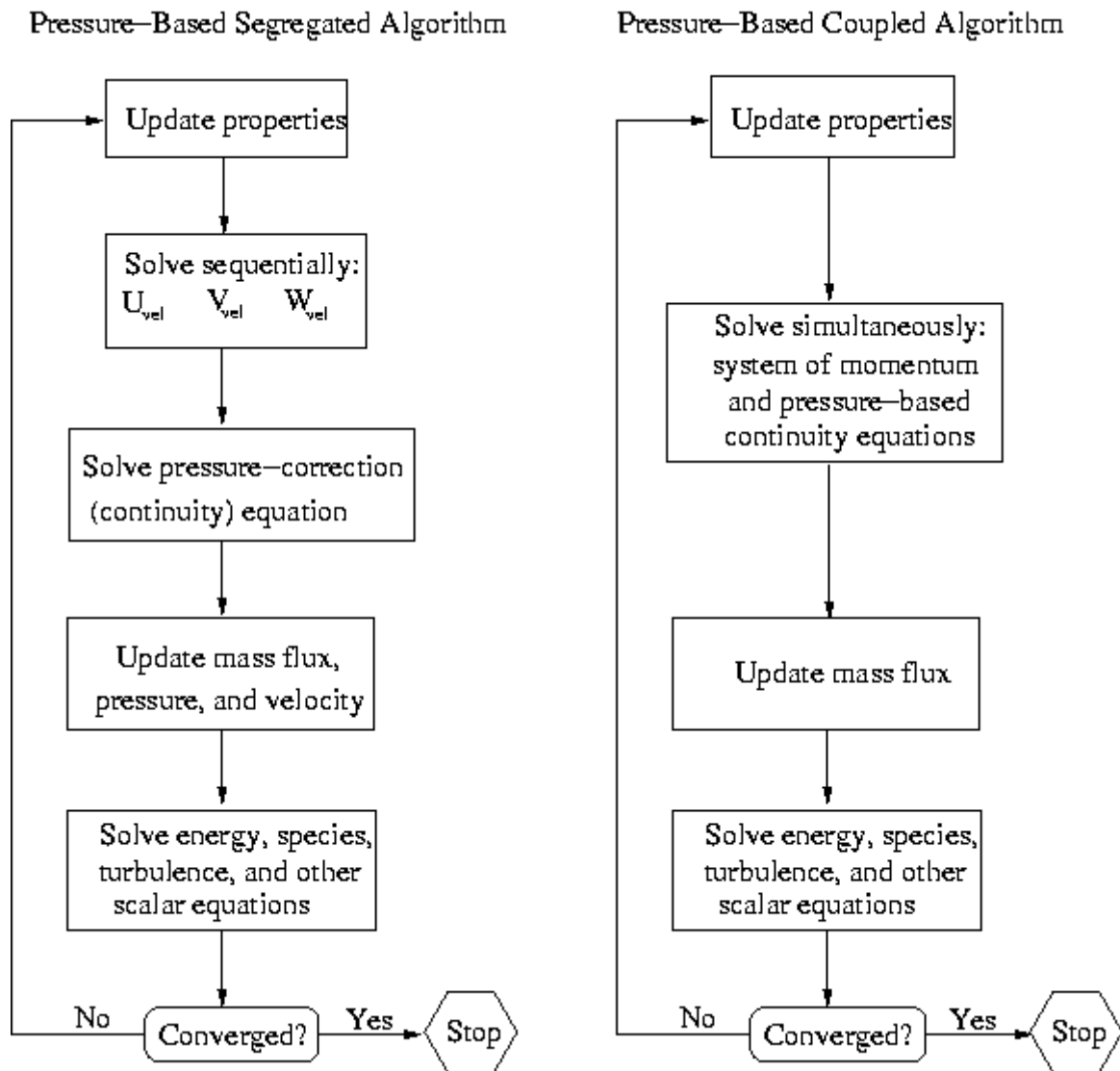


Fig. 6.4 Overview of the Pressure-Based Solution Methods

The Pressure-Based Coupled Algorithm and the density-based solver are not used in this project and therefore they are not presented here.

General Scalar Transport Equation: Discretization and Solution

FLUENT uses a control-volume-based technique to convert the governing equations (momentum, mass and species) to algebraic equations that can be solved numerically. This control volume technique consists of integrating the governing equations about each control volume, yielding discrete equations that conserve each quantity on a control-volume basis.

Discretization of the governing equations can be illustrated most easily by considering the steady-state conservation equation for transport of a scalar quantity ϕ . This is demonstrated by the following equation written in integral form for an arbitrary control volume V as follows:

$$\oint \rho \vec{\phi} \vec{u} \cdot d\vec{A} = \oint \Gamma_{\phi} \nabla \phi \cdot d\vec{A} + \int_V S_{\phi} dV \quad (6.1)$$

where

ρ =density

\vec{u} =velocity vector

$d\vec{A}$ =surface area vector

Γ_{ϕ} =diffusion coefficient for ϕ

$\nabla \phi$ =gradient of ϕ

S_{ϕ} =source of ϕ per unit volume

Equation 28 is applied to each control volume, or cell, in the computational domain. The two-dimensional, triangular cell shown in Figure 6.5 is an example of such a control volume.

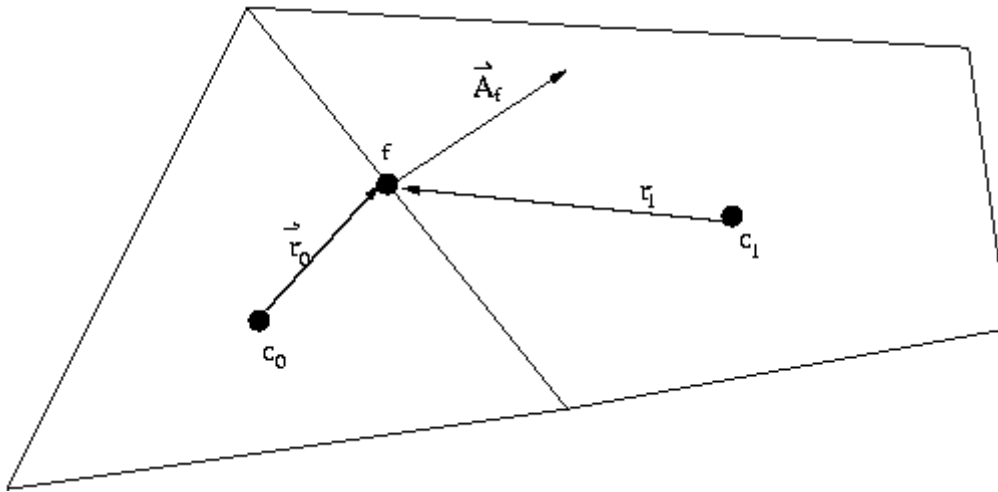


Fig. 6.5 Control Volume Used to Illustrate Discretization of a Scalar Transport Equation

Discretization of Equation 6.1 on a given cell yields

$$\sum_f^{N_{faces}} \rho_f \vec{u}_f \phi_f \cdot \vec{A}_f = \sum_f^{N_{faces}} \Gamma_{\phi} (\nabla \phi)_n \cdot \vec{A}_f + S_{\phi} V \quad (6.2)$$

where

N_{faces} =number of faces enclosing cell

ϕ_f =value of ϕ convected through face f

$\rho_f \vec{u}_f \cdot \vec{A}_f$ =mass flux through the face

\vec{A}_f = area of face f

$$(\nabla \phi)_n = \text{magnitude of } \nabla \phi \text{ normal to face } f$$

$$V = \text{cell volume}$$

The component of the equation which is time dependant has been omitted as we will be concerned only for steady-state flows in this project.

The equations solved by FLUENT take the same general form as the one given above and apply readily to multi-dimensional, unstructured meshes composed of arbitrary polyhedra.

Solving the Linear System

The discretized scalar transport equation (Equation 6.2) contains the unknown scalar variable ϕ at the cell center as well as the unknown values in surrounding neighbor cells. This equation will, in general, be non-linear with respect to these variables. A linearized form of Equation 6.2 can be written as

$$a_P \phi = \sum_{nb} a_{nb} \phi_{nb} + b \quad (6.3)$$

where the subscript nb refers to neighbor cells, and a_P and a_{nb} are the linearized coefficients for ϕ and ϕ_{nb} .

The number of neighbors for each cell depends on the grid topology, but will typically equal the number of faces enclosing the cell (boundary cells being the exception)

Similar equations can be written for each cell in the grid. This results in a set of algebraic equations with a sparse coefficient matrix. For scalar equations, FLUENT solves this linear system using a point implicit (Gauss-Seidel) linear equation solver in conjunction with an algebraic multigrid (AMG) method which is described in later section.

Spatial Discretization

FLUENT stores discrete values of the scalar ϕ at the cell centers (c_0 and c_1 in Figure 6.5). However, face values ϕ_f are required for the convection terms in Equation 29 and must be interpolated from the cell center values. This is accomplished using an upwind scheme.

Upwinding means that the face value ϕ_f is derived from quantities in the cell upstream, or "upwind," relative to the direction of the normal velocity u_n in Equation 6.2. FLUENT allows you to choose from several upwind schemes: first-order upwind, second-order upwind, power law, and QUICK.

The diffusion terms in Equation 6.2 are central-differenced and are always second-order accurate.

First-Order Upwind Scheme

When first-order accuracy is desired, quantities at cell faces are determined by assuming that the cell-center values of any field variable represent a cell-average value and hold throughout the entire cell; the face quantities are identical to the cell quantities. Thus when first-order upwinding is selected, the face value ϕ_f is set equal to the cell-center value of ϕ in the upstream cell.

- First-order upwind is available in the pressure-based and density-based solvers.

Power-Law Scheme

The power-law discretization scheme interpolates the face value of a variable, ϕ , using the exact solution to a one-dimensional convection diffusion equation

$$\frac{\partial}{\partial x}(\rho u \phi) = \frac{\partial}{\partial x} \Gamma \frac{\partial \phi}{\partial x} \quad (6.4)$$

where Γ and ρu are constant across the interval ∂x

Equation 6.4 can be integrated to yield the following solution describing how ϕ varies with x :

$$\frac{\phi(x) - \phi_0}{\phi_L - \phi_0} = \frac{\exp(\text{Pe} \frac{x}{L}) - 1}{\exp(\text{Pe}) - 1} \quad (6.5)$$

where

$$\begin{aligned} \phi_0 &= \phi|_{x=0} \\ \phi_L &= \phi|_{x=L} \end{aligned}$$

And Pe is the Peclet number

$$\text{Pe} = \frac{\rho u L}{\Gamma} \quad (6.6)$$

The variation of $\phi(x)$ between $x = 0$ and $x = L$ is depicted in Figure 6.6 for a range of values of the Peclet number. Figure 6.6 shows that for large Pe , the value of ϕ at $x = L$ is approximately equal to the upstream value. This implies that when the flow is dominated by convection, interpolation can be accomplished by simply letting the face value of a variable be set equal to its "upwind" or upstream value. This is the standard first-order scheme for FLUENT.

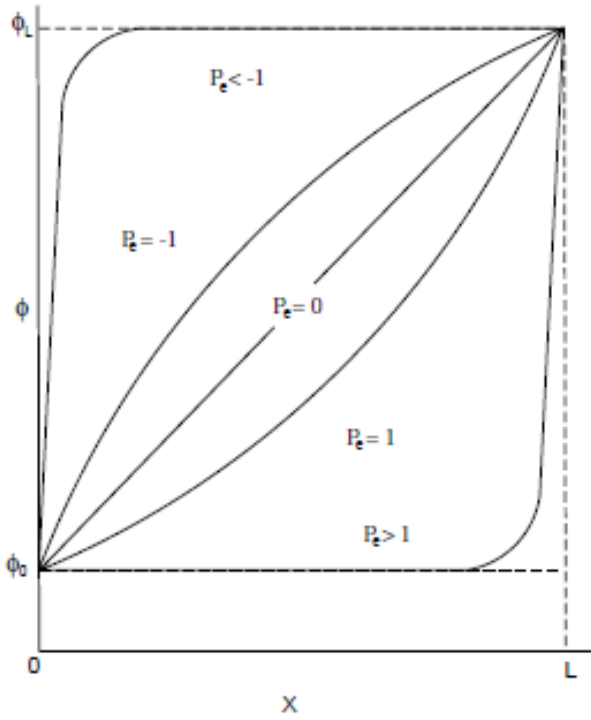


Fig. 6.6 Variation of a Variable ϕ between $x = 0$ and $x = L$ (Equation 6.4)

If the power-law scheme is selected, FLUENT uses Equation 6.5 in an equivalent “power law” format [32], as its interpolation scheme.

Figure 6 shows that for large Pe , the value of ϕ at $x = L=2$ is approximately equal to the upstream value. When $Pe=0$ (no flow, or pure diffusion), Figure 6 shows that ϕ may be interpolated using a simple linear average between the values at $x = 0$ and $x = L$. When the Peclet number has an intermediate value, the interpolated value for ϕ at $x = L=2$ must be derived by applying the “power law” equivalent of Equation 6.5.

- The power-law scheme is available in the pressure-based solver and when solving additional scalar equations in the density-based solver.

Second-Order Upwind Scheme

In this scheme quantities at cell faces are computed using a multidimensional linear reconstruction approach [33]. In this approach, higher-order accuracy is achieved at cell faces through a Taylor series expansion of the cell-centered solution about the cell centroid. Thus when second-order upwinding is selected, the face value ϕ_f is computed using the following expression:

$$\phi_f = \phi + \nabla \phi \cdot \vec{\Delta s} \quad (6.7)$$

where ϕ and $\nabla \phi$ are the cell-centered value and its gradient in the upstream cell, and $\vec{\Delta s}$ is the displacement vector from the upstream cell centroid to the face centroid.

- Second-order upwind is available in the pressure-based and density-based solvers.

Central-Differencing Scheme

The central-differencing scheme calculates the face value for a variable (ϕ_f) as follows:

$$\phi_{f,CD} = \frac{1}{2}(\phi_0 + \phi_1) + \frac{1}{2}(\nabla \phi_{r,0} \cdot \vec{r}_0 + \nabla \phi_{r,1} \cdot \vec{r}_1) \quad (6.8)$$

where the indices 0 and 1 refer to the cells that share face f , $\nabla \phi_{r,0}$ and $\nabla \phi_{r,1}$ are the reconstructed gradients at cells 0 and 1, respectively, and \vec{r} is the vector directed from the cell centroid toward the face centroid.

It is well known that central-differencing schemes can produce unbounded solutions and non-physical wiggles, which can lead to stability problems for the numerical procedure. These stability problems can often be avoided if a deferred approach is used for the central-differencing scheme. In this approach, the face value is calculated as follows:

$$\phi_f = \underbrace{\phi_{f,UP}}_{\text{implicit part}} + \underbrace{(\phi_{f,CD} - \phi_{f,UP})}_{\text{explicit part}} \quad (6.9)$$

where UP stands for upwind. As indicated, the upwind part is treated implicitly while the difference between the central-difference and upwind values is treated explicitly. Provided that the numerical solution converges, this approach leads to pure second-order differencing.

- The central differencing scheme is available only in the pressure-based solver.

QUICK Scheme

For quadrilateral and hexahedral meshes, where unique upstream and downstream faces and cells can be identified, FLUENT also provides the QUICK scheme for computing a higher-order value of the convected variable ϕ at a face. QUICK-type schemes [34] are based on a weighted average of second-order-upwind and central interpolations of the variable.

For the face e in Figure 7, if the flow is from left to right, such a value can be written as

$$\phi_e = \theta \left[\frac{S_d}{S_c + S_d} \phi_P + \frac{S_c}{S_c + S_d} \phi_E \right] + (1 - \theta) \left[\frac{S_u + 2S_c}{S_u + S_c} \phi_P - \frac{S_c}{S_u + S_c} \phi_W \right] \quad (6.10)$$

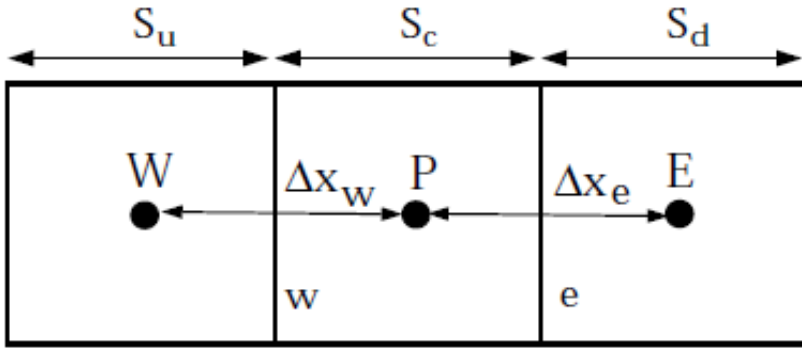


Fig. 6.7 one dimensional control volume

$\theta = 1$ in the above equation results in a central second-order interpolation while $\theta = 0$ yields a second-order upwind value. The traditional QUICK scheme is obtained by setting $\theta = 1/8$. The implementation in FLUENT uses a variable, solution-dependent value of θ chosen so as to avoid introducing new solution extrema. The QUICK scheme will typically be more accurate on structured grids aligned with the flow direction. Note that FLUENT allows the use of the QUICK scheme for unstructured or hybrid grids as well; in such cases the usual second-order upwind discretization scheme will be used at the faces of non-hexahedral (or nonquadrilateral, in 2D) cells. The second-order upwind scheme will also be used at partition boundaries when the parallel solver is used.

- The QUICK scheme is available in the pressure-based solver and when solving additional scalar equations in the density-based solver.

Third-Order MUSCL Scheme

This third-order convection scheme was conceived from the original MUSCL (Monotone Upstream-Centered Schemes for Conservation Laws) [35] by blending a central differencing scheme and second-order upwind scheme as

$$\phi_f = \theta \phi_{f,CD} + (1 - \theta) \phi_{f,SOU} \quad (6.11)$$

where $\phi_{f,CD}$ is defined in Equation 6.9, and $\phi_{f,SOU}$ is computed using the second-order upwind scheme.

Unlike the QUICK scheme which is applicable to structured hex meshes only, the MUSCL scheme is applicable to arbitrary meshes. Compared to the second-order upwind scheme, the third-order MUSCL has a potential to improve spatial accuracy for all types of meshes by reducing numerical diffusion, most significantly for complex three-dimensional flows, and it is available for all transport equations.

- The third-order MUSCL currently implemented in ANSYS FLUENT does not contain any flux-limiter. As a result, it can produce undershoots and overshoots when the flow-field under consideration has discontinuities such as shock waves.

- The MUSCL scheme is available in the pressure-based and density-based solvers.

Discretization of gradient $\nabla \phi$ of a given variable ϕ : Least squares cell based method

Gradients are needed not only for computing secondary diffusion terms and velocity derivatives, but also for constructing values of a scalar at the cell faces. In this method the solution is assumed to vary linearly. In Figure 6.8, the change in cell values between cell c_0 and c_i along the vector δr_i from the centroid of cell c_0 to c_i cell, can be expressed as

$$(\nabla \phi)_{c_0} \cdot \Delta r_i = (\phi_{c_i} - \phi_{c_0}) \quad (6.12)$$

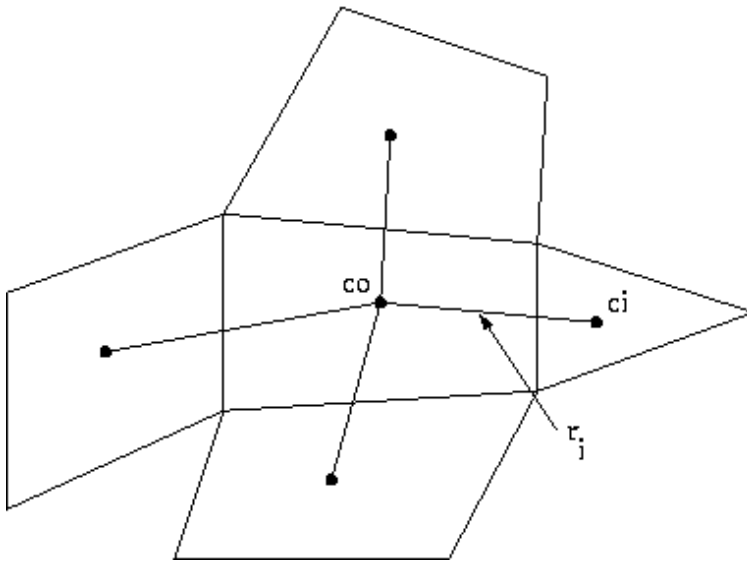


Fig. 6.8 Cell Centroid Evaluation

If we write similar equations for each cell surrounding the cell c_0 , we obtain the following system written in compact form:

$$[J](\nabla \phi)_{c_0} = \Delta \phi, \quad (6.13)$$

where $[J]$ is the coefficient matrix which is purely a function of geometry.

The objective here is to determine the cell gradient $(\nabla \phi_0 = \phi_x \hat{i} + \phi_y \hat{j} + \phi_z \hat{k})$ by solving the minimization problem for the system of the non-square coefficient matrix in a least-squares sense.

The above linear-system of equation is over-determined and can be solved by decomposing the coefficient matrix using the Gram-Schmidt process [30]. This decomposition yields a matrix of

weights for each cell. Thus for our cell-centered scheme this means that the three components of the weights $(W_{i_0}^x, W_{i_0}^y, W_{i_0}^z)$ are produced for each of the faces of cell c_0 .

Therefore, the gradient at the cell center can then be computed by multiplying the weight factors by the difference vector $\Delta\phi = (\phi_{c_i} - \phi_{c_0})$,

$$(\phi_x)_{c_0} = \sum_{i=1}^n W_{i_0}^x \cdot (\phi_{c_i} - \phi_{c_0}) \quad (6.14)$$

$$(\phi_y)_{c_0} = \sum_{i=1}^n W_{i_0}^y \cdot (\phi_{c_i} - \phi_{c_0}) \quad (6.15)$$

$$(\phi_z)_{c_0} = \sum_{i=1}^n W_{i_0}^z \cdot (\phi_{c_i} - \phi_{c_0}) \quad (6.16)$$

-The other methods for the discretization of gradients (Green-Gauss Cell-Based and Green-Gauss Node-Based) are not presented here as they are not used in this project.

-On irregular (skewed and distorted) unstructured meshes, the accuracy of the least-squares gradient method is comparable to that of the node-based gradient (and both are much more superior compared to the cell-based gradient). However, it is less expensive to compute the least-squares gradient than the node-based gradient. Therefore, it has been selected as the default gradient method in the ANSYS FLUENT solver.

-The temporal discretization is also not presented here as the project contains only steady-state flows.

Gradient Limiters

Gradient limiters, also known as slope limiters, are used on the second-order upwind (SOU) scheme to prevent spurious oscillations, which would otherwise appear in the solution flow field near shocks, discontinuities, or near rapid local changes in the flow field. The gradient limiter attempts to invoke and enforce the monotonicity principle by prohibiting the linearly reconstructed field variable on the cell faces to exceed the maximum or minimum values of the neighboring cells.

There are three gradient limiters in the ANSYS FLUENT solvers:

- Standard limiter
- Multidimensional limiter

- Differentiable limiter

Gradient limiters can be categorized into two general groups: non-differentiable limiters and differentiable limiters. Both, the standard limiter and multidimensional limiter are of the non-differentiable form, since they use minimum and maximum types of functions for limiting the solution variables. The third limiter in ANSYS FLUENT, as the name indicates, is a differentiable type of limiter, which uses a smooth function to impose the monotonicity principle.

For each of the above mentioned limiter methods, ANSYS FLUENT provides two limiting directions:

- cell to face limiting, where the limited value of the reconstruction gradient is determined at cell face centers. This is the default method.
- cell to cell limiting, where the limited value of the reconstruction gradient is determined along a scaled line between two adjacent cell centroids. On an orthogonal mesh (or when cell-to-cell direction is parallel to face area direction) this method becomes equivalent to the default cell to face method. For smooth field variation, cell to cell limiting may provide less numerical dissipation on meshes with skewed cells.

On unstructured meshes, ANSYS FLUENT uses the scalar form of the gradient limiter given by the following equation:

$$\Phi_{f_{SOV}} = \Phi + \psi \nabla \phi \cdot \mathbf{r} \quad (6.17)$$

where ψ is a scalar value which limits the gradient $\nabla \Phi$.

Standard Limiter

The standard limiter is the default limiter function in ANSYS FLUENT and is derived from the work of Barth and Jespersen [33]. This limiter is of a non-differentiable type and uses the Minmod function (Minimum Modulus) to limit and clip the reconstructed solution overshoots and undershoots on the cell faces.

Multidimensional Limiter

The multidimensional limiter in ANSYS FLUENT [36] has a similar form to the standard limiter. Since the multidimensional limiter uses a Minmod function for limiting the gradient, it is also classified as a non-differentiable type of limiter. However, in the standard limiter formulation, if limiting took place on any face of the cell, then this will cause the cell gradient to be clipped in an equal manner, in all directions, regardless of whether or not limiting is needed on the other cell faces. This limiting method is rather severe and adds unnecessary dissipation to the numerical scheme. The multidimensional limiter, on the other hand, attempts to lessen the severity of the gradient limiting by carefully examining the gradient on each cell and clipping only the normal components of the gradient to the cell faces. For this procedure to work on a scalar form limiter, the normal components of gradients on cell faces are first sorted out in ascending order of their magnitude so that only the necessary clipping can be applied. The multidimensional limiter is therefore less dissipative than the standard limiter.

Differentiable Limiter

One disadvantage with non-differentiable limiters is that they tend to stall the apparent residual's convergence after a few orders of reduction in residual magnitude. Note that this does not mean that the solution is not converging, but rather the solution continues to converge while the residuals are stalling. This annoying behavior can be directly traced to the non-differentiable nature of the limiting functions. Therefore, the differentiable limiter uses a smooth function to impose the monotonicity condition while allowing the residuals to converge. The differentiable limiter used in ANSYS FLUENT is a modified form [37] of a limiter which was originally proposed by Venkatakrishnan[38].

- ANSYS FLUENT uses gradient or slope limiters and not flux limiters. Gradient limiters are applied to the gradients of the variable field being linearly reconstructed at the cell faces, while flux limiters are used on the system fluxes.

Pressure-based solver

In this section, special practices related to the discretization of the momentum and continuity equations and their solution by means of the segregated solver are addressed. These practices are most easily described by considering the steady-state continuity and momentum equations in integral form:

$$\oint \rho \vec{v} \cdot d\vec{A} = 0 \quad (6.18)$$

$$\oint \rho \vec{v} \vec{v} \cdot d\vec{A} = - \oint p \mathbf{I} \cdot d\vec{A} + \oint \vec{\tau} \cdot d\vec{A} + \int_V \vec{F} dV \quad (6.19)$$

where \mathbf{I} is the identity matrix, $\vec{\tau}$ is the stress tensor, and \vec{F} is the force vector.

Discretization of the momentum equation

The discretization scheme which described in section “discretization” for a scalar transport equation is also used to discretize the momentum equations. The x-momentum equation can be obtained by setting in equation $\phi = u$:

$$a_P u = \sum_{nb} a_{nb} u_{nb} + \sum p_f A \cdot \hat{i} + S \quad (6.20)$$

If the pressure field and face mass fluxes were known, Equation 6.20 could be solved in the manner outlined in section discretization, and a velocity field obtained. However, the pressure field and face mass fluxes are not known a priori and must be obtained as a part of the solution. There are important issues with respect to the storage of pressure and the discretization of the pressure gradient term; these are addressed next.

FLUENT uses a co-located scheme, whereby pressure and velocity are both stored at cell centers. However, Equation 6.20 requires the value of the pressure at the face between cells c_0 and c_1 , shown in Figure 6.5. Therefore, an interpolation scheme is required to compute the face values of pressure from the cell values.

Pressure Interpolation Schemes

The default scheme in FLUENT interpolates the pressure values at the faces using momentum equation coefficients [39]:

$$P_f = \frac{\frac{P_{c_0}}{a_{p,c_0}} + \frac{P_{c_1}}{a_{p,c_1}}}{\frac{1}{a_{p,c_0}} + \frac{1}{a_{p,c_1}}} \quad (6.21)$$

This procedure works well as long as the pressure variation between cell centers is smooth. When there are jumps or large gradients in the momentum source terms between control volumes, the pressure profile has a high gradient at the cell face, and cannot be interpolated using this scheme. If this scheme is used, the discrepancy shows up in overshoots/undershoots of cell velocity.

Flows for which the standard pressure interpolation scheme will have trouble include flows with large body forces, such as in strongly swirling flows, in high-Rayleigh-number natural convection and the like. In such cases, it is necessary to pack the mesh in regions of high gradient to resolve the pressure variation adequately.

Another source of error is that FLUENT assumes that the normal pressure gradient at the wall is zero. This is valid for boundary layers, but not in the presence of body forces or curvature. Again, the failure to correctly account for the wall pressure gradient is manifested in velocity vectors pointing in/out of walls.

Several alternate methods are available for cases in which the standard pressure interpolation scheme is not valid:

- The linear scheme computes the face pressure as the average of the pressure values in the adjacent cells.
- The second-order scheme reconstructs the face pressure in the manner used for second-order accurate convection terms (see Section Second order upwind scheme). This scheme may provide some improvement over the standard and linear schemes, but it may have some trouble if it is used at the start of a calculation and/or with a bad mesh. The second order scheme is not applicable for flows with discontinuous pressure gradients imposed by the presence of a porous medium in the domain or the use of the VOF or mixture model for multiphase flow.
- The body-force-weighted scheme computes the face pressure by assuming that the normal gradient of the difference between pressure and body forces is constant. This

works well if the body forces are known a priori in the momentum equations (e.g., buoyancy and axisymmetric swirl calculations).

-When a case contains porous media, the body-force-weighted scheme is applied only for non-porous faces, where the scheme takes into account the discontinuity of explicit body forces (e.g., gravity, swirl, Coriolis) and the discontinuity of pressure gradients for flows with rapidly changing densities (e.g., natural convection, VOF). All interior and exterior porous faces are treated with a special scheme that preserves the continuity of the normal velocity across cell faces in spite of the discontinuity of the resistance.

- The PRESTO! (PREssure STaggering Option) scheme uses the discrete continuity balance for a “staggered” control volume about the face to compute the “staggered” (i.e., face) pressure. This procedure is similar in spirit to the staggered-grid schemes used with structured meshes [40]. Note that for triangular and tetrahedral meshes, comparable accuracy is obtained using a similar algorithm. The PRESTO! scheme is available for all meshes.

Discretization of the Continuity Equation

Equation 6.18 may be integrated over the control volume in Figure 6.5 to yield the following discrete equation

$$\sum_f^{N_{\text{faces}}} J_f A_f = 0 \quad (6.22)$$

where J_f is the mass flux through face f , ρu_n .

In order to proceed further, it is necessary to relate the face values of velocity, u_n , to the stored values of velocity at the cell centers. Linear interpolation of cell-centered velocities to the face results in unphysical checker-boarding of pressure. ANSYS FLUENT uses a procedure similar to that outlined by Rhie and Chow [41] to prevent checkerboarding. The face value of velocity is not averaged linearly; instead, momentum-weighted averaging, using weighting factors based on the a_p coefficient from equation 6.19, is performed. Using this procedure, the face flux, J_f , may be written as

$$J_f = \rho_f \frac{a_{p,c_0} u_{n,c_0} + a_{p,c_1} u_{n,c_1}}{a_{p,c_0} + a_{p,c_1}} + d_f ((p_{c_0} + (\nabla p)_{c_0} \cdot \vec{r}_0) - (p_{c_1} + (\nabla p)_{c_1} \cdot \vec{r}_1)) = \hat{J}_f + d_f (p_{c_0} - p_{c_1}) \quad (6.23)$$

where P_{c_0} , P_{c_1} , U_{n,c_0} , U_{n,c_1} are the pressures and normal velocities, respectively, within the two cells on either side of the face, and \hat{J}_f contains the influence of velocities in these cells (see Figure 6.5). The term d_f is a function of \bar{a}_P , the average of the momentum equation a_p coefficients for the cells on either side of face f .

Density Interpolation Schemes

For incompressible flows, ANSYS FLUENT uses arithmetic averaging for density. For compressible flow calculations (i.e., calculations that use the ideal gas law for density), ANSYS FLUENT applies upwind interpolation of density at cell faces. Several interpolation schemes are available for the density upwinding at cell faces: first-order upwind (default), second-order upwind, QUICK, MUSCL, and when applicable, central differencing and bounded central differencing.

The first-order upwind scheme (based on [41]) sets the density at the cell face to be the upstream cell-center value. This scheme provides stability for the discretization of the pressure-correction equation, and gives good results for most classes of flows. The first-order scheme is the default scheme for compressible flows. Although this scheme provides the best stability for compressible flow calculations, it gives very diffusive representations of shocks.

The second-order upwind scheme provides stability for supersonic flows and captures shocks better than the first-order upwind scheme. The QUICK scheme for density is similar to the QUICK scheme used for other variables. See Section Spatial Discretization for details.

- In the case of multiphase flows, the selected density scheme is applied to the compressible phase and arithmetic averaging is used for incompressible phases.

- For stability reasons, it is recommended that you achieve a solution with a first order scheme and then switch to a higher order scheme for compressible flow calculations.

Pressure-Velocity Coupling

Pressure-velocity coupling is achieved by using Equation 6.23 to derive an additional condition for pressure by reformatting the continuity equation (Equation 6.22). The pressure-based solver allows you to solve your flow problem in either a segregated or coupled manner. ANSYS FLUENT provides the option to choose among five pressure-velocity coupling algorithms: SIMPLE, SIMPLEC, PISO, Coupled, and (for unsteady flows using the non-iterative time advancement scheme (NITA)) Fractional Step (FSM). All the aforementioned schemes, except the "coupled" scheme, are based on the predictor-corrector approach.

Note that SIMPLE, SIMPLEC, PISO, and Fractional Step use the pressure-based segregated algorithm, while Coupled uses the pressure-based coupled solver.

- The pressure-velocity coupling schemes that are applicable when using the Eulerian multiphase model are Phase Coupled SIMPLE, Multiphase Coupled, and Full Multiphase Coupled.

Segregated Algorithms

SIMPLE

The SIMPLE algorithm uses a relationship between velocity and pressure corrections to enforce mass conservation and to obtain the pressure field.

If the momentum equation is solved with a guessed pressure field P^* , the resulting face flux, J_f^* , computed from Equation 6.23

$$J_f^* = \hat{J}_f^* + d_f (p_{c0}^* - p_{c1}^*) \quad (6.24)$$

does not satisfy the continuity equation. Consequently, a correction J_f' is added to the face flux J_f^* so that the corrected face flux, J_f

$$J_f = J_f^* + J_f' \quad (6.25)$$

satisfies the continuity equation. The SIMPLE algorithm postulates that J_f' be written as

$$J_f' = d_f (p'_{c0} - p'_{c1}) \quad (6.26)$$

where P' is the cell pressure correction.

The SIMPLE algorithm substitutes the flux correction equations (Equations 6.24 and 6.25) into the discrete continuity equation (Equation 6.22) to obtain a discrete equation for the pressure correction P' in the cell:

$$a_P p' = \sum_{nb} a_{nb} p'_{nb} + b \quad (6.27)$$

where the source term b is the net flow rate into the cell:

$$b = \sum_f^{N_{\text{faces}}} J_f^* A_f \quad (6.28)$$

The pressure-correction equation (Equation 6.27) may be solved using the algebraic multigrid (AMG) method described in later section. Once a solution is obtained, the cell pressure and the face flux are corrected using

$$p = p^* + \alpha_p p' \quad (6.29)$$

$$J_f = J_f^* + d_f (p'_{c0} - p'_{c1}) \quad (6.30)$$

Here a_p is the under-relaxation factor for pressure (see later Section for information about under-relaxation). The corrected face flux, J_f , satisfies the discrete continuity equation identically during each iteration.

The other algorithms are not presented here as they have not been used in this project.

Steady-State Iterative Algorithm

If you are performing a steady-state calculation, the governing equations for the pressure-based solver do not contain time-dependent terms. For steady-state flows, Section Discretization describes control-volume-based discretization of the steady-state transport equation (see Equation 6.1).

The time-advancement algorithm is not presented here as the project doesn't contain time-dependent flows.

Under-Relaxation of Variables

The under-relaxation of variables is used in all cases for some material properties, in the NITA solver for solution variables, and in the pressure-based coupled algorithm where this explicit under-relaxation is used for momentum and pressure.

Because of the nonlinearity of the equation set being solved by FLUENT, it is necessary to control the change of ϕ . This is typically achieved by under-relaxation, which reduces the change of ϕ produced during each iteration. In a simple form, the new value of the variable ϕ within a cell depends upon the old value, ϕ_{old} , the computed change in ϕ , $\Delta\phi$, and the under-relaxation factor, α , as follows:

$$\phi = \phi_{old} + \alpha\Delta\phi \quad (6.31)$$

Under-Relaxation of Equations

The under-relaxation of equations, also known as implicit relaxation, is used in the pressure-based solver to stabilize the convergence behavior of the outer nonlinear iterations by introducing selective amounts of ϕ in the system of discretized equations. This is equivalent to the location-specific time step.

$$\frac{a_p\phi}{\alpha} = \sum_{nb} a_{nb}\phi_{nb} + b + \frac{1-\alpha}{\alpha}a_p\phi_{old} \quad (6.32)$$

The CFL number is a solution parameter in the pressure-based coupled algorithm and can be written in terms of α :

$$\frac{1 - \alpha}{\alpha} = \frac{1}{CFL} \quad (6.33)$$

Multigrid Method

Multigrid (MG) methods [42] in numerical analysis are a group of algorithms for solving differential equations using a hierarchy of discretizations. They are an example of a class of techniques called multiresolution methods, very useful in (but not limited to) problems exhibiting multiple scales of behavior.

The main idea of multigrid is to accelerate the convergence of a basic iterative method by *global* correction from time to time, accomplished by solving a coarse problem. This principle is similar to interpolation between coarser and finer grids.

Coarse problem is an auxiliary system of equations used in an iterative method for the solution of a given larger system of equations. A coarse problem is basically a version of the same problem at a lower resolution, retaining its essential characteristics, but with fewer variables. The purpose of the coarse problem is to propagate information throughout the whole problem globally. In multigrid methods for partial differential equations, the coarse problem is typically obtained as a discretization of the same equation on a coarser grid or by a Galerkin approximation on a subspace called a coarse space. Typically, the coarse problem corresponds to a grid that is twice or three times coarser.

Multigrid methods can be applied in combination with any of the common discretization techniques. In these cases, multigrid methods are among the fastest solution techniques known today. In contrast to other methods, multigrid methods are general in that they can treat arbitrary regions and boundary conditions. They do not depend on the separability of the equations or other special properties of the equation. They are also directly applicable to more-complicated non-symmetric and nonlinear systems of equations.

There are many variations of multigrid algorithms, but the common features are that a hierarchy of discretizations (grids) is considered. The important steps are:

- Smoothing – reducing high frequency errors.
- Restriction – downsampling the residual error to a coarser grid.
- Interpolation or Prolongation – interpolating a correction computed on a coarser grid into a finer grid.

The ANSYS FLUENT solver contains two forms of multigrid: algebraic (AMG) and full-approximation storage (FAS). AMG is an essential component of both the pressure-based and density-based implicit solvers, while FAS is an important, but optional, component of the density-based explicit solver.

This section describes the mathematical basis of the multigrid approach.

Approach

ANSYS FLUENT uses a multigrid scheme to accelerate the convergence of the solver by computing corrections on a series of coarse grid levels. The use of this multigrid scheme can greatly reduce the number of iterations and the CPU time required to obtain a converged solution, particularly when your model contains a large number of control volumes.

The Need for Multigrid

Implicit solution of the linearized equations on unstructured meshes is complicated by the fact that there is no equivalent of the line-iterative methods that are commonly used on structured meshes. Since direct matrix inversion is out of the question for realistic problems and "whole-field" solvers that rely on conjugate-gradient (CG) methods have robustness problems associated with them, the methods of choice are point implicit solvers like Gauss-Seidel and ILU. Although the Gauss-Seidel and ILU schemes rapidly remove local (high-frequency) errors in the solution, global (low-frequency) errors are reduced at a rate inversely related to the mesh size. Thus, for a large number of nodes, the solver "stalls" and the residual reduction rate becomes prohibitively low.

The multi-stage scheme used in the density-based explicit solver can efficiently remove local (high-frequency) errors as well. That is, the effect of the solution in one cell is communicated to adjacent cells relatively quickly. However, the scheme is less effective at reducing global (low-frequency) errors—errors which exist over a large number of control volumes. Thus, global corrections to the solution across a large number of control volumes occur slowly, over many iterations. This implies that performance of the multi-stage scheme will deteriorate as the number of control volumes increases.

Multigrid techniques allow global error to be addressed by using a sequence of successively coarser meshes. This method is based upon the principle that global (low-frequency) error existing on a fine mesh can be represented on a coarse mesh where it again becomes accessible as local (high-frequency) error: because there are fewer coarse cells overall, the global corrections can be communicated more quickly between adjacent cells. Since computations can be performed at an exponentially decaying expense in both CPU time and memory storage on coarser meshes, there is the potential for very efficient elimination of global error. The fine-grid relaxation scheme or "smoother", in this case either the point-implicit linear solvers (Section AMG) or the explicit multi-stage scheme, is not required to be particularly effective at reducing global error and can be tuned for efficient reduction of local error.

The Basic Concept in Multigrid

Consider the set of discretized linear (or linearized) equations given by

$$A\phi_e + b = 0 \quad (6.34)$$

where ϕ_e is the exact solution. Before the solution has converged there will be a defect d associated with the approximate solution ϕ :

$$A\phi + b = d \quad (6.35)$$

We seek a correction ψ to ϕ such that the exact solution is given by

$$\phi_e = \phi + \psi \quad (6.36)$$

Substituting Equation 6.36 into Equation 6.34 gives

$$A(\phi + \psi) + b = 0 \quad (6.37)$$

$$A\psi + (A\phi + b) = 0 \quad (6.38)$$

Now using Equations 6.35 and 6.38 we obtain

$$A\psi + d = 0 \quad (6.39)$$

Which is an equation for the correction in terms of the original fine level operator A and the defect d . Assuming the local (high-frequency) errors have been sufficiently damped by the relaxation scheme on the fine level, the correction ψ will be smooth and therefore more effectively solved on the next coarser level.

Restriction and Prolongation

Solving for corrections on the coarse level requires transferring the defect down from the fine level (restriction), computing corrections, and then transferring the corrections back up from the coarse level (prolongation). We can write the equations for coarse level corrections ψ^H as

$$A^H \psi^H + R d = 0 \quad (6.40)$$

where A^H is the coarse level operator and R the restriction operator responsible for transferring the fine level defect down to the coarse level. Solution of Equation 6.40 is followed by an update of the fine level solution given by

$$\phi^{\text{new}} = \phi + P \psi^H \quad (6.41)$$

where P is the prolongation operator used to transfer the coarse level corrections up to the fine level.

Unstructured Multigrid

The primary difficulty with using multigrid on unstructured meshes is the creation and use of the coarse grid hierarchy. On a structured mesh, the coarse meshes can be formed simply by removing every other mesh line from the fine meshes and the prolongation and restriction operators are simple to formulate (e.g., injection and bilinear interpolation).

The difficulties of applying multigrid on unstructured meshes are overcome in a separate fashion by each of the two multigrid methods used in ANSYS FLUENT. While the basic principles discussed so far and the cycling strategy described in the next section are the same, the techniques for construction of restriction, prolongation, and coarse mesh operators are different for the AMG and FAS methods.

Multigrid Cycles

A multigrid cycle can be defined as a recursive procedure that is applied at each grid level as it moves through the grid hierarchy. Four types of multigrid cycles are available in ANSYS FLUENT: the V, W, F, and flexible ("flex") cycles. The V and W cycles are available in both AMG and FAS, while the F and flexible cycles are restricted to the AMG method only. (The W and flexible AMG cycles are not available for solving the coupled equation set due to the amount of computation required.)

The V and W Cycles

Figures 6.9 and 6.10 show the V and W multigrid cycles (defined below). In each figure, the multigrid cycle is represented by a square, and then expanded recursively to show the individual steps that are performed within the cycle. The individual steps are represented by a circle, one or more squares, and a triangle, connected by lines: circle-square-triangle for a V cycle, or circle-square-square-triangle for a W cycle. The squares in this group expand again, into circle-square-triangle or circle-square-square-triangle, and so on. You may want to follow along in the figures as you read the steps below.

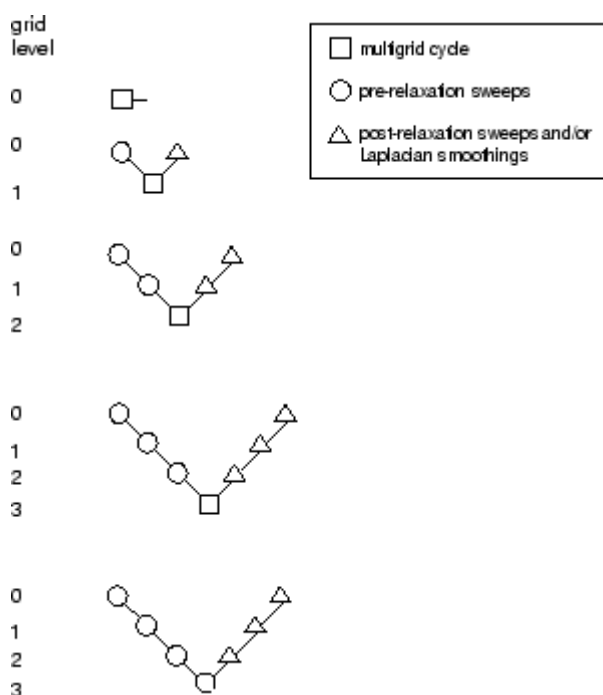


Fig. 6.9 V-Cycle Multigrid

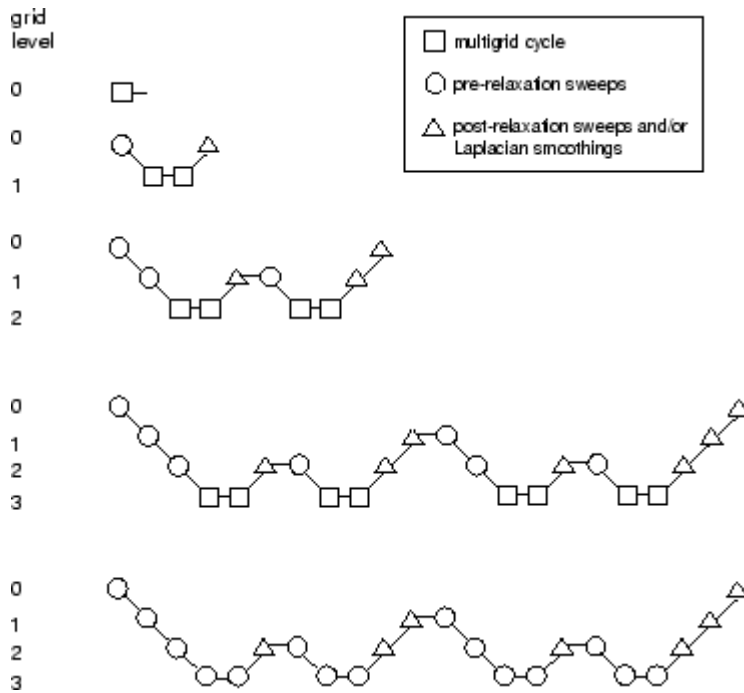


Fig. 6.10 W-Cycle Multigrid

For the V and W cycles, the traversal of the hierarchy is governed by three parameters, β_1 , β_2 , and β_3 , as follows:

1. First, iterations are performed on the current grid level to reduce the high-frequency components of the error (local error). For AMG, one iteration consists of one forward and one backward Gauss-Seidel sweep. For FAS, one iteration consists of one pass of the multi-stage scheme.

These iterations are referred to as pre-relaxation sweeps because they are performed before moving to the next coarser grid level. The number of pre-relaxation sweeps is specified by β_1 .

In Figures 6.9 and 6.10 this step is represented by a circle and marks the start of a multigrid cycle. The high-wave-number components of error should be reduced until the remaining error is expressible on the next coarser mesh without significant aliasing.

If this is the coarsest grid level, then the multigrid cycle on this level is complete. (In Figures 6.9 and 6.10 there are 3 coarse grid levels, so the square representing the multigrid cycle on level 3 is equivalent to a circle, as shown in the final diagram in each figure.)

-In the AMG method, the default value of β_1 is zero (i.e., no pre-relaxation sweeps are performed).

2. Next, the problem is "restricted" to the next coarser grid level using Equation 6.40.

In Figures 6.9 and 6.10, the restriction from a finer grid level to a coarser grid level is designated by a downward-sloping line.

3. The error on the coarse grid is reduced by performing a specified number (β_2) of multigrid cycles (represented in Figures 6.9 and 6.10 as squares). Commonly, for fixed multigrid strategies β_2 is either 1 or 2, corresponding to V-cycle and W-cycle multigrid, respectively.

4. Next, the cumulative correction computed on the coarse grid is "interpolated" back to the fine grid using Equation 6.41 and added to the fine grid solution. In the FAS method, the corrections are additionally smoothed during this step using the Laplacian smoothing operator.

In Figures 6.9 and 6.10 the prolongation is represented by an upward-sloping line.

The high-frequency error now present at the fine grid level is due to the prolongation procedure used to transfer the correction.

5. In the final step, iterations are performed on the fine grid to remove the high-frequency error introduced on the coarse grid by the multigrid cycles. These iterations are referred to as post-relaxation sweeps because they are performed after returning from the next coarser grid level. The number of post-relaxation sweeps is specified by β_3 .

In Figures 6.9 and 6.10, this relaxation procedure is represented by a single triangle.

For AMG, the default value of β_3 is 1.

-Note, however, that if you are using AMG with V-cycle to solve an energy equation with a solid conduction model presented with anisotropic or very high conductivity coefficient, there is a possibility of divergence with a default post-relaxation sweep of 1. In such cases you should increase the post-relaxation sweep (e.g., to 2) in the AMG section for better convergence, or change the cycle type to F-cycle or W-cycle, with an under-relaxation factor set to 1. This is especially effective when calculating pure heat conduction or conjugate heat transfer. Any instability observed when using the F-cycle or W-cycle can be remedied by increasing the pre-relaxation sweep count to 1. Although the default value of 0 is optimal for most cases, increasing the pre-relaxation sweep value to 1 or 2 can improve convergence.

Since the default value for β_1 is 0 (i.e., pre-relaxation sweeps are not performed), this procedure is roughly equivalent to using the solution from the coarse level as the initial guess for the solution at the fine level.

For FAS, the default value of β_3 is zero (i.e., post-relaxation sweeps are not performed); post-relaxation sweeps are never performed at the end of the cycle for the finest grid level, regardless of the value of β_3 . This is because for FAS, post-relaxation sweeps at the fine level are equivalent to pre-relaxation sweeps during the next cycle.

Algebraic Multigrid (AMG)

This algorithm is referred to as an "algebraic" multigrid scheme because, as we shall see, the coarse level equations are generated without the use of any geometry or re-discretization on the coarse levels; a feature that makes AMG particularly attractive for use on unstructured meshes.

The advantage being that no coarse meshes have to be constructed or stored, and no fluxes or source terms need to be evaluated on the coarse levels. This approach is in contrast with FAS (sometimes called "geometric") multigrid in which a hierarchy of meshes is required and the discretized equations are evaluated on every level. In theory, the advantage of FAS over AMG is that the former should perform better for non-linear problems since non-linearities in the system are carried down to the coarse levels through the re-discretization; when using AMG, once the system is linearized, non-linearities are not "felt" by the solver until the fine level operator is next updated.

AMG Restriction and Prolongation Operators

The restriction and prolongation operators used here are based on the additive correction (AC) strategy described for structured meshes by Hutchinson and Raithby [43]. Inter-level transfer is accomplished by piecewise constant interpolation and prolongation. The defect in any coarse level cell is given by the sum of those from the fine level cells it contains, while fine level corrections are obtained by injection of coarse level values. In this manner the prolongation operator is given by the transpose of the restriction operator

$$P=R^T \quad (6.42)$$

The restriction operator is defined by a coarsening or "grouping" of fine level cells into coarse level ones. In this process each fine level cell is grouped with one or more of its "strongest" neighbors, with a preference given to currently ungrouped neighbors. The algorithm attempts to collect cells into groups of fixed size, typically two or four, but any number can be specified. In the context of grouping, strongest refers to the neighbor j of the current cell i for which the coefficient A_{ij} is largest. For sets of coupled equations A_{ij} is a block matrix and the measure of its magnitude is simply taken to be the magnitude of its first element. In addition, the set of coupled equations for a given cell are treated together and not divided amongst different coarse cells. This results in the same coarsening for each equation in the system.

AMG Coarse Level Operator

The coarse level operator A^H is constructed using a Galerkin approach. Here we require that the defect associated with the corrected fine level solution must vanish when transferred back to the coarse level. Therefore we may write

$$Rd^{new}=0 \quad (6.43)$$

Upon substituting Equation 6.35 and 6.41 for d^{new} and ϕ^{new} we have

$$R[A\phi^{new}+b]=0 \quad (6.44)$$

$$R[A(\phi+P\psi^H)+b]=0 \quad (6.45)$$

Now rearranging and using Equation 6.35 once again gives

$$RAP\psi^H+R(A\phi+b)=0 \quad (6.46)$$

$$RAP\psi^H+Rd=0 \quad (6.47)$$

Comparison of Equation 6.47 with Equation 6.40 leads to the following expression for the coarse level operator:

$$A^H = RAP \quad (6.48)$$

The construction of coarse level operators thus reduces to a summation of diagonal and corresponding off-diagonal blocks for all fine level cells within a group to form the diagonal block of that group's coarse cell.

The F Cycle

The multigrid F cycle is essentially a combination of the V and W cycles described in the previous Section.

Recall that the multigrid cycle is a recursive procedure. The procedure is expanded to the next coarsest grid level by performing a single multigrid cycle on the current level. Referring to Figures 6.9 and 6.10, this means replacing the square on the current level (representing a single cycle) with the procedure shown for the 0-1 level cycle (the second diagram in each figure). We see that a V cycle consists of:

pre sweep → restrict → V cycle → prolongate → post sweep

and a W cycle:

pre sweep → restrict → W cycle → W cycle → prolongate → post sweep

An F cycle is formed by a W cycle followed by a V cycle:

pre sweep → restrict → W cycle → V cycle → prolongate → post sweep

As expected, the F cycle requires more computation than the V cycle, but less than the W cycle. However, its convergence properties turn out to be better than the V cycle and roughly equivalent to the W cycle. The F cycle is the default AMG cycle type for the coupled equation set.

The Flexible Cycle

For the flexible cycle, the calculation and use of coarse grid corrections is controlled in the multigrid procedure by the logic illustrated in Figure 11. This logic ensures that coarser grid calculations are invoked when the rate of residual reduction on the current grid level is too slow. In addition, the multigrid controls dictate when the iterative solution of the correction on the current coarse grid level is sufficiently converged and should thus be applied to the solution on the next finer grid. These two decisions are controlled by the parameters α and β shown in Figure 6.11, as described in detail below. Note that the logic of the multigrid procedure is such that grid levels may be visited repeatedly during a single global iteration on an equation. For a set of 4 multigrid levels, referred to as 0, 1, 2, and 3, the flex-cycle multigrid procedure for solving a given transport equation might consist of visiting grid levels as 0-1-2-3-2-3-2-1-0-1-2-1-0, for example.

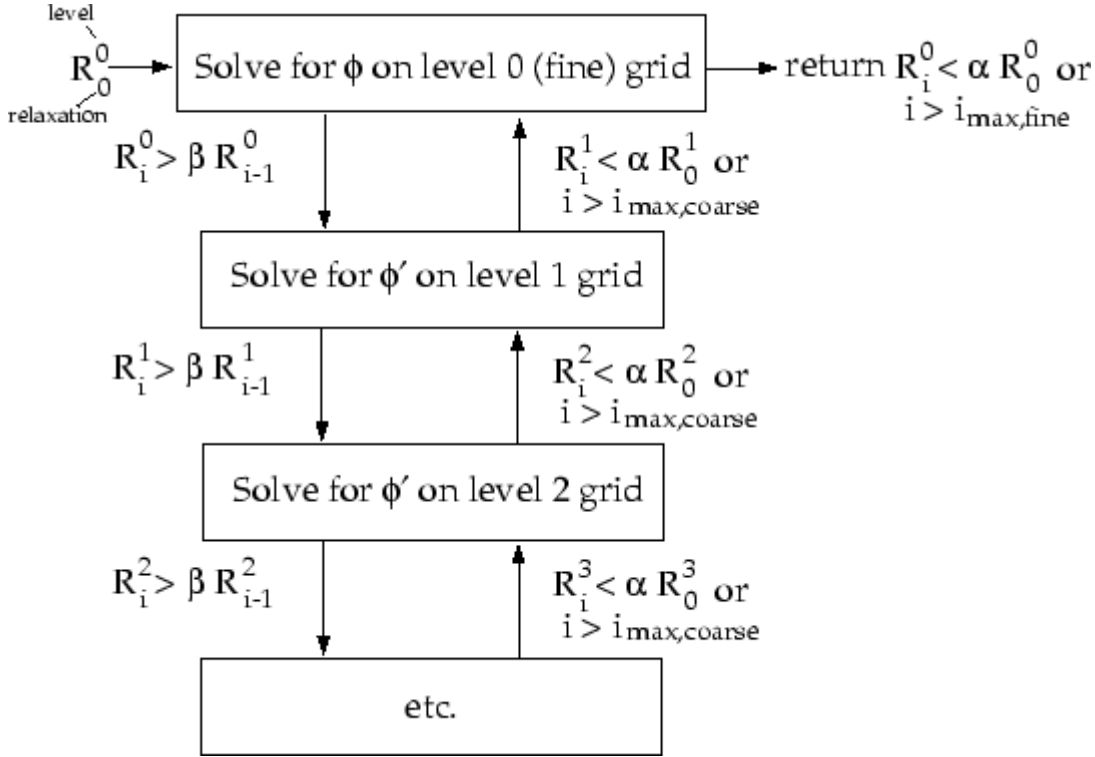


Fig. 6.11 Logic Controlling the Flex Multigrid Cycle

The main difference between the flexible cycle and the V and W cycles is that the satisfaction of the residual reduction tolerance and termination criterion determine when and how often each level is visited in the flexible cycle, whereas in the V and W cycles the traversal pattern is explicitly defined.

The Residual Reduction Rate Criteria

The multigrid procedure invokes calculations on the next coarser grid level when the error reduction rate on the current level is insufficient, as defined by

$$R_i > \beta R_{i-1} \quad (6.49)$$

Here R_i is the absolute sum of residuals (defect) computed on the current grid level after the i th relaxation on this level. The above equation states that if the residual present in the iterative solution after i relaxations is greater than some fraction, β (between 0 and 1), of the residual present after the $(i-1)$ th relaxation, the next coarser grid level should be visited. Thus β is referred to as the residual reduction tolerance, and determines when to "give up" on the iterative solution at the current grid level and move to solving the correction equations on the next coarser grid. The value of β controls the frequency with which coarser grid levels are visited. The default value is 0.7. A larger value will result in less frequent visits, and a smaller value will result in more frequent visits.

The Termination Criteria

Provided that the residual reduction rate is sufficiently rapid, the correction equations will be converged on the current grid level and the result applied to the solution field on the next finer grid level.

The correction equations on the current grid level are considered sufficiently converged when the error in the correction solution is reduced to some fraction, α (between 0 and 1), of the original error on this grid level:

$$R_i < \alpha R_0 \quad (6.50)$$

Here, R_i is the residual on the current grid level after the i th iteration on this level, and R_0 is the residual that was initially obtained on this grid level at the current global iteration. The parameter α , referred to as the termination criterion, has a default value of 0.1. Note that the above equation is also used to terminate calculations on the lowest (finest) grid level during the multigrid procedure. Thus, relaxations are continued on each grid level (including the finest grid level) until the criterion of this equation is obeyed (or until a maximum number of relaxations has been completed, in the case that the specified criterion is never achieved).

The Coupled and Scalar AMG Solvers

The scalar AMG solver is used for the solution of linear systems obtained from the discretization of the individual transport equations.

$$a_{ij}x_j = b_i \quad (6.51)$$

where the above equation contains scalar variables.

The coupled AMG solver is used to solve linear transport equations using implicit discretization from coupled systems such as flow variables for the density-based solver, pressure-velocity variables for the coupled pressure-based schemes and inter-phase coupled individual equations for Eulerian multiphase flows.

$$[A]_{ij}\vec{X}_j = \vec{B}_i \quad (6.52)$$

where the influence of a cell i on a cell j has the form

$$A_{ij} = \begin{bmatrix} a_{ij}^{11} & a_{ij}^{12} & \dots & a_{ij}^{1N} \\ a_{ij}^{21} & \cdot & & \cdot \\ \vdots & & \cdot & \cdot \\ a_{ij}^{N1} & & & a_{ij}^{NN} \end{bmatrix} \quad (6.53)$$

and the unknown and source vectors have the form

$$\vec{X}_j = \begin{bmatrix} x_j^1 \\ \cdot \\ \cdot \\ x_j^N \end{bmatrix} \quad (6.54)$$

$$\vec{B}_i = \begin{bmatrix} b_i^1 \\ \cdot \\ \cdot \\ b_i^N \end{bmatrix} \quad (6.55)$$

The above resultant system of equations is solved in ANSYS FLUENT using either the Gauss-Seidel smoother or the Incomplete Lower Upper decomposition (ILU) smoother. If a scalar system of equations is to be solved then the point-method (Gauss-Seidel or ILU) smoother is used, while for a coupled system of equations the block-method (Gauss-Seidel or ILU) smoother is used.

Gauss-Seidel

The Gauss-Seidel method is a technique for solving a linear system of equations one at a time and in sequence. It uses the previously computed results as soon as they become available. It performs two sweeps on the unknowns in forward and backward directions. Both point or block method Gauss-Seidel smoothers are available in ANSYS FLUENT to solve for either the scalar AMG system of equations or the coupled AMG system of equations.

The Gauss-Seidel procedure can be illustrated using the scalar system, Equation 6.50. The forward sweep can be written as:

$$x_i^{k+1/2} = (b_i - \sum_{j<i} a_{ij}x_j^{k+1/2} - \sum_{j>i} a_{ij}x_j^k) / a_{ii} \quad (i=1, \dots, N) \quad (6.56)$$

where N is the number of unknowns. The forward sweep is followed by a backward sweep which can be written as:

$$x_i^{k+1} = (b_i - \sum_{j<i} a_{ij}x_j^{k+1/2} - \sum_{j>i} a_{ij}x_j^{k+1}) / a_{ii} \quad (6.57)$$

Following from Equations 6.56 and 6.57, symmetric Gauss-Seidel can be expressed in matrix form as a two-step recursive solution of the system

$$(D_A + L_A)D_A^{-1}(D_A + U_A)(x^{k+1} - x^k) = b - Ax^k \quad (6.58)$$

where D_A , L_A , and U_A represent diagonal, lower tridiagonal, and upper tridiagonal parts of matrix A , respectively.

Symmetric Gauss-Seidel has a somewhat limited rate of smoothing of residuals between levels of AMG, unless the coarsening factor is set to 2.

The Incomplete Lower Upper decomposition (ILU) smoother is not presented here as it has not been used in this project.

Also, the Full-Approximation Storage (FAS) Multigrid has not been used and therefore it is not presented.

6.3.2 Applied settings and configurations in FLUENT 12 for the current project

1) Flow Solver

Pressure-based solver

2) Models

For the solution of conservation equations the laminar viscous model has been enabled (steady-state and without gravity) and for the diffusion of freshwater the species transport model.

3) Spatial Discretization

Gradient: Least squares cell based method

Momentum: Second Order Upwind scheme

Pressure Body Forces Weighted method

Species Transport: First Order Upwind scheme

4) Solution Methods

Simple pressure-velocity coupling (Algebraic Multigrid (AMG) and point-method Gauss-Seidel smoother)

5) Under-Relaxation Factors

Pressure 0.3, Density 1, Body Forces 1, Momentum 0.7, Species transport 1

6) Working fluid

Mixture fresh water (fluent database: $\rho=998.2 \text{ kg/m}^3$, $\mu=0.001003 \text{ kg/m}\cdot\text{s}$) and salt water ($\rho=1025 \text{ kg/m}^3$, $\mu=0.00096 \text{ kg/m}\cdot\text{s}$): concentration $C=35\text{g/L}$, density: volume weighted mixing law, viscosity: mass weighted mixing law and exponential model for $T=298.15 \text{ K}$ for the salt water, which is considered equal to that of the mixture (the mixture is consisted mainly from salt water).

7) Boundary Conditions

As a boundary condition on the inlet it has been given the volumetric flow and on the outlet the hydraulic pressure, the number of which differs in each case.

Initially the membrane has been simulated using a uniform mass flow inlet using the Darcy's law (general equation of osmosis)

$$\frac{Q}{E} = A \cdot (\Delta\pi - \Delta P), \quad (6.59)$$

where E is the effective membrane area and $\Delta\pi = 2 \cdot \Delta C_{\text{NaCl}} \cdot R \cdot T$.

As a second approach the equation of the flow (velocity) through the membrane has been solved using a function written in C, which is called User-Defined Function (UDF) model in FLUENT, and periodically regenerates a profile file. This function is given as a boundary condition on the membrane area and calculates the velocity inlet of freshwater into the saltwater in each cell adjacent to the membrane, using the general equation of osmosis $U = A \cdot (\Delta\pi - \Delta P)$. $\Delta\pi$ is the osmotic pressure difference between the area above (fresh water $C=0 \text{ g/L}$) and below (salt water $C=\text{variable}$) each cell and is given by the equation $\Delta\pi = 2 \cdot \Delta C_{\text{NaCl}} \cdot R \cdot T$. This UDF is cited at the end of the thesis.

8) Initial Conditions

Gauge pressure the same as the pressure on the outlet, mass fraction of salt water $Y_{\text{salt}}=1$, and of fresh water $Y_{\text{fresh}}=0$.

9) Reference values

Reference quantities used for computing normalized flow field variables.

Area 1, density 1.225, enthalpy 0, length 1, pressure 0(Pascal), temperature 288.16, velocity 1, viscosity $1.7894\text{e-}05$, ratio of specific heats 1.4

10) Number of Iterations: 5000

6.4 Techplot 360

The programs techplot 360 and Origin Pro 8 have been used for the post-processing of the results:

- Techplot 360: Contours, Vector and Streamlines Plots, Videos
- Origin Pro 8: Graphs

CHAPTER 7.

RESULTS & DISCUSSION

Runs, Parametric Analysis, Critical Review

In the following table are presented the different cases which are examined with CFD.

Case	Geometry	Grid	Solver	Inlet Boundary	Outlet Boundary	Membrane	Working Fluid	
1	HTI standard HPS	coarse (700K)	FLUENT 12	0.5 L/h	14 bar	Wall	Fresh water ρ=998.2 kg/m³ μ=0.001003 kg/m*s (FLUENT Database)	
2		dense (1.5M)						
3		hyper (3M)						
4		Adequate Resolution: Dense 1.5M				Mass flow inlet: HTI membrane		
5				0.5 L/h	14 bar		Dynamic conditions: HTI membrane	Mixture: Salt water C=35g/L, ρ=1025 kg/m³, μ=0.00096 kg/m*s (Exponential model for T=298.15 K) and fresh water C=0 g/L
6					15.8 bar			
7				1 L/h	1 bar			
8				0.5 L/min	1 bar			
9					15.8 bar	Dynamic conditions: Oasys Water membrane		
10								
11						New Design 1	Dynamic conditions: HTI membrane	
12		New Design 2						

Fig. 7.1 Different cases examined with CFD

Before proceeding to each case separately here is presented the computational domain in FLUENT. Also, a global axis system is defined same for all the cases:

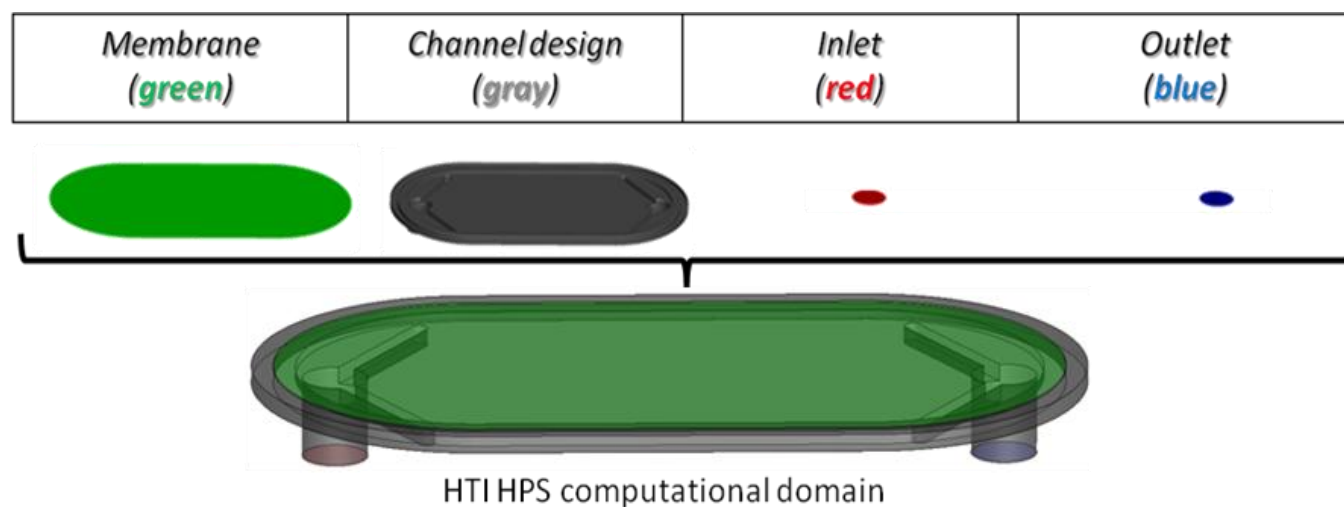


Fig. 7.2 Computational design

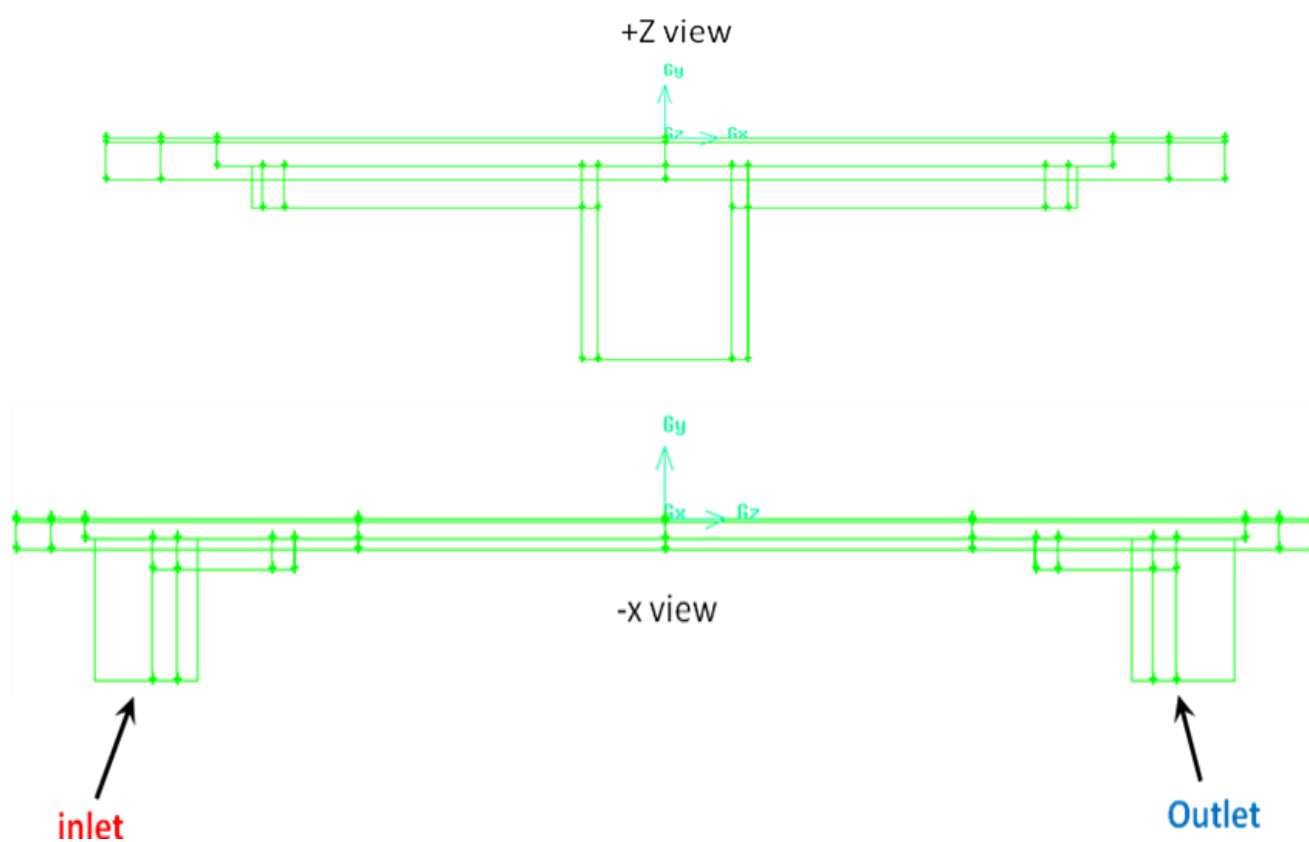


Fig. 7.3 Global Axis System

7.1 Cases 1-3

7.1.1 Simulation Conditions

The cases 1-3 simulate the flow of water on the high pressure side (HPS) of the HTI test cell. In this initial step the **membrane surface** has been considered as **wall** for the boundary conditions and the **working fluid** is **fresh water** (FLUENT database: $\rho=998.2 \text{ kg/m}^3$, $\mu=0.001003 \text{ kg/m}\cdot\text{s}$). Moreover, the conditions on the inlet and outlet are shown on the table. The **inlet** volumetric flow rate **0.5 L/h** has been chosen equal to twice the number of the inlet flow rate on the fresh water side, which is considered equal to the theoretical flow rate through the membrane. This inlet flow rate is theoretically the optimum according to the energy and costs needed to handle it. The hydraulic pressure **outlet** has been chosen **14 bar** in order to get a hydraulic pressure difference of the two membrane sides equal to 13 bar (14 salt water – 1 fresh water). This hydraulic pressure difference is approximately equal to half the osmotic pressure difference of the two membrane sides ($\approx 26 \text{ bar}$) and gives maximum power density.

<i>Membrane (green)</i>	<i>Channel design (gray)</i>	<i>Inlet (red)</i>	<i>Outlet (blue)</i>
Wall	Wall	0.5 L/h	14 bar

Fig. 7.4 Boundary conditions cases 1-3

7.1.2 Grid Sensitivity Study

The initial part of the study is investigating the solution's sensitivity for different grid patterns. For this purpose **three grid densities** have been tested, each one utilizing **different number of cells in the y direction (height)** of the flow channel. The other directions (z length and x width) have the same number of cells in all the grids.

Grids:

- (a) **coarse** 700 Thousand cells in total, 11 in the Y direction
- (b) **dense** 1.5 Million cells in total, 23 in the Y direction
- (c) **hyper dense** 3 Million cells in total, 46 in the Y direction

The figure below shows the three different grid densities from the -z view:

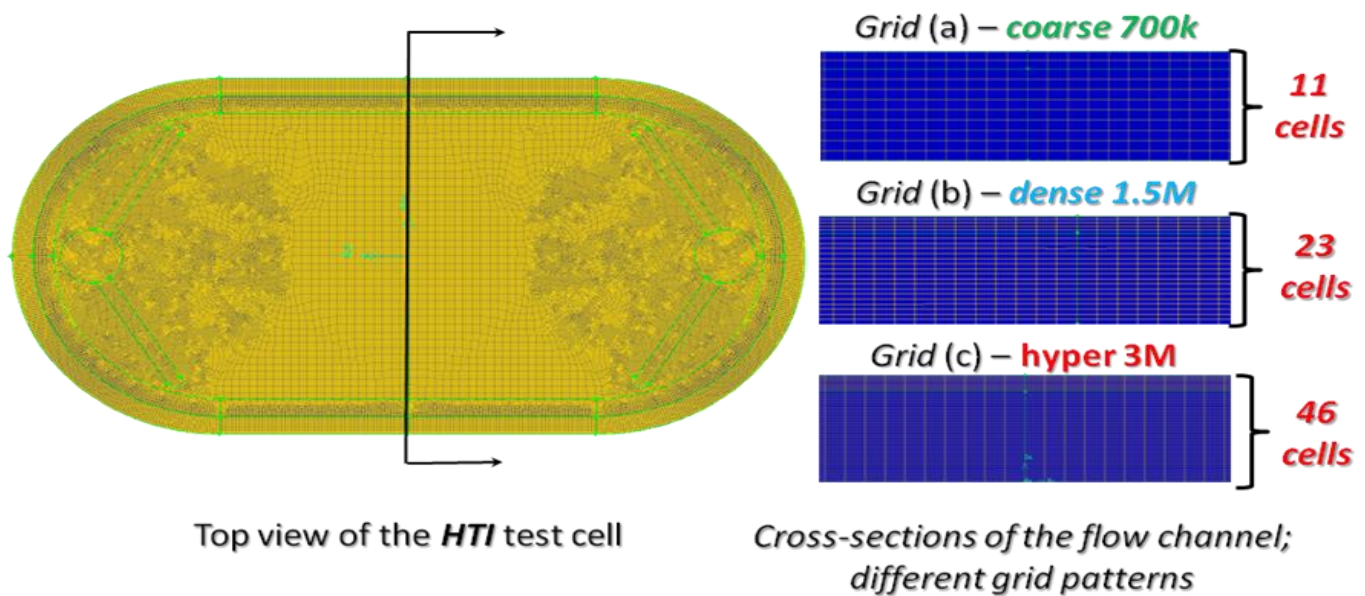


Fig. 7.5 Grid a, b, c densities in the $-z$ view

7.1.2.1 Results of the grid sensitivity study

The contour slices display the velocity magnitude for each grid at the top view of the HTI test cell and in middle of the main channel ($y=-0.254\text{mm}$). The levels are normalized with the inlet velocity ($U_{in}=4.91\text{E-}04\text{ m/s}$).

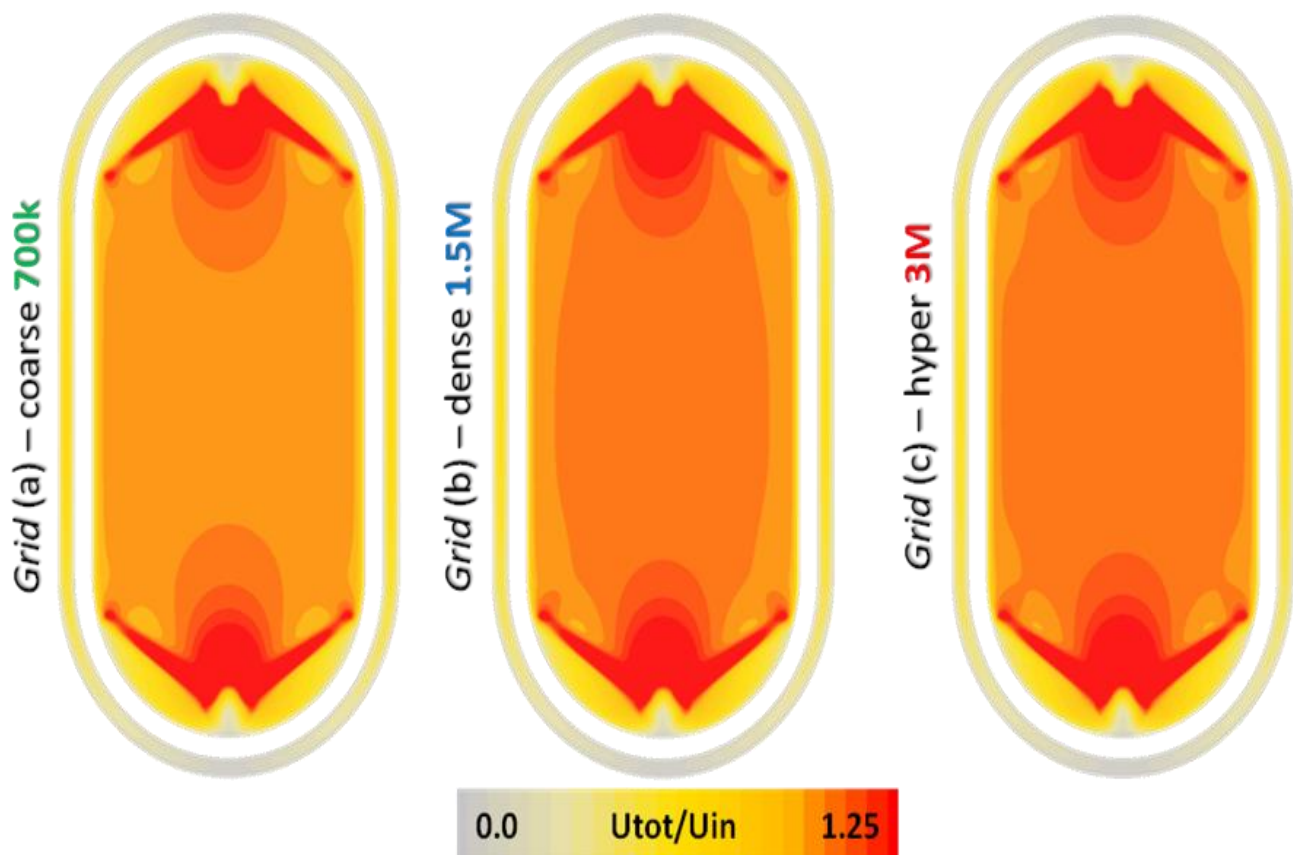


Fig. 7.6 Normalized velocity magnitude for each grid

The charts below (fig. 7.8) present for each grid the normalized z velocity (U_z/U_{in}) in the y axis (normalized with Y_{max}) in three different spots on the z direction (main flow): $z=0$, $z=6.35\text{mm}$ and $z=-6.35\text{mm}$.

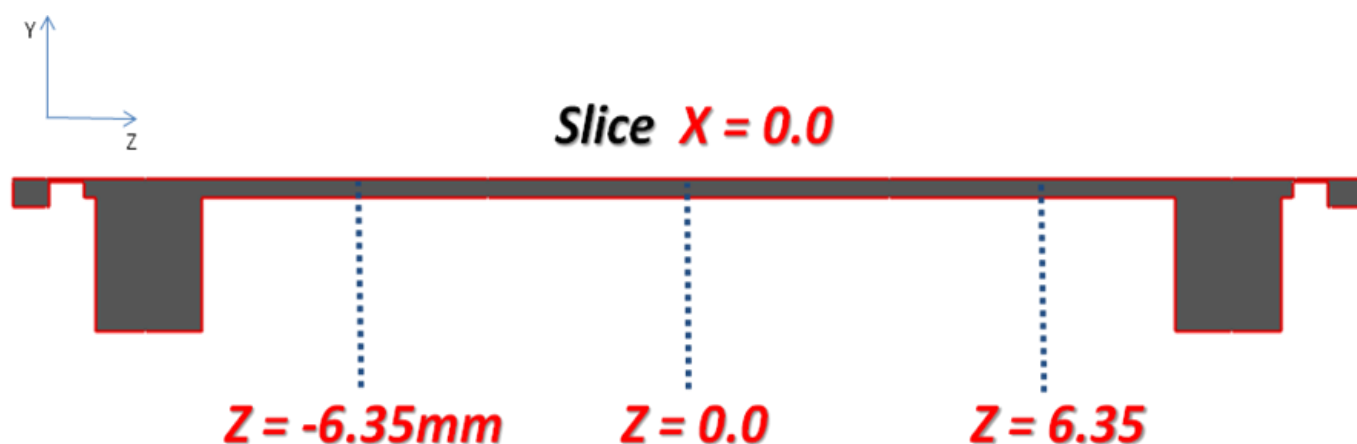
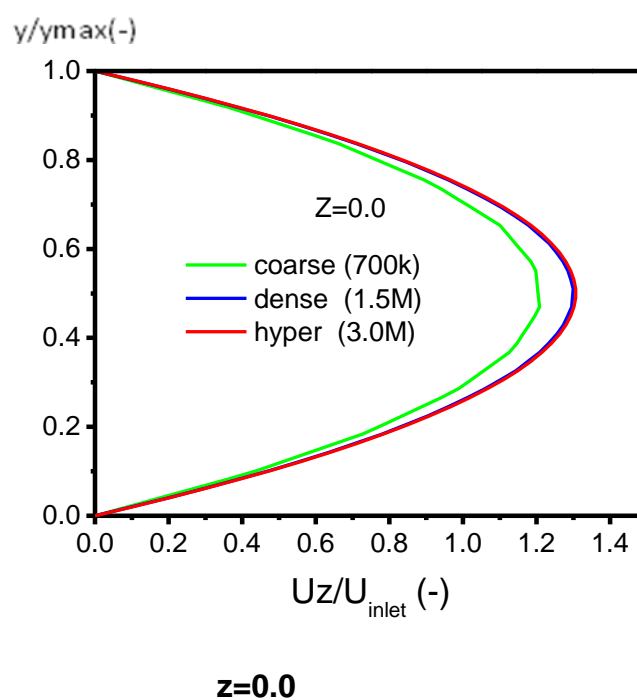
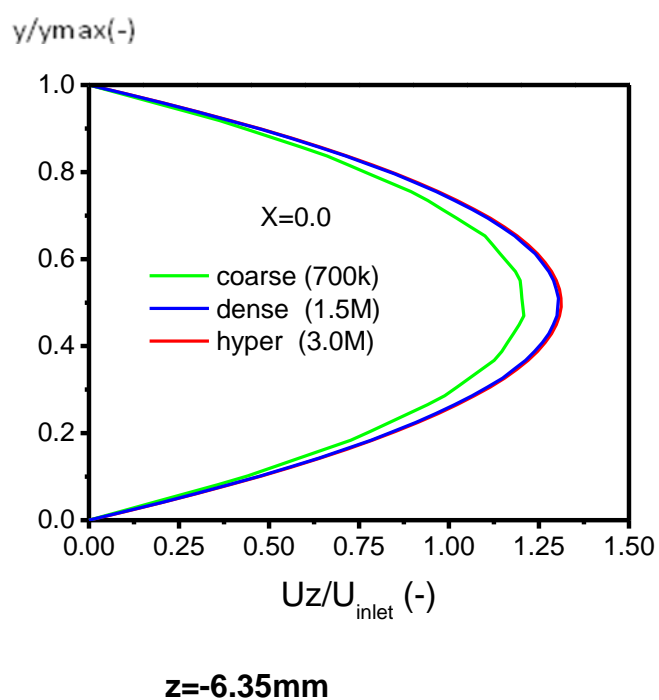


Fig. 7.7 Spots on the z direction



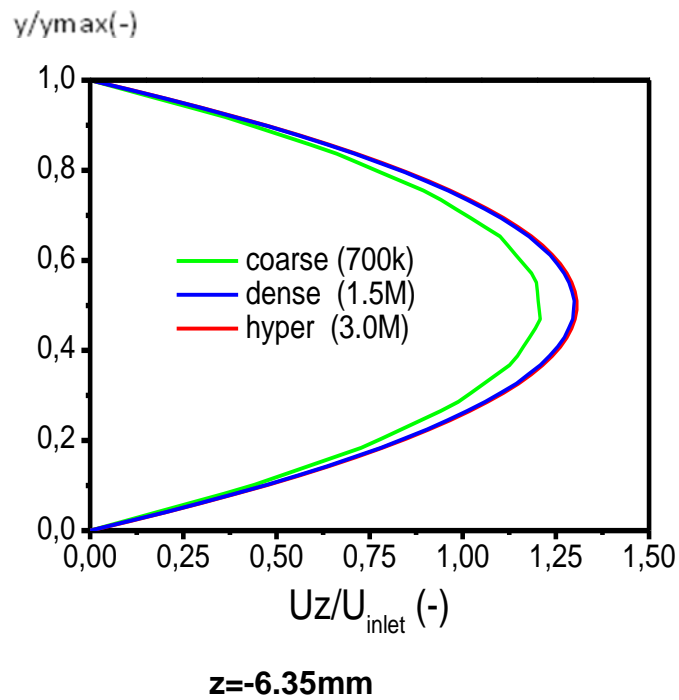


Fig. 7.8 Parabolic velocity profiles on the main flow

The following charts present the parabolic velocity profiles on the secondary flow (fig. 7.9) and on the flow guidelines (fig. 7.10):

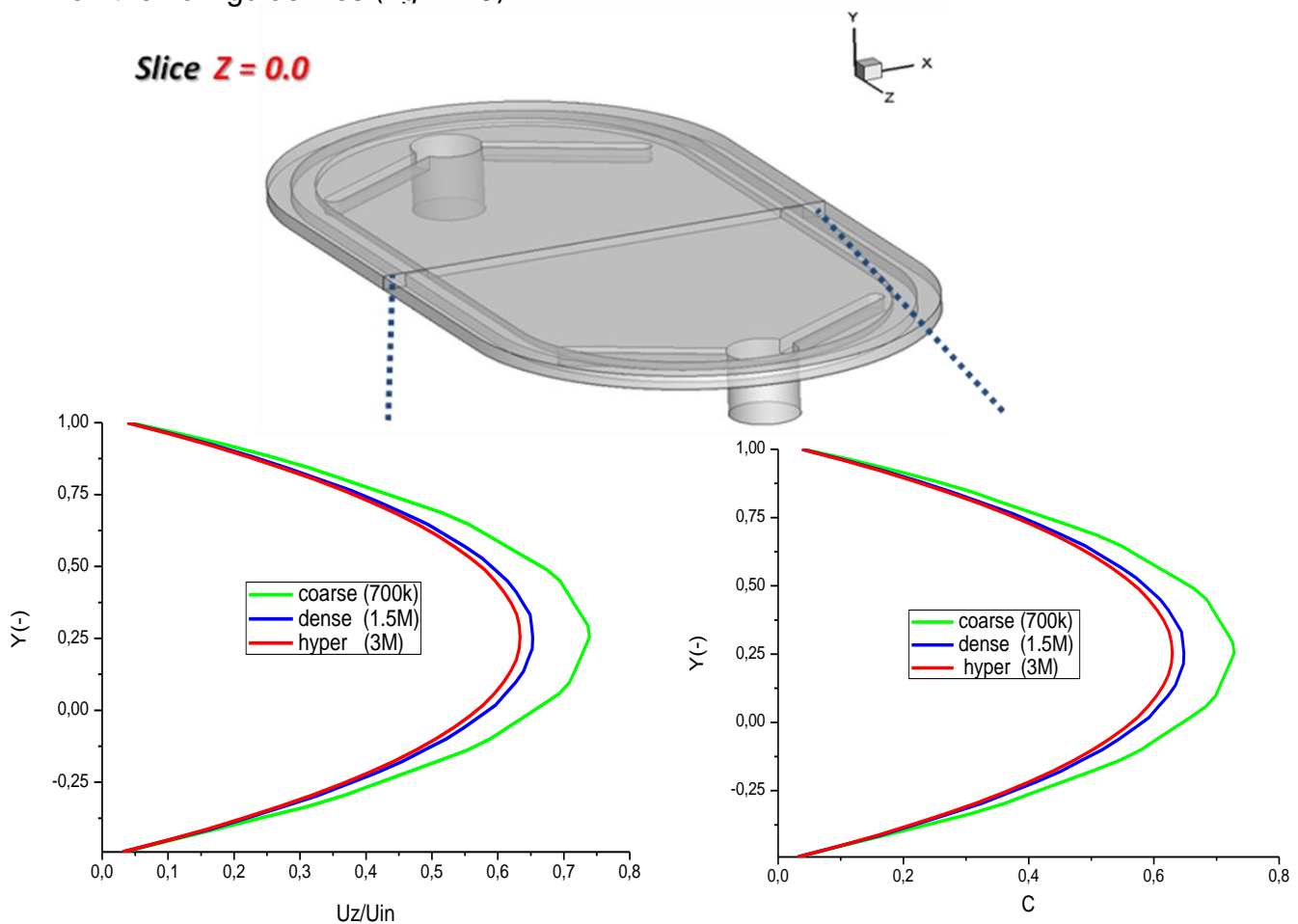


Fig. 7.9 Parabolic velocity profiles on the secondary flow

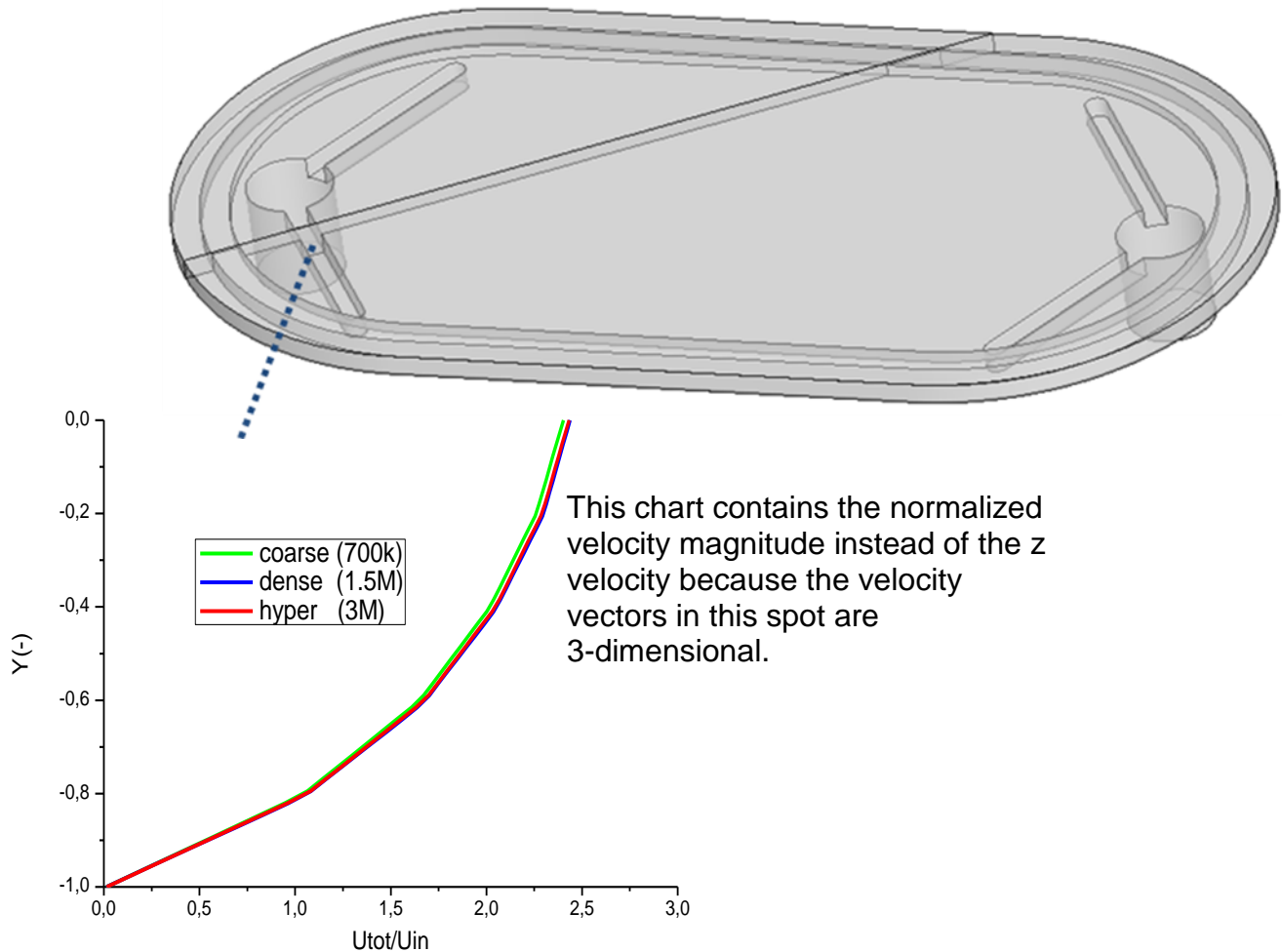


Fig. 7.10 Parabolic velocity profiles on the flow guidelines

Discussion of the results and conclusion of the grid sensitivity study

- The differences in the results of the three grids are greater as the velocity magnitude decreases, according to the velocity profiles: in the periphery where the velocity magnitude is too low the results differ a lot, while in the guidelines where the velocity magnitude reaches its higher levels the differences are negligible.
- More specifically, the dense (1.5 M) and hyper dense (3M) grids give results which are very close in all the three plots, while the results of the coarse grid (700K) differ significantly from those of the other two, mainly on the secondary and main flow plots.
- Therefore the **most suitable** mesh for the high pressure side of the PRO HTI test cell is the **dense (1.5M)**, which gives accurate results while being as coarse as possible in order to minimize the time needed to run a fluent application using it.

7.1.3 Results and discussion cases 1-3

7.1.3.1 Flow Field

Here is presented the flow field of the case 2 (1.5 M mesh) which is similar with that of cases 1 and 3.

The figure below (fig. 7.11) presents the streamlines from the inlet (colored with the normalized z-velocity), along with some comments which explain the flow field.

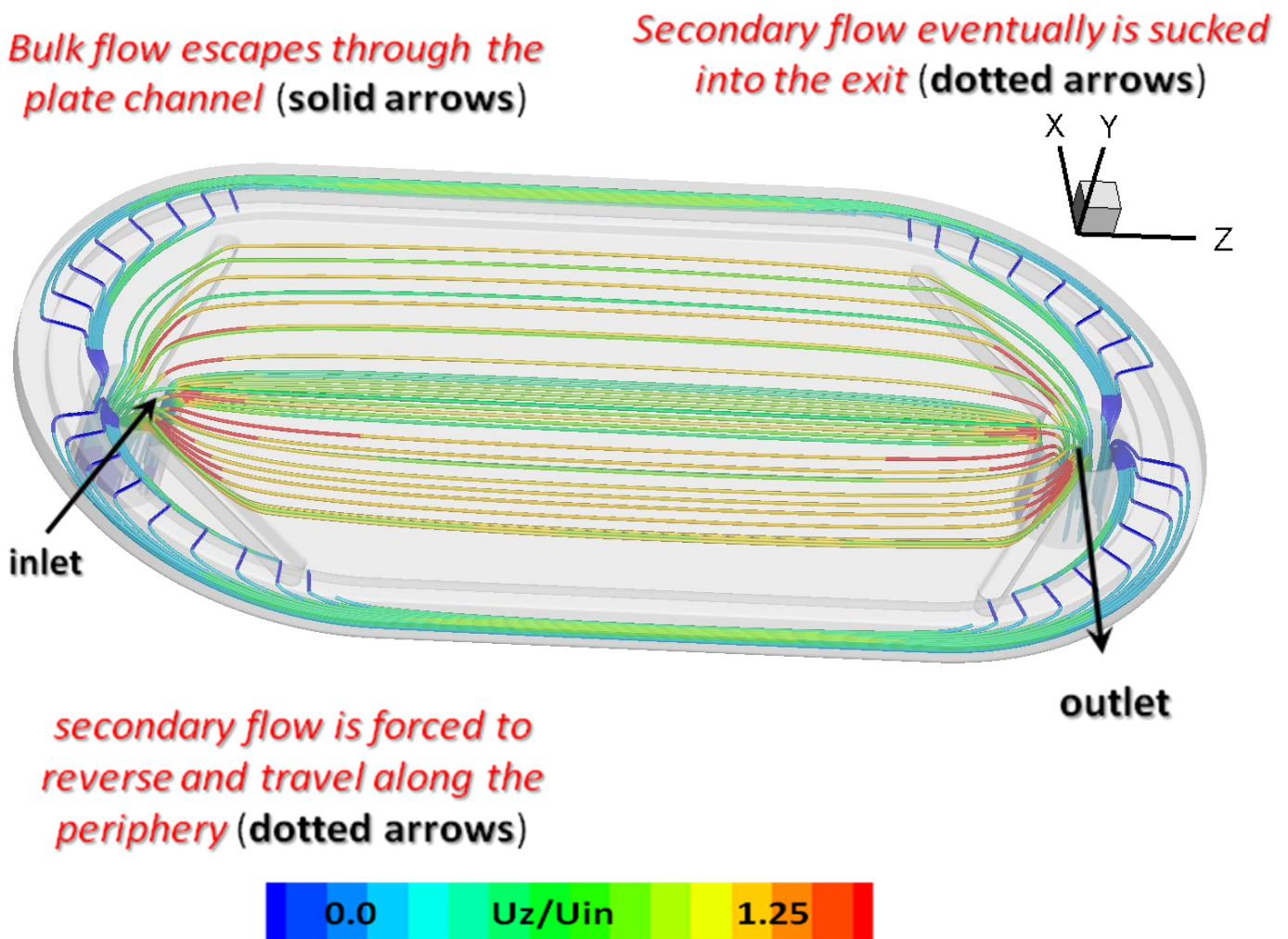


Fig. 7.11 Streamlines from the inlet colored with normalized z-velocity

There is also a video with animated streamlines colored with normalized velocity magnitude which is cited in the CD of the project.

The next figure (fig. 7.12) shows the vector plot (colored with normalized velocity magnitude) along with explanatory comments.

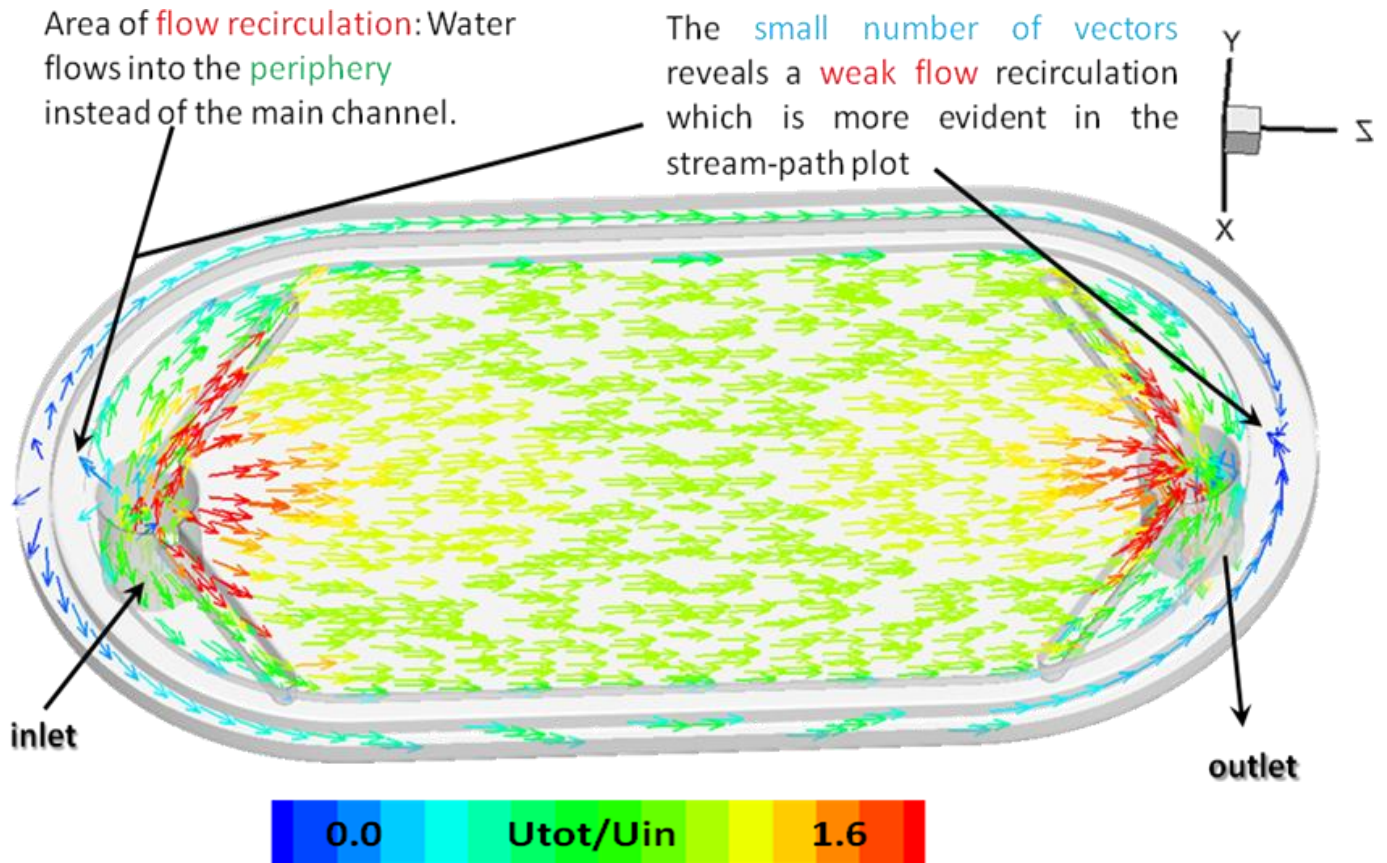


Fig. 7.12 Flow vectors colored with normalized velocity magnitude

7.2 Case 4

7.2.1 Simulation Conditions

In this case the flow of water on the HTI HPS test cell has been simulated considering a **uniform volumetric flow rate through the membrane** as boundary condition instead of wall. The dense grid (1.5 M) has been used as it is the most suitable according to the grid sensitivity study. In addition, the boundary conditions for the **inlet** and **outlet** are the same as those on the cases 1-3 ($Q_{in}=0.5$ L/h, $P_{out}=14$ bar), and also the **working fluid** is the same i.e. **fresh water**. The volumetric flow rate is equal to **0.26 L/h** and has been calculated using the **Darcy's law** combined with the **van't hoff equation** for the osmotic pressure which is referred to ideal conditions. The calculations are presented in the next section. The figure 7.13 shows the boundary conditions for the case 4.

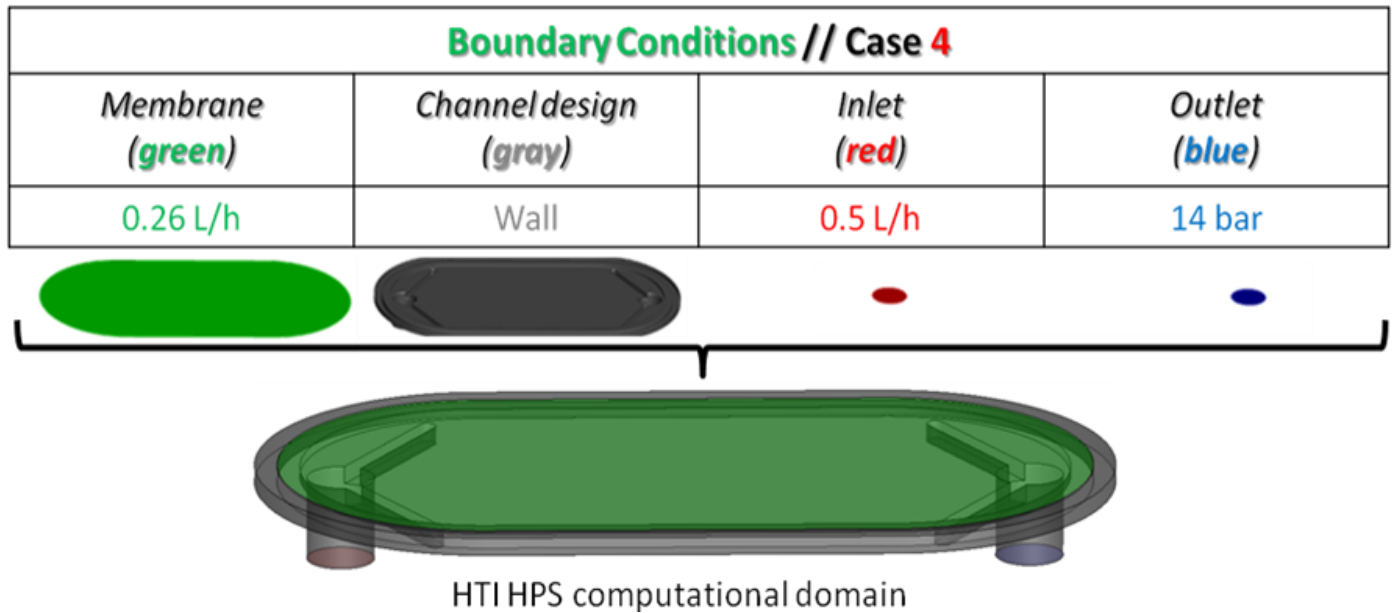


Fig. 7.13 Boundary conditions

Calculation of the volumetric flow rate through the membrane

The **Darcy's Law** gives the volumetric flow rate through a porous medium as function of the pressure difference between the two sides of the medium:

$$\frac{Q}{E} = \frac{k}{\mu \cdot L} (\Delta\pi - \Delta P), \quad (7.1)$$

where Q (m^3/s) is the volumetric flow rate through the porous medium, μ ($\text{Pa}\cdot\text{s}$) the viscosity of the fluid, $\Delta\pi$ (Pa) and ΔP (Pa) the osmotic and hydraulic pressure differences between the two sides and k (m^2), L (m) and E (m^2) the permeability, thickness and effective area of the medium, respectively.

Comparing the **Darcy's Law** with the **general equation of osmosis**:

$$\frac{Q}{E} = A \cdot (\Delta\pi - \Delta P), \quad (7.2)$$

where A ($\frac{\text{m}}{\text{s} \cdot \text{Pa}}$) the water permeability of the membrane (porous medium),

it is concluded that $A = \frac{k}{\mu \cdot L}$ (7.3).

The **water permeability A** based on experimental results with an HTI CTA

FO membrane is 1.87×10^{-12} ($\frac{\text{m}}{\text{s} \cdot \text{Pa}}$) while the effective membrane area E has

been calculated equal to 0.0233249 m^2 .

The **osmotic pressure difference** between the two membrane sides for ideal conditions can be calculated using the **Van't Hoff equation**:

$$\Delta\pi = 2 \cdot \Delta C_{\text{NaCl}} \cdot R \cdot T, \quad (7.4)$$

where ΔC_{NaCl} ($\frac{\text{g}}{\text{L}} = \frac{\text{kg}}{\text{m}^3}$) is the salt concentration difference between the two membrane sides, R ($\frac{\text{m}^2}{\text{K} \cdot \text{s}^2}$) the gas constant and T (K) the absolute temperature of the fresh and salt water.

- **R** has been calculated as $\frac{8.314}{\text{molecular mass of NaCl}} = \frac{8.314}{0.0585} = 142.2 \quad (\frac{\text{m}^2}{\text{K} \cdot \text{s}^2})$
 - **ΔC_{NaCl}** has been chosen equal to **35 g/L**, which is the average salt concentration of sea water [5], minus 0 which is the concentration of salt in fresh water.
 - **T** has been taken equal to **298.16 K**.
- By putting the above values in **van't hof equation** (7.4) the osmotic pressure difference between the two membrane sides (**$\Delta\pi$**) is calculated **29.66207 bars**. With the use of the **general equation of osmosis** (7.2) the **volumetric flow rate through the membrane** is calculated equal to **0.26 L/h**.

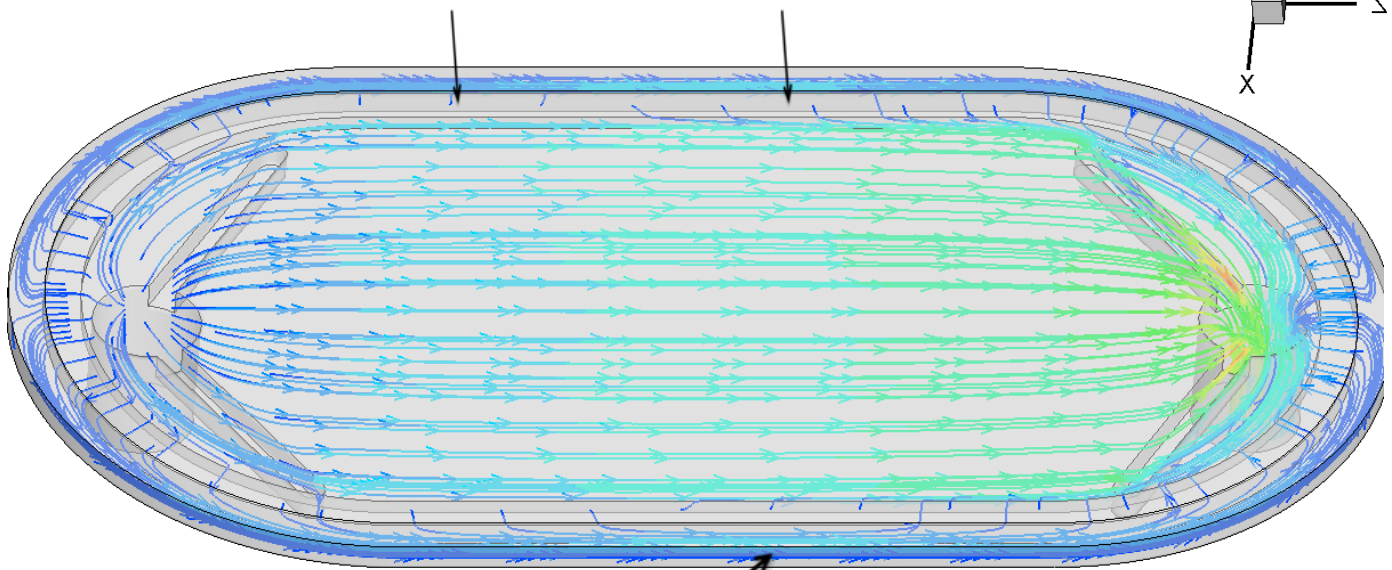
7.2.2 Results and discussion

7.2.2.1 Flow field

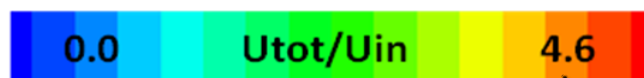
The following figures (7.14-7.17) present the streamlines and vector plots from the inlet and membrane surface of the case 4, along with explanatory comments.

There is also a video with animated streamlines colored with normalized velocity magnitude which is contained in the CD of the project.

The stream from the membrane surface which flows in the area between the main and the secondary flow follows two paths depending on the Z coordinate: in the area near the inlet escapes into the periphery while near the outlet follows the main stream.



Some part of the secondary flow returns to the main flow before reaches the outlet which is more evident on the flow vector plot.



The maximum normalized velocity magnitude for the cases 1-3 was 2.8 while for the case 4 is significantly greater reaching 4.8

Fig. 7.14 Streamlines from the membrane surface colored with normalized velocity magnitude

Only a few streamlines from the inlet escape into the periphery as the flow from the membrane surface blocks the stream towards Y + coordinate

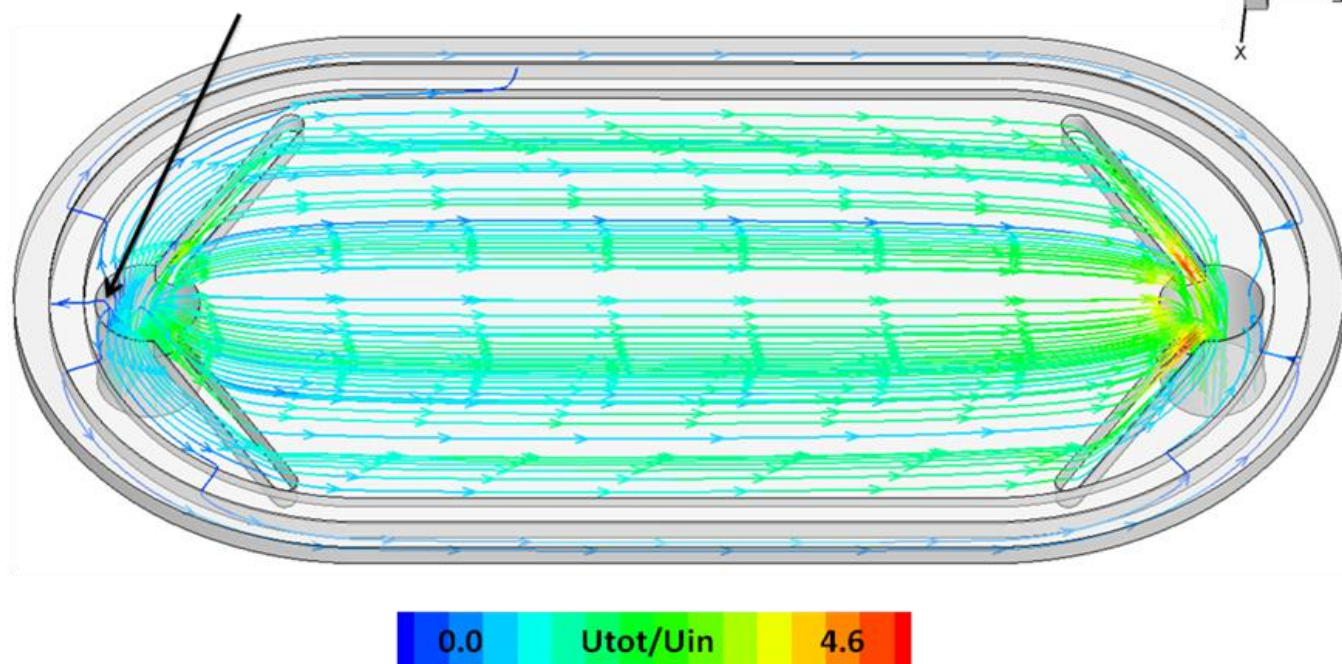


Fig. 7.15 Streamlines from the inlet colored with normalized velocity magnitude

The velocity magnitude near the membrane surface is lower than the magnitude in the middle of the channel.

The flow is slightly accelerating as it reaches the outlet.

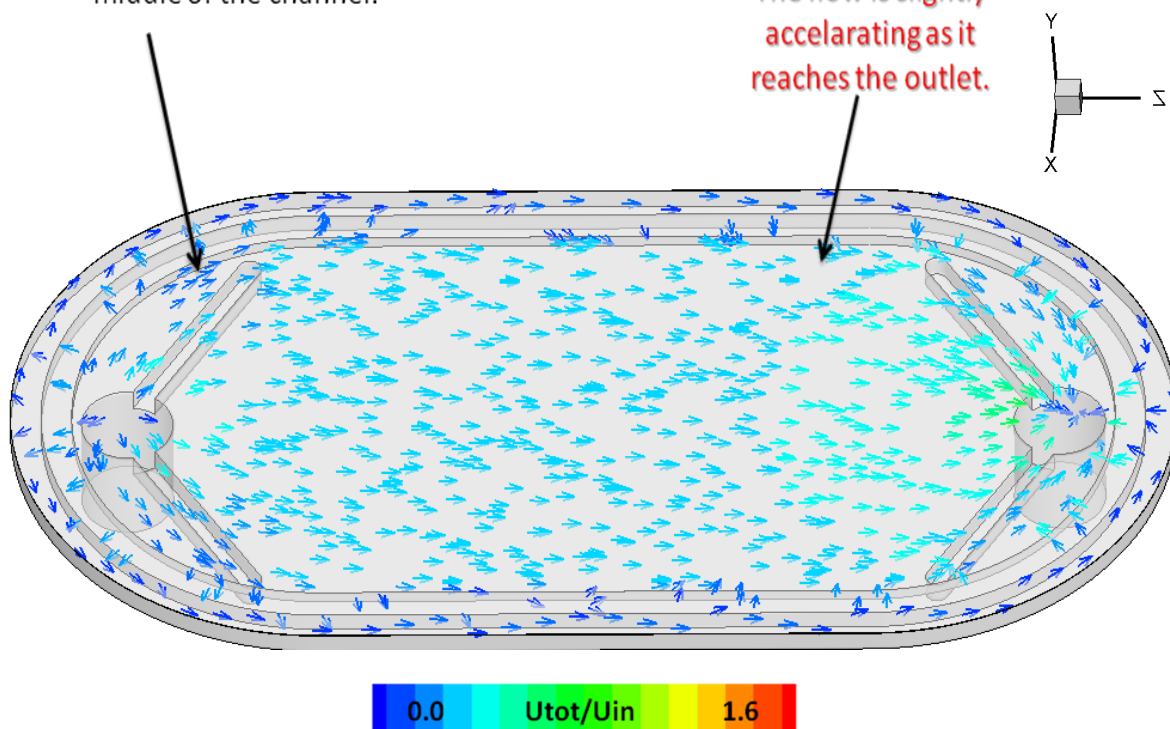


Fig. 7.16 Flow vectors near the membrane surface colored with normalized velocity magnitude

The flow in is accelerating as it reaches the outlet while on the cases 1-3 the colours are simetrical.

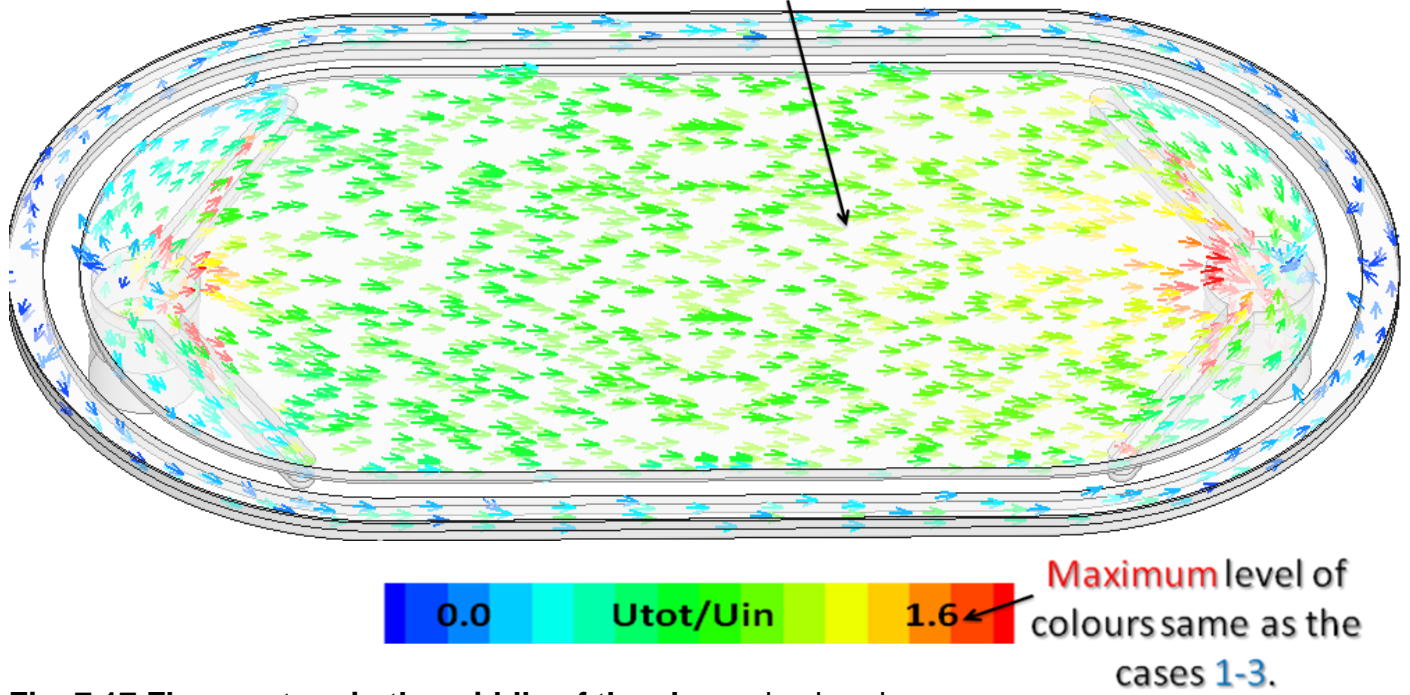


Fig. 7.17 Flow vectors in the middle of the channel colored with normalized velocity magnitude

The figures 7.18 and 7.19 depict the parabolic velocity (U_z) profiles on the main and secondary flow.

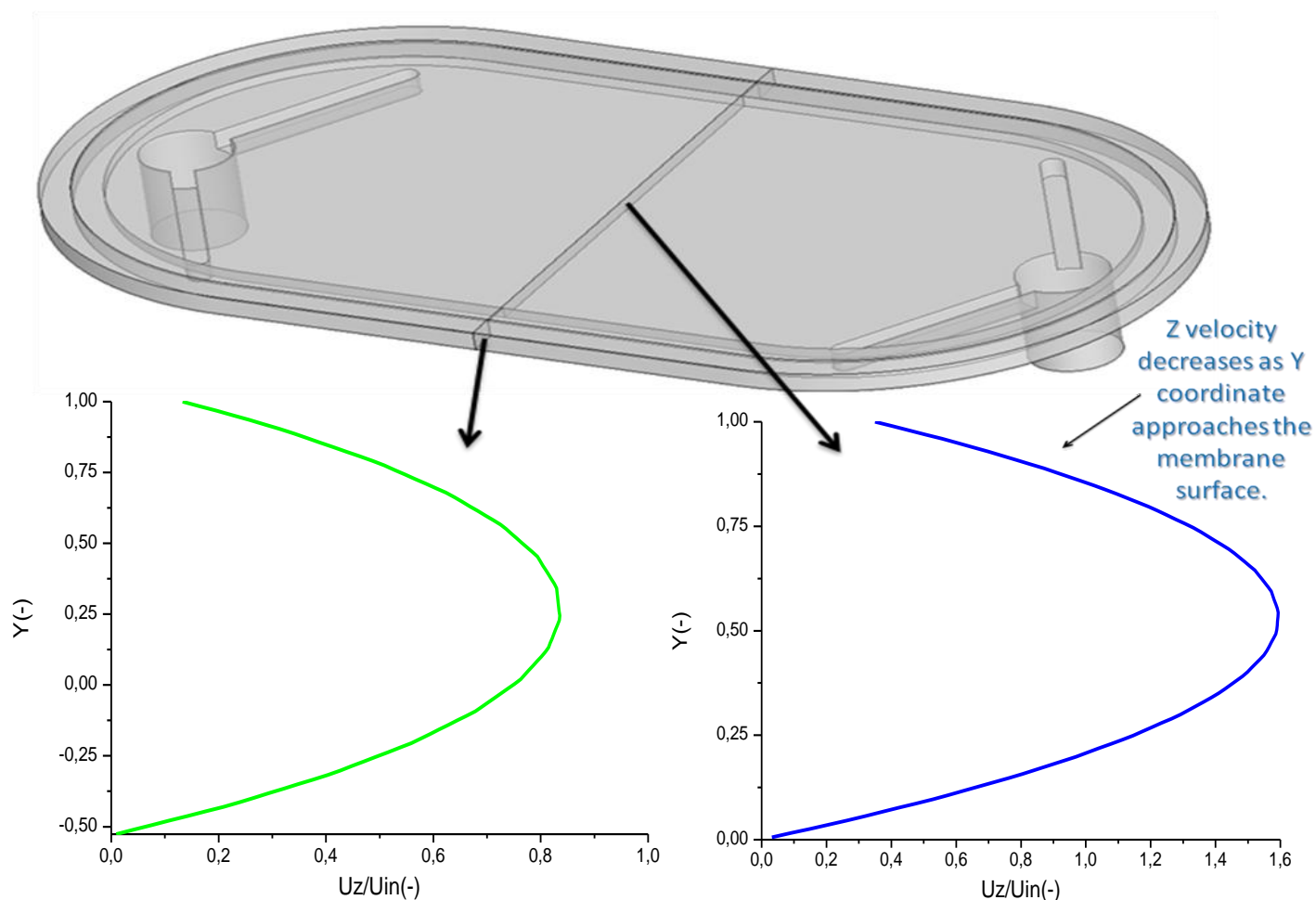


Fig. 7.18 Parabolic velocity profile on the secondary flow

Fig. 7.19 Parabolic velocity profile on the main flow

7.3 Cases 5-10

7.3.1 Simulation Conditions

The following simulation cases are related with the transport of the **fresh water** from the low-pressure side **through the membrane** into the high-pressure side of the flow cell which is **initially** filled with **salt water** ($\rho=1025 \text{ kg/m}^3$, $\mu=0.00096 \text{ kg/m}\cdot\text{s}$), with concentration of salt **C=35g/L**. The **working fluid** is a **mixture** of salt water and fresh water.

The table below presents the boundary conditions that have been used in each case:

Boundary Conditions // Cases 5-10				
Case	Membrane (green)	Channel design (gray)	Inlet (red)	Outlet (blue)
5	Dynamic conditions: HTI membrane	Wall	0.5 L/h	14 bar
6				15.8 bar
7			1 L/h	1 bar
8			0.5 L/min	15.8 bar
9				
10	Oasys Water membrane			

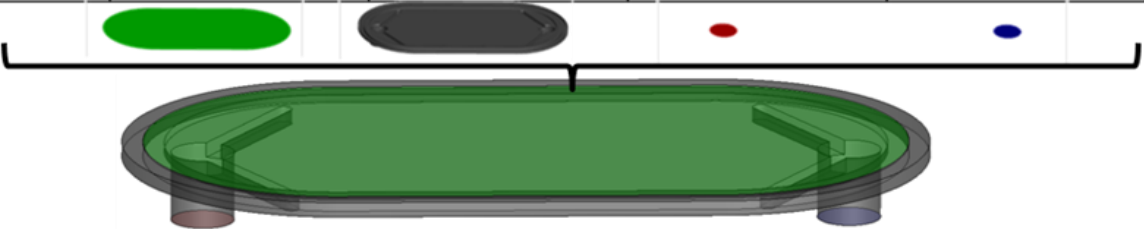


Fig. 7.20 Boundary conditions

7.3.1.1 Boundary Condition on the membrane surface

In order to simulate the **flow of fresh water through the membrane** a velocity boundary condition has been used on the membrane surface, which is given by a function programmed for FLUENT (**UDF**). This function calculates the velocity in each cell adjacent to the membrane using the general equation of osmosis $U = A \cdot (\Delta\pi - \Delta P)$, where A is the water permeability coefficient of the membrane, ΔP the hydraulic pressure difference of the two membrane sides and $\Delta\pi$ the osmotic pressure difference between the area above (fresh water $C=0$ g/L) and below (salt water $C=\text{variable}$) each cell.

Water permeability is equal to $1.87\text{E-}12 \left(\frac{\text{m}}{\text{s} \cdot \text{Pa}} \right)$ for the cases 5-8 (HTI

membrane) and $3.18\text{E-}12 \left(\frac{\text{m}}{\text{s} \cdot \text{Pa}} \right)$ for the cases 9 and 10 (Oasys Water membrane [1],[2]).

Hydraulic pressure difference changes in each case as the pressure on the high pressure side is different, as shown in the table above (pressure in the fresh water side is constant in all the 5 cases equal to 1 bar).

Osmotic pressure difference is calculated for each cell using the equation $\Delta\pi = 2 \cdot \Delta C_{\text{NaCl}} \cdot R \cdot T$, where R is the gas constant $142.2 \left(\frac{\text{m}}{\text{K} \cdot \text{s}^2} \right) \Delta C_{\text{NaCl}}$ the

concentration difference between the area above and below each cell and T is the temperature 298.15 K.

The **convection and diffusion of the mixture**, fresh water and salt water, is captured with an additional **species transport model**, with mass diffusivity of salt water in fresh water $D=2.65E-09 \text{ m}^2/\text{s}$ (equal to the self diffusion coefficient of water at $P=14 \text{ bar}$ and $T=298.16 \text{ K}$ [3]).

7.4 Case 5

7.4.1 Boundary Conditions on the inlet and outlet

In this case the boundary conditions on the **inlet** and **outlet** are the same as in case 4 i.e. **$Q_{in}=0.5 \text{ L/h}$** and **$P_{out}=14\text{bar}$** , in order to compare their results. While both use the same equations for the calculation of the flow through the membrane, the difference is that in case 4 is given as a uniform flow rate while for the case 5 the flow is calculated for each cell separately according to the local concentration.

7.4.2 Results and discussion

7.4.2.1 Volumetric flow rate through the membrane and generated power

The **flow through the membrane** is calculated **0.096 L/h** while for the case 4 is 0.26 L/h , i.e. approximately 3 times less than the theoretical. This is attributed to the lower osmotic pressure difference between the two membrane sides, as the dilution of seawater from the fresh water has been considered in this case. The effect of dilution can be reduced by increasing the flow rate of the sea water coming from the inlet, as the fresh water coming from the membrane will be removed faster (see later section).

The **power** that can be produced per unit of membrane area (i.e. Power density) is equal to the hydraulic pressure difference between the two membrane sides multiplied by the velocity through the membrane. For this case it is calculated equal to **1.48 W/m^2** while the ideal is 4.05 W/m^2 . This difference is caused by the decreased flow rate through the membrane.

7.4.2.2 Flow field

The figures 7.21-7.26 present the absolute pressure profile on y-z plane ($x=0$), the streamline and vector plots, and the salt concentration profile on y-z plane ($x=0$), with comments and explanations where is necessary:

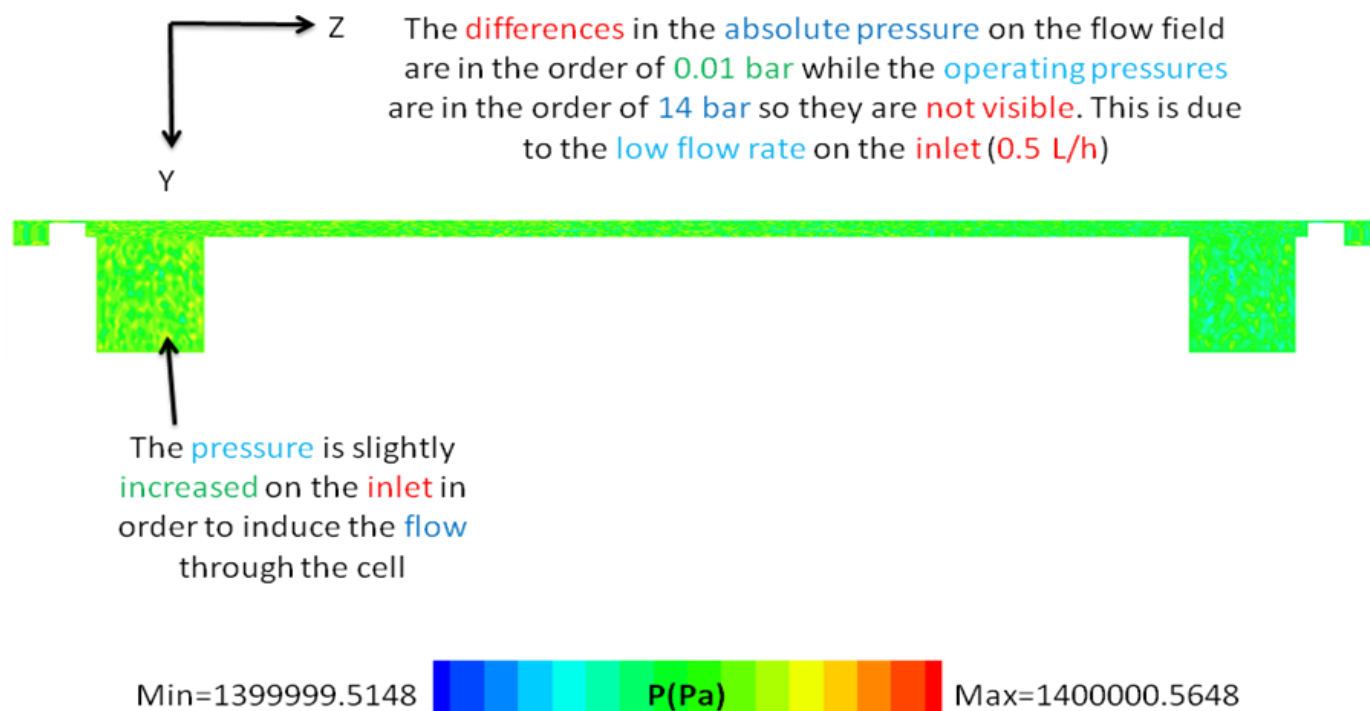


Fig. 7.21 Absolute pressure profile on y-z plane (x=0)

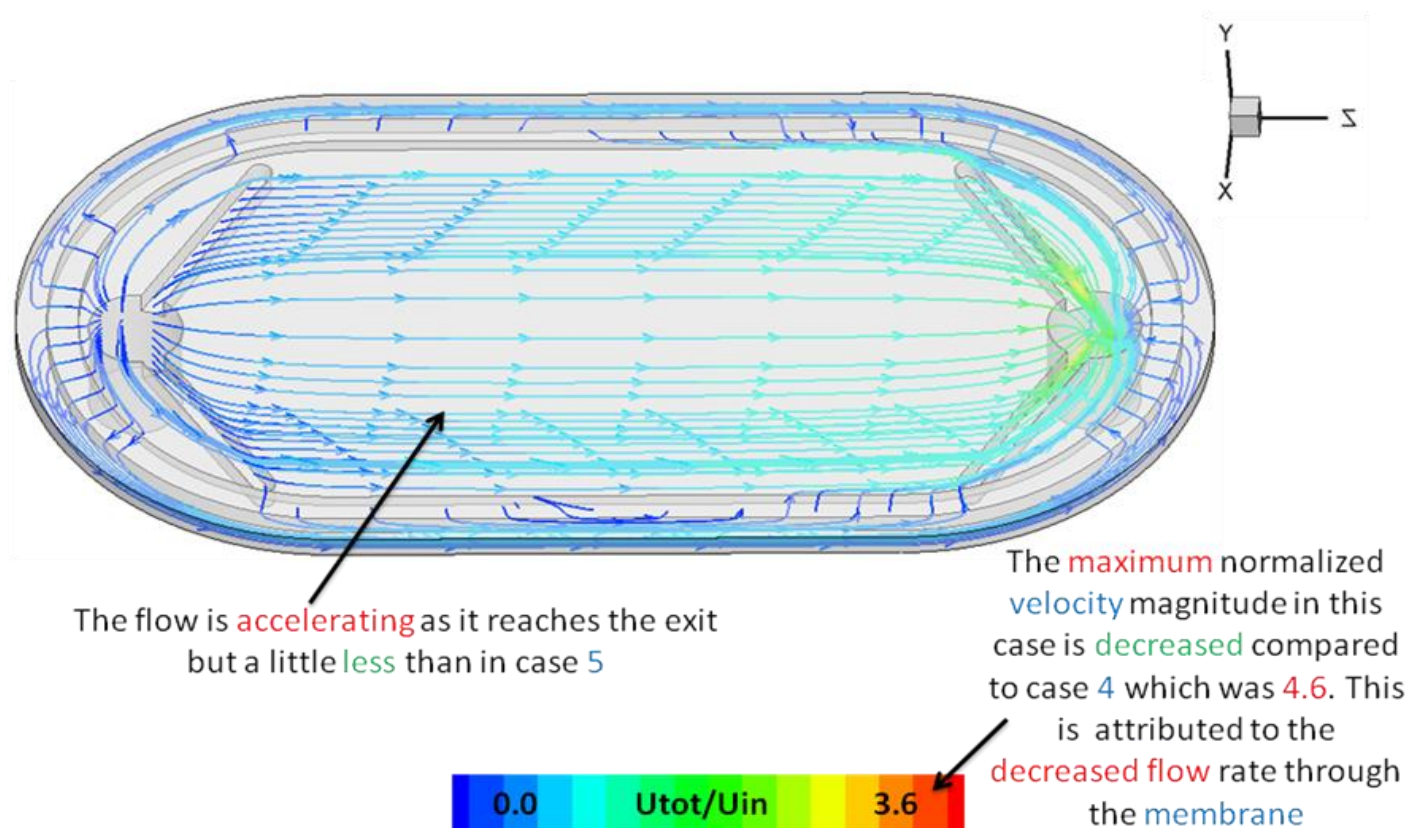
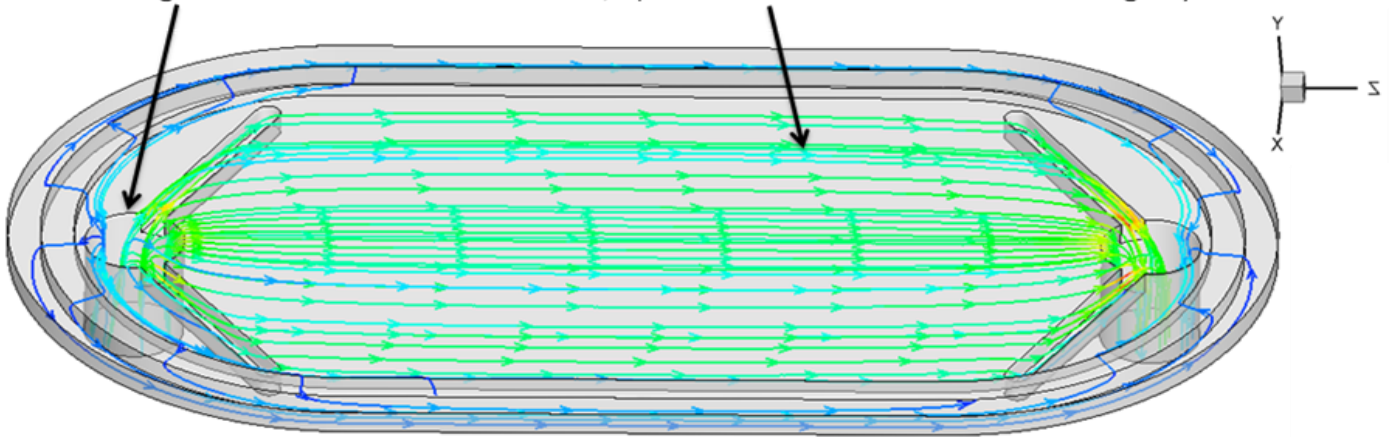


Fig. 7.22 Streamlines from the membrane surface colored with normalized velocity magnitude

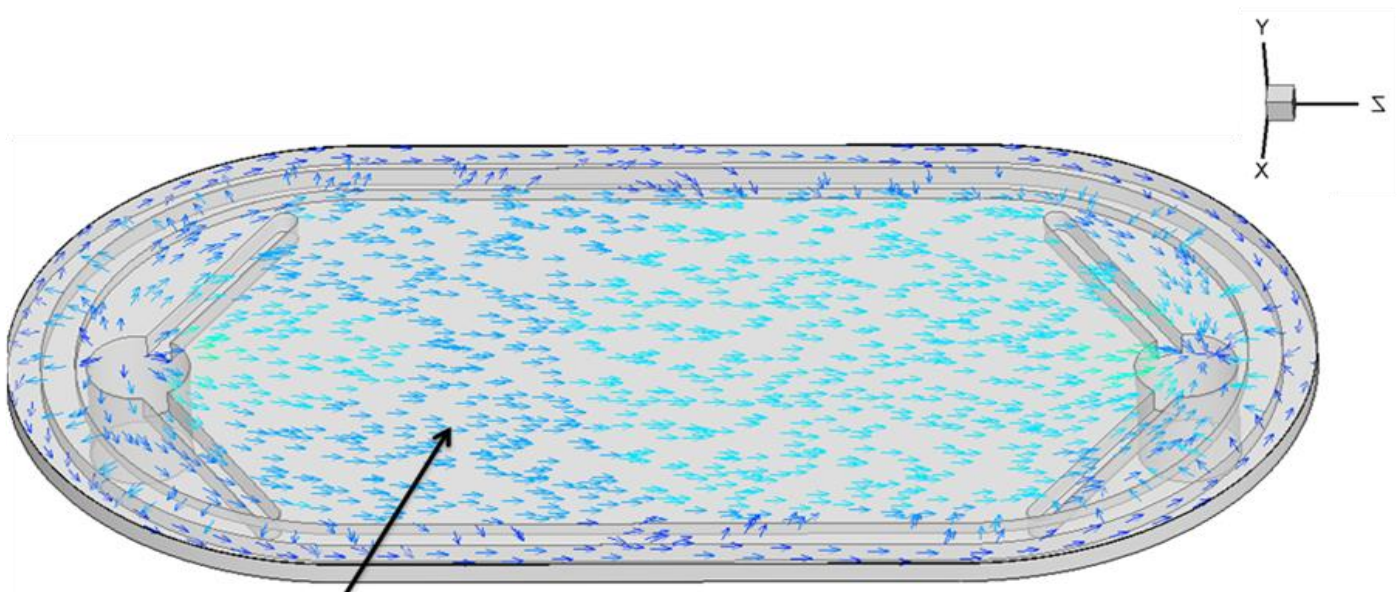
The flow field is **similar** with that of the case 4 with only two **differences**: i) **more** streamlines from the inlet **escape into the periphery** as the resistance from the flow through the membrane is decreased, ii) the **acceleration** of the flow is slightly **decreased**



The **differences** are attributed to the **decreased** flow rate through the **membrane**



Fig. 7.23 Streamlines from the inlet colored with normalized velocity magnitude



The **velocity** magnitude in the area near the **inlet** is **lower** than in case 4



Maximum normalized **velocity** magnitude same as in case 4

Fig. 7.24 Flow vectors near the membrane surface colored with normalized velocity magnitude

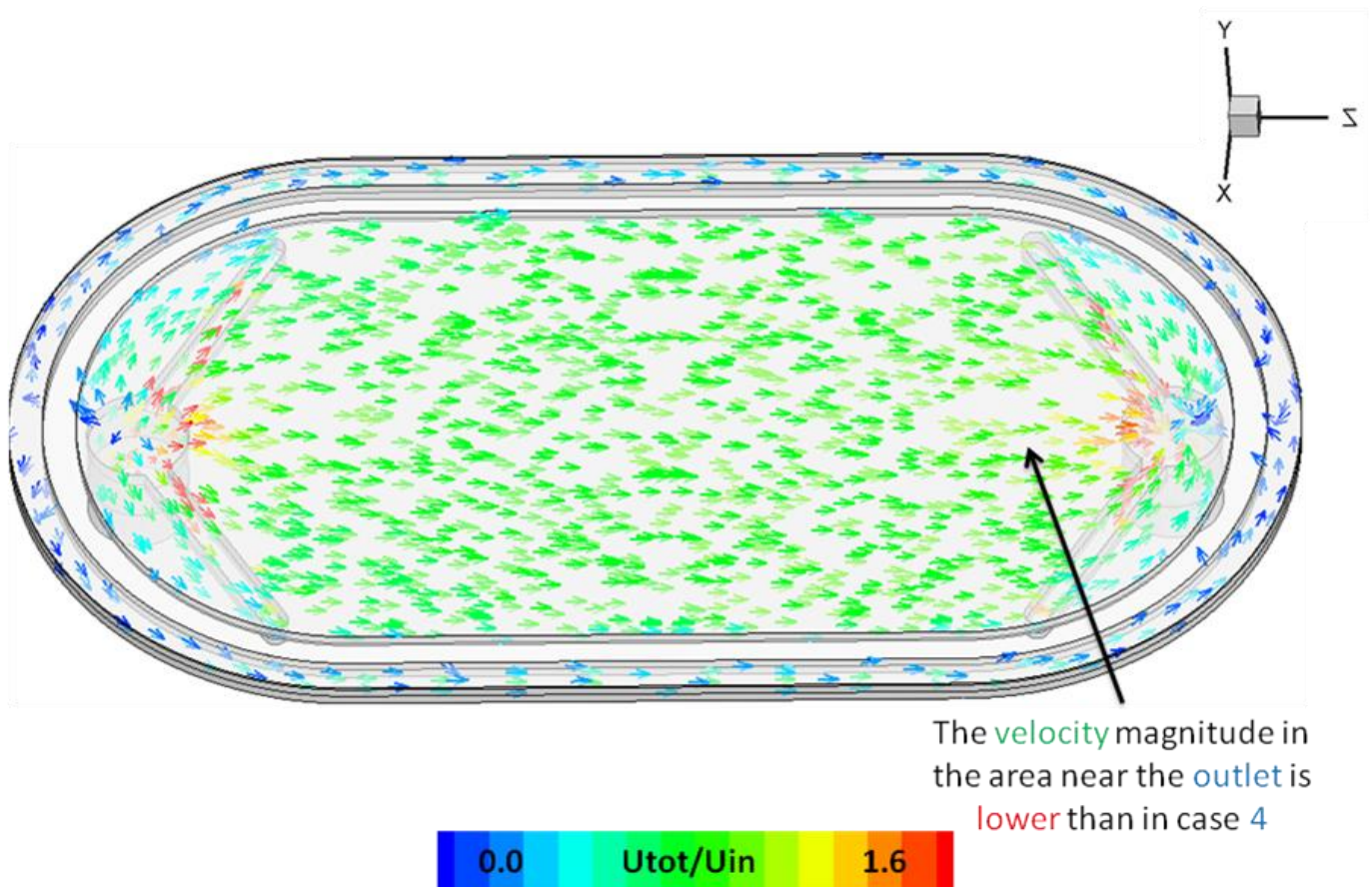


Fig. 7.25 Flow vectors in the middle of the channel colored with normalized velocity magnitude

The salt concentration profiles can be created if the mass fraction of salt water is multiplied by 35 g/L, which is the initial concentration of salt in salt water.

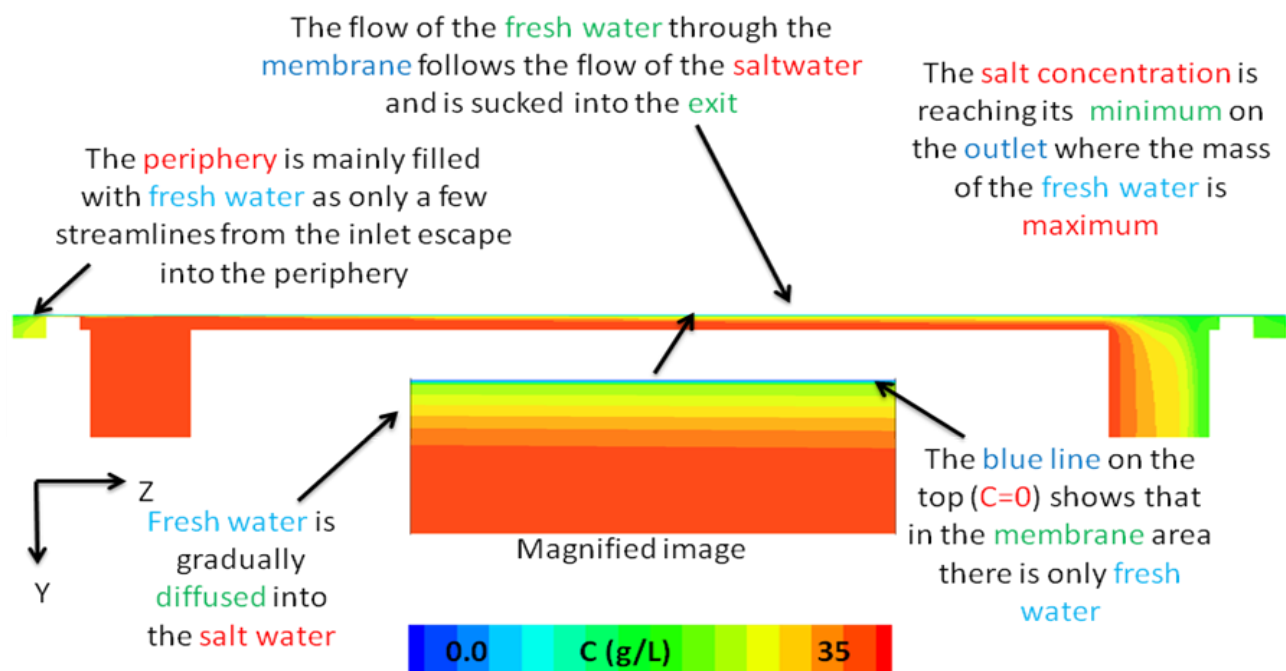


Fig. 7.26 Salt concentration profile on y-z plane ($x=0$)

7.5 Case 6

7.5.1 Boundary conditions on the inlet and outlet

In this case the boundary condition on the **inlet** remains the same (**$Q_{in}=0.5\text{L/h}$**) while on the **outlet** the pressure is **15.8 bar**. This pressure gives hydraulic pressure difference between the two membrane sides equal to 14.8 bar (15.8 bar HPS-1 bar LPS), which is equal to half the ideal osmotic pressure difference (=29.6 bar), and yields the maximum power for this situation.

7.5.2 Results and discussion

7.5.2.1 Volumetric flow rate through the membrane and generated power

The fresh **water flowing through the membrane** is **0.09 L/h** while the ideal is 0.23 L/h. This flow rate is slightly decreased compared to case 5 (0.096 L/h) as the hydraulic pressure difference between the two membrane sides is increased from 13 bar to 14.8 bar.

The **power** per unit of membrane area that can be generated in this case is **1.58 W/m^2** while the ideal is 4.11 W/m^2 . This power is slightly increased compared to that of the case 5 (1.48 W/m^2) despite the decrease of the flow rate through the membrane. This is caused by the increased hydraulic pressure difference which had a greater effect on the power than the decreased flow rate through the membrane.

7.5.2.2 Flow field

The **flow field** and the **salt concentration profile** are **very similar** with that in **case 5** as there is only a slight difference in the flow through the membrane. The only difference is that the maximum normalized velocity magnitude is 3.5 instead of 3.6 in case 5.

7.6 Case 7

7.6.1 Boundary conditions on the inlet and outlet

This case presents the conditions for an experiment without the use of high pressure on the salt water side, which is easier to establish. The pressure on the **outlet** is **1 bar**, which gives maximum flow through the membrane but zero power density as the hydraulic pressure difference between the two membrane sides is equal to zero. The volumetric flow on the **inlet** is **1 L/h** which is approximately twice the flow through the membrane for these conditions.

7.6.2 Results and discussion

7.6.2.1 Volumetric flow rate through the membrane and generated power

The **volumetric flow through the membrane** is **0.236 L/h** while the ideal (i.e. without the effect of dilution) is 0.466 L/h, approximately twice the calculated. The **generated power** is **zero** as the hydraulic pressure difference between the two membrane sides is also zero.

7.6.2.2 Flow Field

The **flow field** is **similar** with that in the **cases 5-6**. Here it is only presented the **salt concentration profile** (fig. 7.27), which can be measured in the experiment, using a laser technique or salinity meters, which described in previous section.

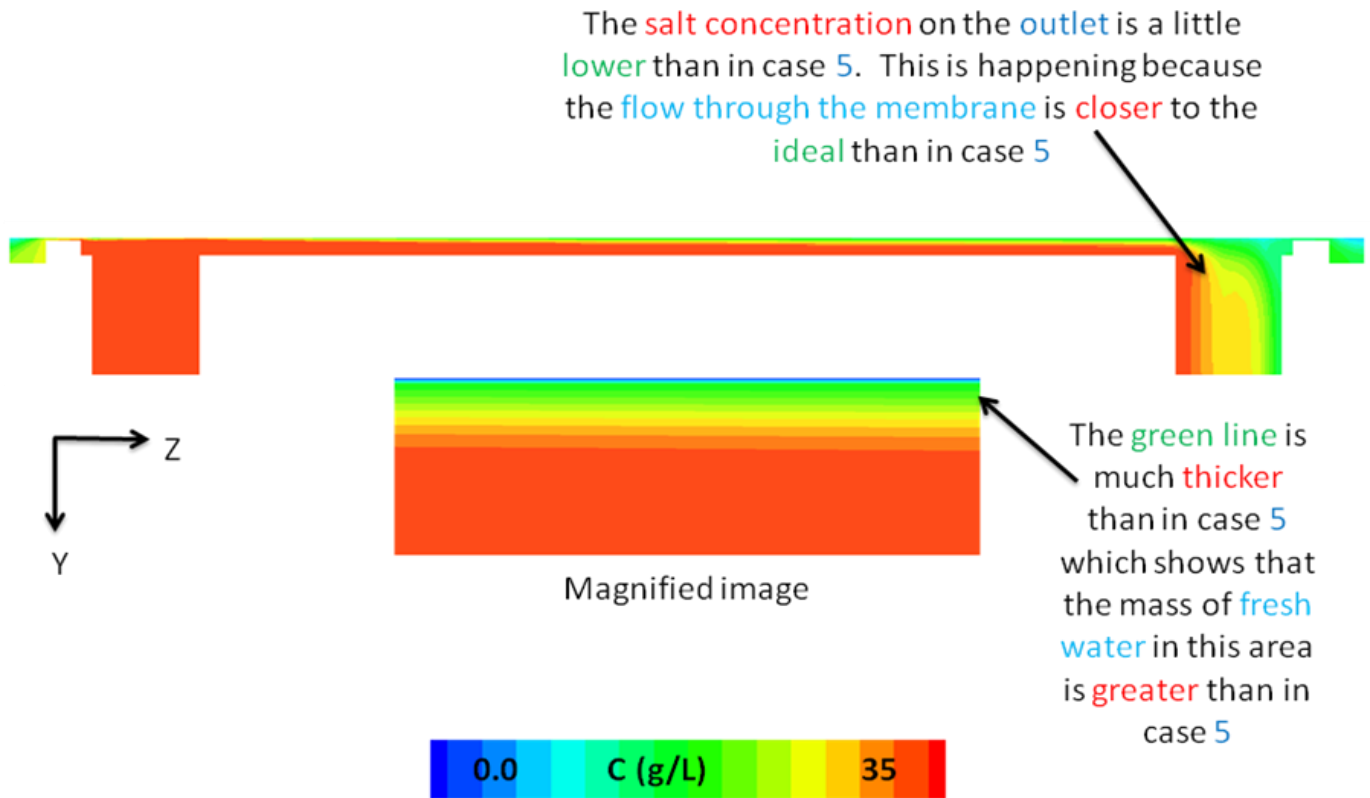


Fig. 7.27 Salt concentration profile on y-z plane ($x=0$)

7.7 Case 8

7.7.1 Boundary conditions on the inlet and outlet

The boundary condition on the **outlet** in this case is the same as in case 7 (**$P_{out}=1$ bar**). The volumetric flow rate on the **inlet** is **0.5 L/min**, which has been used in the published experiments [4] and is 120 times greater than the flow rate in the cases 1-6 ($Q_{in}=0.5$ L/h).

7.7.2 Results and discussion

7.7.2.1 Volumetric flow rate through the membrane and generated power

The **volumetric flow rate through the membrane** is **0.413 L/h** while in the case 7 was 0.236 L/h, i.e. 75% increase. The ideal flow rate is 0.466 L/h being only (compared to the previous cases) 12.8% greater. This difference between the two cases is attributed to the increased flow rate on the inlet which removes faster the fresh water through the membrane and decreases the effect of dilution.

7.7.2.2 Flow field

The **flow field** is **similar** with that in **case 9** and it will be presented in that case. This shows that the increase on the flow rate through the membrane, with flow rate in the inlet 0.5 L/min, does not make a lot of difference in the flow field.

Here will be presented only the **salt concentration profile**.

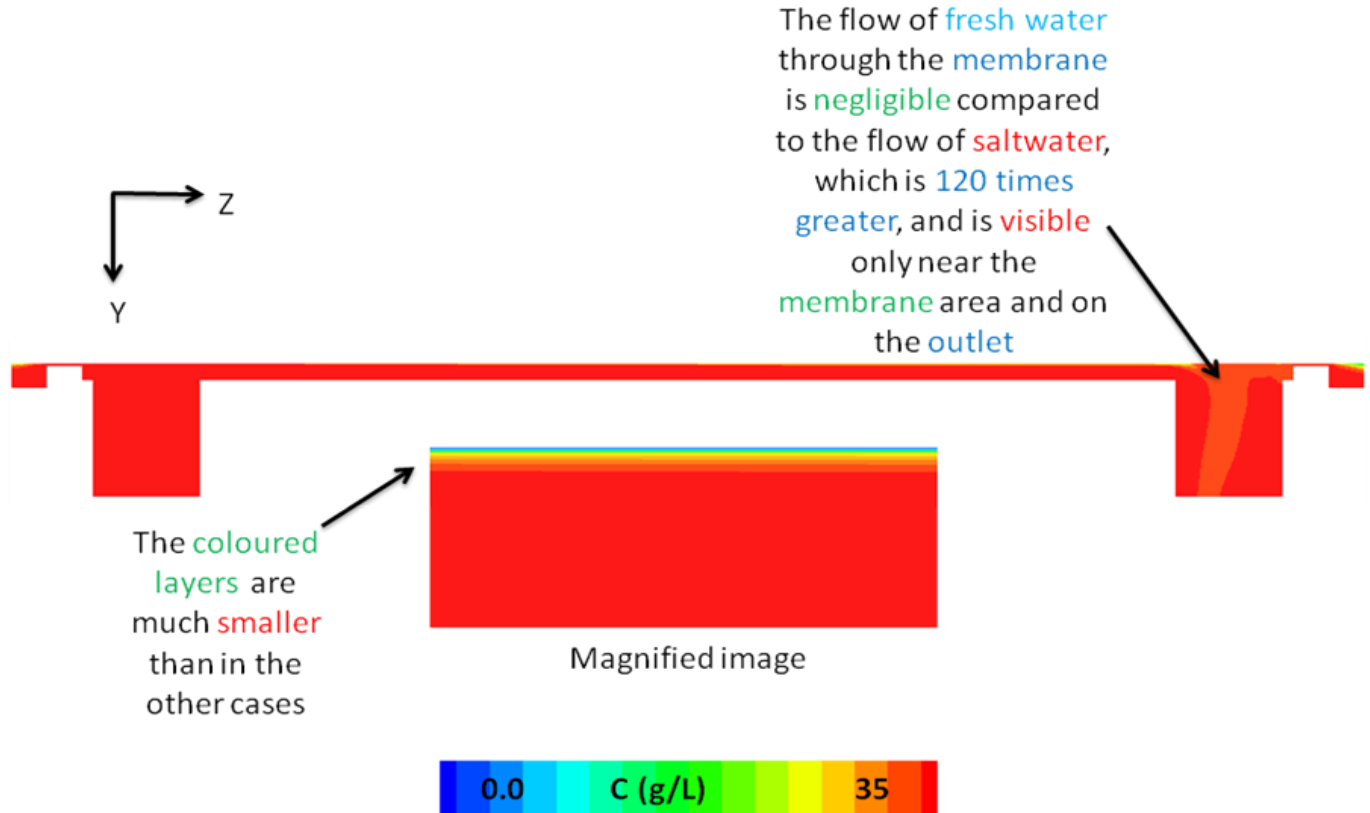


Fig. 7.28 Salt concentration profile on y-z plane ($x=0$)

7.8 Case 9

7.8.1 Boundary conditions on the inlet and outlet

In this case the boundary condition on the **inlet** is the same as in the previous case, i.e. **0.5 L/min**, while on the **outlet** the pressure is **15.8 bar**.

7.8.2 Results and discussion

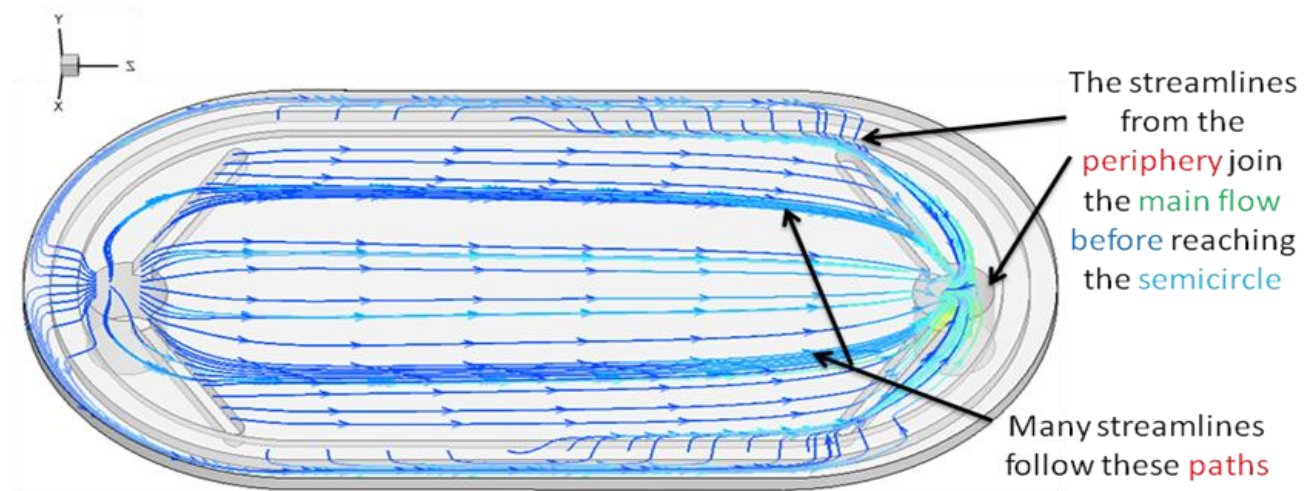
7.8.2.1 Volumetric flow through the membrane and generated power

The flow rate of fresh water through the membrane is **0.203 L/h** while in case 6 was 0.09 L/h, i.e. 125% increase. The ideal flow rate is 0.23 L/h which means that it is only (compared to cases 6-8) 13.3 % grater.

The **power density** that can be produced is **3.58 W/m²** and it is 125% increased compared to case 7 (1.58 W/m²). The ideal power density is 4.11 W/m² (13.3% grater).

7.8.2.2 Flow field

The **salt concentration profile** is the **same as in the previous case** so here is presented only the **flow field**.



The **maximum** normalized **velocity** magnitude is **decreased** compared to the cases 5-7 reaching the **levels** of cases 1-3 where there was no flow through the membrane. This is happening **because** the **velocity** on the **membrane surface** is four orders of magnitude **lower** than the **velocity** on the **inlet** and therefore it does not influence a lot the main flow. In the previous cases the difference was two orders of magnitude.



Fig. 7.29 Streamlines from the membrane surface colored with normalized velocity magnitude

Very **few** streamlines from the **inlet** escape into the **periphery** which means that **more salt water** flows into the **main flow** where the **osmosis** takes place.

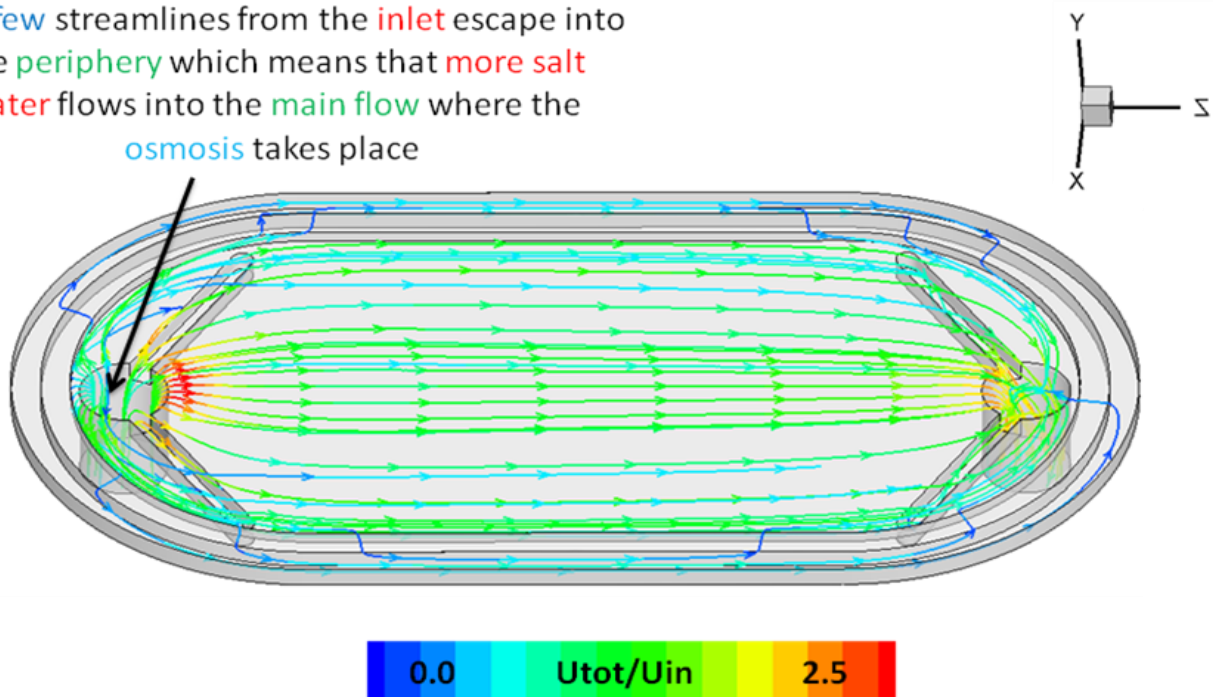


Fig. 7.30 Streamlines from the inlet colored with normalized velocity magnitude

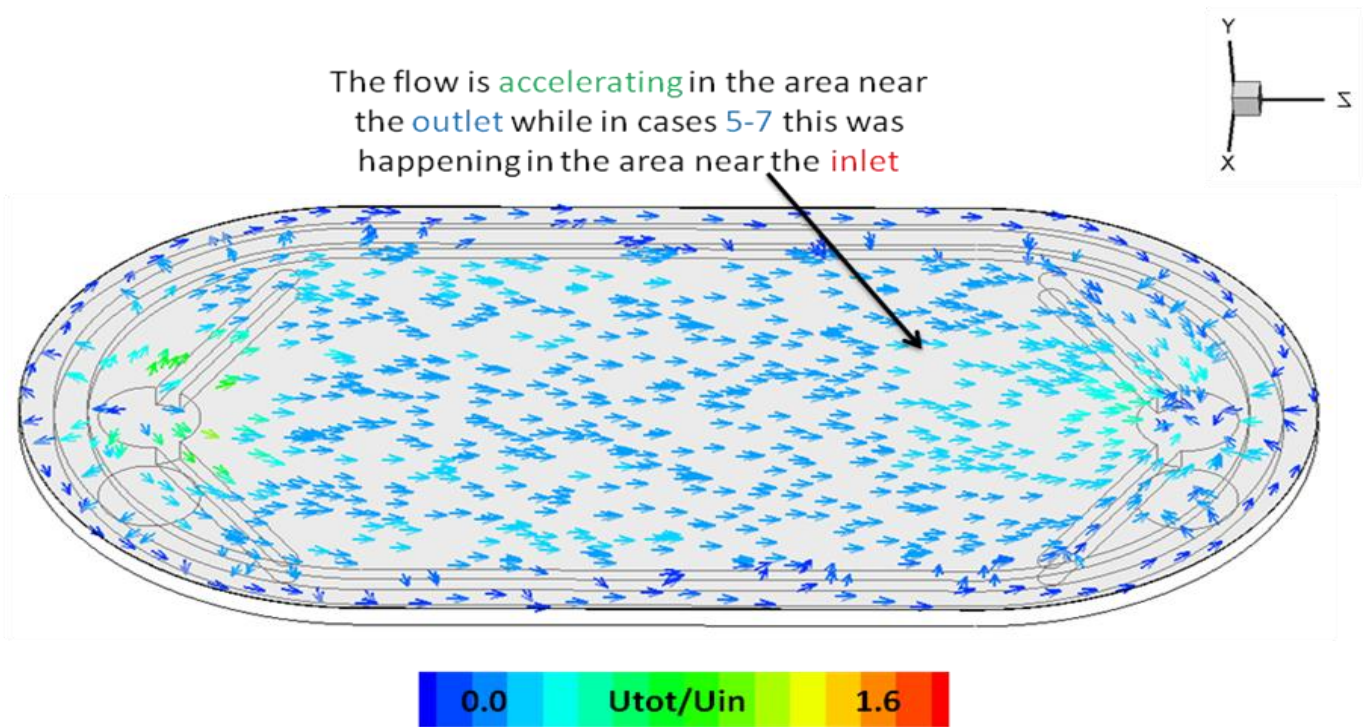


Fig. 7.31 Flow vectors near the membrane surface colored with normalized velocity magnitude

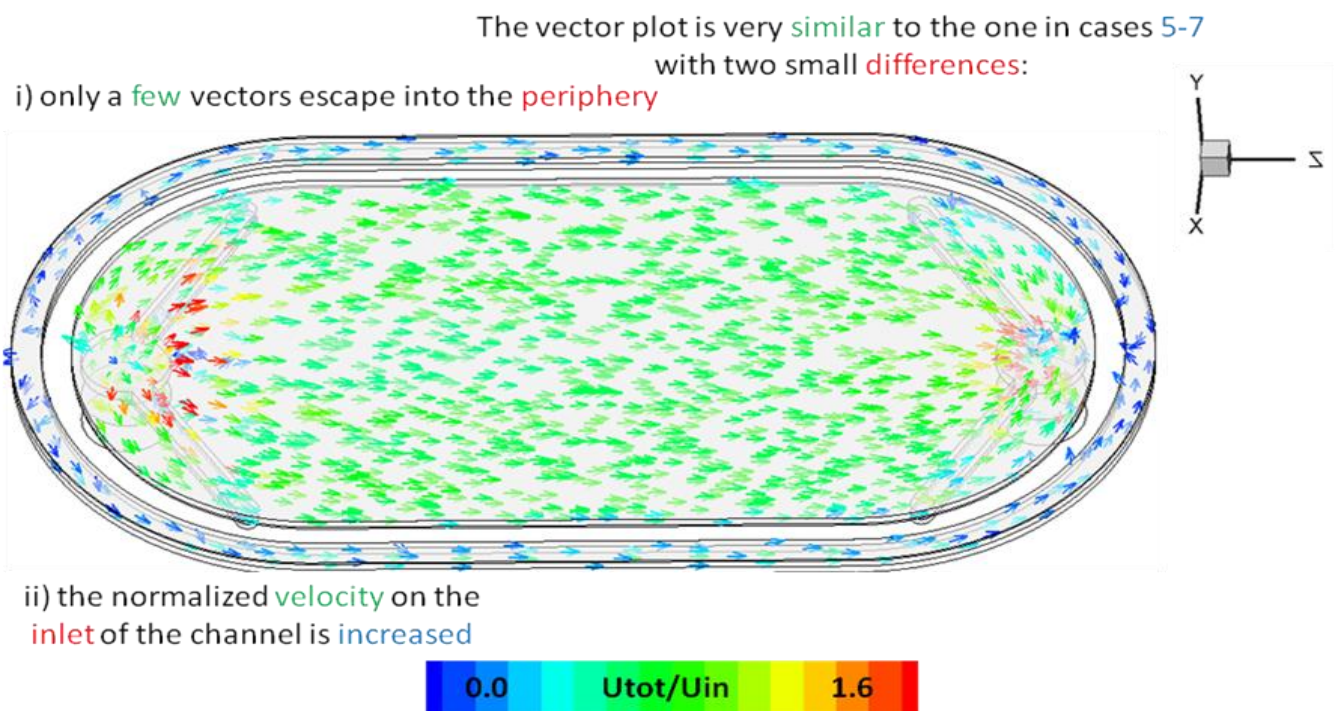


Fig. 7.32 Flow vectors in the middle of the channel colored with normalized velocity magnitude

7.9 Cases 5-9 Parametric Diagrams

Using the **same boundary condition on the membrane surface** as in **cases 5-9** and **different conditions on the inlet, outlet and salt concentration** difference between the two membrane sides the **following parametric diagrams** has been created:

- i) Velocity through the membrane (**J_w**) as function of hydraulic pressure difference (**ΔP**) between fresh and salt water, when **$Q_{in}=0.5$ L/min and $\Delta C=35$ g/L**.
- ii) Power generated per unit of membrane area (**$W=J_w \cdot \Delta P$**) as function of hydraulic pressure difference (**ΔP**), when **$Q_{in}=0.5$ L/min and $\Delta C=35$ g/L**.
- iii) Volumetric flow rate through the membrane (**Q_m**) as function of the volumetric flow rate on the inlet (**Q_{in}**), when **$\Delta P=14.8$ bar** (gives maximum power for ideal conditions).
- iv) Volumetric flow rate through the membrane (**Q_m**) as function of the salt concentration difference (**ΔC**) between the two membrane sides, when **$Q_{in}=0.5$ L/min and $\Delta P=14.8$ bar**.

7.9.1 Diagrams i and ii

The diagrams i and ii are presented along with the experimental and model results from the publication:

Power generation with pressure retarded osmosis: An experimental and theoretical investigation, Andrea Achilli , Tzahi Y. Cath, Amy E. Childress
in order to compare them. This publication uses the same conditions ($T=25^\circ\text{C}$, $\Delta C=35$ g/L, $Q_{in}=0.5$ L/min) and the same membrane ($A=1.87 \text{ E-}12 \text{ m}^2/(\text{s} \cdot \text{Pa})$).

These diagrams have been created using 9 points which come from 9 different simulations, for **$\Delta P=0$ bar – 29.6611 bar**.

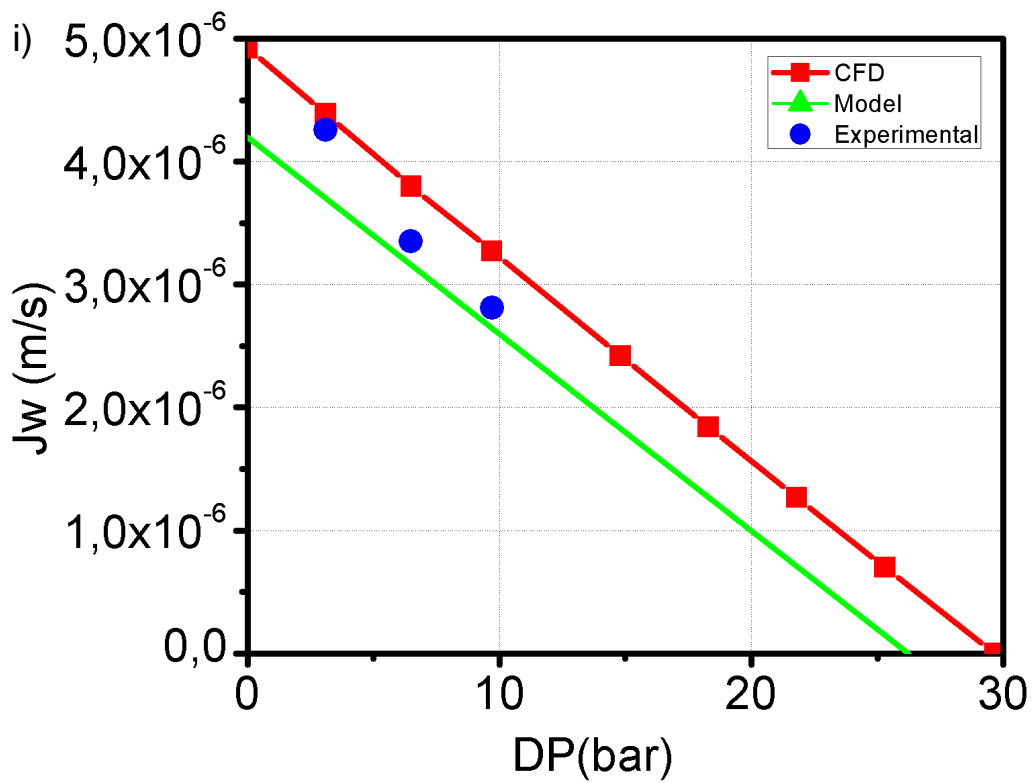


Fig. 7.33 Velocity through the membrane (J_w) as function of hydraulic pressure difference (DP)

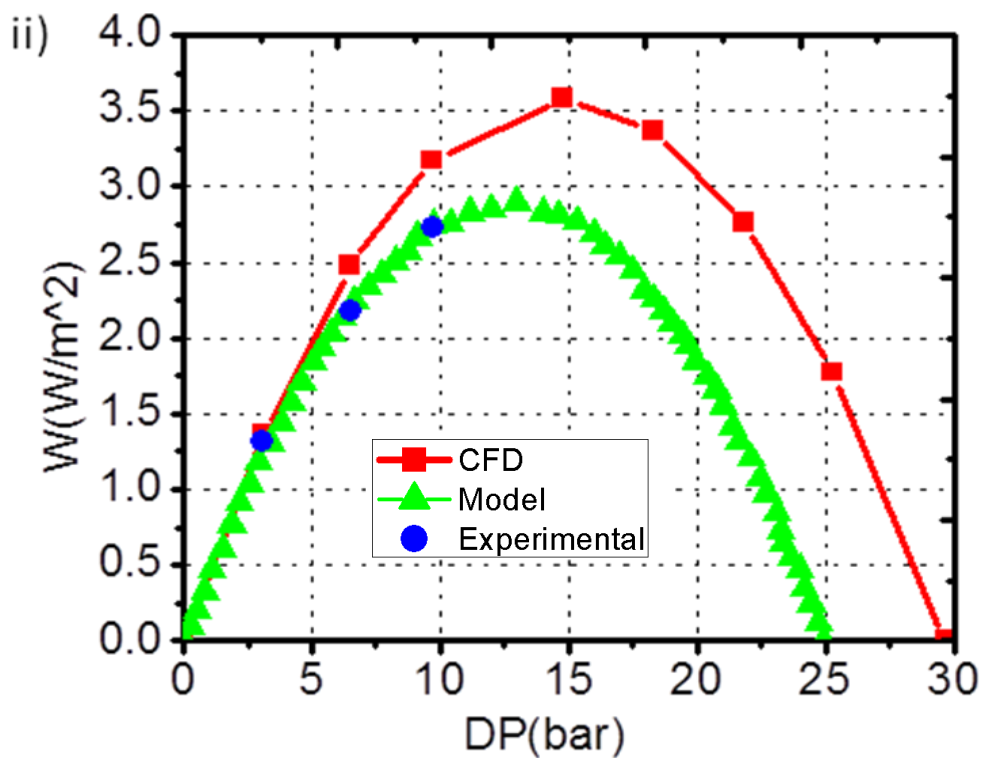


Fig. 7.34 Power density (W) as function of hydraulic pressure difference (DP)

7.9.1.1 Discussion of the results

These diagrams show that the CFD results follow the general trend of the experimental and model results (straight line in the first and parabolic in the second), but they are slightly increased. The increase on the first diagram is constant while on the second is proportionate to the hydraulic pressure difference (ΔP), as the generated power is also proportionate to ΔP ($W = J_w \cdot \Delta P$). This increase is mainly attributed to two reasons:

- i) The maximum osmotic pressure difference in the model for the ideal conditions is 27.63 bar (26.25 bar for the actual conditions) while for the CFD is 29.6611 bar, which means that the osmotic pressure in the model has been calculated with a different equation than $\Delta \Pi = 2 \Delta C R T$, which gives lower osmotic pressure and therefore lower velocity and power.
- ii) The CFD calculations consider only the effect of dilution of the sea water from the fresh water coming from the membrane (i.e. external concentration polarization) and do not calculate the effect of salt moving from the sea water to fresh water, which decreases the salt concentration difference between the two membrane sides and therefore the osmotic pressure difference which leads to decreased velocity and power. Also, the movement of salt induces the effect of internal concentration polarization (salt trapped inside the membrane), which is also not calculated and decreases the effective osmotic pressure and the generated power.

The maximum difference between model and CFD results for the $W-\Delta P$ diagram appears when ΔP is 14.8 bar and it is 26.6%.

For the experimental results ($W-\Delta P$ diagram) the differences from CFD results are: 3% when $\Delta P = 3.1$ bar, 13.8% when $\Delta P = 6.5$ bar, 16.3% when $\Delta P = 9.7$ bar, which means that as the hydraulic pressure difference increases the deviation increases too.

7.9.2 Diagram iii

The third diagram has been created with 10 points from 10 different simulations for **$Q_{in} = 6.94E-08 \text{ m}^3/\text{s} - 1.41E-04 \text{ m}^3/\text{s}$** .

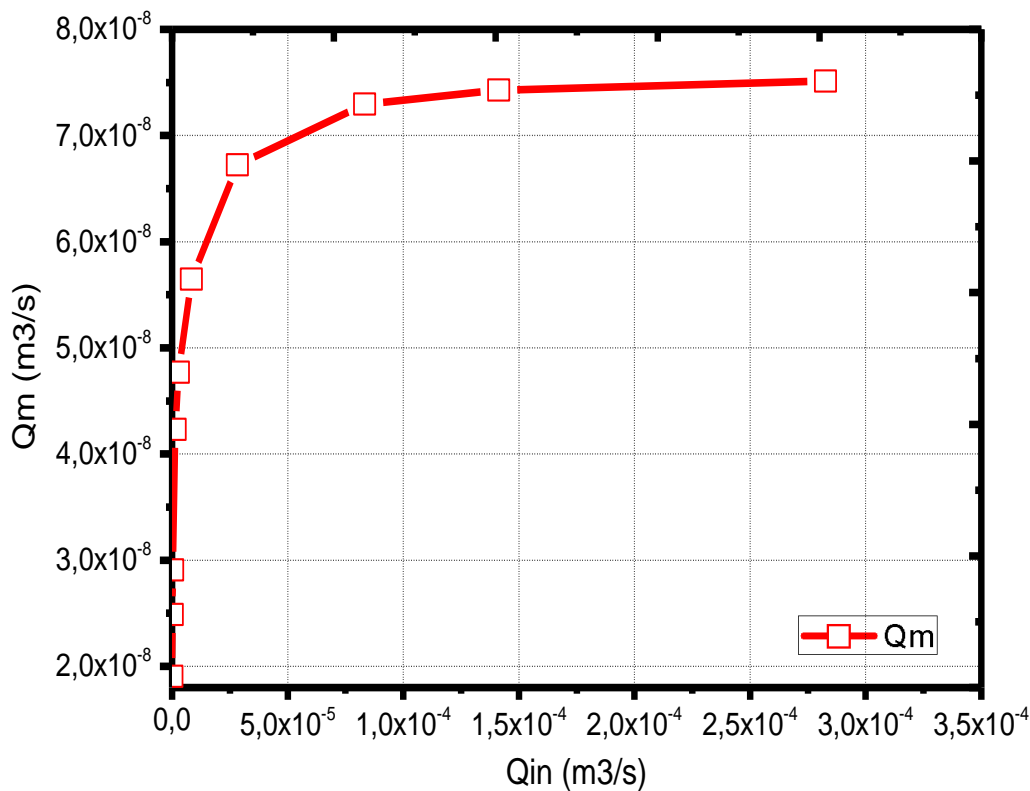


Fig. 7.35 Volumetric flow through the membrane (Q_m) as function of volumetric flow from the inlet (Q_{in})

- The lowest volumetric flow from the inlet (Q_{in}) that has been calculated is $6.9 \times 10^{-8} \text{ m}^3/\text{s}$ (0.25 L/h) which is approximately equal to the maximum flow through the membrane (Q_m) for these conditions (i.e. relatively low). The FLUENT results for the flow through the membrane for this point varies between 3 values. The presented graph contains the average of them ($1.9 \times 10^{-8} \text{ m}^3/\text{s}$).

7.9.2.1 Discussion of the results

As the inlet volumetric flow increases from $Q_{in} = 1.9 \times 10^{-8}$ to $8.32 \times 10^{-8} \text{ m}^3/\text{s}$, the flow through the membrane increases rapidly. Above this point the increase in the flow from the inlet gives a minor increase in the flow through the membrane (logarithmic curve). Therefore, for each different conditions there is an optimum flow from the inlet (Q_{in}) which gives a combination of as much as possible flow through the membrane (Q_m), and therefore generated power, with as low as possible cost (flow from the inlet).

7.9.3 Diagram iv

This diagram has been created using 6 points coming from 6 different simulations, for $\Delta C = 20\text{--}45 \text{ g/L}$. The salt concentration on the fresh water side is considered 0 which means that actually the 6 points correspond to 6 different salt concentrations on the salt water side. For salt concentrations below 20 g/L the results are not accurate and thus they are not presented.

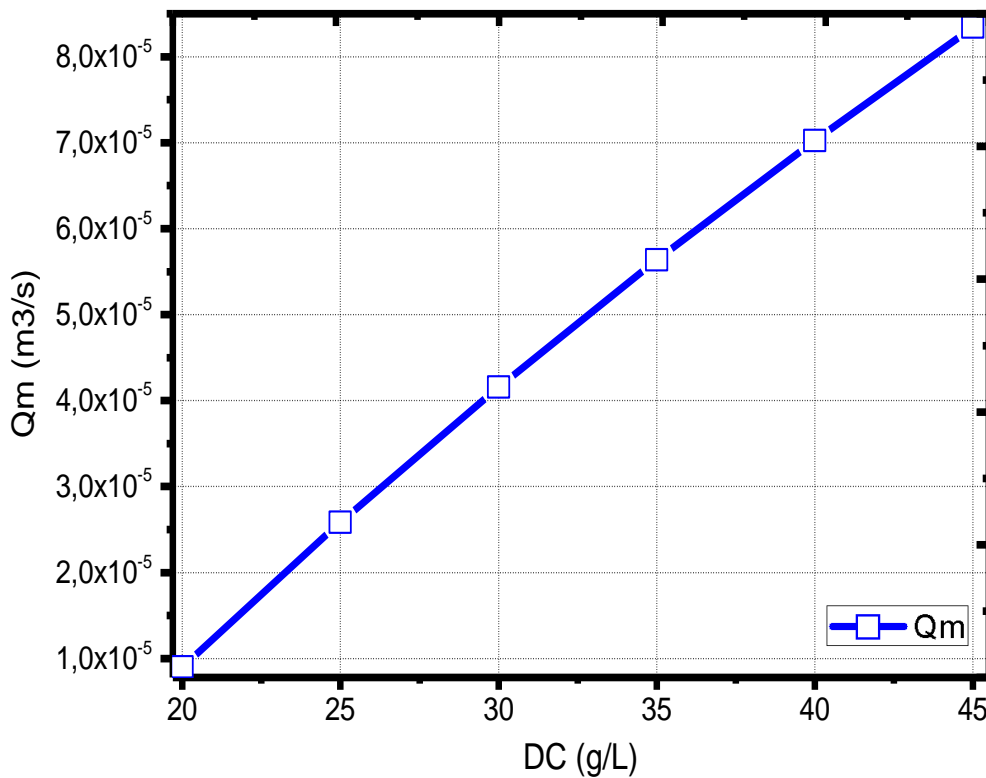


Fig. 7.36 Volumetric flow through the membrane (Q_m) as function of salt concentration difference between the two membrane sides (DC)

7.9.3.1 Discussion of the results

It is evident that the volumetric flow rate through the membrane (Q_m) is tending to be proportionate to the salt concentration difference (ΔC) between the two membrane sides.

This result is expected as: the flow rate through the membrane is calculated as the sum of the flow rate in each cell of the membrane surface, which is the product of the cell area (DE) and the velocity (U) in each cell. The velocity is given by the equation $U = A \cdot (\Delta\pi - \Delta P)$, where $\Delta\pi = 2 \cdot \Delta C_{NaCl} \cdot R \cdot T$ (ΔC_{NaCl} = topic salt concentration difference) and ΔP , A , R , T = constants. The cell area is also constant thus the only variable for calculating the membrane flow rate in each cell is the topic salt concentration difference ΔC_{NaCl} . The rated salt concentration difference ΔC determines the topic salt concentration difference for all the cells (slightly decreased) and therefore the overall flow rate through the membrane.

7.10 Case 10

7.10.1 Boundary conditions

This case simulates the flow on the HPS test cell using the characteristics of an Oasys Water membrane [1], [2]. The boundary conditions on the **inlet** and **outlet** are the same as in case 9: **$Q_{in}=0.5$ L/min, $P_{out}=15.8$ bar**. The difference is that the **water permeability coefficient A** is **$3.18E-12$ ($\frac{m}{s \cdot Pa}$)**

instead of $1.87E-12$ ($\frac{m}{s \cdot Pa}$). This constant is used in the equation $U = A \cdot (\Delta\pi - \Delta P)$

which determines the velocity in each cell on the membrane surface.

7.10.2 Results and discussion

7.10.2.1 Volumetric flow through the membrane and power generated

The **volumetric flow rate through the membrane** is **0.299 L/h** while in case 9 it was 0.203 L/h. This means that a 70% increase in the water permeability has given a 47.2% increase in the flow rate. The flow through the membrane is proportionate to the water permeability so the 70% increase to the water permeability should have given approximately 70% percent increase. This is not happening as the effect of dilution is greater while the flow of fresh water through the membrane is increasing. Therefore, in order to get a proportionate increase on the flow rate with the increase of the water permeability it is necessary to increase the volumetric flow rate in the inlet. For example with 1 L/min volumetric flow on the inlet the flow rate through the membrane is calculated 0.349 L/h i.e. 71.9% greater than in case 9. The ideal flow rate through the membrane is reaching 0.397 L/h which is 32.8% greater than the flow rate in this case.

The **power** that can be produced is **5.26 W/m²** while in case 9 it was 3.58 W/m², with the ideal being equal to 6.99 W/m². With 1 L/min flow rate on the inlet, which gives 0.349 L/h flow rate through the membrane, the power that can be generated is 6.15 W/m².

7.10.2.2 Flow field

The **flow field** and the salt **concentration profile** are **similar** with that in **case 9** with the maximum normalized velocity being in the same level, approximately equal to 2.5.

7.11 Cases 11-12

In the PRO process the design of the test cell plays an important role, as given the volumetric flow from the inlet it can reduce the effect of external concentration polarization (i.e. the dilution of salt water from the fresh water coming from the membrane) (see chapter 3) , by removing the incoming fresh water faster.

In cases 11 and 12 two **new designs** for the test cell are tested for their performance in PRO. The designs are based on the original one (HTI) with some modifications:

- The main and periphery channel are the same as the original one, while the inlet and outlet have been modified.
- The area and volume of the inlet and outlet have been kept the same as the original design in order to retain the same flow volume and boundary conditions.

7.11.1 Boundary conditions

The boundary conditions that have been used are the same as in case 9 **Q_{in}=0.5 L/min**, **P_{out}=15.8 bar**, HTI membrane **A=1.87E-12 ($\frac{m}{s \cdot Pa}$)**

7.11.2 Case 11 design No. 2

The figure below presents the geometry of the design No.2 along with explanations:

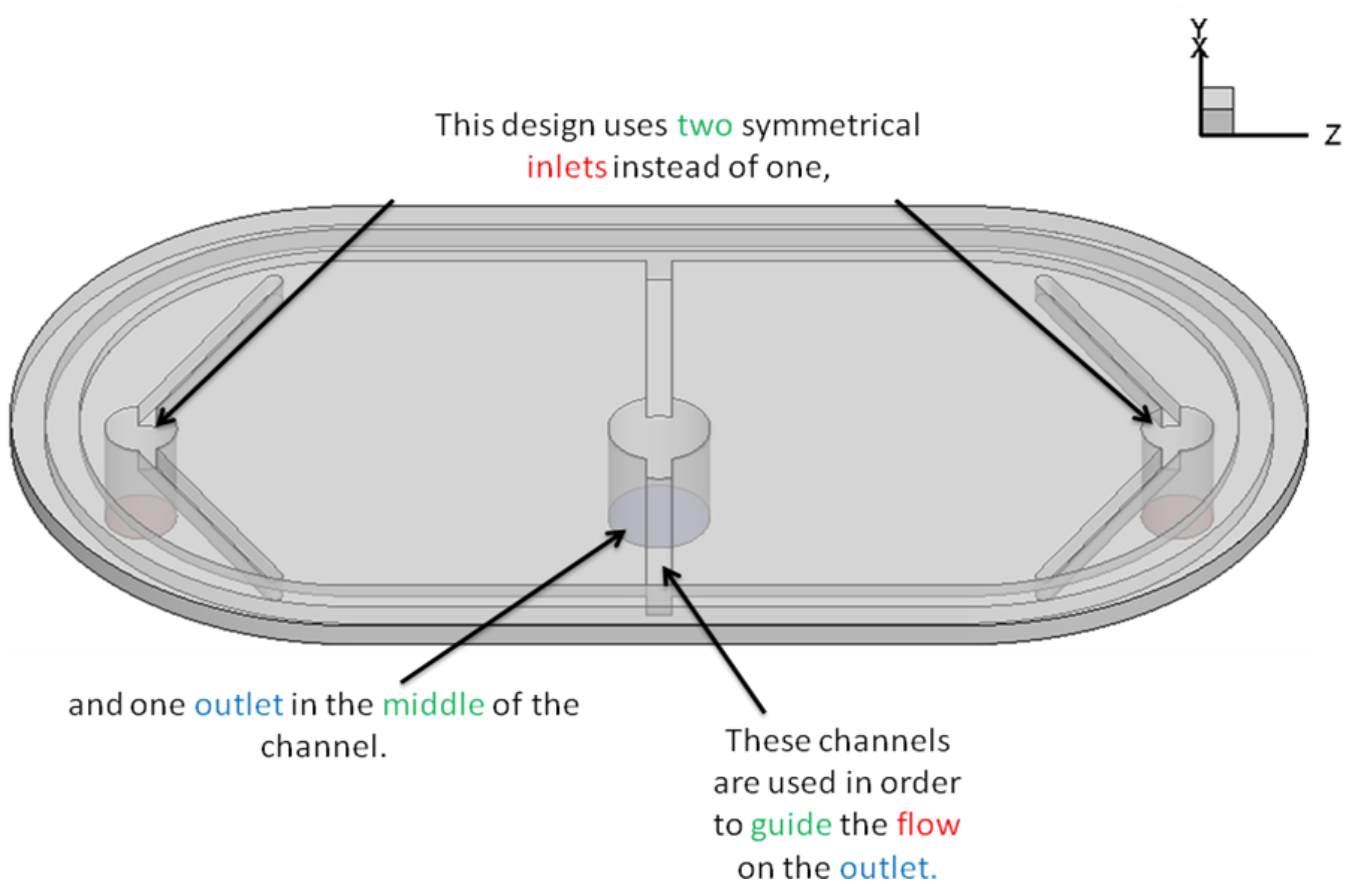


Fig. 7.37 Design No.2

7.11.2.1 Flow field

The figures that will be presented show the streamline and vector plots followed with the appropriate comments.

There are **no streamlines** in this area that **flow** into the **periphery**. This has a **negative effect** on magnitude of the **flow through the membrane** as the fresh water that flows into the main channel dilutes the salt water and therefore decreases the effective osmotic pressure.

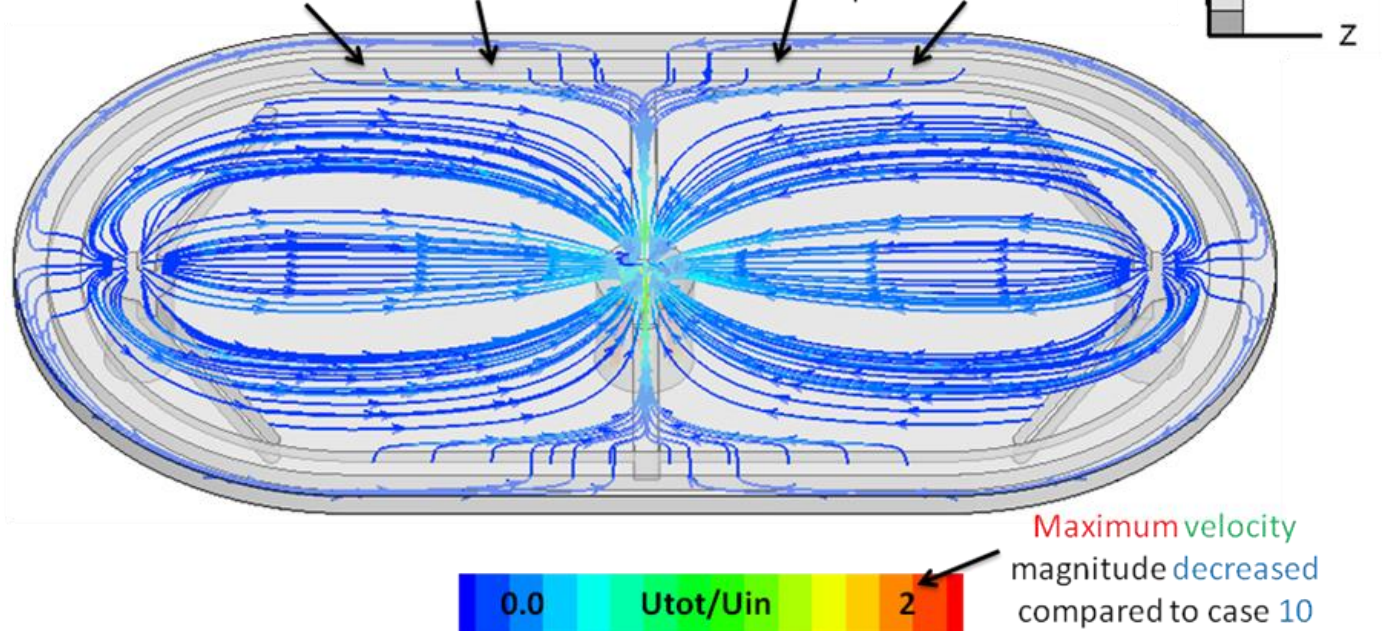
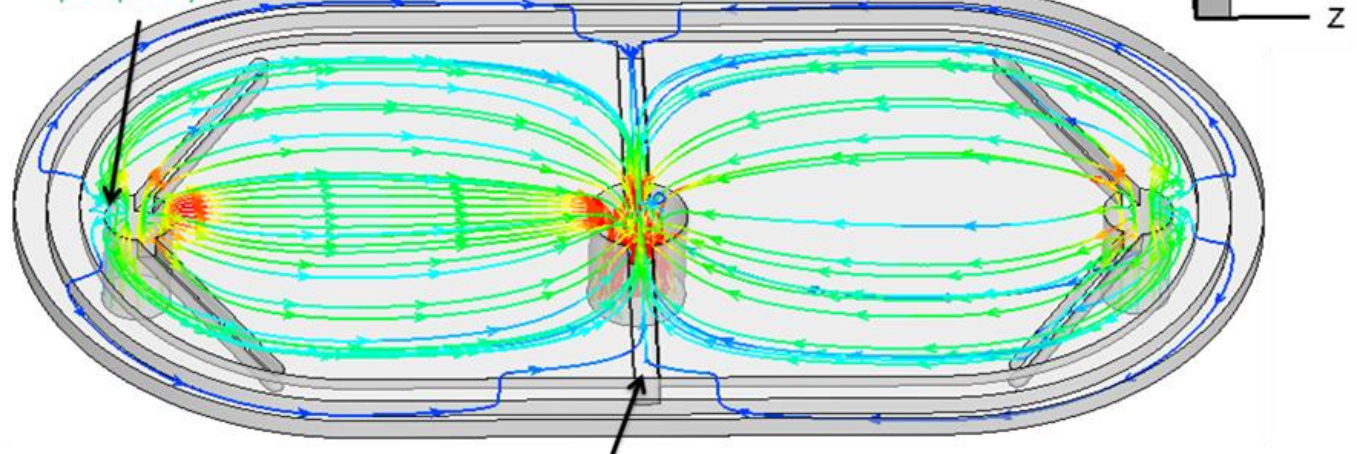


Fig. 7.38 Streamlines from the membrane surface colored with the normalized velocity magnitude

Very **few** **streamlines** escape into the **periphery**



The previous contour and this one show that the **flow** from the **periphery** is sucked into the outlet through the **guiding channels** which means that the fresh water coming from the membrane in this area interferes with the salt water as little as possible.



Fig. 7.39 Streamlines from the inlet colored with normalized velocity magnitude

The flow of **fresh water** through the membrane is slightly accelerated (larger area near the outlet) compared to the original design which means that it is **removed faster**

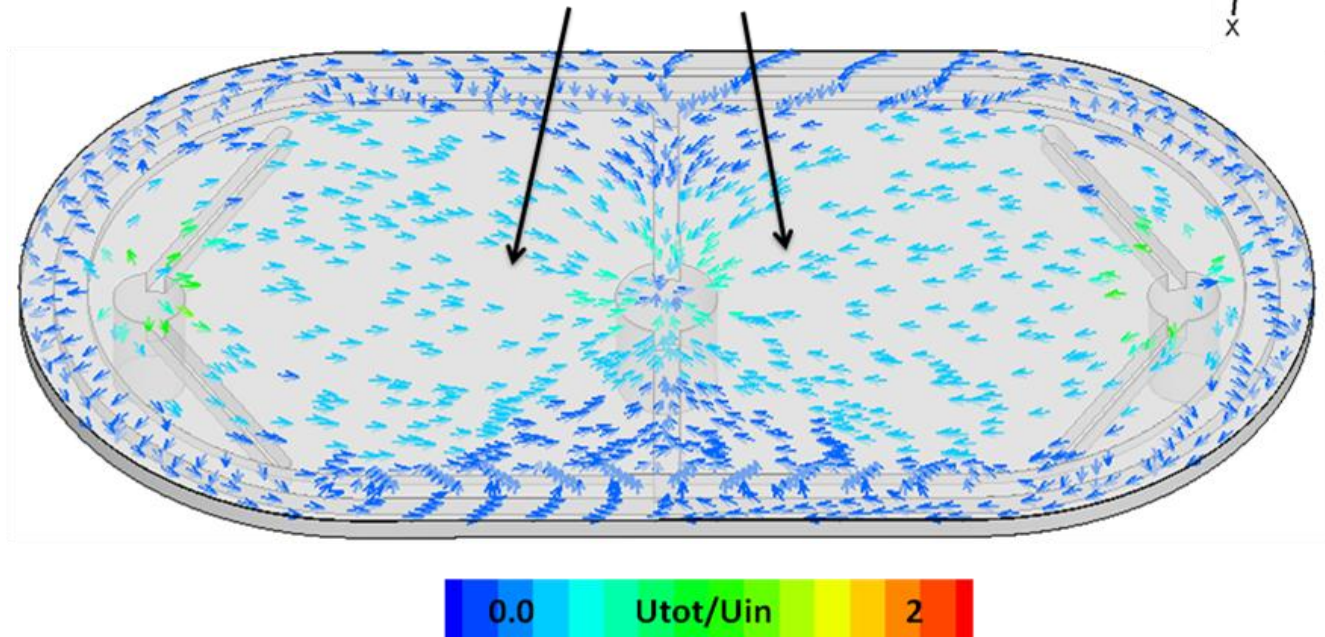
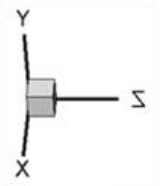


Fig. 7.40 Flow vectors near the membrane surface colored with normalized velocity magnitude

Like the flow of fresh water, the **flow of salt water** is also slightly **accelerated** compared to the original design which has a **negative effect** on the **flow through the membrane**

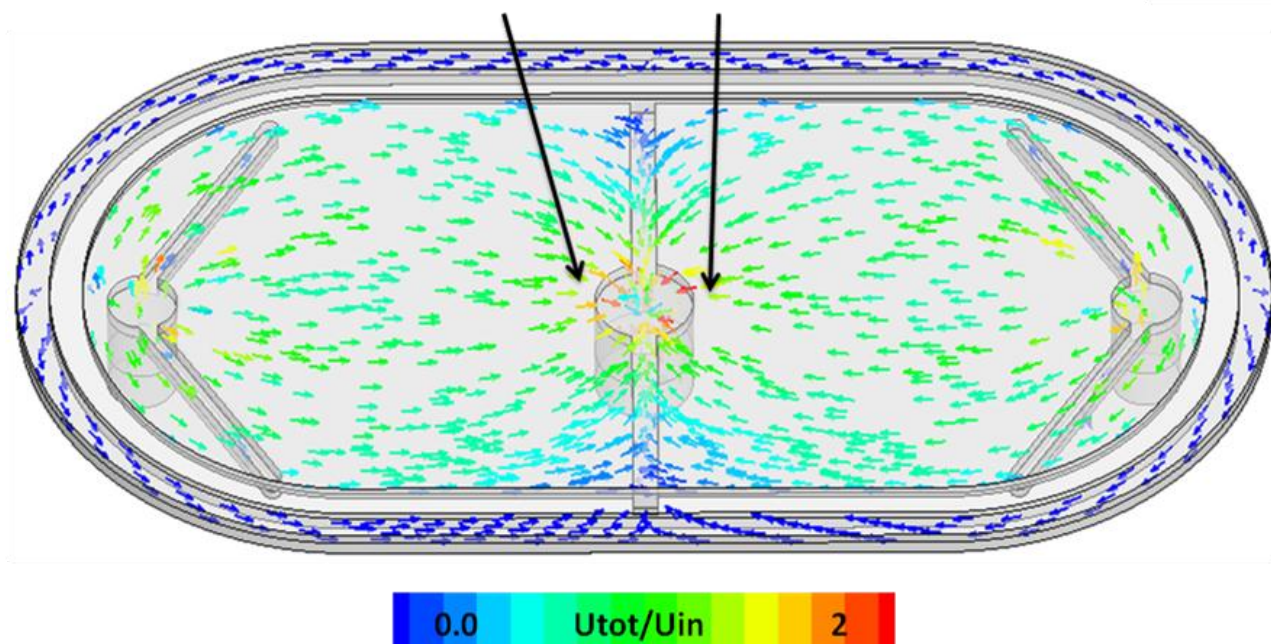
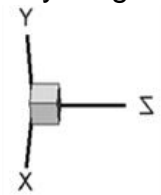


Fig. 7.41 Flow vectors in the middle of the channel colored with normalized velocity magnitude

7.11.3 Case 12 design No.3

The figure shows the geometry of the design No.3 with the appropriate explanations:

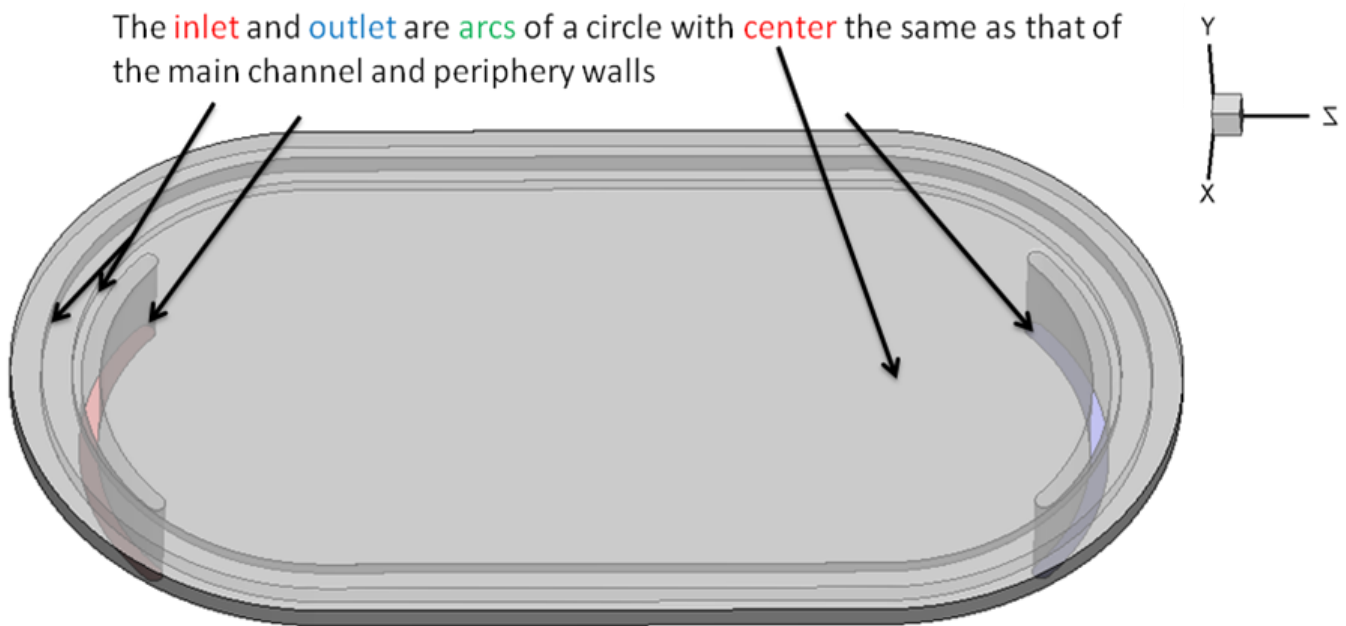


Fig. 7.42 Design No.3

7.11.3.1 Flow field

Here are presented the streamline and vector plots along with comments.

Many streamlines escape into the periphery which means that less fresh water is mixed with salt water of the main flow

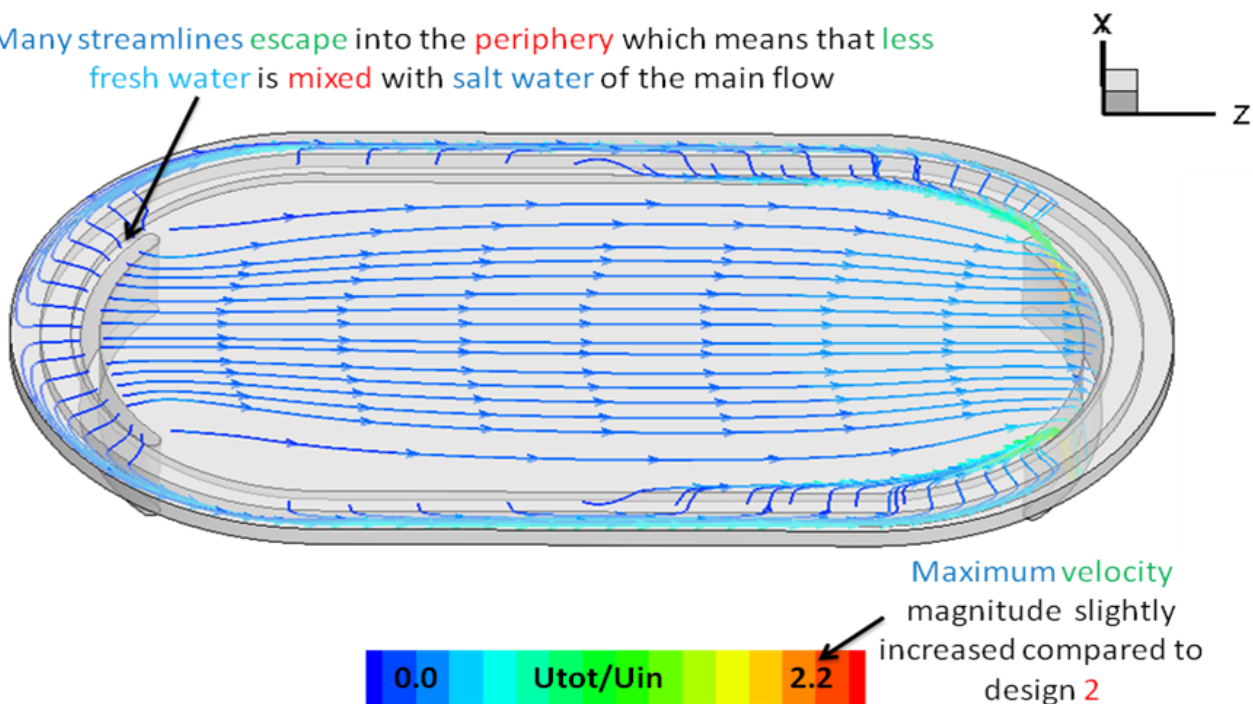


Fig. 7.43 Streamlines from the membrane surface colored with normalized velocity magnitude

Many streamlines from the inlet escape into the periphery compared to designs 1 and 2 which means that less salt water flows into the main channel where the osmosis takes place

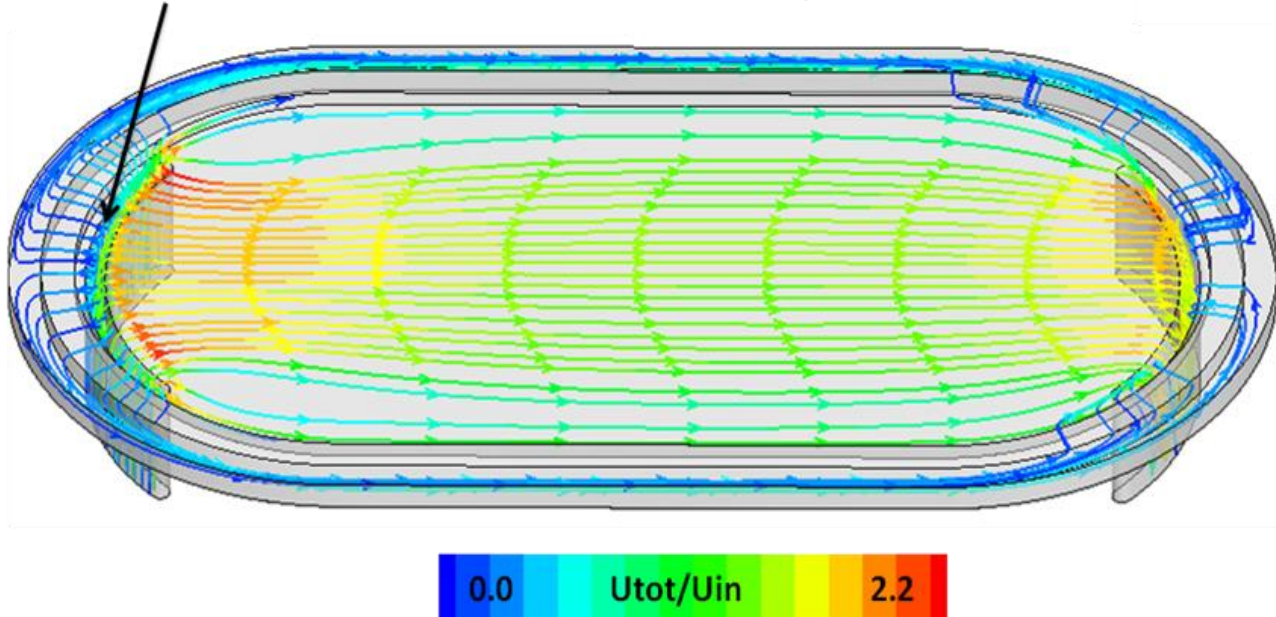


Fig. 7.44 Streamlines from the inlet colored with normalized velocity magnitude

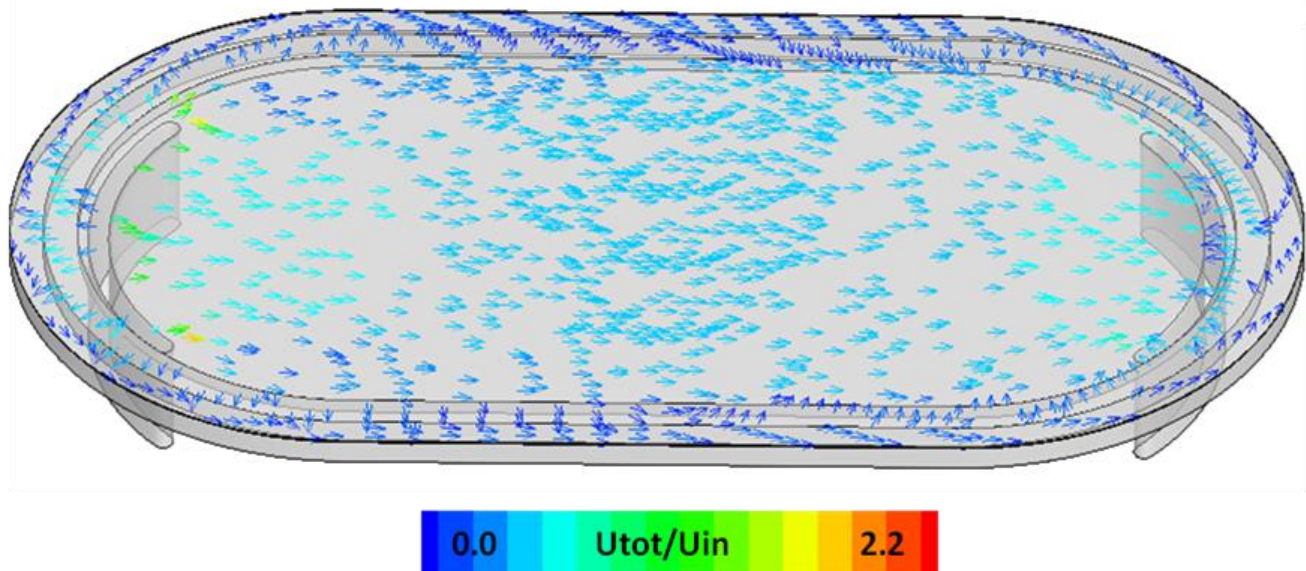
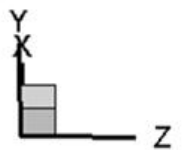


Fig. 7.45 Flow vectors near the membrane surface colored with normalized velocity magnitude

The **flow field** (both near the membrane surface and in the middle of the channel) is **similar** with that in the **1st** design. The main difference is visible and has been mentioned in the streamline plot

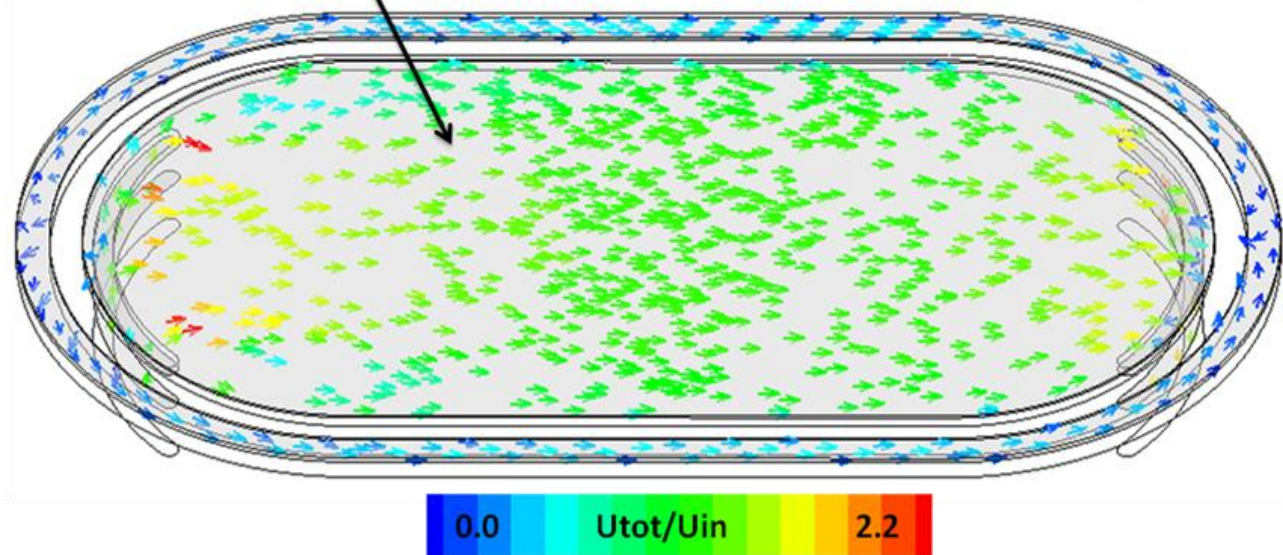
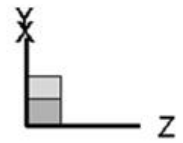


Fig. 7.46 Flow vectors in the middle of the channel colored with normalized velocity magnitude

7.11.4 Comparison of the three designs – cases 9, 11, 12

The **Q_{in}** (inlet volumetric flow)- **Q_m** (volumetric flow through the membrane) plots for each design are presented together in one diagram in order to compare their performance according to the flow through the membrane for the **same conditions**.

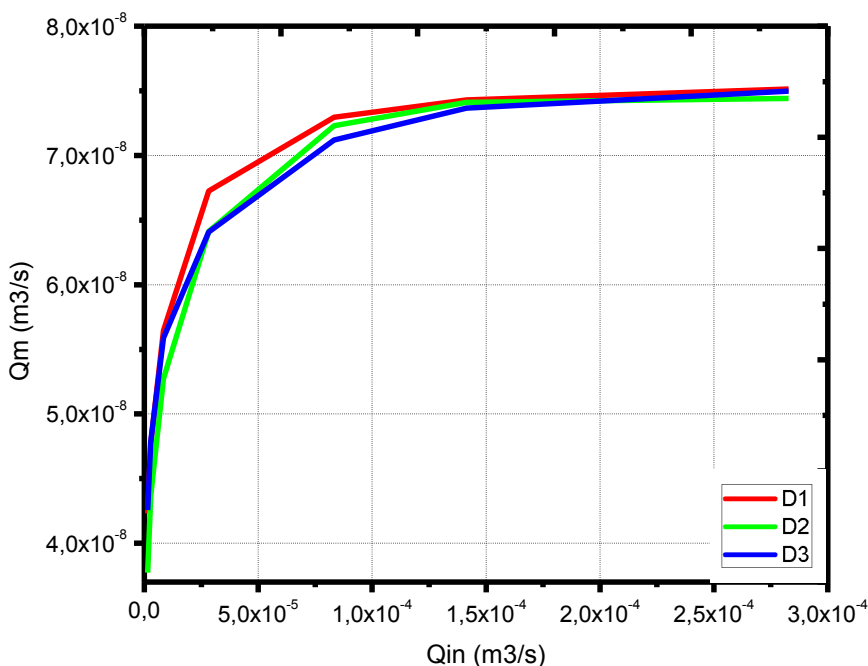


Fig. 7.47 Q_{in} – Q_m plots for the three designs

7.11.4.1 Discussion of the results

- The maximum Q_m for the 3 designs is approximately the same ($\approx 7.5 \cdot 10^{-8} \text{ m}^3/\text{s}$) and the Q_{in} in which they reach it is also the same ($\approx 2.8 \cdot 10^{-4} \text{ m}^3/\text{s}$).
- It is evident that for lower Q_{ins} the first design is performing better than the other 2.
- The 3rd design is performing better than the second for small Q_{ins} (till approximately $2.5 \cdot 10^{-5} \text{ m}^3/\text{s}$), while the second performs better for greater Q_{ins} .

7.12 Volumetric flow rate through the membrane calculated for each different grid density

For the **boundary conditions** used in case 9 ($Q_{in}=0.5 \text{ L/min}$, $P_{out}=15.8$

bar, $A=1.87 \cdot 10^{-12} \left(\frac{\text{m}}{\text{s} \cdot \text{Pa}} \right)$) the volumetric flow rate from the membrane surface

has been calculated for each different grid density, as shown in fig. 48.

Grid	Coarse (700K)	Dense (1.5M)	Hyper (3M)
$Q_m \text{ (m}^3/\text{s)}$	6.36E-05	5.64E-05	5.36E-05

Fig. 7.48 Q_m for each different grid

7.12.1 Discussion of the results

- As the grid is being denser the flow through the membrane is decreasing. This can be an additional reason for the increased CFD results in comparison with the experimental and model (see chapter parametric diagrams i and ii).
- The difference in Q_m between dense and hyper dense grid is small (5.2%), as was expected from the grid sensitivity study, but not negligible, while between dense and coarse grid is much greater (12.7%).

As it is shown in the fig. 7.48 the grid density has a great effect on the calculated volumetric flow rate through the membrane, which plays a key role in the PRO process, and therefore a careful selection of the mesh is necessary.

This dependence of the flow through the membrane from the mesh might be attributed to the fact that the volumetric flow rate in the main channel is 120 times greater than the volumetric flow rate through the membrane.

7.13 Volumetric flow rate through the membrane calculated for each different spatial discretization method of the momentum equation in FLUENT 12

Using different methods in FLUENT 12 for discretizing the momentum equation gives different results for the volumetric flow through the membrane (Q_m), as shown in the table below (boundary conditions same as in case 9):

Discretization method	First Order Upwind	Second Order Upwind	Third Order msc1	Quick	Power Law
Q_m (m ³ /s)	5.6E-05	5.64E-05	5.63E-05	5.63E-05	5.61E-05

Fig. 7.49 Values of Q_m for different discretization methods

7.13.1 Discussion of the results

The differences in Q_m using different discretization methods are negligible (in the order of 0.1%), with the highest being equal to 0.71% between the First Order Upwind and the Power Law.

CHAPTER 8.

CONCLUSIONS & FUTURE WORK

8.1 Summary of the final results

In this Diploma Thesis, the performance of PRO in a HTI test cell has been investigated. For this purpose a CFD model has been applied using ANSYS FLUENT 12.

The initial part of this work includes the study of the mesh dependency of the given geometry. Three different grids have been tested in the high pressure side of the test cell, where as a first step is considered to contain fresh water (instead of mixture of salt water and fresh water) and the membrane is considered to be wall: coarse 700K cells, dense 1.5M cells and hyper dense 3M cells. The differences in the flow field between the dense and hyper dense meshes have been negligible while the coarse mesh differs a lot. Therefore, the dense mesh (1.5M cells) has been chosen for the further simulations, which combines accurate results with the minimum number of cells.

The second step of the investigation simulates the membrane with a boundary condition of a uniform volumetric flow rate as an inlet which is

calculated from the general equation of osmosis $\frac{Q}{E} = A \cdot (\Delta\pi - \Delta P)$,

combined with the van't Hoff equation $\Delta\pi = 2\Delta CRT$. In this step the membrane is considered to have the characteristics of an HTI CTA FO membrane. The flow field and the parabolic velocity profiles have been presented and discussed, and also compared with that of the previous step.

For a better simulation of the membrane an algorithm has been created for the third part of the research. This algorithm applies the general equation of osmosis $U=A(\Delta\pi-\Delta P)$ (velocity of fresh water through the membrane) in each cell adjacent to the membrane area and is integrated in FLUENT as a boundary condition on the membrane through a UDF (User Defined Function). This approach needs the calculation of salt concentration in the flow field and therefore the species transport model of FLUENT has been enabled and the working fluid is considered a mixture of salt water and fresh water (salt water mainly with a small portion of fresh water which comes from the membrane).

With the given conditions, five different combinations of volumetric flow rate on the inlet and hydraulic pressure on the outlet have been tested: this included the minimum flow rate, one used in a published experiment and one for a proposed experiment. The hydraulic pressure included the optimum and the minimum ones. The results contain flow fields and salt concentration profiles, which have been discussed and compared. Also, the volumetric flow rate through the membrane has been calculated for each case and therefore the generated power, which have been also discussed and compared.

For the parametric analysis of the PRO concept in a test cell, it has been run a consecutive number of simulations using the same approach with different boundary conditions on the inlet and outlet. In each run the volumetric flow rate through the membrane has been calculated and therefore the velocity through the membrane and the generated power, when needed. This led to four parametric diagrams:

- i) Velocity through the membrane (J_w) as function of hydraulic pressure difference (ΔP) between fresh and salt water
- ii) Power generated per unit of membrane area (W) as function of hydraulic pressure difference (ΔP)
- iii) Volumetric flow rate through the membrane (Q_m) as function of the volumetric flow rate on the inlet (Q_{in})
- iv) Volumetric flow rate through the membrane (Q_m) as function of the salt concentration difference (ΔC) between the two membrane sides

The results have been discussed and conclusions about the PRO process have been made about: the reliability of the CFD model for the PRO process (comparison of the results with published experiments), the effect of volumetric flow rate on the inlet upon the flow through the membrane and consequently on the generated power, its significance and the need for optimization, and also the validation of the fact that the volumetric flow through the membrane is proportionate to the salt concentration difference between the two membrane sides, which therefore has a great effect upon the first. The conclusions are presented in more detail in the Chapter 8.

The next step of the research investigates the performance of a different membrane (Oasys Water) using the same approach and conditions. The volumetric flow from the membrane surface has been calculated along with the generated power. The results have been discussed and compared with the HTI membrane. In this step the importance of the membrane in the PRO concept is highlighted (more details in Chapter 8).

As a final part of this work two new designs of the test cell have been tested for their performance in PRO, which have been created based on the original one (HTI) with some modifications:

- The main and periphery channel are the same as the original one, while the inlet and outlet have been modified.
- The area and volume of the inlet and outlet have been kept the same as the original design in order to retain the same flow volume and boundary conditions.

The flow fields of the two designs have been presented and discussed, in comparison with the original one. Also, the volumetric flow from the membrane surface has been calculated for different values of the hydraulic pressure on the outlet, and a diagram has been created based on these results, which compares the three designs. Some conclusions about the importance of design have been deduced (see Chapter 8).

Finally, some configurations concerning the solution method in FLUENT have been changed in order to investigate their effect on the process: five different spatial discretization methods have been used for the momentum equation and the three different grid densities, while the volumetric flow rate through the membrane has been calculated in each case. The results have been discussed and have led to conclusions about the grid sensitivity and the effect of spatial discretization.

8.2 Conclusions & Future Work

This Diploma Thesis investigates the PRO process in a test cell using a CFD model in FLUENT, which provides a 3-dimensional approach instead of the one-dimensional, which is used so far and contains empirical equations (see Chapter 3). This means that with the use of CFD a flow field is generated, which contains the pressure, velocity and salt concentration in the whole volume of the test cell, instead of calculating only the salt concentration near the membrane area and the flow through the membrane. Not only does this provide more precision in the results, but also enables an in-depth investigation of the process, which can improve the design of the geometry. This of course requires a greater computational cost.

8.2.1 Accuracy of the CFD model using FLUENT 12 and future improvements

The first conclusions made in this project are concerning the accuracy of the CFD model. The following charts, which were also presented in Chapter 7, compare our CFD results, with the

experimental and model results from the publication [3] of Andrea Achilli , Tzahi Y. Cath, Amy E. Childress, entitled:

Power generation with pressure retarded osmosis: An experimental and theoretical investigation

The first figure (fig. 8.1) presents the velocity through the membrane (J_w) as function of the hydraulic pressure difference (DP) between the two membrane sides, while the second (fig. 8.2) shows the power density (W) as function of DP.

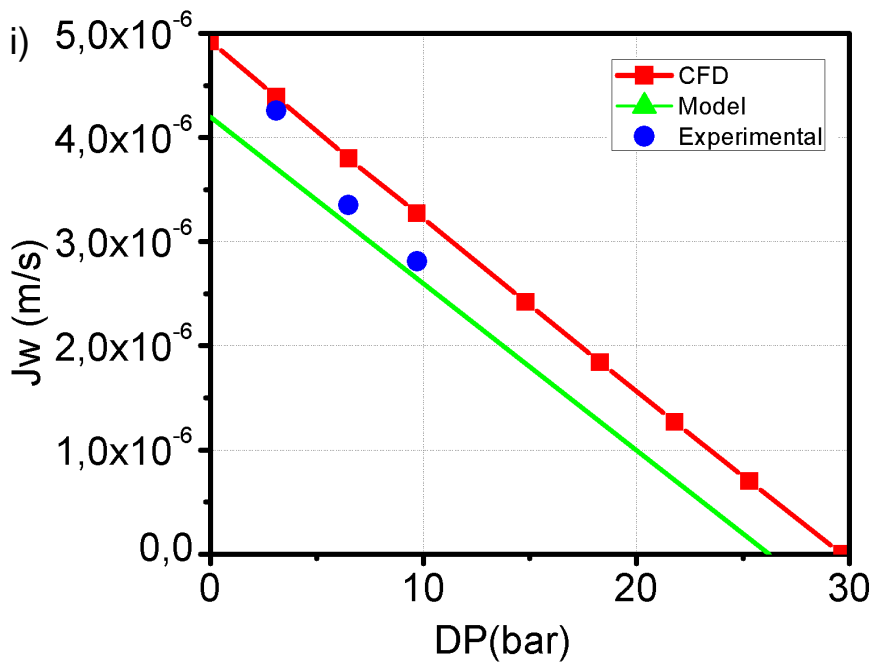


Fig. 8.1 Velocity through the membrane (J_w) as function of hydraulic pressure difference (DP)

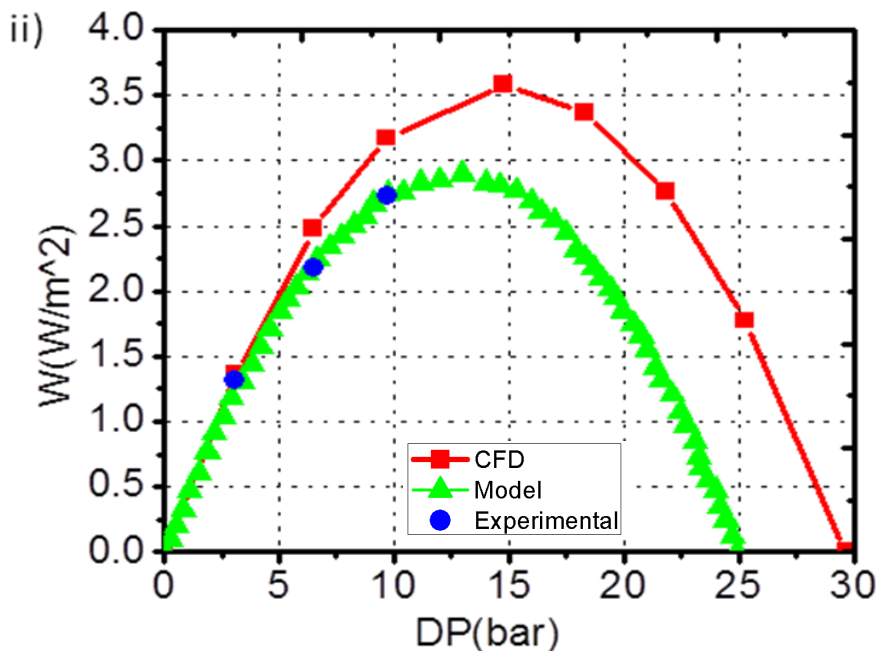


Fig. 8.2 Power density (W) as function of hydraulic pressure difference (DP)

Both diagrams show that CFD have captured the general trend of the experimental and model results (straight line in the first chart and parabolic in the second), but the values of the variables on the y-axis for CFD are increased compared to them. This combined with the chart for volumetric flow rate through the membrane as function of salt concentration difference between the two membrane sides (fig. 8.3), which shows that the flow through the membrane is proportionate to the salt concentration difference as it was expected, prove that the generated model in CFD has the potential to provide a very accurate prediction of the PRO process.

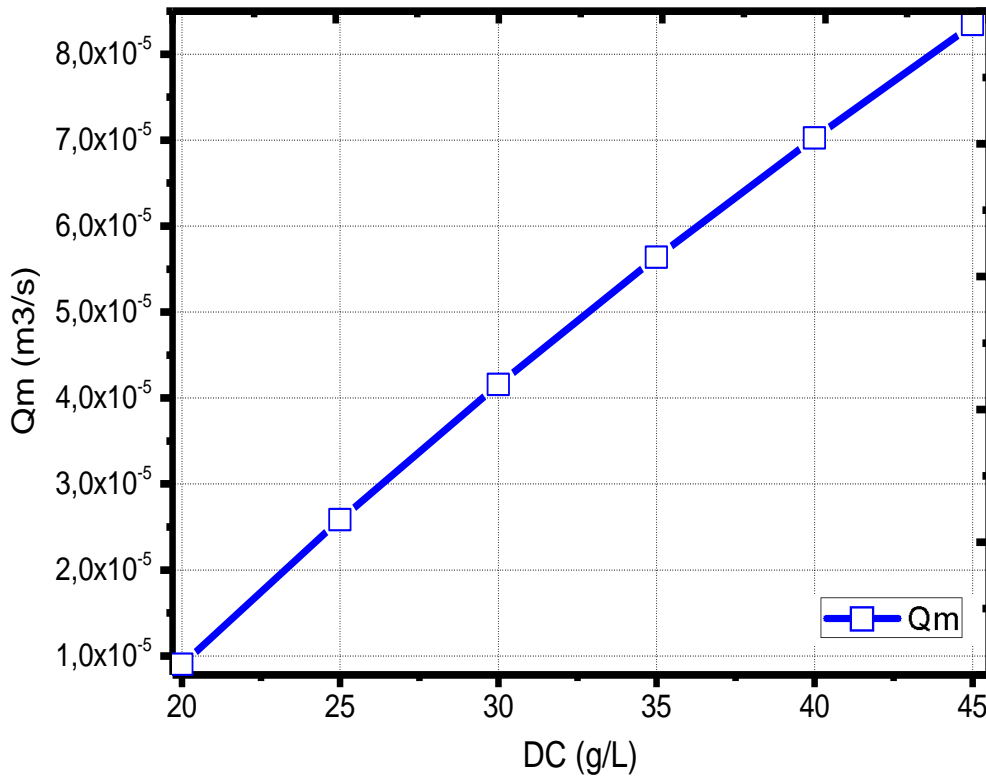


Fig. 8.3 Volumetric flow through the membrane (Q_m) as function of salt concentration difference (DC)

However, in order to achieve this, some improvements must be made to the CFD model first, which will minimize the increase of the results:

This CFD model takes into consideration only the effect of external concentration polarization (i.e. the dilution of salt water from the fresh water), but in the PRO process two other phenomena also take place, which reduce the flow through the membrane: the movement of salt from the salt water to the fresh water and the internal concentration polarization (i.e. salt being trapped inside the membrane) (see section 3.4.3).

There are three ways to integrate these phenomena to the CFD model:

i) The first idea is to integrate in the algorithm for the boundary condition on the membrane surface (UDF) two more equations: the equation for salt transport $J_s = B \cdot \Delta C_{NaCl}$ (8.1), where B is

salt permeability coefficient, along with the equation of the existing one-dimensional model for the velocity through the membrane corrected to include the effect internal concentration polarization (chapter 3)

$$J_w = A \cdot \left[\pi_4 \cdot \frac{1 - \frac{C_2}{C_4} \cdot \exp(J_w \cdot K)}{1 + \frac{B}{J_w} \cdot [\exp(J_w \cdot K) - 1]} - \Delta P \right] \quad (8.2)$$

where $C_2 = C_{\text{fresh water}}$, $C_4 = C_{\text{salt water}}$ and K is a constant of the membrane, which will be solved numerically.

ii) A second more complicated solution is to solve using FLUENT 12 not only the salt water side but also the fresh water side and the inside of the membrane, which will use the equation (8.1) for transport of salt through the membrane and simultaneously the general equation of osmosis $J_w = A(\Delta\pi - \Delta P)$ (8.3) for the transport of fresh water through the membrane. This approach requires information about the morphology of the membrane and therefore is very difficult to achieve.

iii) The third solution is a combination of the first two and will use the equation (8.2) for the flow through the membrane and the equation (8.1) for the salt transport through the membrane, while solving the fresh water side to obtain C_2 and C_4 .

Another reason why the results are increased in CFD compared to the experimental and model might be the grid density. As shown in the table below (fig. 8.4), as the number of cells in the grid is increasing the flow through the membrane is decreasing.

Grid	Coarse (700K)	Dense (1.5M)	Hyper (3M)
Qm (m ³ /s)	6.36E-05	5.64E-05	5.36E-05

Fig. 8.4 Volumetric flow rate through the membrane (Qm) for each different grid

Therefore, a larger variety of grids (some between 1.5 and 3 million cells and some greater than 3 million) must be tested (calculation of the flow through the membrane) using different boundary conditions mainly on the inlet (volumetric flow rate) and secondary on the outlet (pressure outlet), in order to find the appropriate one.

On the other hand the table below (fig. 8.5) shows that the spatial discretization method used in FLUENT 12 does not affect the results in a significant level.

Discretization method	First Order Upwind	Second Order Upwind	Third Order msc1	Quick	Power Law
Qm (m ³ /s)	5.6E-05	5.64E-05	5.63E-05	5.63E-05	5.61E-05

Fig. 8.5 Values of Qm for different discretization methods

But in order to conclude that the CFD PRO model is independent from the solution method used in FLUENT 12, more solution settings (see section 6.3.2) must be altered and compared for their results.

Moreover, a significant reason for the increase of the results in CFD is that in the published results (model) the osmotic pressure between the two membrane sides is 27.63 bar while for the same conditions on the CFD is 29.66 bar, which means that a different equation than the van't hoff ($\Delta\pi=2\Delta C_{\text{nacl}}RT$ (8.4)) for the osmotic pressure is used.

Finally, for the improvement of the CFD model the general equation of osmosis (8.4), which is used in the UDF (see section 7.3.1.1), can use the topic hydraulic pressure difference (i.e. between the above and the below cell of the membrane) instead of the rated for each side. But that will improve slightly the results, as the pressure values in the flow field differ slightly, while having a huge computational cost, as it requires the solution of the fresh water side.

8.2.2 Relation between the flow from the inlet and the flow through the membrane - the need for optimization

The following chart shows the volumetric flow rate through the membrane as function of the volumetric flow from the inlet (fig. 8.6):

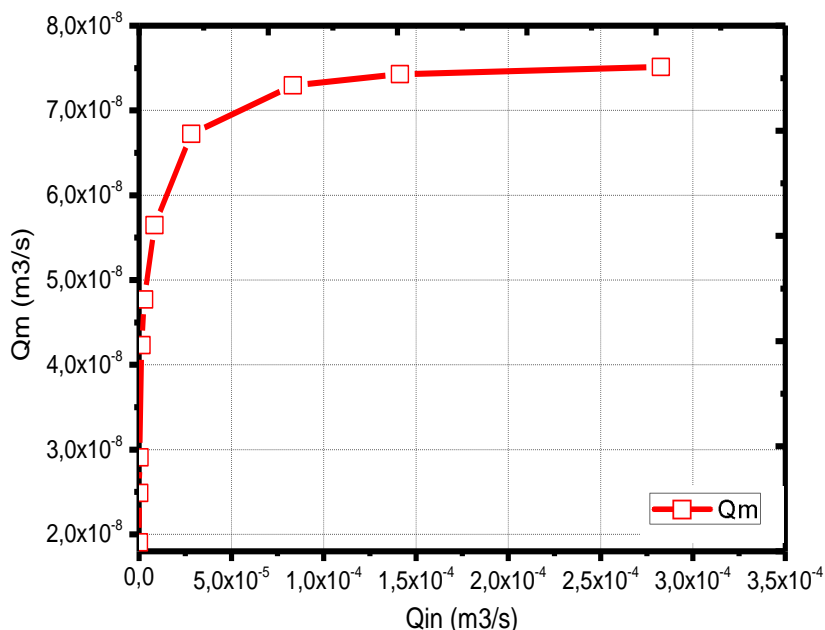


Fig. 8.6 Volumetric flow through the membrane (**Qm**) as function of volumetric flow from the inlet (**Qin**)

It is evidently that as the flow from the inlet is increasing the flow through the membrane is also increasing, rapidly in the beginning and almost negligibly in the end. And as the produced power (and therefore the profit from PRO process) is proportionate to the flow through the membrane, an optimization for the flow from the inlet must be done taking into account the power needed to provide the inlet flow, and its cost. This can be done in each PRO case separately or if possible to create a general relation between the flow through the membrane (as a portion of the maximum) and the optimum flow from the inlet.

8.2.3 Modification of the design and further investigation for its improvement

Two new designs of the test cell have been tested in this project with the main objective to increase the flow through the membrane given the inlet flow (by removing the incoming fresh water faster and reducing the effect of external concentration polarization). The designs are based on the original one and the area and volume of the inlet and outlet have been kept the same in order to retain the same flow volume.

The results are presented in the following chart (fig. 8.7):

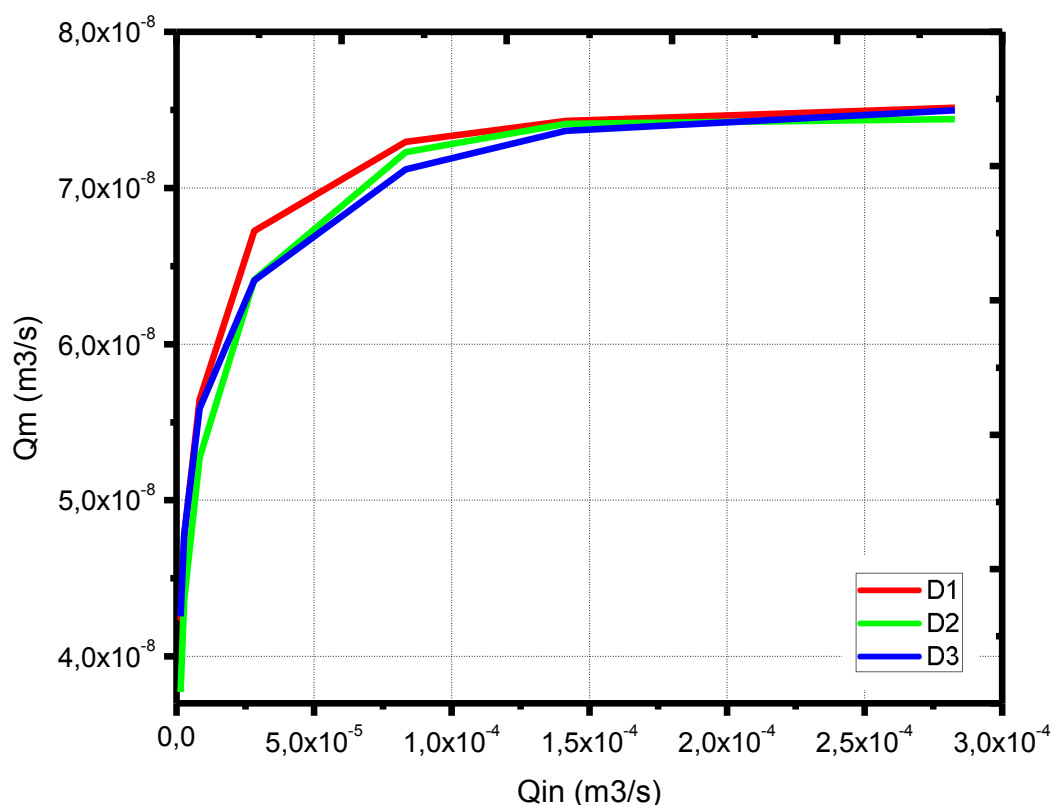


Fig. 8.7 Qin-Qm plots for the three designs

The chart shows that the differences in Qm for different values of Qin for the three designs are negligible. This means that the changes made in the original design (the shape and position of the inlet and outlet) had a little effect on the flow through the membrane.

Therefore, a further investigation is needed in order to improve the design of the test cell. This, given the original design, can be achieved by changing the area and volume of the inlet and

outlet, modifying the dimensions, shape and position of the main and periphery channel, or that of the flow guidelines, and by altering the shape and dimensions of the effective membrane area. Finally, completely new designs can be tested (cylindrical for example) (see chapter 3 for membrane modules).

8.2.4 Effect of the performance of the membrane and the salt concentration difference in the PRO process

By testing the performance of a new membrane (Oasys Water) in the PRO process, it has been deduced the conclusion that the membrane plays the most important role in the process, as it was mentioned in many publications [4], [6].

For the same conditions on the inlet, outlet and salt concentration the Oasys Water membrane gives 47.2% greater volumetric flow rate through the membrane than the HTI membrane, and thus 47.2% increased power density. This is attributed to the increased water permeability coefficient (A) of the new membrane.

If we have taken into consideration the effect of internal concentration polarization (i.e. salt trapped inside the membrane) and the movement of salt into the fresh water, the new membrane would have given a greater increase on the flow through the membrane, as it's morphology is more suitable for the PRO process and also it rejects better the transport of salt (lower salt permeability coefficient B).

The final conclusion made in this work is concerning the dependence of the flow through the membrane from the salt concentration difference: as shown in figure 3 the Q_m is proportionate to ΔC (as it was expected), and therefore the salt concentration difference between the two membrane sides plays also an important role in the PRO process.

8.2.5 Overview

The present work introduces a CFD model to study the PRO process in a test cell, examines its accuracy by comparing these results with those of an experiment and of an existing model, and makes suggestions for improvements in order to provide more precision. The role, also, of the grid and of the solution method have been addressed. Moreover, the effects of basic variables (inlet volumetric flow, salt concentration difference, water permeability of the membrane) in the PRO process have been investigated and conclusions were made about their role in PRO. Finally, by testing two new designs, conclusions have arisen about how certain modifications in the design affect the process and also suggestions for further investigation of the design have been made.

REFERENCES

Chapter 1

- [1] Wiesz, P.B. (2004). Basic Choices and Constraints on Long-Term Energy Supplies. *Physics today*. pp:47-57
- [2] Bahgat, G. (2006). Europe's energy security: challenges and opportunities. *International Affairs*. Nr. 82:PP961
- [3] Meadows, D.H., Meadows, D.L., Randers, J. And Behrens III, W.W. (1972). *The Limits to Growth. A Report to The Club of Rome*. New York: University Books.
- [4] WCED (1987). *Our Common Future*. World Commission on Environment & Development, Oxford: Oxford University Press.
- [5] Dryzek, J.S. (2005). *The politics of the Earth. Environmental Discourses* (2nd ed.) Oxford: Oxford University Press.
- [6] European Commission (1997). *Energy for the future: renewable sources of energy*. White paper for a Communication Strategy and Action plan. COM (97) 599 final (26/11/1997).
- [9]http://europa.eu/legislation_summaries/energy/european_energy_policy/l27062_en.htm
- [8] Jacobsson, S and Johnson, A. (2000). The diffusion of renewable energy technology: an analytical framework and key issues for research. *Energy Policy*, 28(9), 625-640.

Chapter 2

- [1] U.S. DEPARTMENT OF ENERGY, Energy Efficiency & Renewable Energy <http://www.eere.energy.gov>
- [2] *Science Applications International Corporation / PIX 13464*
- [3] REN21, http://www.ren21.net/pdf/RE_GSR_2009_Update.pdf
- [4] REN21 2011, "[Renewables 2011: Global Status Report](#)"
- [5] World Energy Statistics/ Energy Supply & Demands/ Energynet <http://www.enerdata.net>

Chapter 3 & 4

- [1] Øystein Skråmestø, Sandvik & Stein Erik Skilhagen, Status of technologies for harnessing Salinity Power and the current Osmotic Power activities, Article to the **2008** Annual report of the IEA-OES.
- [2] Tzahi Y. Cath, Amy E. Childress, Menachem Elimelech, Forward osmosis: Principles, applications, and recent development, *Journal of Membrane Science* 281 (**2006**) 70–87.
- [3] Andrea Achilli, Tzahi Y. Cath, Amy E. Childress, Power generation with pressure retarded osmosis: An experimental and theoretical investigation, *Journal of Membrane Science* 343 (**2009**) 42–52.
- [4] The Energy Information Administration, <http://www.eia.doe.gov/>
- [5] Øystein S. Skråmestø, Stein Erik Skilhagen, Werner Kofod Nielsen, Power Production based on Osmotic Pressure, Article Waterpower XVI.
- [6] Thor Thorsen, Torleif Holt, The potential for power production from salinity gradients by pressure retarded osmosis, *Journal of Membrane Science* 335 (**2009**) 103–110.
- [7] <http://en.wikipedia.org/wiki/Osmosis>
- [8] Karen Gerstandt, K.V. Peinemann, Stein Erik Skilhagen, Thor Thorsen, Torleif Holt, Membrane processes in energy supply for an osmotic power plant, *Desalination* 224 (**2008**) 64–70.

- [9] Øystein Skråmestø Sandvik, Peter Hersleth, Karin Seelos, Hydro **2009**, Unleashing renewable energies from the ocean: Statkraft's experience in developing business opportunities in immature technologies and markets, The forces of osmosis and tidal currents.
- [10] www.thegreentechnologyblog.com
- [11] www.miketechnology.wordpress.com
- [12] Statkraft Energi AS, ICTPOL, SINTEF Teknologi og samfunn, Helsinki University of Technology, GKSS Forschungszentrum, The salinity power project: Power production from the osmotic pressure difference between fresh water and sea water.
- [13] Andrea Achilli, Amy E. Childress, Pressure retarded osmosis: From the vision of Sidney Loeb to the first prototype installation — Review, Desalination 261 (2010) 205-211.
- [14] http://www.powermag.com/issues/departments/global_monitor/Norway-Inaugurates-Osmotic-Power-Plant_2425.html
- [15] Stein Erik Skilhagen, Osmotic power, A new renewable energy source, Statkraft **2010**.
- [16] <http://www.globalpost.com/sites/default/files/Norway-Osmotic-Power-Statkraft.jpg>
- [17] <http://www.statkraft.com/energy-sources/osmotic-power/osmotic-power-in-brief/>
- [18] Statkraft, Osmotic Power **2010**.
- [19] Mark C. Porter, Handbook of industrial membrane technology.
- [20] K.L. Lee, R.W. Baker, H.K. Lonsdale, Membranes for power generation by pressure-retarded osmosis, Journal of Membrane Science 8 (1981) 141-171.
- [21] Eric M.V. Hoek, Jeff Allred, Tom Knoell, Byeong-Heon Jeong, Modeling the effects of fouling on full-scale reverse osmosis processes, Journal of Membrane Science 314 (2008) 33–49.
- [22] United States environmental protection agency, Office of research and development Washington DC, Technology transfer, Capsule report, Reverse osmosis process.
- [23] Lau Kok Keong, (Ph.D Thesis **2009**) Feed spacer of spiral wound membrane module for nanofiltration and reverse osmosis: modeling, simulation and design.
- [24] Product information, FILMTEC Membranes, Why FILMTEC Thin-Film Composite RO Membranes Outperform Cellulose Acetate Membranes in Water Purification Service.
- [25] T.Y. Cath, S. Gormly, E.G. Beaudry, M.T. Flynn, V.D. Adams, A.E. Childress, Membrane contactor processes for wastewater reclamation in space. I. Direct osmotic concentration as pretreatment for reverse osmosis, Journal of Membrane Science 257 (2005) 85–98.
- [26] A. Achilli, T. Cath, E. Marchand, A. Childress, Osmotic Membrane Bioreactor and PRO MBR for Wastewater treatment and Water Desalination, in International Congress on Membranes and Membrane Processes (ICOM 2008), July 12-18, **2008**, Honolulu, Hawaii USA.
- [27] Yuan Xu, Xiaoyu Peng, Chuyang Y. Tang, Q. Shiang Fu, Shengzhe Nie, Effect of draw solution concentration and operating conditions on forward osmosis and pressure retarded osmosis performance in a spiral wound module, Journal of Membrane Science, 348 (2010) 298–309.
- [28] Jincai Su, Sui Zhang, Hangzheng Chen, Hongmin Chen, Y.C. Jean, Tai-Shung Chung, Effects of annealing on the microstructure and performance of cellulose acetate membranes for pressure-retarded osmosis processes, Journal of Membrane Science, 364 (2010) 344-353.
- [29] Jincai Su, Qian Yang, Joo Fuat Teo, Tai-Shung Chung, Cellulose acetate nanofiltration hollow fiber membranes for forward osmosis processes, Journal of Membrane Science, 355 (2010) 36–44.

Chapter 5

[1] Jon P. Longtin and Ching-Hua Fan, Precision laser-based concentration and refractive index measurement of liquids, *Microscale Thermophysical Engineering*, 2:261 ± 272, **1998**.

[2] <http://www.vernier.com/probes/sal-bta.html>,
http://www.coleparmer.co.uk/catalog/product_view.asp?sku=0575300&pfx=,
http://store.rmsupply.co.uk/index.php?main_page=product_info&products_id=82,
<http://www.omega.co.uk/ppt/pptsc.asp?ref=CDH45>.

Chapter 6

[30] FLUENT 12 Theory Guide, Solver Theory

[31] A. J. Chorin, Numerical solution of navier-stokes equations, *Mathematics of Computation*, 22:745-762, **1968**.

[32] S. V. Patankar, Numerical Heat Transfer and Fluid Flow, *Hemisphere*, Washington, DC, **1980**.

[33] T. J. Barth and D. Jespersen, The design and application of upwind schemes on unstructured meshes, Technical Report AIAA-89-0366, AIAA 27th Aerospace Sciences Meeting, Reno, Nevada, **1989**.

[34] B. P. Leonard and S. Mokhtari, ULTRA-SHARP Nonoscillatory Convection Schemes for High-Speed Steady Multidimensional Flow, NASA TM 1-2568 (ICOMP-90-12), NASA Lewis Research Center, **1990**.

[35] B. Van Leer, Toward the Ultimate Conservative Difference Scheme. IV, A Second Order Sequel to Godunov's Method, *Journal of Computational Physics*, 32:101-136, **1979**.

[36] S. Kim, D. Caraeni, and B. Makarov, A Multidimensional Linear Reconstruction Scheme for Arbitrary Unstructured Grids, Technical report, American Institute of Aeronautics and Astronautics, AIAA 16th Computational Fluid Dynamics Conference, Orlando, Florida, June **2003**.

[37] Z. J. Wang, A Fast Nested Multi-grid Viscous Flow Solver for Adaptive Cartesian/Quad Grids, *International Journal for Numerical Methods in Fluids*, 33:657-680, **2000**.

[38] V. Venkatakrishnan, On The Accuracy of Limiters and Convergence to Steady State Solutions, Technical Report AIAA-93-0880, American Institute of Aeronautics and Astronautics, January **1993**.

[39] C. M. Rhie and W. L. Chow, Numerical Study of the Turbulent Flow Past an Airfoil with Trailing Edge Separation, *AIAA Journal*, 21(11):1525-1532, November **1983**.

[40] S. V. Patankar, Numerical Heat Transfer and Fluid Flow, Hemisphere, Washington, DC, **1980**.

[41] C. M. Rhie and W. L. Chow, Numerical Study of the Turbulent Flow Past an Airfoil with Trailing Edge Separation, *AIAA Journal*, 21(11):1525-1532, November 1983.

[41] K. C. Karki and S. V. Patankar, Pressure-Based Calculation Procedure for Viscous Flows at All Speeds in Arbitrary Configurations, *AIAA Journal*, 27: 1167-1174, **1989**.

[42] http://en.wikipedia.org/wiki/Multigrid_method

[43] B. R. Hutchinson and G. D. Raithby, A Multigrid Method Based on the Additive Correction Strategy, Numerical Heat Transfer, 9:511-537, **1986**

Chapter 7

[1] N. Gay Yin Yip, Alberto Tiraferri, William A. Philip, Jessica D. Schiffman, and Menachem Elimelech, High Performance Thin-Film Composite Forward Osmosis Membrane, Environ. Sci. Technol., 44, 3812–3818, **2010**

[2] Water Desalination Report, Volume 46, Number 45, 22 November **2010** [3] V. V. Kisel'nik, N. G. Malyuk, A. N. Toryanik, and V. M. Toryanik, Effect of pressure and temperature on self diffusion of water, Translated from Zhurnal Strukturnoi Khimii, Vol. 14, No. 6, pp. 963-967, **1973**

[4] Andrea Achilli, Tzahi Y. Cath, Amy E. Childress, Power generation with pressure retarded osmosis: An experimental and theoretical investigation, Journal of Membrane Science 343 (**2009**) 42–52.

[5] <http://en.wikipedia.org/wiki/Seawater>

[6] Thor Thorsen, Torleif Holt, The potential for power production from salinity gradients by pressure retarded osmosis, Journal of Membrane Science 335 (**2009**) 103–110.

ABSTRACT

The energy released from the mixing of freshwater with saltwater is a source of renewable energy that can be harvested using pressure retarded osmosis (PRO). In PRO, water from a low salinity solution permeates through a membrane into a pressurized, high salinity solution; power is obtained by depressurizing the permeate through a hydro turbine. The combination of increased interest in renewable and sustainable sources of power production and recent progress in membrane science has led to a high increase in PRO interest in the last decade. This interest led in the first prototype installation of PRO which opened in Norway in late 2009. Although many researchers have studied the power production through PRO there is still lack of theoretical and experimental investigations to ensure the success of PRO.

The present work introduces a Computational Fluid Dynamics (CFD) model to study the PRO process in a test cell, examines its accuracy by comparing these results with those experimental and of an existing model, and makes suggestions for improvements in order to provide more precision. The role, also, of the grid and of the solution method have been addressed. Moreover, the effects of basic variables (inlet volumetric flow, salt concentration difference, water permeability of the membrane) in the PRO process have been investigated and conclusions were made about their role in PRO. Finally, by testing two new designs, conclusions have arisen about how certain modifications in the design affect the process and also suggestions for further investigation of the design have been made.

Appendix

Algorithm (UDF) for the calculation of the velocity through the membrane

```
DEFINE_PROFIL (inlet_y_velocity_mix, thread, position)
{
    real xbound[ND_ND];
    real xin[ND_ND];
    real area[ND_ND];

    face_t f;
    cell_t c;
    FILE *fp;
    int i1;

    real
    areatot,salinity,rgas,mbsalt,dp,temp,effarea,perm,flowrate,vel,dpi,dcondconcinlet,dconna
    cl;

    i1=0;

    salinity=35; /* g/L */
    rgas=8.314;
    mbsalt=0.0585;
    effarea=0.0233;
    perm=1.87E-12;
    temp=298.15;
    dp=14.8E+5;

    //fp=fopen("eras1.dat","w");

    begin_f_loop(f,thread)
    {
        F_CENTROID(xbound, f, thread);
        F_AREA(area, f, thread);
        areatot=pow((pow(area[0],2)+pow(area[1],2)+pow(area[2],2)),0.5);

        c=F_C0(f,thread);

        C_CENTROID(xin, c, THREAD_T0(thread));

        dconc=(1.0-C_YI(c,THREAD_T0(thread),0)); /* concentration of fresh
        water in adjacent cell */
    }
```

```

dconcinlet=1.; /* concentration of fresh water in inlet of membrane */

dconnac1=(1.0-dconc)*salinity; /* that is the NaCl concentration difference
between membrane inlet and adjacent inside cell */

// dconc=(1.-C_YI(c,THREAD_T0(thread),0)); /* concentration of salt water in
adjacent cell */

// dconcinlet=1.; /* concentration of salt water in inlet of membrane */

dpi=2.*dconnac1*(rgas/mbsalt)*temp;
flowrate=perm*(dpi-dp);
vel=flowrate;

F_PROFILE(f, thread, position) = vel;

// fprintf(fp,"%12.8f %12.8f %12.8f",xbound[0],xbound[1],xbound[2]);
// fprintf(fp,"%12.8f %12.8f %12.8f",xin[0],xin[1],xin[2]);
// fprintf(fp,"%12.8f %12.8f %12.8f",area[0],area[1],area[2]);
// fprintf(fp,"%12.8e %12.8e %12.8e",dconc,flowrate,vel);
// fprintf(fp,"\n");

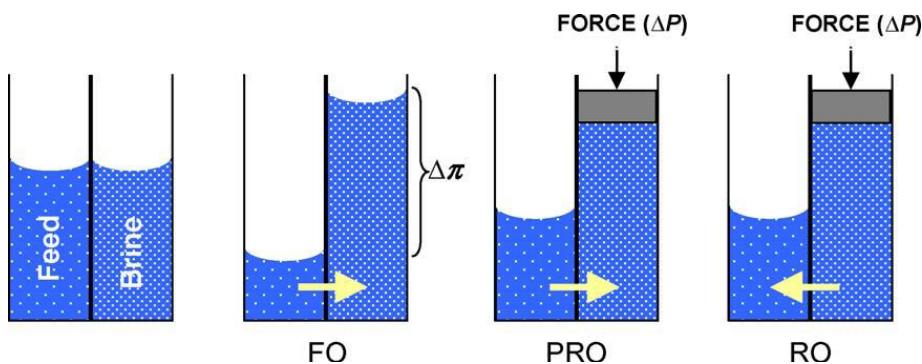
}
end_f_loop(f, thread)

//fclose(fp);
}

```

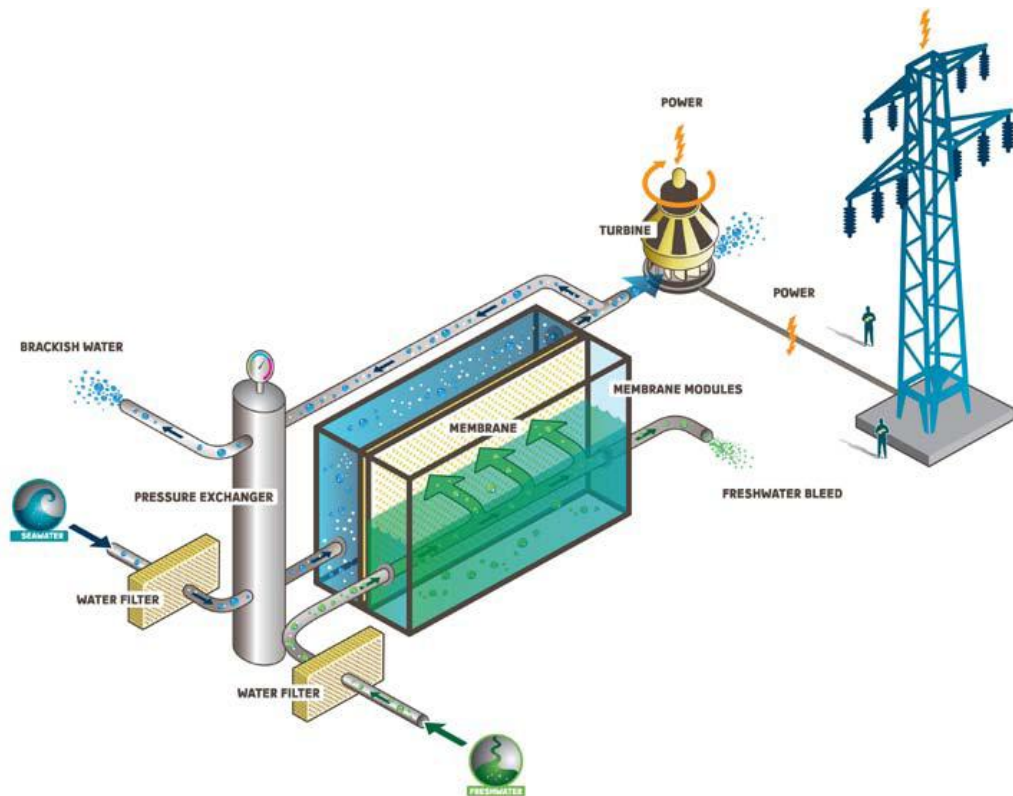
ΕΚΤΕΤΑΜΕΝΗ ΠΕΡΙΛΗΨΗ ΔΙΠΛΩΜΑΤΙΚΗΣ ΕΡΓΑΣΙΑΣ ΕΜΠ

Το αντικείμενο της παρούσας Διπλωματικής Εργασίας είναι η μελέτη της παραγωγής ενέργειας μέσω της αξιοποίησης της ωσμωτικής πίεσης (Pressure Retarded Osmosis - PRO). Η αξιοποίηση των ανανεώσιμων πηγών ενέργειας αποτελεί βασικό αντικείμενο της έρευνας που διεξάγεται σε παγκόσμιο επίπεδο. Ώσμωση είναι η ροή του νερού από ένα διάλυμα χαμηλής συγκέντρωσης άλατος (π.χ. γλυκό νερό) σε ένα διάλυμα υψηλής περιεκτικότητας σε αλάτι (π.χ. θαλασσία ύδατα) μέσω μιας επιλεκτικά διαπερατής μεμβράνης (διαπερατή για το νερό, μη διαπερατή από το αλάτι), και οδηγείται από τη διαφορά πίεσης, η οποία ονομάζεται ωσμωτική πίεση. Η ωσμωτική πίεση οφείλεται στη διαφορά συγκέντρωσης άλατος των διαλυμάτων που διαχωρίζονται από την μεμβράνη και ενεργοποιείται από τη δύναμη της φύσης για τη δημιουργία ισορροπίας μεταξύ των διαφόρων συγκεντρώσεων στα υγρά. Στο παρακάτω σχήμα φαίνεται η ροή στην ευθεία, αντίστροφη και καθυστερημένη ώσμωση:



Σχ. 1 Ροή στην ευθεία, αντίστροφη και καθυστερημένη ώσμωση

Όταν το γλυκό νερό ρέει μέσω της μεμβράνης προς το θαλασσινό, προκαλεί την αραίωσή του και την αύξηση του όγκου του και της αντίστοιχης παροχής του. Αν το θαλασσινό νερό βρίσκεται υπό πίεση μπορεί να παραχθεί ισχύς από την αποσυμπίεση κινώντας έναν υδροστρόβιλο του οποίου ο άξονας είναι συνδεδεμένος με μια γεννήτρια η οποία παράγει ηλεκτρικό ρεύμα, όπως φαίνεται στο παρακάτω σχήμα:



Σχ. 2 Απλοποιημένο εργοστάσιο παραγωγής ηλεκτρικής ενέργειας PRO

Το φαινόμενο διέπεται από τέσσερις βασικές εξισώσεις: μία για τη ροή του γλυκού νερού μέσα από τη μεμβράνη (J_w), μία για τη ροή του αλατιού από το αλμυρό στο γλυκό νερό (J_s) (οι μεμβράνες δεν είναι απόλυτα ημιπερατές), μία για την διαφορά ωσμωτικής πίεσης μεταξύ αλατόνευρου και γλυκού νερού ($\Delta\pi$) και μία για την παραγόμενη ισχύ ανά μονάδα επιφάνειας (W):

$$J_w = A \cdot (\Delta\pi - \Delta P) \quad (1)$$

$$-J_s = B \cdot \Delta C_{NaCl} \quad (2)$$

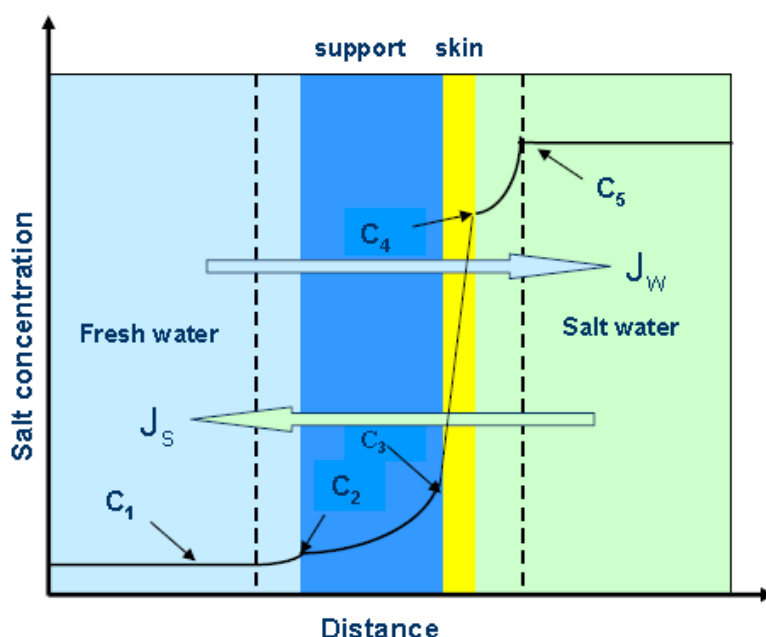
$$\Delta\pi_{osmotic} = 2 \cdot \Delta C_{NaCl} \cdot R \cdot T \quad (3)$$

$$W = J_w \cdot \Delta P = A \cdot (\Delta\pi - \Delta P) \cdot \Delta P \quad (4)$$

όπου A συντελεστής περατότητας της μεμβράνης, B ο συντελεστής απόρριψης του αλατιού από τη μεμβράνη, ΔP η διαφορά υδραυλικής πίεσης μεταξύ αλμυρού και γλυκού νερού, Δc η διαφορά συγκέντρωσης, T η θερμοκρασία των 2 ρευστών και R παγκόσμια σταθερά των αερίων για το αλατόνευρο.

Οι μεμβράνες που χρησιμοποιούνται στην ώσμωση αποτελούνται από 2 στρώματα: ένα για την απόρριψη του αλατιού, που ονομάζεται *skin*, και ένα υποστηρικτικό για να αντέχει τις υψηλές υδραυλικές πιέσεις, που ονομάζεται *support*. Η ροή του γλυκού νερού μέσα από αυτή επηρεάζεται αρνητικά από δύο σημαντικά φαινόμενα που ονομάζονται *external concentration polarization*: αραιώση του αλμυρού νερού από το γλυκό στην περιοχή κοντά στη μεμβράνη και

internal concentration polarization: εγκλωβισμός του αλατιού στο υποστηρικτικό στρώμα της μεμβράνης, όπως φαίνεται στο παρακάτω σχήμα:



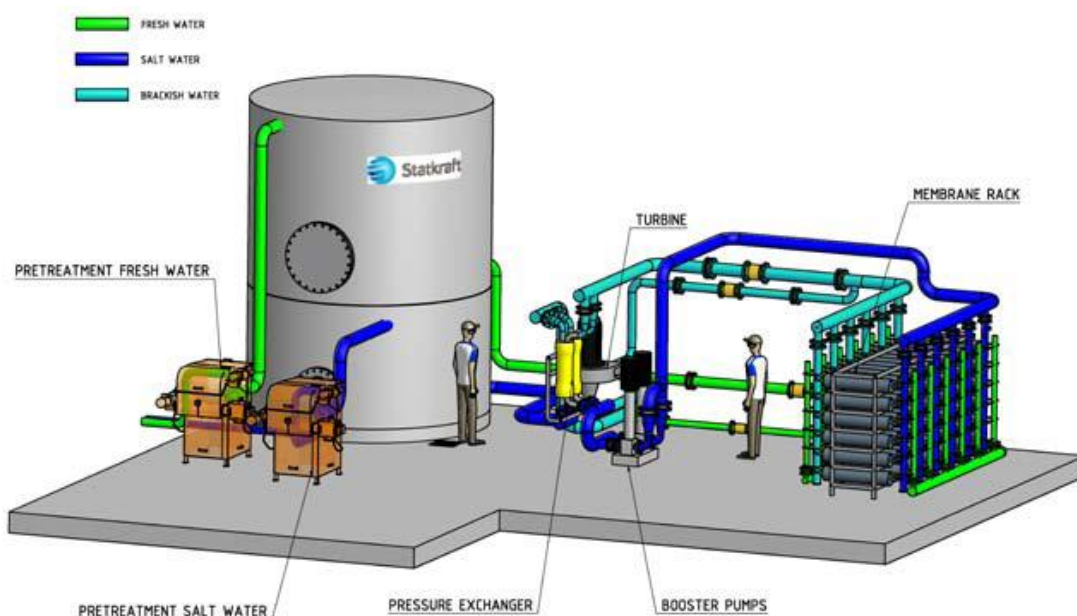
Σχ. 3 Στρώματα της μεμβράνης, ροή νερού και αλατιού, κατανομή της συγκέντρωσης

Υπό την προϋπόθεση ότι PRO τεχνολογία εφαρμόζεται στις εκβολές των ποταμών μπορεί να παράγει ανανεώσιμη, σταθερή ισχύ 24 ώρες την ημέρα, για όλο το χρόνο και επίσης μπορεί να παράγει ενέργεια σε περιοχές όπου άλλες ανανεώσιμες πηγές ενέργειας δεν είναι αρκετά αποτελεσματικές. Έχει εκτιμηθεί ότι μέσω του PRO είναι δυνατό να παραχθούν 1700 TWh ενέργειας το χρόνο παγκοσμίως, από τις οποίες οι 160 είναι στην Ευρώπη.

Η ιδέα του PRO προέκυψε στα μέσα της δεκαετίας του 1950, αλλά ελάχιστες έρευνες έχουν γίνει από τότε, κυρίως λόγω των ακατάλληλων μεμβρανών. Οι έρευνες έχουν επικεντρωθεί στην δοκιμή διαφορετικών μεμβρανών, λειτουργικών μονάδων (θαλάμου δοκιμής), αλλά και μοντέλων σχεδιασμένων για να περιγράψουν την PRO και να αξιολογήσουν ό, τι απαιτείται για να αυξηθεί η αποτελεσματικότητά της. Ο σχεδιασμός της μεμβράνης, της λειτουργικής μονάδας και επίσης οι συνθήκες ροής του γλυκού και θαλασσινού νερού παίζουν πολύ σημαντικό ρόλο.

Την ιδέα του PRO εφάρμοσαν Νορβηγοί επιστήμονες σε έναν πρωτότυπο ωσμωτικό σταθμό παραγωγής ηλεκτρικού ρεύματος (pilot plant) το 2009 στο Tofte της Νορβηγίας κοντά στο fjord του Oslo (σχ. 4). Ο σταθμός αυτός λειτουργεί για πειραματικούς λόγους και χρησιμοποιεί 2000 m² μεμβράνης, 66 αντλίες, εναλλάκτες πίεσης και μία τουρμπίνα, για την παραγωγή 10 kw. Ένα κανονικό εργοστάσιο παραγωγής ηλεκτρικής ενέργειας που θα παράγει 25 MW, δηλαδή θα μπορεί να παρέχει ενέργεια σε 30000 ευρωπαϊκά σπίτια, θα απαιτεί 2 εκατομμύρια m² μεμβράνης, 25 m²/δευτερόλεπτο γλυκό νερό και 50 m²/δευτερόλεπτο θαλασσινό σε πίεση περίπου 12 bar, πράγμα που σημαίνει ότι θα έχει το μέγεθος ενός γηπέδου ποδοσφαίρου. Οι υπολογισμοί αυτοί έγιναν με την προϋπόθεση ότι 1 m² μεμβράνης παράγει 5 W, σε αντίθεση με το υπάρχον εργοστάσιο που παράγει λιγότερο από 1 W/m². Οι υπάρχουσες μεμβράνες μπορούν να παράγουν 3.5 W/m², αλλά ο στόχος των 5 W/m² είναι εφικτός καθώς οι υπάρχουσες μεμβράνες είναι είτε για κανονική είτε για αντίστροφη ώσμωση, και έχουν μειωμένη

απόδοση. Αυτό οφείλεται στο ότι έχουν φτιαχτεί για να αντέχουν πίεση μεγαλύτερη των 25 bar, που στην τεχνολογία PRO αυτό δεν είναι απαραίτητο, και επίσης η ικανότητα τους να επιτρέπουν στο γλυκό νερό να περνάει με μεγαλύτερη ταχύτητα δεν παίζει τόσο σημαντικό ρόλο όσο στο PRO, όπου υπάρχουν αρκετά περιθώρια βελτίωσης ώστε να επιτευχθεί ο στόχος και ακόμα περισσότερο.

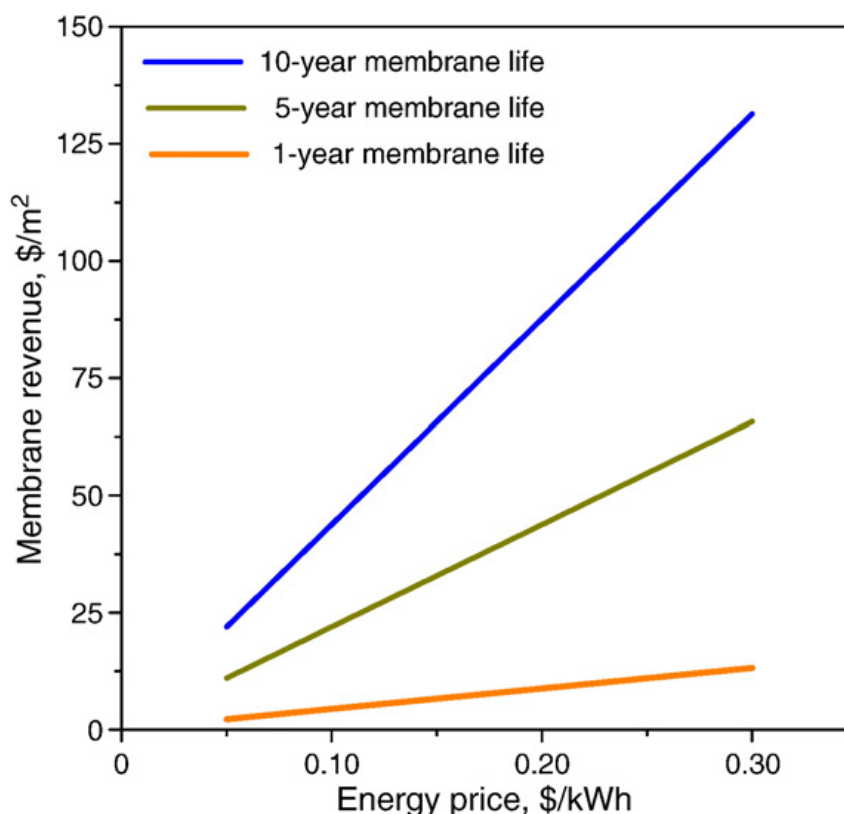


Σχ. 4 Μοντέλο εργοστασίου παραγωγής ηλεκτρικής ενέργειας PRO

Από τα παραπάνω είναι προφανές ότι το αρχικό κόστος μιας εγκαταστάτης PRO είναι αρκετά μεγάλο (μεγαλύτερο από τις υπάρχουσες νέες εναλλακτικές πηγές ενέργειας: βιομάζα, κύματα, παλίρροια, αιολική offshore), αλλά το γεγονός ότι λειτουργεί 365 μέρες το χρόνο, 24 ώρες τη μέρα κάνει ένα MW αρκετά παραγωγικό, όπου το κόστος ανέρχεται στα 50-100 €/MWh, δηλαδή ανταγωνίζεται τις υπόλοιπες νέες εναλλακτικές πηγές ενέργειας. Για να εκτιμηθεί η οικονομική βιωσιμότητα του PRO χρησιμοποιείται ο τύπος:

$$\frac{\text{Revenue}}{\text{Membrane area} \cdot \text{year}} = \text{Power density} \cdot \text{Energy price} \quad (5)$$

που δίνει τα έσοδα ανά τετραγωνικό μέτρο μεμβράνης ανά έτος. Θεωρώντας την πυκνότητα ισχύος της μεμβράνης 5 W/m^2 , που είναι ο επιτεύξιμος στόχος, την παρούσα τιμή της ενέργειας $0.10 \text{ \$/kWh}$, βρίσκουμε $4.4 \text{ \$ έσοδα ανά m}^2 \text{ μεμβράνης ανά έτος (\$/m}^2\text{y)}$. Το σχήμα που ακολουθεί δείχνει τα έσοδα ανά m^2 μεμβράνης σαν συνάρτηση της τιμής της ενέργειας για 3 διαφορετικές διάρκειες ζωής της μεμβράνης:



Σχ. 5 Έσοδα ανά m^2 μεμβράνης σε συνάρτηση της τιμής της ενέργειας για 3 διαφορετικές διάρκειες ζωής της μεμβράνης

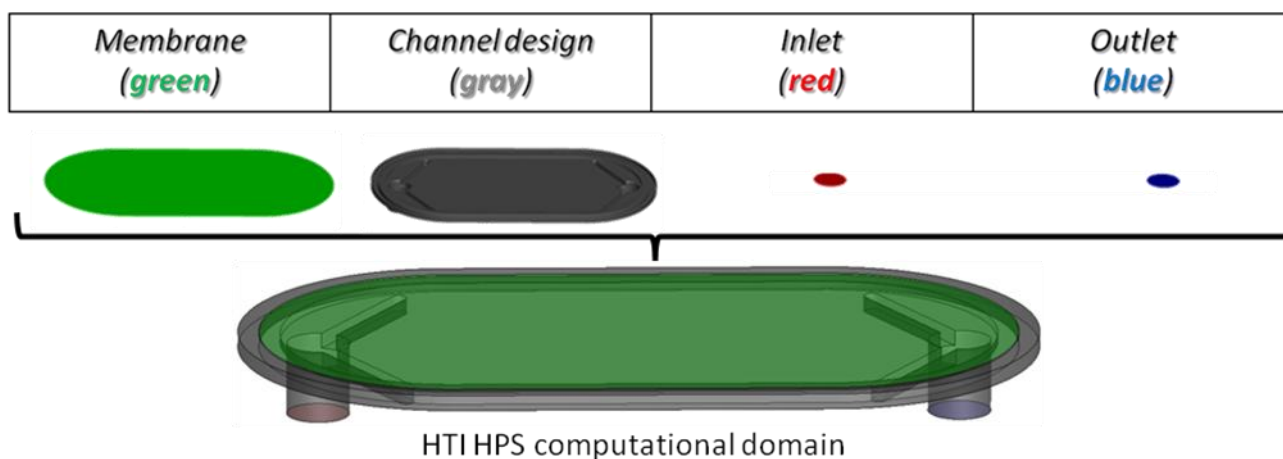
Όπως είναι αναμενόμενο τα έσοδα ανεβαίνουν με την αύξηση ζωής της μεμβράνης και την αύξηση της τιμής πώλησης της ενέργειας. Με τις παρούσες τιμές για την ενέργεια, την επιτεύξιμη πυκνότητα ισχύος της μεμβράνης και για διάρκεια ζωής της μεμβράνης 5 έτη, τα έσοδα ανά m^2 μεμβράνης είναι 22 \$/m². Με δεδομένο κόστος μεμβρανών 20-40 \$/m² (μεμβράνες για αντίστροφη ώσμωση) είναι φανερό ότι το PRO με τα υπάρχοντα δεδομένα δεν φαίνεται να μπορεί να παράγει ενέργεια σε ανταγωνιστικό κόστος. Για να επιτευχθεί αυτό πρέπει να υπάρξει βελτίωση είτε στην πυκνότητα ισχύος των μεμβρανών, είτε στη διάρκεια ζωής τους, είτε μείωση του κόστους τους.

Σε αυτήν την εργασία, μελετήθηκε για πρώτη φορά, η διαδικασία της καθυστερημένης ωσμωτικής πίεσης (PRO), σε ένα ειδικά διαμορφωμένο θάλαμο δοκιμής PRO, με προσομοιώσεις με την χρήση υπολογιστικής ρευστομηχανικής (CFD), η οποία παρέχει μια τρισδιάστατη απεικόνιση του φαινομένου σε αντίθεση με τις ήδη υπάρχουσες μονοδιάστατες, πράγμα το οποίο επιτρέπει την εξέταση της ροής στο θάλαμο δοκιμής. Εξετάστηκαν τα αποτελέσματα της επίδρασης των βασικών παραμέτρων, δηλαδή πίεσης, ογκομετρικής ροής και συγκέντρωσης του αλατιού στο θαλασσινό νερό, καθώς επίσης και τα χαρακτηριστικά της μεμβράνης, στην απόδοση της διαδικασίας. Επιπλέον μελετήθηκε, η επίδραση του σχεδιασμού του θαλάμου δοκιμής, εξετάζοντας διαφορετικά σχέδια. Εξετάστηκαν επίσης η ορθότητα και η ακρίβεια των αποτελεσμάτων. Τέλος, διερευνήθηκαν οι δυνατότητες και οι περιορισμοί της διεργασίας PRO.

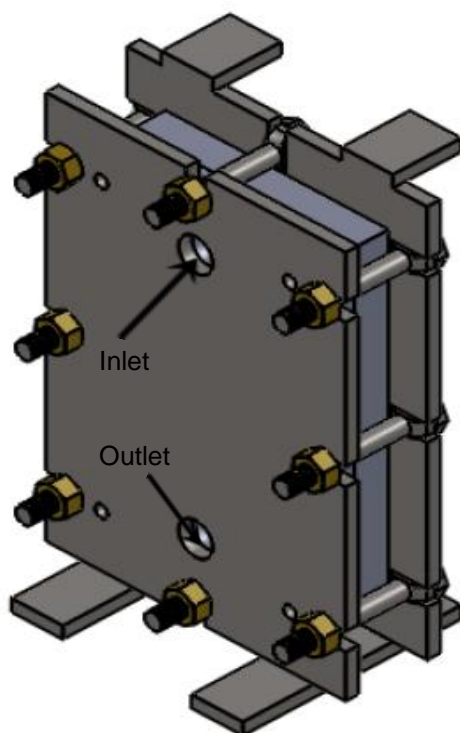
Για τη μελέτη αυτή χρησιμοποιήθηκαν 4 βασικά προγράμματα για την προσομοίωση της ροής στην πλευρά υψηλής πίεσεως (αλατόνερο) του θαλάμου δοκιμής (η πλευρά του γλυκού νερού θεωρείται ότι έχει ατμοσφαιρική πίεση και συγκέντρωση αλατιού μηδενική): solid works 2010 για τη σχεδίαση του θαλάμου δοκιμής, gambit 2.4.6 για τη δημιουργία του πλέγματος, ANSYS

FLUENT 12 για την επίλυση των εξισώσεων και Techplot 360 2009 για την επεξεργασία των αποτελεσμάτων.

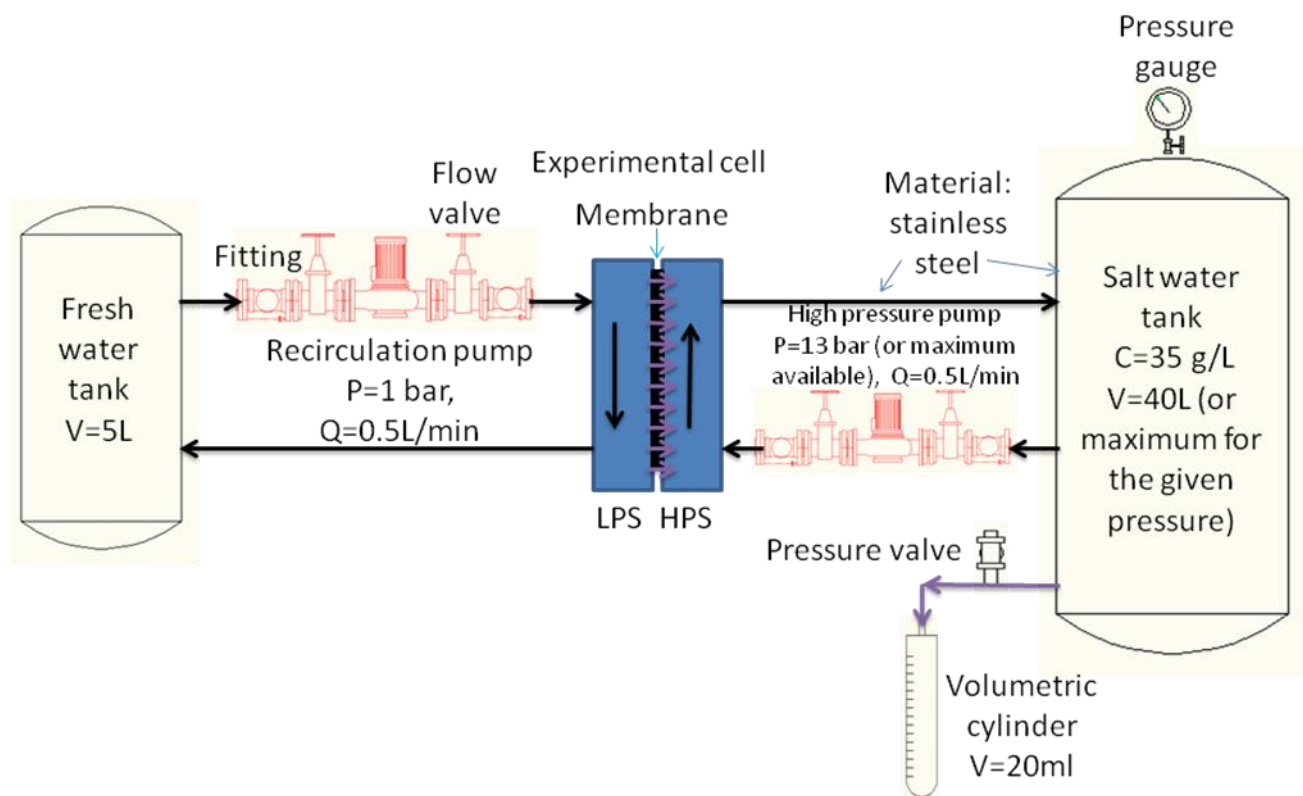
Τα σχήματα και ο πίνακας που ακολουθούν παρουσιάζουν τη γεωμετρία που έχει μελετηθεί (σχέδια από την εταιρία HTI), μια πειραματική διάταξη που περιέχει το συγκεκριμένο θάλαμο δοκιμής και μπορεί να αναπαράγει τις συνθήκες που μελετώνται στην εργασία, μια φωτογραφία της μεμβράνης που πάρθηκε από ηλεκτρονικό μικροσκόπιο στο εργαστήριο του Δημόκριτου καθώς επίσης και τις διαφορετικές περιπτώσεις που έχουν εξετασθεί στην εργασία:



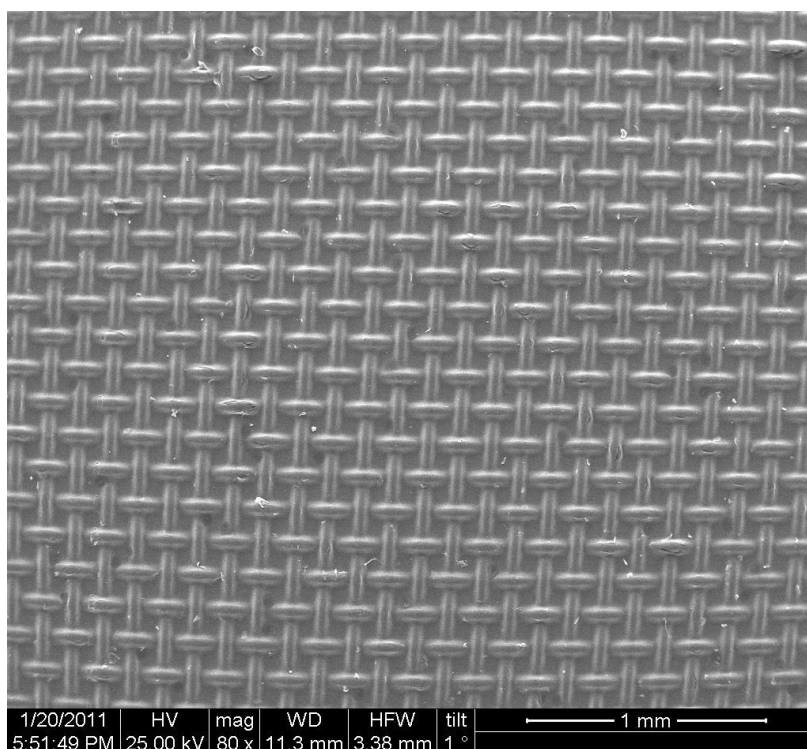
Σχ. 6 Εσωτερικό του θαλάμου δοκιμής - πλευρά με το αλατόνερο



Σχ. 7 Εξωτερικό του θαλάμου δοκιμής



Σχ. 8 Πειραματική διάταξη

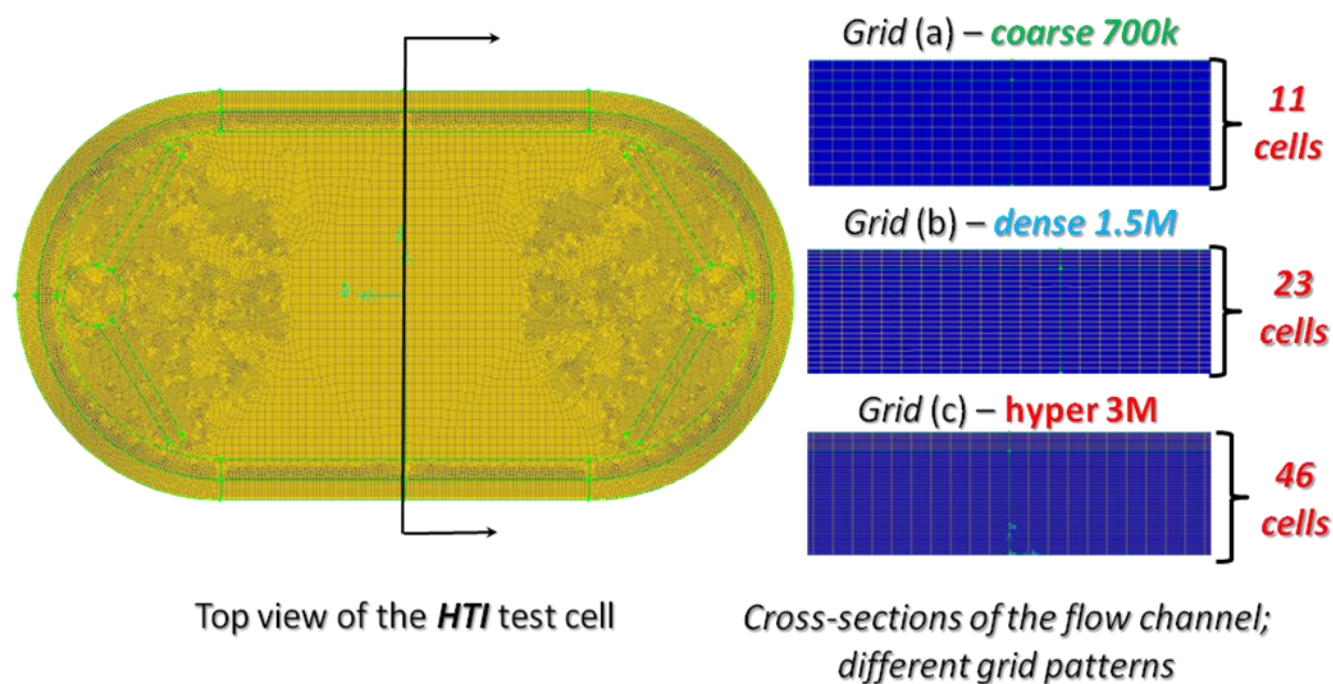


Σχ. 9 Υποστηρικτικό στρώμα της μεμβράνης (zoom x80)

Case	Geometry	Grid	Solver	Inlet Boundary	Outlet Boundary	Membrane	Working Fluid	
1	HTI standard HPS	coarse (700K)	FLUENT 12	0.5 L/h	14 bar	Wall	Fresh water ρ=998.2 kg/m³ μ=0.001003 kg/m*s (FLUENT Database)	
2		dense (1.5M)						
3		hyper (3M)						
4		Adequate Resolution: Dense 1.5M				Mass flow inlet: HTI membrane		
5				0.5 L/h	14 bar		Dynamic conditions: HTI membrane	Mixture: Salt water C=35g/L, ρ=1025 kg/m³, μ=0.00096 kg/m*s (Exponential model for T=298.15 K) and fresh water C=0 g/L
6					15.8 bar			
7				1 L/h	1 bar			
8				0.5 L/min	1 bar			
9					15.8 bar	Dynamic conditions: Oasys Water membrane		
10								
11						New Design 1	Dynamic conditions: HTI membrane	
12		New Design 2						

Σχ. 10 Διαφορετικές περιπτώσεις που εξετάσθηκαν με το CFD

Το πρώτο μέρος της εργασίας αυτής (περίπτώσεις 1-3) περιλαμβάνει τη μελέτη της ανεξαρτησίας πλέγματος της συγκεκριμένης γεωμετρίας. Τρία διαφορετικά πλέγματα έχουν δοκιμαστεί, καθένα με διαφορετικό αριθμό κελιών στη διάσταση του ύψους y (46, 23 και 11 όπως φαίνονται στο σχήμα), θεωρώντας τη μεμβράνη ως τοίχωμα και σαν πρώτη φάση ότι περιέχεται γλυκό νερό αντί για αλατόνευρο: κελιά 700K, 1.5M και 3M. Οι διαφορές στη ροή ανάμεσα στα πυκνά 1.5M και υπερ-πυκνά 3M πλέγματα ήταν αμελητέες, ενώ το πλέγμα 700K διαφέρει πολύ. Ως εκ τούτου, το πυκνό πλέγμα (1.5M κελιά) έχει επιλεγεί για τις περαιτέρω προσομοιώσεις, το οποίο συνδυάζει τα ακριβή αποτελέσματα με τον ελάχιστο αριθμό κελιών.



Σχ. 11 Πυκνότητα κελιών του κάθε πλέγματος στη διάσταση του ύψους y

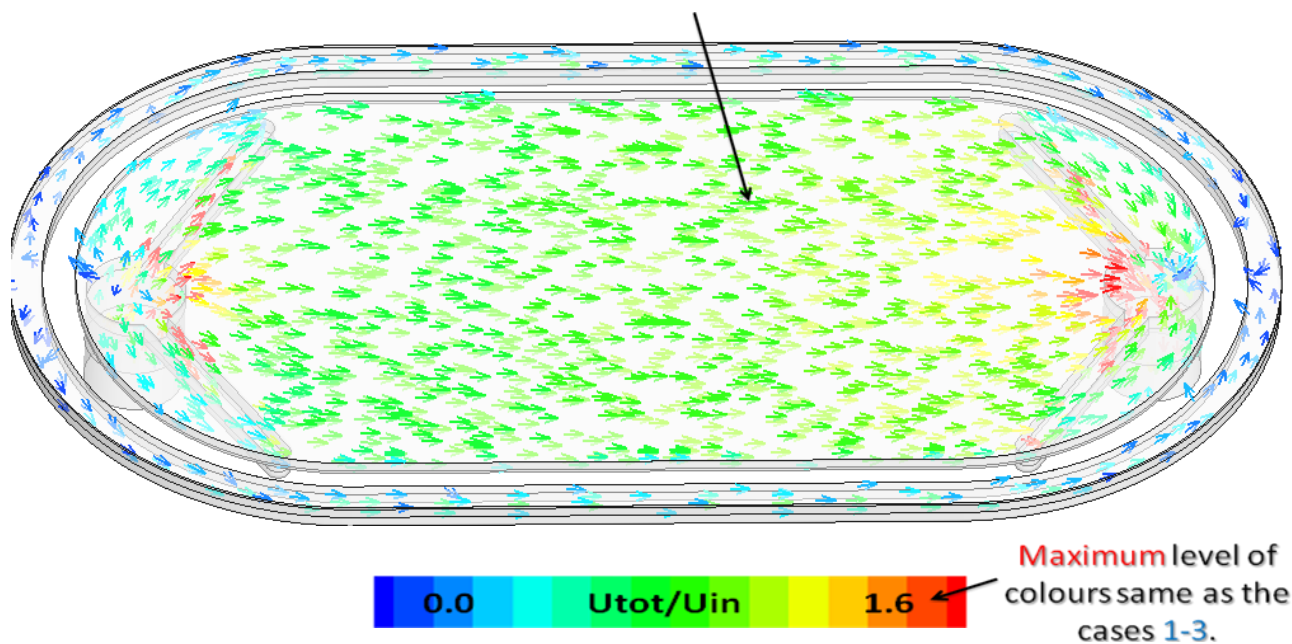
Το δεύτερο βήμα της έρευνας (περίπτωση 4) προσομοιώνει τη μεμβράνη με μια οριακή συνθήκη ομοιόμορφης παροχής που υπολογίζεται από τις εξισώσεις

$$\frac{Q}{E} = A \cdot (\Delta\pi - \Delta P),$$

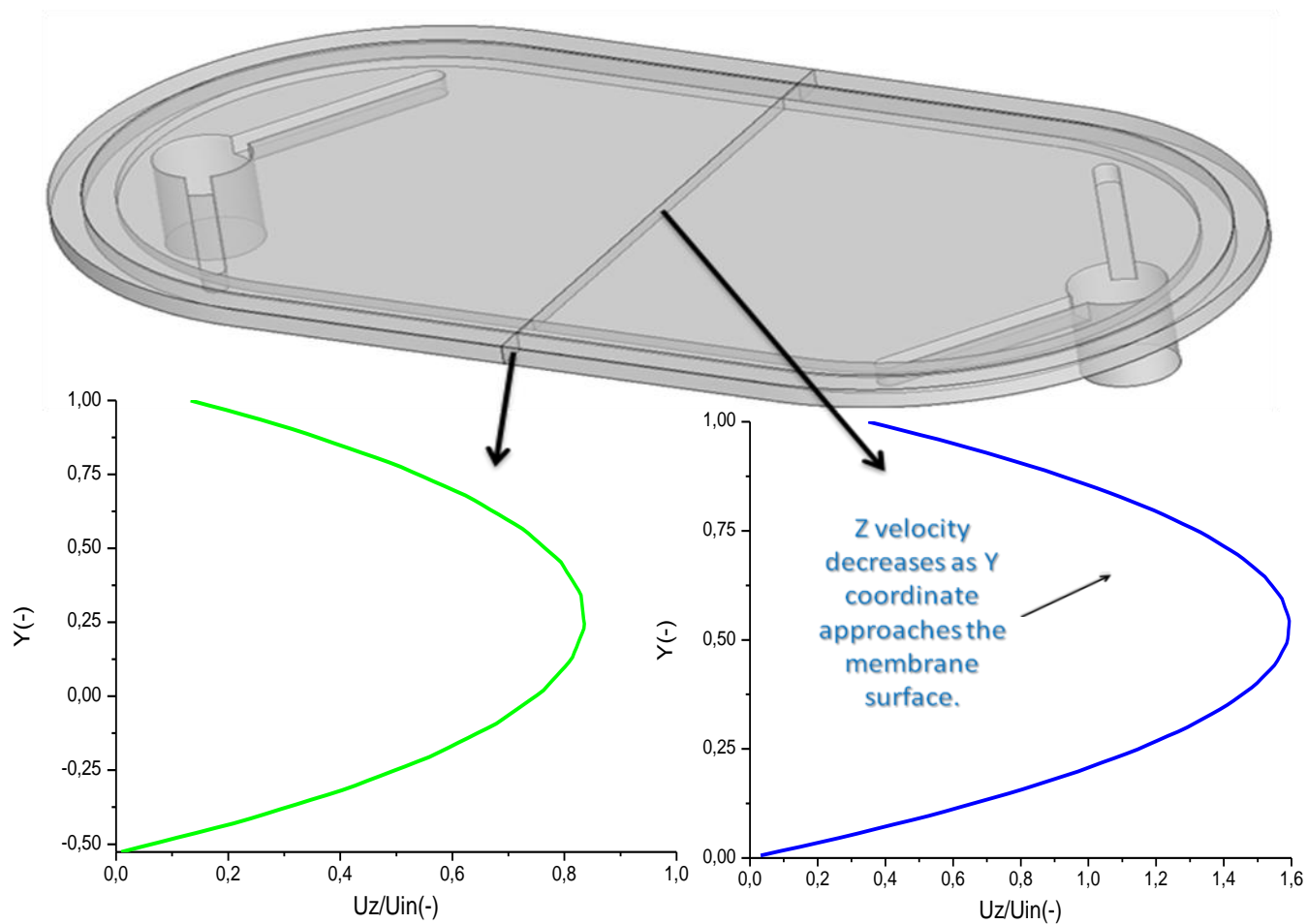
$$\Delta\pi = 2 \cdot \Delta C_{\text{NaCl}} \cdot R \cdot T,$$

Στα παρακάτω σχήματα φαίνεται η ροή στο θάλαμο δοκιμής και τα παραβολικά προφίλ ταχύτητας στην κυρίως και την περιφερειακή ροή:

The flow in is accelerating as it reaches the outlet while on the cases 1-3 the colours are simetrical.



Σχ. 12 Διανύσματα ταχύτητας στο μέσο του καναλιού



Σχ. 13 Παραβολικά προφίλ ταχύτητας στην κυρίως και περιφερειακά ροή

Στο τρίτο μέρος της έρευνας (περιπτώσεις 5-10) χρησιμοποιείται ένας αλγόριθμος για την καλύτερη προσομοίωση της μεμβράνης. Ο αλγόριθμος αυτός εφαρμόζει τη γενική εξίσωση της όσμωσης $U = A (\Delta\pi - \Delta P)$ (ταχύτητα του γλυκού νερού μέσω της μεμβράνης) σε κάθε κελί της μεμβράνης. Η διαφορά της οσμωτικής πίεσης υπολογίζεται για κάθε κελί από την εξίσωση $\Delta\pi = 2 \cdot \Delta C_{NaCl} \cdot R \cdot T$.

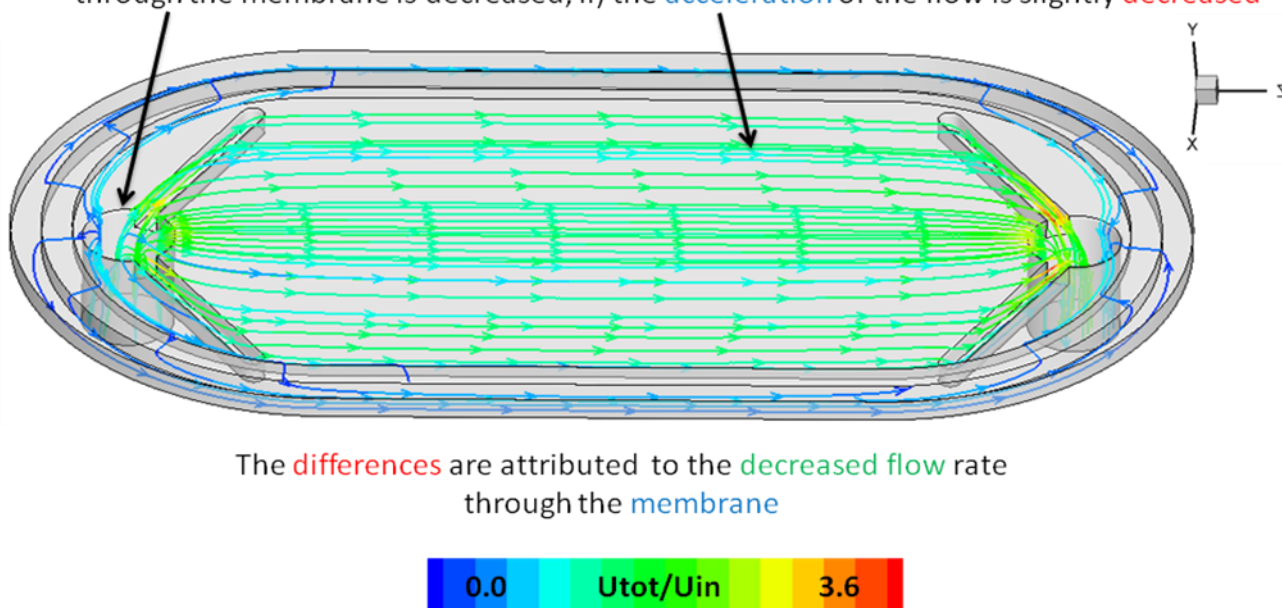
Στο παρακάτω Πίνακα (Σχ.14) φαίνονται οι συνθήκες στην είσοδο, έξοδο και στη μεμβράνη :

Boundary Conditions // Cases 5-10				
Case	Membrane (green)	Channel design (gray)	Inlet (red)	Outlet (blue)
5	Dynamic conditions: HTI membrane	Wall	0.5 L/h	14 bar
6				15.8 bar
7			1 L/h	1 bar
8			0.5 L/min	15.8 bar
9				
10	Oasys Water membrane			

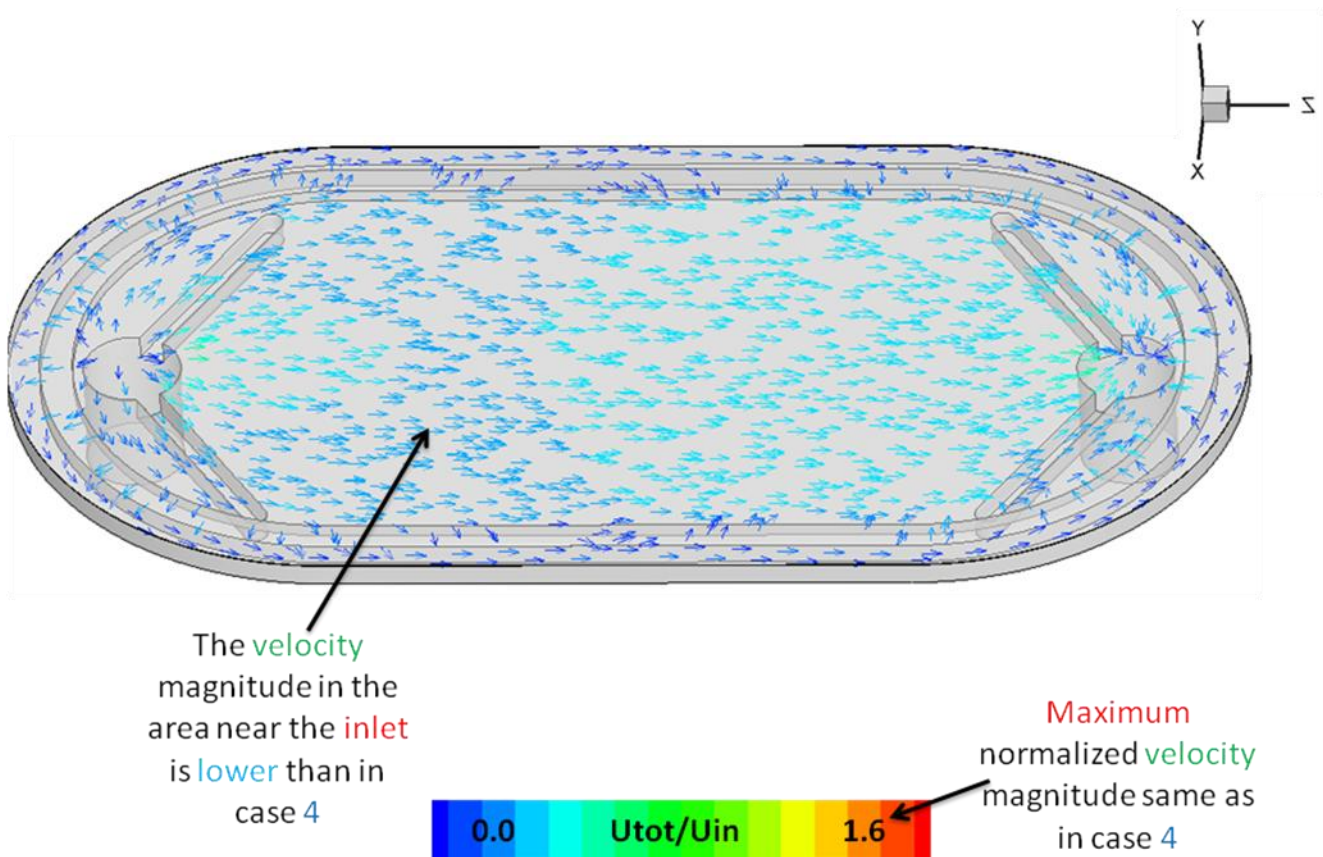
Σχ. 14 Οριακές συνθήκες στις περιπτώσεις 5-10

Η ροή στο θάλαμο δοκιμής, που είναι παρόμοια σε όλες τις περιπτώσεις, καθώς και η συγκέντρωση του αλατιού, ίδια για τις περιπτώσεις 5-7 και διαφορετική για τις 8-10, φαίνεται στα παρακάτω σχήματα:

The flow field is similar with that of the case 4 with only two differences: i) more streamlines from the inlet escape into the periphery as the resistance from the flow through the membrane is decreased, ii) the acceleration of the flow is slightly decreased

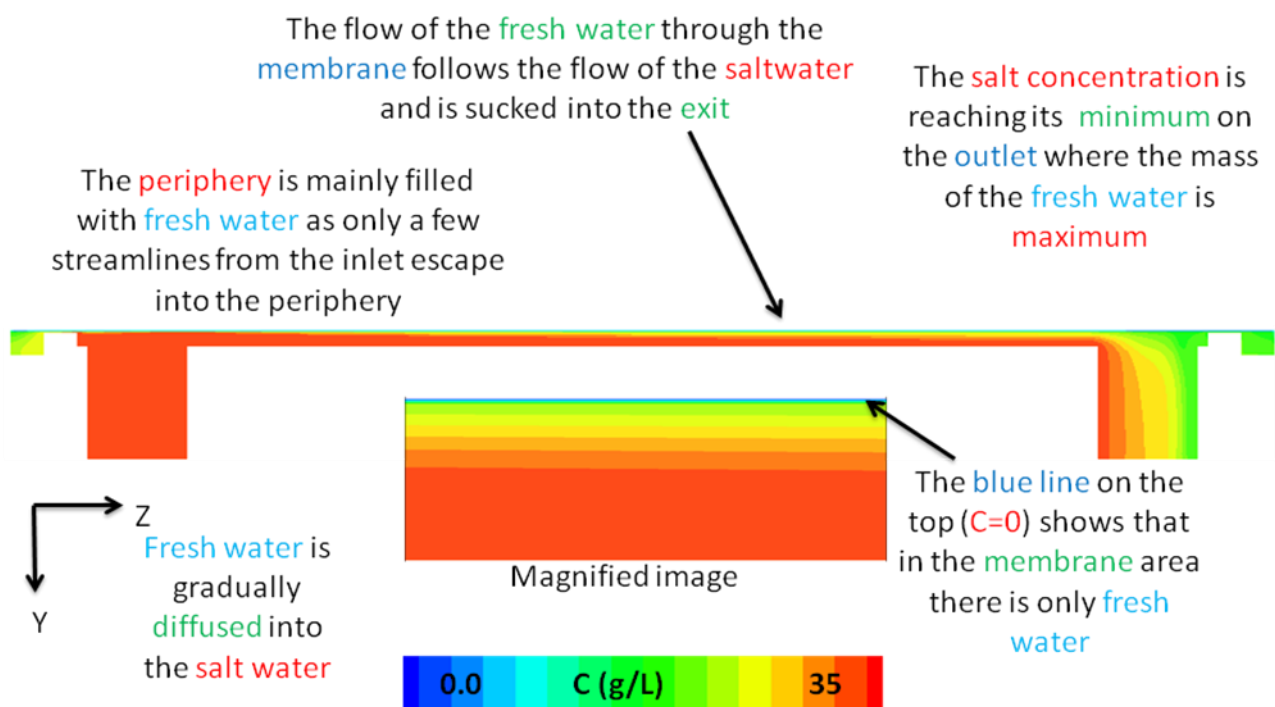


Σχ. 15 Γραμμές ροής από την είσοδο

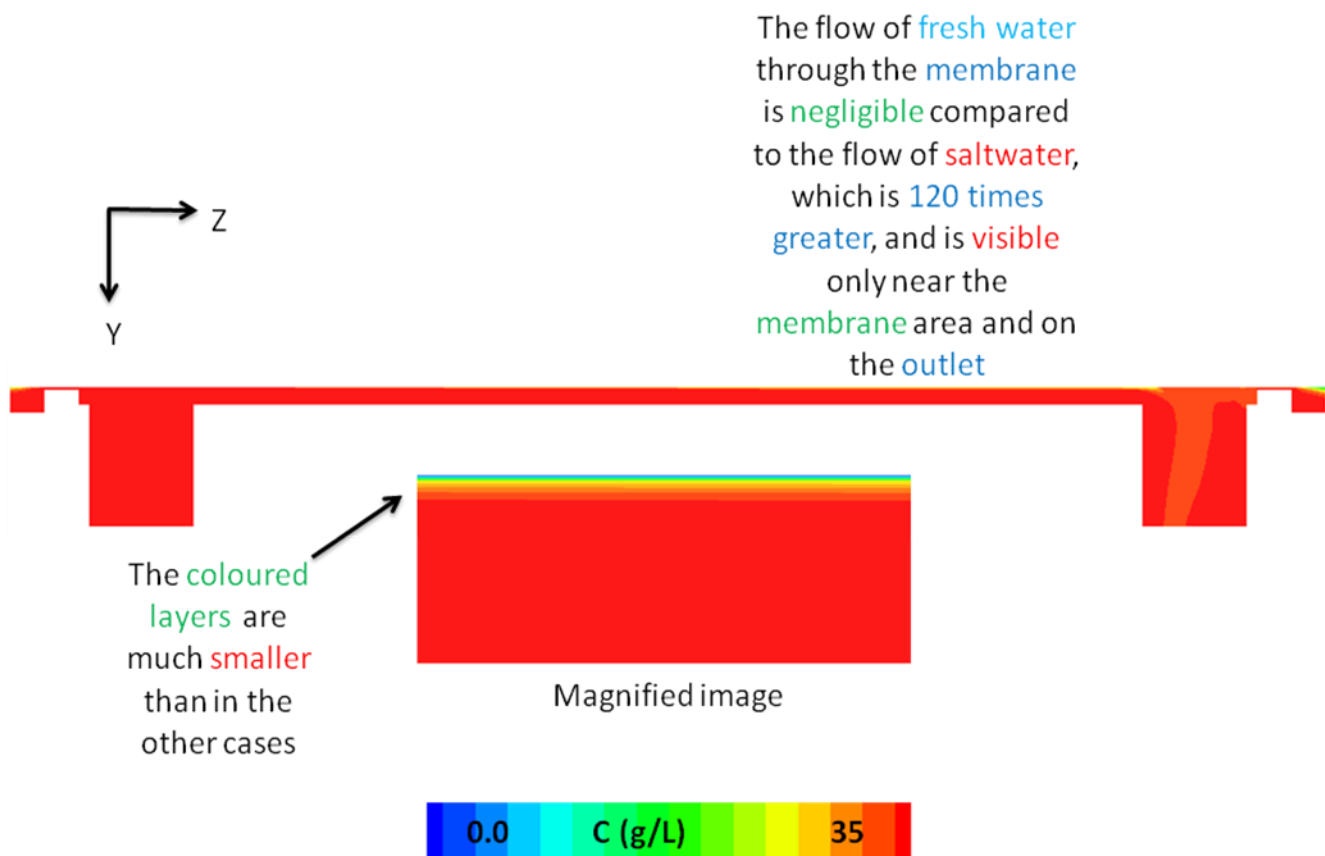


Σχ. 16 Διανύσματα ταχύτητας κοντά στην επιφάνεια της μεμβράνης

The salt concentration profiles can be created if the mass fraction of salt water is multiplied by 35 g/L, which is the initial concentration of salt in salt water.



Σχ. 17 Συγκέντρωση αλατιού στο επίπεδο y-z για τις περιπτώσεις 5-7



Σχ. 18 Συγκέντρωση αλατιού στο επίπεδο y-z για τις περιπτώσεις 8-10

Για κάθε μία περίπτωση μετράται η ροή μέσα από τη μεμβράνη και αντίστοιχα η παραγόμενη ισχύς, όπως φαίνεται στον παρακάτω πίνακα:

Case	Volumetric flow through the membrane (Qm)	Generated power (W)
5	0.096 L/h	1.48 W/m ²
6	0.09 L/h	1.58 W/m ²
7	0.236 L/h	0
8	0.413 L/h	0
9	0.203 L/h	3.58 W/m ²
10	0.299 L/h	5.26 W/m ²

Σχ.19 Παροχή μέσα από τη μεμβράνη και παραγόμενη ισχύς για τις περιπτώσεις 5-10

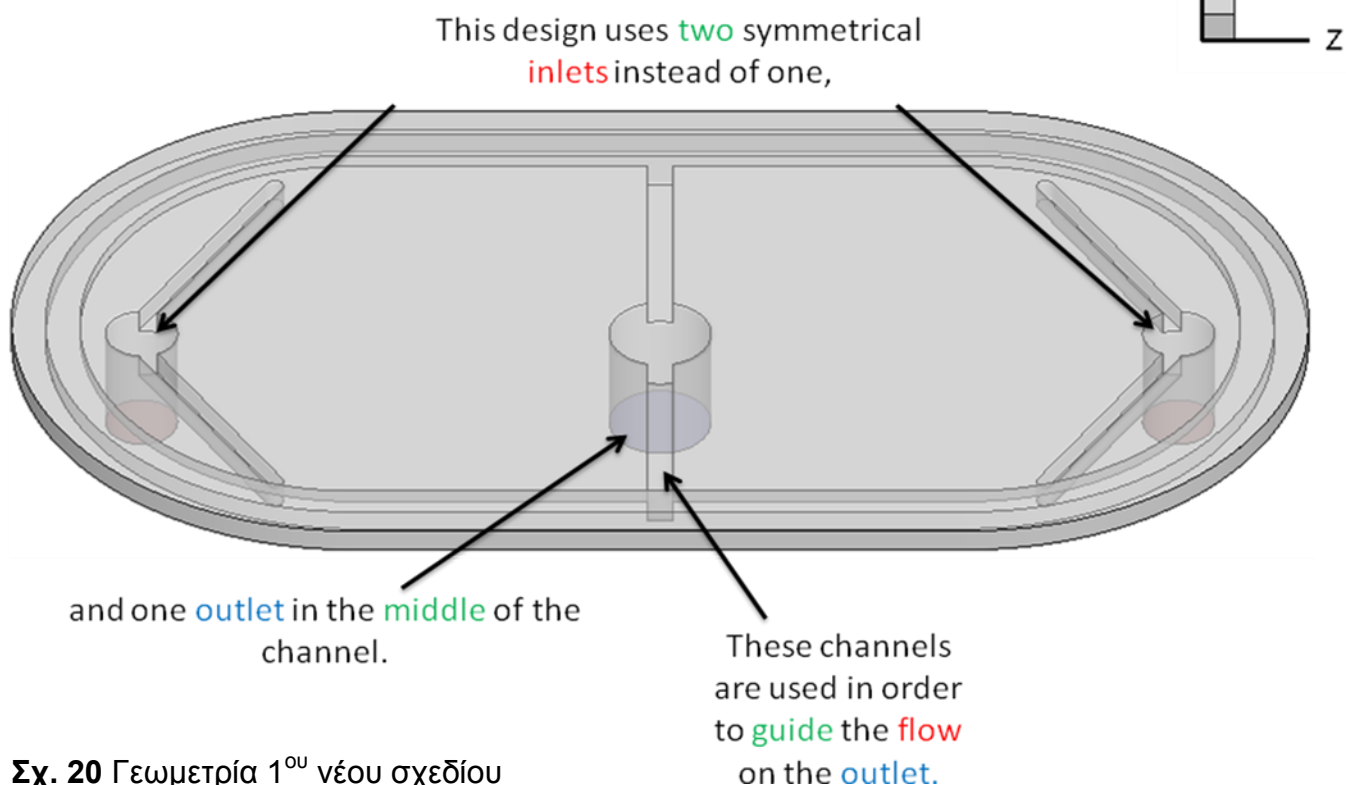
Παρατηρούμε ότι στην περίπτωση 9, όπου η παροχή εισόδου γίνεται 60 φορές μεγαλύτερη από αυτή της περίπτωσης 6, η ισχύς αυξάνεται κατά 125%. Αυτό συμβαίνει διότι το γλυκό νερό που εισέρχεται στο αλατόνερο μέσω της μεμβράνης απομακρύνεται γρηγορότερα.

Επίσης, στην περίπτωση 10 όπου χρησιμοποιείται διαφορετική μεμβράνη με μεγαλύτερο A (συντελεστής περατότητας της μεμβράνης) η ισχύς αυξάνεται κατά 47.2%, πράγμα το οποίο δείχνει το πόσο σημαντικό ρόλο παίζει η μεμβράνη στην τεχνολογία PRO. Επιπλέον, η μεμβράνη επηρεάζει και με έναν άλλο τρόπο το φαινόμενο: η ικανότητα της να απορρίπτει το αλάτι και η μορφολογία του υποστηρικτικού στρώματος καθορίζουν το πόσο έντονο θα είναι το φαινόμενο του internal concentration polarization (εγκλωβισμός του αλατιού στο υποστηρικτικό στρώμα της μεμβράνης) το οποίο επηρεάζει σημαντικά τη ροή μέσα από τη μεμβράνη και την αντίστοιχη παραγόμενη ισχύ.

Το επόμενο στάδιο της έρευνας (περιπτώσεις 11-12) περιλαμβάνει τη δημιουργία 2 καινούριων σχεδίων του θαλάμου δοκιμής και τη δοκιμή τους ως προς τις επιδόσεις στην τεχνολογία PRO. Τα 2 αυτά καινούρια σχέδια είναι βασισμένα στο αρχικό της HTI με μερικές τροποποιήσεις:

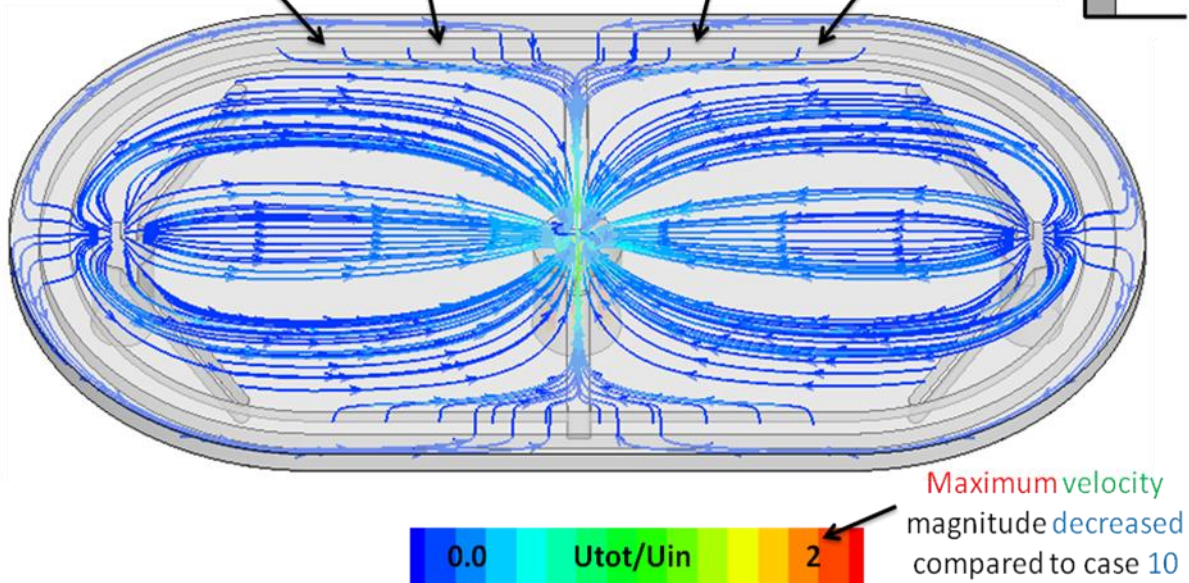
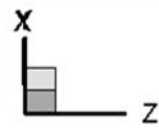
- Έχουν το ίδιο κανάλι κεντρικής και περιφερειακής ροής, ενώ η είσοδος και η έξοδος έχουν τροποποιηθεί.
- Η επιφάνεια και ο όγκος της εισόδου και της εξόδου έχουν παραμείνει ίδια με το αρχικό έτσι ώστε ο όγκος ροής να παραμένει ίδιος καθώς και οι οριακές συνθήκες.

Τα σχήματα που ακολουθούν παρουσιάζουν τις 2 γεωμετρίες επισημαίνοντας τις Y Z καθώς επίσης και τη ροή σε αυτές:



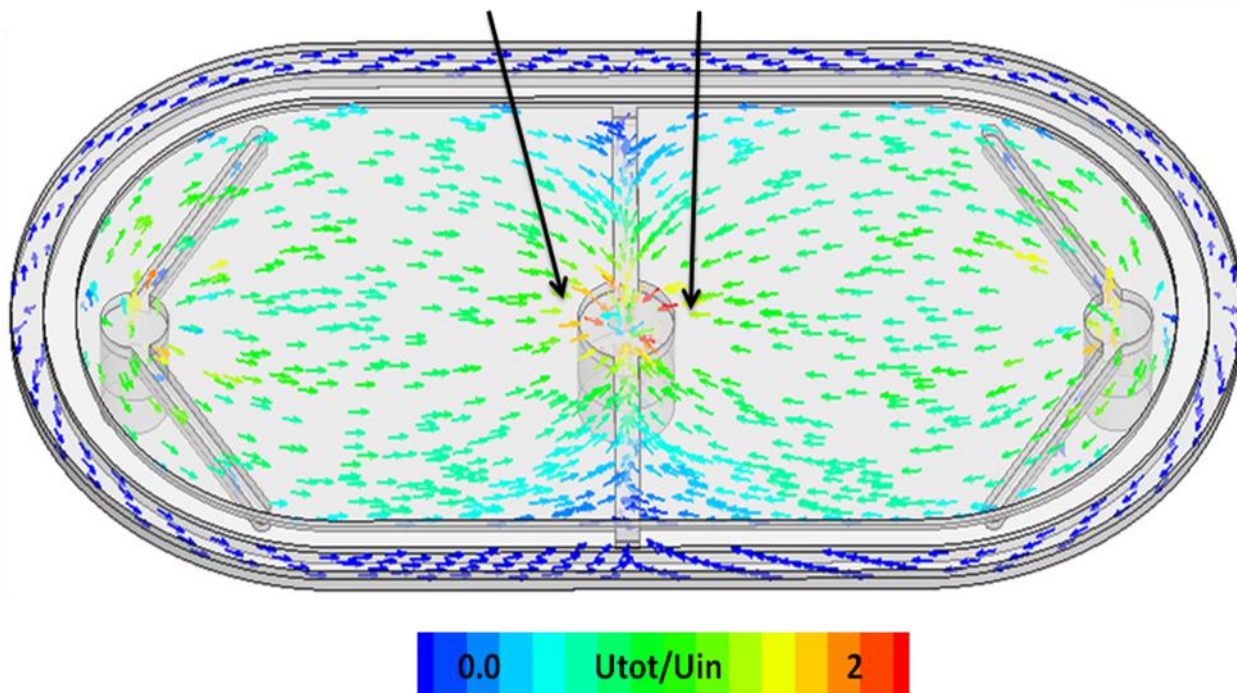
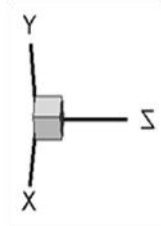
Σχ. 20 Γεωμετρία 1^{ου} νέου σχεδίου

There are **no streamlines** in this area that **flow** into the **periphery**. This has a **negative effect** on magnitude of the **flow through the membrane** as the fresh water that flows into the main channel dilutes the salt water and therefore decreases the effective osmotic pressure.

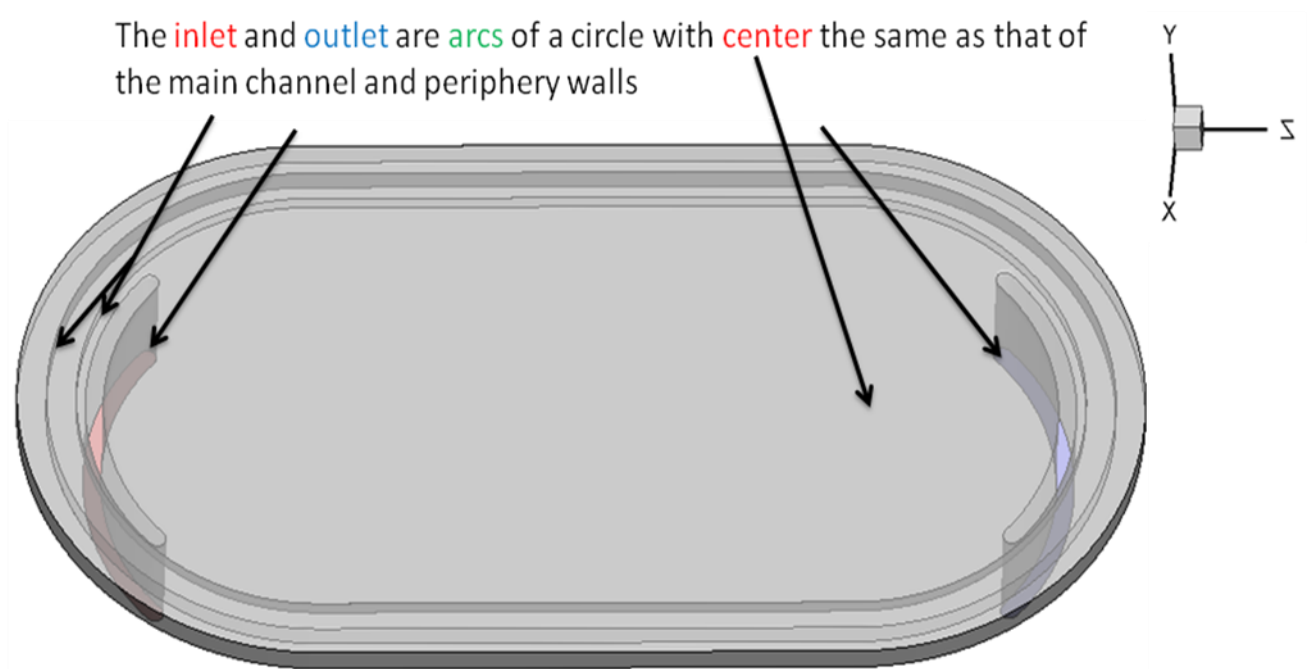


Σχ. 21 Γραμμές ροής από την επιφάνεια της μεμβράνης

Like the flow of fresh water, the **flow of salt water** is also slightly **accelerated** compared to the original design which has a **negative effect** on the **flow through the membrane**

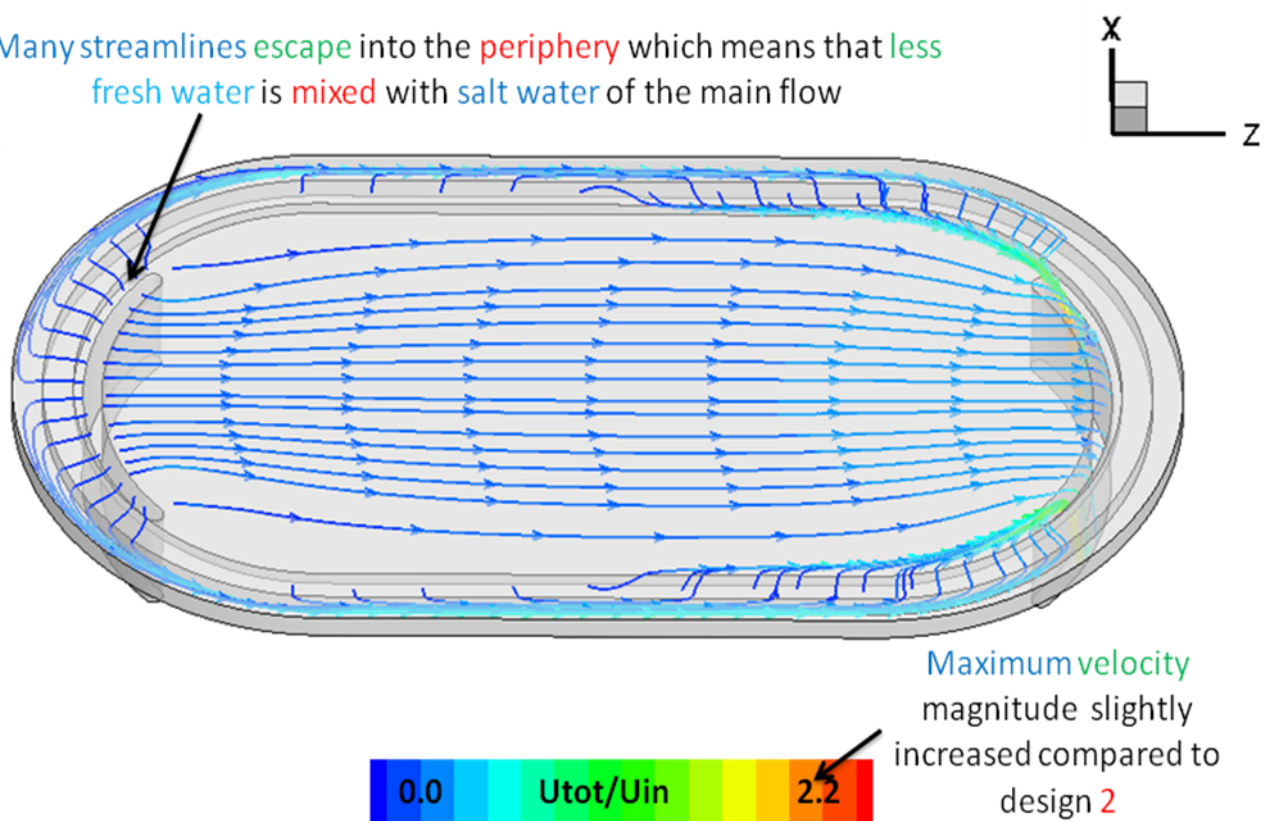


Σχ. 22 Διανύσματα ταχύτητας στη μέση του καναλιού

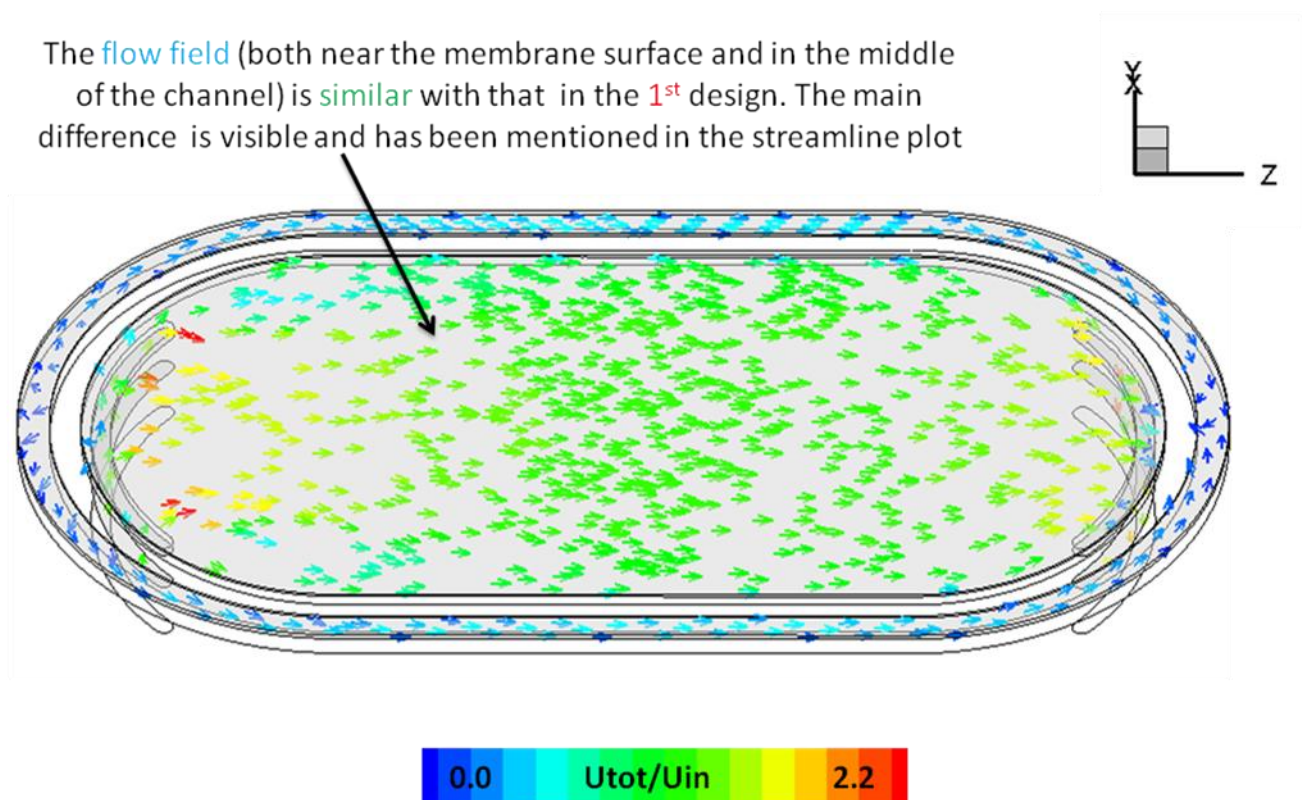


Σχ. 23 2^ο νέο σχέδιο

Many streamlines escape into the periphery which means that less fresh water is mixed with salt water of the main flow



Σχ. 24 Γραμμές ροής από την επιφάνεια της μεμβράνης

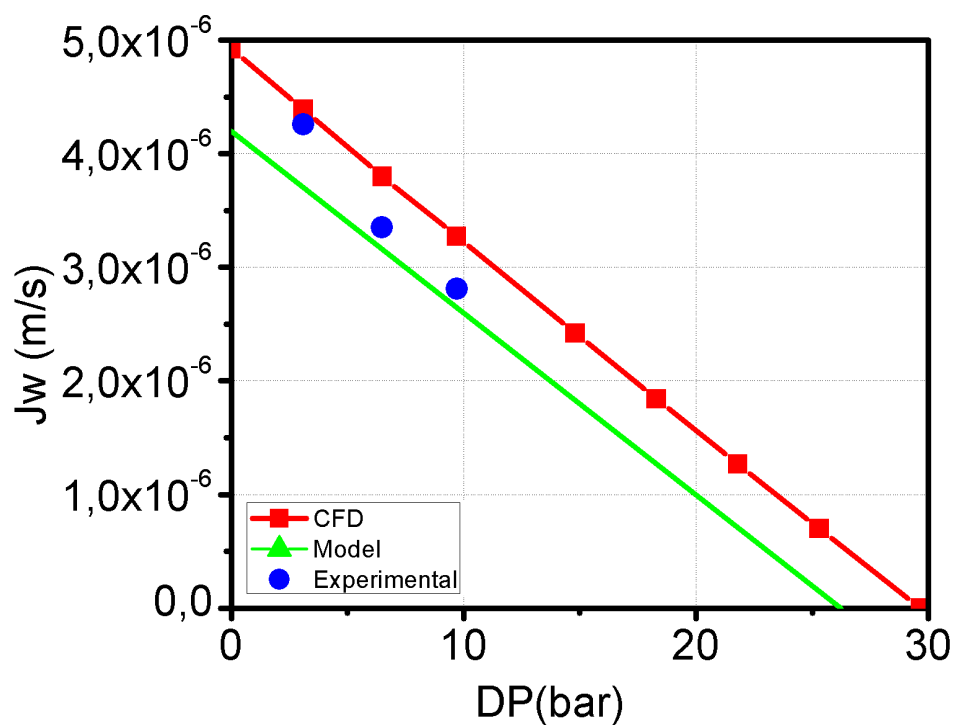


Σχ. 25 Διανύσματα ταχύτητας στη μέση του καναλιού

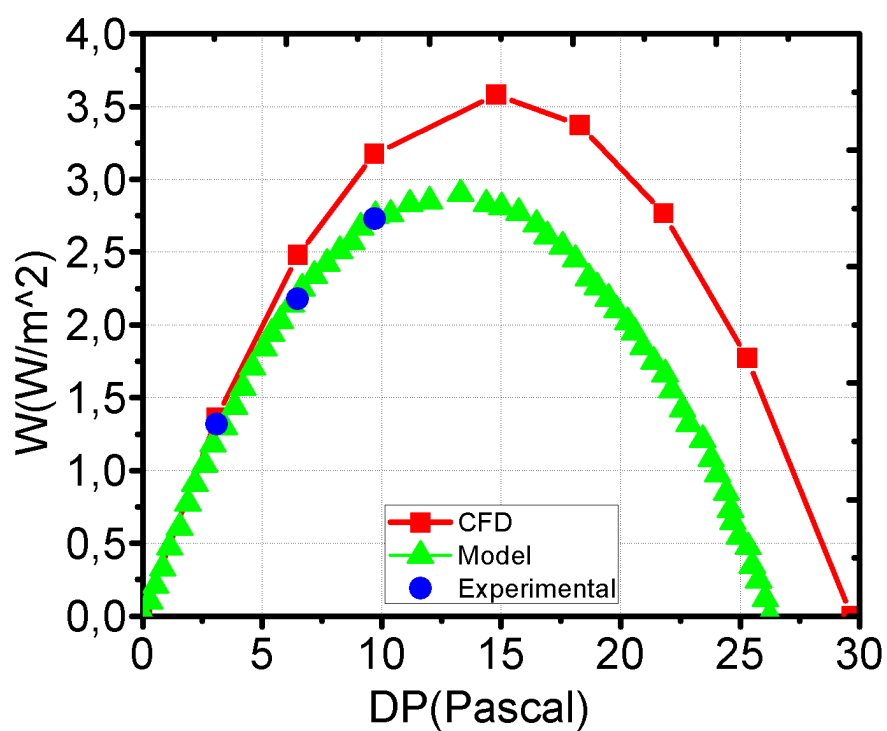
Το τελευταίο μέρος της έρευνας περιλαμβάνει τη δημιουργία παραμετρικών διαγραμμάτων, τα οποία συγκρίνονται με δημοσιευμένα, τη σύγκριση των νέων σχεδίων του θαλάμου δοκιμής και την επιρροή των παραμέτρων της υπολογιστικής επίλυσης στα τελικά αποτελέσματα. Με βάση αυτά έχουν εξαχθεί τελικά συμπεράσματα και προτάσεις για μελλοντική εργασία.

Τα 2 πρώτα παραμετρικά διαγράμματα που δημιουργήθηκαν χρησιμοποιούν τις συνθήκες εισόδου της περίπτωσης 9 (0.5 L/min) και δίνουν για 9 διαφορετικές συνθήκες εξόδου (υδραυλική πίεση από 0 έως 29.66 bar που είναι η ωσμωτική πίεση) τη ροή του γλυκού νερού μέσα από τη μεμβράνη και την αντίστοιχη παραγόμενη ισχύ. Τα αποτελέσματα συγκρίνονται με τα πειραματικά και αυτά του μοντέλου της δημοσίευσης:

Andrea Achilli , Tzahi Y. Cath, Amy E. Childress, Power generation with pressure retarded osmosis: An experimental and theoretical investigation, J. Membrane Sci. 343 (2009) 42-52.



Σχ. 26 Ροή μέσα από τη μεμβράνη σαν συνάρτηση της διαφοράς υδραυλικής πίεσης



Σχ. 27 Παραγόμενη ισχύς ανά μονάδα επιφάνειας σαν συνάρτηση της διαφοράς υδραυλικής πίεσης

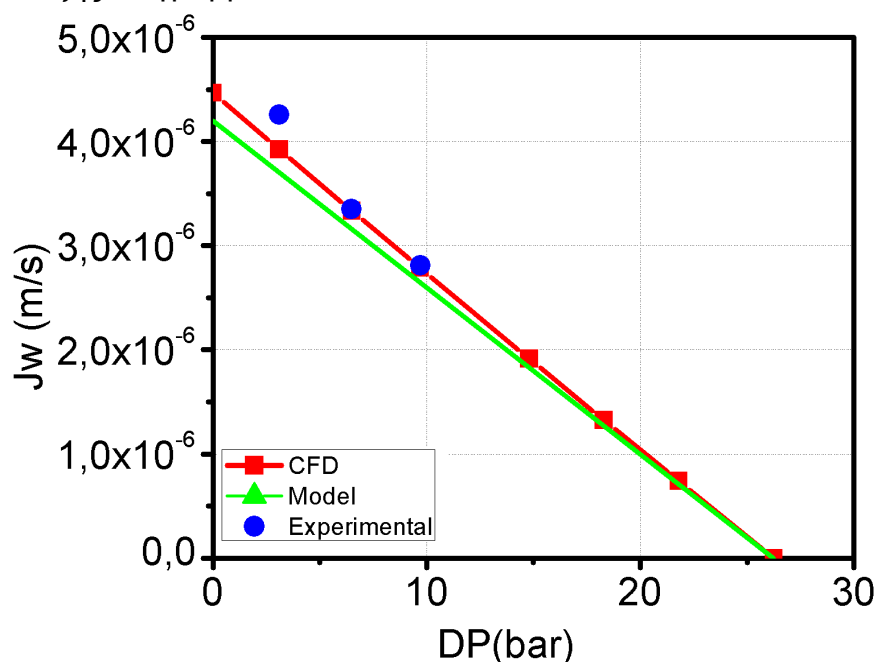
Στα δυο αυτά διαγράμματα φαίνεται ότι τα αποτελέσματα που δίνει το CFD ακολουθούν τη γενική τάση των αποτελεσμάτων της δημοσίευσης και διαφέρουν στο ότι είναι ελαφρώς αυξημένες οι τιμές τους. Αυτό οφείλεται κυρίως σε 2 λόγους:

- Στη δημοσίευση χρησιμοποιείται διαφορετικός τύπος για τον υπολογισμό της ωσμωτικής πίεσης, ο οποίος για τις ίδιες συνθήκες δίνει 27,63 bar, σε αντίθεση με τα 29,66 που υπολογίζονται στην εργασία αυτή.
- Η επίδραση του internal concentration polarization (εγκλωβισμός του αλατιού στο υποστηρικτικό στρώμα της μεμβράνης) δεν υπολογίζεται από το CFD καθώς δεν επιλύεται η ροή μέσα από τη μεμβράνη. Αυτό μπορεί να επιτευχθεί είτε με την επίλυση και των 2 πλευρών του κελύφους δοκιμής και της ροής μέσα από τη μεμβράνη, χρησιμοποιώντας τον τύπο $J_s = B\Delta c$ για τη ροή του αλατιού από το αλμυρό στο γλυκό νερό, πράγμα που απαιτεί τη μορφολογία της μεμβράνης και είναι αρκετά δύσκολο, είτε με την εισαγωγή ενός διορθωτικού συντελεστή για τη ροή μέσα από τη μεμβράνη, ο οποίος χρησιμοποιείται στη δημοσίευση και θα επιλυθεί αριθμητικά,

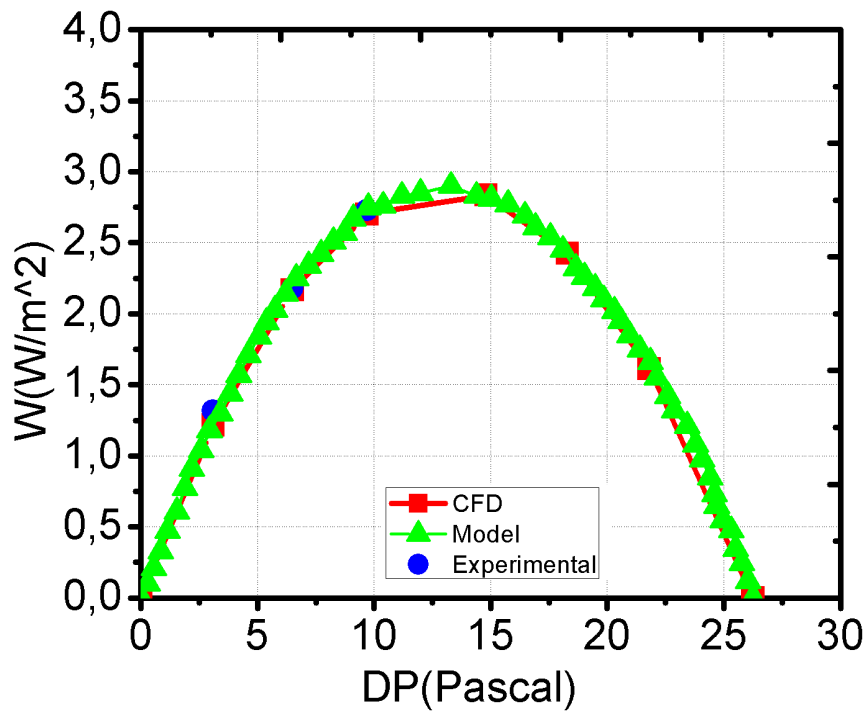
$$J_w = A \cdot [\pi_4 \cdot \frac{1 - \frac{C_2}{C_4} \cdot \exp(J_w \cdot K)}{1 + \frac{B}{J_w} \cdot [\exp(J_w \cdot K) - 1]} - \Delta P] , \text{ είτε τέλος με το συνδυασμό των παραπάνω όπου}$$

θα γίνεται επίλυση της πλευράς του γλυκού νερού και θα χρησιμοποιείται ο παραπάνω τύπος για τη ροή μέσα από τη μεμβράνη.

Αν η διαφορά συγκέντρωσης μεταξύ της πλευράς του αλατόνευρου και του γλυκού νερού γίνει 31 g/L, αντί για 35 g/L, που δίνει ωσμωτική πίεση 26,25 bar, δηλαδή όσο στη δημοσίευση με υπολογισμένη και τη μείωση για την επίδραση του internal concentration polarization, τότε προκύπτουν τα εξής διαγράμματα:



Σχ. 28 Ροή μέσα από τη μεμβράνη σαν συνάρτηση της διαφοράς υδραυλικής πίεσης



Σχ. 29 Παραγόμενη ισχύς ανά μονάδα επιφάνειας σαν συνάρτηση της διαφοράς υδραυλικής πίεσης

Είναι φανερό ότι τα αποτελέσματα του CFD και στα 2 διαγράμματα επαληθεύουν ακριβώς και τα πειραματικά και τα αποτελέσματα του μοντέλου από τη δημοσίευση. Αυτό σημαίνει ότι αν ενσωματωθούν οι παραπάνω τροποποιήσεις στο CFD τότε θα μπορεί να περιγράψει επακριβώς το φαινόμενο της ωσμωτικής πίεσης.

Στο παρακάτω σχήμα παρουσιάζεται η παροχή μέσα από τη μεμβράνη για τις συνθήκες της περίπτωσης 9 (HTI membrane, $Q_{in}=0.5$ L/min, $P_{out}=15.8$ bar) για τα 3 διαφορετικά πλέγματα:

Grid	Coarse (700K)	Dense (1.5M)	Hyper (3M)
Q_m (m ³ /s)	6.36E-05	5.64E-05	5.36E-05

Σχ. 30 Παροχή μέσα από τη μεμβράνη για τα 3 διαφορετικά πλέγματα

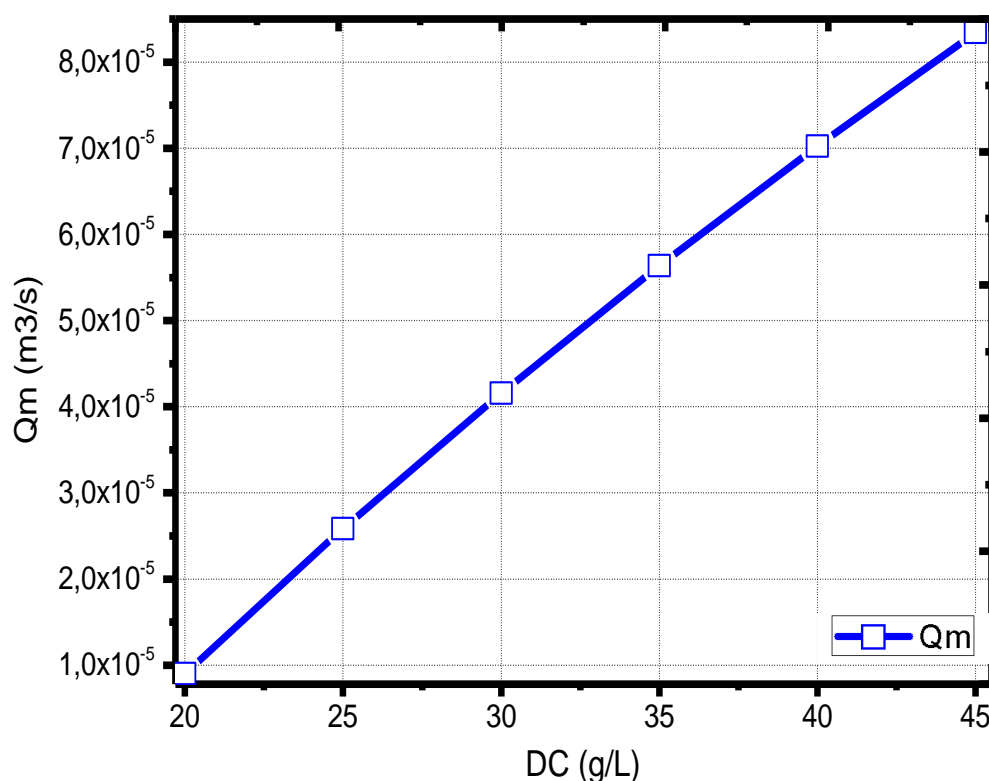
Παρατηρούμε ότι μεταξύ του πλέγματος με τα 1,5 M κελιά που έχει επιλεγεί ως καταλληλότερο και αυτού με τα 3 M παρατηρείται διαφορά στην παροχή μέσα από τη μεμβράνη, αν και δεν υπήρχαν διαφορές στο πεδίο ροής. Για να επιλυθεί αυτό απαιτείται η χρήση πλεγμάτων με μεγαλύτερο αριθμό κελιών (π.χ. 5 εκατομμύρια) και μέτρηση της παροχής που δίνουν για διάφορες συνθήκες εισόδου και εξόδου ώστε να επιλεγεί το καταλληλότερο.

Σε αντίθεση με την επιλογή του πλέγματος που επηρεάζει τα αποτελέσματα η μέθοδος διακριτοποίησης που χρησιμοποιείται στο FLUENT δεν επηρεάζει τα αποτελέσματα όπως φαίνεται και στο παρακάτω σχήμα:

Discretization method	First Order Upwind	Second Order Upwind	Third Order msc1	Quick	Power Law
Qm (m ³ /s)	5.6E-05	5.64E-05	5.63E-05	5.63E-05	5.61E-05

Σχ. 31 Παροχή μέσα από τη μεμβράνη για τους 5 διαφορετικούς τρόπους διακριτοποίησης των εξισώσεων

Ένα άλλο παραμετρικό διάγραμμα που δημιουργήθηκε στην εργασία είναι αυτό που δίνει την παροχή μέσα από τη μεμβράνη σε συνάρτηση της διαφοράς συγκέντρωσης μεταξύ αλατόνευρου και γλυκού νερού (συνθήκες όπως της περίπτωσης 9), για ΔC από 20-45 g/L:

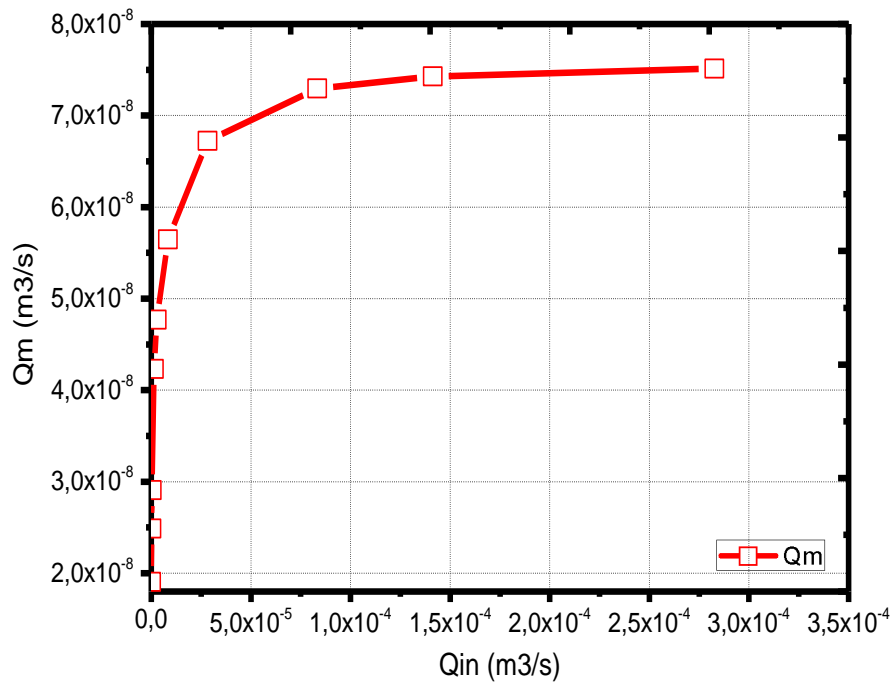


Σχ. 32 Ροή μέσα από τη μεμβράνη σε συνάρτηση της διαφοράς συγκέντρωσης

Το διάγραμμα αυτό δείχνει ότι η σχέση μεταξύ παροχής και διαφοράς συγκέντρωσης είναι γραμμική, πράγμα το οποίο ήταν αναμενόμενο με βάση τις εξισώσεις για τη ροή μέσα από τη μεμβράνη (1) και αυτή για τη διαφορά ωσμωτικής πίεσης (3).

Τέλος, στην εργασία μελετήθηκε το παραμετρικό διάγραμμα της παροχής μέσα από τη μεμβράνη σε συνάρτηση της παροχής

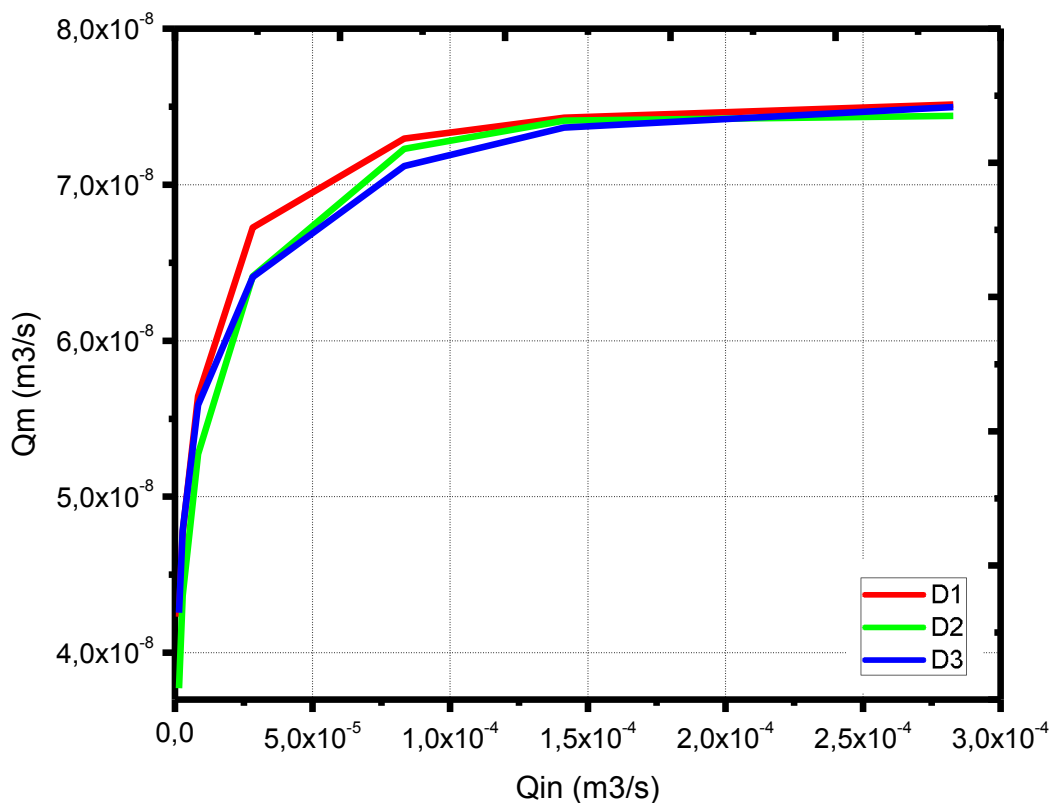
εισόδου, με βάση το οποίο συγκρίνονται και τα 3 διαφορετικά σχέδια του θαλάμου δοκιμής. Το διάγραμμα που προέκυψε για τις συνθήκες εξόδου και μεμβράνης όπως στην περίπτωση 9 ($P_{out}=15.8$ bar, HTI μεμβράνη) και εξόδου 10 διαφορετικές παροχές από $Q_{in}=6.94E-08$ m³/s – $1.41E-04$ m³/s, είναι το εξής:



Σχ. 33 Παροχή μέσα από τη μεμβράνη σε συνάρτηση της παροχής εισόδου

Είναι φανερό ότι η παροχή μέσα από τη μεμβράνη αυξάνεται με την αύξηση της παροχής εισόδου, ραγδαία στην αρχή και λιγότερο στο τέλος, και τείνει να σταθεροποιηθεί σε μία μέγιστη τιμή. Αυτό συμβαίνει διότι όσο αυξάνεται η παροχή εισόδου τόσο γρηγορότερα απομακρύνεται το γλυκό νερό που εισέρχεται στο αλατόνερο, δηλαδή μειώνεται η επίδραση του φαινομένου external concentration polarization. Το διάγραμμα αυτό δείχνει ότι σε κάθε περίπτωση του PRO απαιτείται μια βελτιστοποίηση της παροχής εισόδου που θα δίνει τη μέγιστη δυνατή παροχή εξόδου, και άρα μέγιστο δυνατό παραγόμενο έργο, με το ελάχιστο δυνατό κόστος για τη διαχείριση της παροχής εισόδου.

Το διάγραμμα αυτό δημιουργήθηκε και για τα 3 σχέδια του θαλάμου δοκιμής, έτσι ώστε να μπορούν να συγκριθούν:



Σχ. 34 Qm-Qin διάγραμμα για τα 3 σχέδια του θαλάμου δοκιμής

Είναι φανερό ότι τα 3 σχέδια έχουν ελάχιστες διαφορές με βάση την παροχή μέσα από τη μεμβράνη που δίνουν για τα τις ίδιες παροχές εισόδου, και πιο συγκεκριμένα για μικρά Q_{in} τα Q_m είναι ίδια, ενώ για μεγάλα Q_{in} και τα 3 συγκλίνουν στην ίδια μέγιστη τιμή του Q_m . Οι μόνες διαφορές είναι για μεσαία Q_{in} όπου το αρχικό σχέδιο δίνει μεγαλύτερες τιμές για το Q_m και συγκλίνει γρηγορότερα στη μέγιστη τιμή.

Από αυτό συμπεραίνουμε ότι οι αλλαγές στην είσοδο και την έξοδο του σχεδίου έδωσαν πολύ μικρές αλλαγές στην παροχή μέσα από τη μεμβράνη. Έτσι για τη βελτίωση του θαλάμου δοκιμής πρέπει να γίνουν δοκιμές με αλλαγές στο κυρίως και στο περιφερειακό κανάλι της ροής, είτε στους κατευθυντήρες της. Τέλος, με τη δοκιμή νέων σχεδίων θαλάμου δοκιμής π.χ. κυλινδρικού μπορεί να παρατηρηθούν βελτιώσεις στην ροή μέσα από τη μεμβράνη.